DEVELOPMENT OF OPTOFLUIDIC SENSORS FOR

REMOTE MONITORING APPLICATIONS

DEVELOPMENT OF OPTOFLUIDIC SENSORS FOR REMOTE MONITORING APPLICATIONS

By ERIC JAMES MAHONEY, B.TECH.

A Thesis

Submitted to the School of Graduate Studies

In Partial Fulfillment of the Requirements for the Degree

Doctor of Philosophy

McMaster University

DOCTOR OF PHILOSOPHY (2020)   McMaster University

School of Biomedical Engineering   Hamilton, Ontario

TITLE: Development of Optofluidic Sensors for Remote

                               Monitoring Applications

AUTHOR: Eric Mahoney, B.Tech., McMaster University

SUPERVISOR: Professor Qiyin. Fang

COMMITTEE: Professor P. Ravi. Selvaganapathy

                               Professor H. Schellhorn

NUMBER OF PAGES: XXVI, 210

Lay Abstract

Dissolved gases have been detected in fluid samples as indicators of health and microbial activity by measuring changes in the intensity of fluorescence emitted from gas sensitive fluorescent dyes. These sensors can often be miniaturized and integrated to measure several parameters from a single platform. Several sensing platforms may be integrated into a continuous monitoring network. However, the cost of complete remote sensing networks prohibits the widespread deployment of these devices. The aim of this research was to improve the sensitivity of fluorescence-based sensors, reducing dependence on expensive detectors and light sources. The sensitivity of a fluorescence based dissolved oxygen sensor was optimized using Total Internal Reflection. A computer model was developed to identify important design parameters and their contributions to sensor performance. The model was validated by comparison with experimental measurements. Finally, an optical ammonia sensor is under development based on the dissolved oxygen experiments and model results.

Abstract

In this dissertation fluorescence-based sensors for dissolved gases were developed for remote health monitoring applications including urine analysis. Detection of dissolved gases demonstrate diagnostic potential in body fluids, and indicate the metabolism of microorganisms driven by contaminated water. The emphasis of this research was on optimizing the sensitivity of fluorescence-based fluid sensing systems by configuring key design parameters towards cost reduction. A review of urine analysis indicated several methods for imaging, particle analysis, and detection of dissolved analytes. The review encourages readers to consider integrating sensing systems to provide additional context to results. An optical Dissolved Oxygen (DO) sensor was reproduced using phosphorescent organometallic dyes. The sensitivity of the DO sensor was experimentally optimized by employing Total Internal Reflection (TIR) of excitation light within the multilayered device by controlling the incident angle and sensitive film thickness. Novel 3D ray tracing-based computer models were developed based on the experimental results to explain the sensitivity enhancement mechanism of TIR. The path of light within the device and fluorescence generation sites were visualized and relative sensitivity was predicted. The model was validated by comparison with experimental results and expanded to predict the relative sensitivity of devices using different coupling strategies. This new optical model enables researchers to select an optimal coupling and detection scheme given their unique sensor design and application. A fluorescence based optofluidic sensor for Ammonia was redesigned based on experiment and simulation results. An optofluidic chip reader was produced to measure fluorescence sensors using low cost consumer electronics. The sensitivity of the ammonia sensor module has not been demonstrated; however, identified design challenges will be overcome in future efforts. As a result of this research, the cost of optofluidic sensing systems may be reduced towards enabling widely deployed remote monitoring networks for health and water quality.

Acknowledgements

I would like to thank my supervisor Dr. Qiyin Fang for giving me the opportunity to work with his team. Thank you very much for your thoughtful guidance and advice that made it possible for me to greatly expand my skills and interests during my studies. I must also thank the members of my supervisory committee, Dr. Ravi Selvaganapathy, and Dr. Schellhorn for their guidance as my project developed. Thank you for asking key questions that led me to consider new facets of my project, and for helping me with adjusting my methods and approach to problem solving. I would like to thank Dr. Deen for inspiring me to expand my understanding of sensors, actuators, programming, and hardware design. Thanks to our discussions I was able to develop a prototype smart enclosure. Thank you, Dr. Chan, for involving me in the eDosette project that first exposed me to the Raspberry Pi and Python programming which has since become one of my most valuable tools. Thank you, Dr. Haugen, for giving me the opportunity to speak to your students about what I have learned from experimenting with Arduino and Raspberry Pi.

Thanks to all of the members of our lab who I have had the pleasure to work with during this experience. Thank you Dr. Hirmez and Dr. Tsikouras for your assistance, especially in my early years with the group, for familiarizing me with optical design and system alignment. Thanks to Dr. Yeh, Ms. Fiona Du, and Mr. Bo Xiong for improving my understanding of fluorescence and fluorescence measurement techniques. Thank you, Dr. Leo Hsu, for first exposing me to 3D modelling, photolithography, and device fabrication procedures. To everyone in our lab, thank you very much for your support and for helping me to maintain my health and sanity.

I must thank my instructors from the Bachelor of Technology program at McMaster University for providing me with the foundation that I needed to succeed in my graduate studies. Thank you Dr. Geng for the summer work experience that helped greatly with my approach to lab work and troubleshooting approaches from our HPLC work together. Thanks to your guidance I met Dr. Fang and was able to continue my studies at the graduate level. Thank you to Dr. Singh and Dr. Alani for the many discussions and unplanned stairwell and hallway meetings. Many great ideas were generated from those short encounters. A special thanks goes to

Mrs. Paula Gremmen who I believe influenced my lab work process more than anyone. Thank you very much Paula for the incredible training experience. Your efforts have helped me to approach problems pragmatically, and to keep safety and hazard assessment at the core of every experimental procedure.

More than anyone I give my thanks and appreciation to my late mother Judy Mahoney. Any time I had my doubts your unwavering faith and confidence brought me back to my work. There is no doubt in my mind that I would have chosen a different path if it weren't for your support. Thank you so much for editing my earlier work. I pray this volume will find its place beside yours on the shelf. I wish more than anything that you could have seen what I had accomplished. Thanks go to my father, siblings, grandparents, and the rest of my family for their support through this chapter of challenges. Special thanks to my late godfather Ron S. Jones for teaching me to hunt and helping me to see the forest through the trees. Thanks to the love and support I have received from friends, family, and the incredible faculty here at McMaster University I have been able to persevere through this most challenging and also most rewarding chapter of my life thus far. I truly could not have done it without you.

Contents

List of Figures

List of Tables

List of Abbreviations

µPAD	Paper based Analytic Devices
2D	2 Dimensional
3D	3 Dimensional
AC	Alternating Current
ADC	Analog to Digital Converter
ADL	Activities of Daily Living
APD	Avalanche Photodiodes
APTES	3-aminopropyltriethoxysilane
BC	Bladder Cancer
BSB	Burke Science Building
Cac	Cellulose Acetate
Cacp	Cellulose Acetate Propionate
CAD	Canadian Dollar
CCD	Charge Coupled Device
CEAB	Canadian Engineering Accreditation Board
CFI	Canadian Foundation of Innovation
CFU	Colony Forming Unit
CMOS	Complementary Metal-Oxide-Semiconductor
CNDN	Canada's National Design Network
Cr	Creatine
Crn	Creatinine
CSV	Comma Separated Value
DAQ	Data Acquisition System
DC	Direct Current
DCC	N,N'-dicyclohexylcarbodiimide

DI	Deionized
DNA	Deoxyribonucleic Acid
DO	Dissolved Oxygen
dsDNA	double stranded DNA
ELISA	Enzyme Linked Immunosorbent Assay
EMIT	Enzyme Multiplied Immunoassay Technique
FDA	Food and Drug Administration
FOV	Field of View
FPS	Frames per Second
FWHM	Full Width at Half Maximum
HPF	High Powered Field
HPLC	High Performance Liquid Chromatography
HPV	Human Papillomavirus
HRP	Horseradish Peroxidase
HSI	Hyperspectral Imaging
HVAC	Heating Ventilation and Air Conditioning
IC	Integrated Circuit
ID	Identification
IoT	Internet of Things
IPA	Isopropyl Alcohol
IR	Infrared
LAMP	Loop Mediated Isothermal Amplification
LCD	Liquid Crystal Display
LC-MS	Liquid Chromatography – Mass Spectrometry
LDR	Light Dependent Resistor
LED	Light Emitting Diode
LFA	Lateral Flow Assay
LFIA	Lateral Flow Immunoassay

MALDI-TOF-MS	Matrix Assisted Laser Desorption/Ionization – Time of Flight – Mass Spectrometry
MF	Microfluidic
MLC	Micellar Liquid Chromatography
MOSFET	Metal Oxide Semiconductor Field-Effect Transistor
mRNA	Messenger RNA
MS	Mass Spectrometry
MSA	Methanesulfonic Acid
MSI	Multispectral Imaging
MW	Molecular Weight
MWCNT	Multiwalled Carbon Nanotubes
NA	Numerical Aperture
ND	Neutral Density
NIR	Near Infrared
NSERC	Natural Science and Engineering Research Council
NTC	Negative Temperature Coefficient
OD	Optical Density
OF	Optofluidic
ORF-RE	Ontario Research Fund-Research Excellence
PBS	Phosphate Buffered Saline
PCR	Polymerase Chain Reaction
PDMS	Poly dimethylsiloxane
PEDD	Paired Emitter-Detector Diode
PEGDA	Poly(ethylene glycol) dicarboxylic acid
PID	Product Integral Difference
PMT	Photomultiplier Tubes

PoC	Point of Care
PTC	Positive Temperature Coefficient
PWM	Pulse Width Modulation
QD	Quantum Dot
QoL	Quality of Life
qRT-PCR	Quantitative Realtime PCR
RBC	Red Blood Cell
RFID	Radio Frequency Identification
RH	Relative Humidity
RI	Refractive Index
RNA	Ribonucleic Acid
RPA	Recombinase Polymerase Amplification
RPi	Raspberry Pi Computer
RTD	Resistive Temperature Detector
$Ru(dpp)_3$	Tris(4,7-diphenyl-1,10-phenanthroline) Ruthenium(II) dichloride complex
SG	Specific Gravity
SNR	Signal to Noise Ratio
SPR	Surface Plasmon Resonance
STI	Sexually Transmitted Infection
TA	Teaching Assistant
TIR	Total Internal Reflection
TIRF	Total Internal Reflection Fluorescence
UA	Uric Acid
UCNP	Upconverting Nanoparticles
USD	United States Dollar
UTI	Urinary Tract Infection
UV	Ultraviolet

UVC	Ultraviolet-C
WASPLab	Walk Away Specimen Processor and smart incubator
WBC	White Blood Cell
Wi-Fi	Wireless Fidelity
WTP	Wastewater Treatment Plant

Declaration of Academic Achievement

Academic Works

First-Author Publications

Eric Mahoney, Jessica Kun, Marek Smieja, Qiyin Fang. (2020). Review—Point-of-Care Urinalysis with Emerging Sensing and Imaging Technologies. Journal of Electrochemical Society. 167(3): 037518. Available from: http://dx.doi.org/10.1149/2.0182003JES

Eric Mahoney, Huan-Hsuan (Leo) Hsu, Fei Du, Bo Xiong, P. Ravi Selvaganapathy, Qiyin Fang. (2019). Optofluidic Dissolved Oxygen Sensing With Sensitivity Enhancement Through Multiple Reflections. IEEE Sensors Journal. 19(22): 10452-10460. Available from: http://dx.doi.org/10.1109/JSEN.2019.2932414

Eric Mahoney, Bo Xiong, Qiyin Fang. (2020). Optical Model of Light Propagation in Total Internal Reflection Fluorescence Sensors. OSA Journal of Applied Optics. Accepted for publication on Oct. 14, 2020 – In press.

Eric Mahoney, Bo Xiong, Herb. E. Schellhorn, P. Ravi Selvaganapathy, and Qiyin Fang. (2020). Fluorescence-Based Ammonia and Creatinine Sensing for Environmental and Point of Care Monitoring. Manuscript in preparation for submission to IEEE Sensors Journal.

Co-Authored Publications

Bo Xiong, Eric Mahoney, Joe Lo, Qiyin Fang. (2020). A Frequency-domain optofluidic dissolved oxygen sensor with total internal reflection design for in situ monitoring. IEEE Journal of Selected Topics in Quantum Electronics. JSTQE-CON-BP2021-083. Available from: http://dx.doi.org/10.1109/JSTQE.2020.2997810

Gabardo C, Adams-McGavin R, Fung B, Mahoney E, Fang Q, Soleymani L. (2017). Rapid prototyping of all-solution- processed multi-lengthscale electrodes using polymer-induced thin film wrinkling. Scientific Reports. 7(42543): 1-9. Available from: http://dx.doi.org/10.1038/srep42543

Conference Presentations

Eric Mahoney, Colleen Chau, Qiyin Fang. Experiential learning of data acquisition and sensor networks with a cloud computing platform. Proc. SPIE 11143, Fifteenth Conference on Education and Training in Optics and Photonics: ETOP 2019, 111433X, July 02, (**2019**).

Eric Mahoney, Fiona Du, Qiyin Fang. Optofluidic Dissolved Oxygen Sensor for Integrated Water Quality Monitoring. IC-IMPACTS Summer Institute on Nanotechnologies, University of Alberta, Edmonton, AB, June 06, (**2016**).

Eric Mahoney, Fei Geng. Analysis of Phosphorylation Isoforms of Intact Protein by HPLC. Space Vision and Advanced Robotics Workshop, Brampton, ON, May 21, (**2014**).

Eric Mahoney, Fei Geng. Analysis of Phosphorylation Isoforms of Intact Protein by HPLC. EnviroAnalysis 2013, Toronto, ON, September 15-18, (**2013**).

Project Contributions

The Review of urine analysis methods for detecting targets in urine samples and urination related activities of daily living (**Chapter 2**) was conducted my me and Ms. Jessica Kun. My contribution to the review paper included the sections regarding chemical analysis methods and monitoring activities of daily living related to urination. Our review was guided by urologist Dr. Smieja, and Dr. Qiyin Fang.

The original optofluidic dissolved oxygen sensor highlighted in **Chapter 3** was developed by the previous Masters student Ms. Fiona Du with the support of Dr. Leo Hsu, Dr. P. Ravi Selvaganapathy, and Dr. Qiyin Fang. I assisted with fluorescence intensity measurements and expanded on the numerical model initially prepared by Ms. Fiona Du. Mr. Bo Xiong reviewed the work and contributed to the discussion of the sensitivity enhancement mechanism. I completed the manuscript started by Dr. Hsu and revised the manuscript with feedback from the coauthors.

I Developed a novel 3D model in Zemax Opticstudio (**Chapter 4**) expanding on previous TIR models and the work presented in Chapter 3 to demonstrate relative sensitivity profiles for a variety of coupling scenarios. I performed the simulations of collimated input and focused input myself. Another PhD student, Mr. Bo Xiong, suggested adding the prism coupling

simulations and provided initial CAD models of prisms that I adapted for use in the simulations. The series of simulations I have conducted using the model demonstrate the path of light within multilayered optical sensors. I present the relationship between incident angle and device sensitivity graphically for various coupling scenarios based on quantitative optical power predictions. I validate the model by comparing the focused coupling simulation results to the experimental results presented in Chapter 3. My latest simulations demonstrate the intensity of incident light within the sensitive fluorescent layer of the multilayer sensor showing changes in the size and shape of excitation spots, and the distribution of spots within the sensor. I perform independent calculations to identify the importance of variations in experimental and simulated light sources in simulation accuracy. I performed all simulations and wrote the manuscript for this work supported by Dr. Qiyin Fang. I revised the manuscript with feedback from coauthors.

I used the model to produce an ammonia sensor (**Chapter 5**) using a sensor structure based on the DO sensor shown in Chapter 3 and ammonia sensing results reported by other researchers. All of the reagents and standards used were prepared by myself. I performed all of the device fabrication steps and conducted all measurements during experiments. A prototype optofluidic chip reader was designed and developed by myself. The Python code to generate the GUI to control the system including light source, camera, and automating measurements was written by me. I designed and fabricated the custom circuit board used to distribute power between components, and to interface the light source with the Raspberry Pi computer. Undergraduate student Yasemin Al-Banna assisted with 3D printing the angle adjusting mount that I installed in the portable setup. Undergraduate student Lauren Sabatini assisted with 3D printing the water channel mold that I used for soft lithography during device fabrication. A manuscript has been prepared by me based on the current progress towards ammonia sensor development supported by Dr. P. Ravi Selvaganapathy, Dr. Herb. E. Schellhorn, and Dr. Qiyin Fang.

Chapter 1

Introduction

As the population of older adults continues to increase, an increase in the demand for medical services is expected (1,2). The comfort and quality of the lives of older adults can be improved by enabling aging in place while also reducing medical costs (3). Point- of-care (PoC) health monitoring devices have been proposed for early diagnosis of developing health challenges for optimal care outcomes (4,5). However, the costs associated with remote sensing networks and the challenges with integrating several sensing devices prevent their widespread use. Cost reduction of remote fluid analysis devices will also enable the deployment of environmental water quality monitoring systems (6). There is a need to further develop low cost remote monitoring systems capable of the continuous assessment of fluid samples for applications in point of care diagnostics.

1.1. MOTIVATION

Our ultimate goal was to enable aging in place of older adults with reduced medical costs to improve their quality-of-life (QoL). This has been addressed by making the home more accessible to older adults and by monitoring health from home (7,8). We decided to approach our goal from a health monitoring perspective because health is dynamic, changing continuously over time, and it can be difficult to capture developing chronic illnesses with periodic visits to clinics (9). Realizing continuous point of care health monitoring devices remains challenging but has significant potential to benefit society when successfully overcome. Remote health monitoring has been approached from the perspective of wearable devices (10–12), and monitoring devices built into the environment including smart home systems and fluid monitoring devices (8,13).

We identified continuous point of measurement fluid monitoring as an ideal subject for investigation because fluids with diagnostic potential such as urine and saliva can be easily obtained non-invasively on a continuous basis. Urine samples are particularly interesting because they are usually available in sufficient quantities and contain analytes that are useful as internal standards of reference such as Creatinine. Recent work towards the development of smartphone-based sensors (14–16), portable diagnostic kits (17), and Smart Toilets (18–20) indicates interest in solving these challenges. The cost associated with deploying and maintaining a distributed remote sensing network prevents their use. Reduction of costs while improving the sensitivity of each remote monitoring platform would enable widespread deployment of these sensing systems (9).

Our objective was to advance the realization of continuous remote fluid sensing systems. To be realized, several requirements must be addressed including the non-invasive collection and processing of fluid samples, obtaining analytes of interest in detectable quantities, and in sufficient volumes. Urine samples were identified as an excellent candidate given these selection criteria. In the ideal situation, sensing platforms would be deployed in the home that can measure sample constituents on a continuous basis to provide longitudinal health data. Longitudinal results can be used to identify trends indicative of developing challenges enabling early intervention and optimized outcomes (9). To do this, fluid monitoring devices need to be produced to have optimized sensitivity, low power requirements, and uncostly light sources, detectors, and controls. These devices should be deployed for extended periods of time without requiring maintenance, while continuously transmitting measurement results. Ideally, each platform would be capable of sensing a variety of analytes, while integrating with other platforms to provide additional context to measurements.

Optimizing the sensor module was identified as a key element of the first stage towards remote monitoring networks. Fluorescence based optofluidic devices have been demonstrated for monitoring dissolved gases in fluid samples (21,22). These optical sensors are well suited for miniaturization and integration in remote sensing platforms without suffering the drawbacks of aging electrodes associated with electrochemical sensing methods. An existing fluorescence based dissolved oxygen (DO) sensor was optimized to identify significant design parameters contributing

to device sensitivity (23). Monitoring DO in fluid samples over time is an important indicator of oxygen dependent microbial activity that can be used to determine urinary tract infection, and is also correlated with renal function and serum Creatinine (24). A simplified numerical model was prepared based on the DO sensor optimization results to understand the mechanism of sensitivity enhancement that could be applied to new sensors in the future. An advanced 3D optical model was produced as an extension of the simplified model to identify significant design considerations for optimizing multilayered optical sensors using alternative configurations.

Efforts were made to adapt the existing sensor module for alternative analytes to produce a single platform that can be deployed for testing in several environments. Ammonia was selected as a common target of interest that can be detected directly or indirectly as an indicator of other additional analytes such as Urea or Creatinine for health monitoring (25,26), and environment monitoring applications such as groundwater assessment (22). As new sensor modules were produced for alternative analytes, the experimental setup was packaged as a portable optofluidic chip reading platform.

1.2. RESEARCH ROAD MAP

A road map was developed to direct research towards the realization of remote sensing networks for longitudinal health monitoring. The development of continuous remote monitoring networks has been organized into three stages: development of independent measurement platforms, deployment of individual sensing platforms in high usage locations, and finally platform integration. The work presented in this research focuses on the first stage, development of individual sensing platforms with a focus on urine analysis. Sensor integration can be conducted in parallel to platform development in order to increase the number of analytes that can be detected on each individual system.

The development of an individual remote sensing platform can be broken down into a series of modules including the sensor module, light source, detector, sample handing, and maintenance. Once the sensing platform has been developed, the measurement results obtained from the platform can be transmitted to a server for analysis. In this work, we focused on the development of sensor modules, the light source module, and the detector module. Remote transmission of continuous

measurements has been demonstrated from a sensor station developed independently of the optofluidic sensing platform.

Sensor module development is an iterative process that involves fabrication of sensing devices for targets of interest found in fluid samples and the adaptation of sensor structures for detection of alternative analytes. In this work, urine samples have been identified as ideal target as they are easily collected non-invasively, and they contain several analytes with diagnostic potential. Once a sensor module has been produced that demonstrates sensitivity to the target analyte, the module can be optimized to improve sensitivity while reducing dependence on costly light sources and detectors. A sensor module for DO has been experimentally optimized and new sensor modules are being developed for dissolved ammonia based on the DO sensor structure.

The light source module is developed based on requirements of the sensor module. Considerations for the light source include the wavelength and intensity distribution, the divergence of the light source, and strategy used to couple the incident light to the sensor structure. Light sources may be operated continuously or pulsed depending on whether steady state or frequency domain measurements are required. The combination of specifications used will determine the relative sensitivity profile of the sensor system and the strategy used to detect the signal from the sensor. The light source module also incorporates any required excitation filters and coupling optics used to deliver the incident light to the sensor module.

The detector module is developed based on the sensor structure, light source, and coupling strategy employed, with consideration of requirements for spatial information. The detector module itself consists of the detector element, emission filters, and coupling optics to relay the signal to the detector element. If spatial information is not required, then an optical power meter can be employed for steady state fluorescence intensity measurements. If spatial information should be preserved (such as when particle tracking is required in conjunction with fluorescence measurement) then a camera module may be employed.

Reporting and analysis can be addressed once the sensor module is capable of capturing measurements. The system is connected to a wireless network to transmit measurement results continuously to a remote server for analysis.

Automated sample handling is essential for the remote deployment of the sensing platform where an operator is not available to control the device. Reservoirs, pumps, and valves required for automated sample handling may be developed in parallel with other modules of the measurement platform. Antifouling coatings can be developed to prevent the accumulation of biofilms in the sensor module in order to extend the useful lifetime of each device before maintenance is required.

Once a remote measurement platform is available it should be deployed where it can benefit a large number of users from a single location to provide the greatest benefit with respect to cost. At this stage the reliability of the system is established and adjustments can be made to optimize each platform for its final application. Ideal situations include care centers where samples from several subjects can be processed routinely for longitudinal health monitoring applications. Integration of new sensing modules into each sensing platform can be conducted in parallel to improve the amount of information collected from each device.

Finally, once remote sensing platforms have been developed and cost is further reduced through iterative improvements, several platforms can be integrated to form a distributed sensing network. Platforms may be deployed in individual homes for health monitoring applications in the form of smart toilets for example.
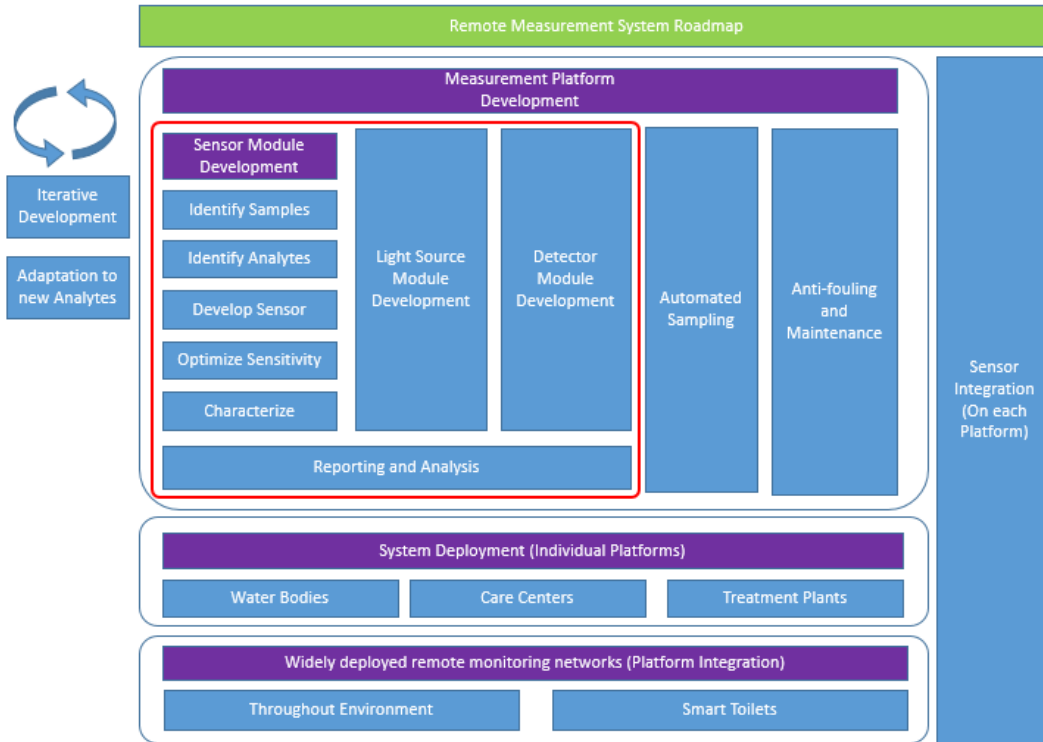
Figure 1.1 Proposed research roadmap for the development of continuous remote monitoring networks.

It should be recognized that several of the challenges facing the widespread deployment of remote health monitoring networks are common to applications in environmental water quality monitoring. The research roadmap provided here may also serve as a guide to the development of remote water quality monitoring technologies. Integrated remote water quality monitoring networks may be deployed in water treatment plants or deployed throughout the environment in places that are not easily accessible or in places without available power sources.

1.3.   THESIS OVERVIEW

The goal of this research was to develop technologies to assist the aging in place of older adults by enabling continuous non-invasive point of care health monitoring. Continuous point of care urine analysis was identified as an effective approach to non-invasive assessment of health over time with significant diagnostic potential. The successful development and integration of urine analysis devices on a single measurement platform would serve to increase the diagnostic potential of such remote monitoring

systems. Five milestones have been addressed over the course of this research towards the realization of an integrated remote health monitoring platform.

First, urine samples were identified as an ideal target for continuous non-invasive point of care diagnostics. The available methods to monitor targets of interest and activities of daily living associated with urination and their diagnostic potential were critically reviewed. Researchers are encouraged to consider the integration of compatible sensor modules to provide additional context to measurement results on a longitudinal basis. Several of the methods identified may also be applied to alternative remote fluid sensing applications.

Second, an optofluidic fluorescence-based DO sensor was optimized to enhance device sensitivity. The sensitivity of the device is assessed by measuring DO samples in the range of 0-20 ppm prepared by sparging. 0 ppm controls are prepared scavenging DO from the water with the addition of sodium sulfite. Total Internal Reflection of excitation light was used to improve the sensitivity of the sensor module to reduce dependence on costly detectors and light sources. A model was developed to describe the influence of incident angle and sensitive layer thickness on the average distance between reflection spots and device sensitivity. The design parameters identified by the simplified model provided a foundation for more advanced models to be applied to optimization of new multilayered optofluidic devices. The design of the experimentally optimized DO sensor can be modified to develop novel urine analysis devices with improved sensitivity.

Third, a 3D ray tracing-based model was developed through a series of simulations to identify significant design parameters for future device designs. The simulation was validated by comparison to experimental results. The size, shape, distribution, and relative intensity of reflection spots in the sensitive volume were predicted with respect to the coupling strategy employed. Relative sensitivity profiles for different coupling scenarios can be considered when designing a remote sensing system to strike a balance between sensitivity to target analytes and insensitivity to misalignment. The configuration of new optofluidic devices can be selected for each application with consideration of the requirements for spatial information in measurement results.

Fourth, progress was made towards the development of a multilayered optofluidic sensor module for fluorescence-based detection of ammonia. Improvements were made to the light source module and controls module to ensure light source stability during measurement. Improvements were made to the detection module to obtain consistent images from the sensor while preserving spatial information. The relative sensitivity profile of the sensor with respect to incident angle was predicted using our new advanced model. Although the prototype ammonia sensor did not demonstrate sensitivity to ammonia experimentally, significant design challenges have been identified and discussed. Further development of the current sensor prototype may lead to the realization of a successful sensor for the direct assessment of dissolved ammonia and indirect detection of additional analytes on the same monitoring platform.

Finally, a portable optofluidic chip reading prototype was developed using relatively low-cost consumer electronics for the alignment and measurement of fluorescence-based fluid sensors. An adjustable angle clamp allows the quick installation and replacement of optofluidic chips and adjustment of incident angle. The mount can be translated laterally with respect to the light source module to switch between bottom side coupling and edge coupling. The light source module can also be easily interchanged. The platform is capable of transmitting measurement results continuously over a wireless network. Further development of the prototype fluorescence chip reader may enable the automation of sample collection and processing, and may be deployed as part of a smart toilet platform for non-invasive longitudinal health monitoring.

1.4.   THESIS ORGANIZATION

The introduction chapter presented here as **Chapter 1** provides an overview of the motivations for performing this research while identifying challenges associated with the development of optofluidic devices for continuous remote monitoring of urine samples from the point of care.

Chapter 2 provides a critical review of urine analysis targets and detection methods that are useful for clinical diagnosis of health challenges. Urine analysis is identified as a promising approach to continuous non-invasive monitoring of body fluids from the point of care. Approaches to urine analysis using imaging techniques, chemical analysis methods, and urination related activities of daily living are discussed. The importance of

integrating compatible sensing devices into continuous remote monitoring platforms is identified.

Chapter 3 demonstrates the optimization of an experimental optofluidic dissolved oxygen sensor. The sensitivity of the sensor module is assessed by measuring DO standards in the range of 0-20 ppm prepared by sparging. The importance of the incident angle used to generate fluorescence and the sensitive layer thickness for optimizing the sensitivity of DO sensors using a focused collimated input are discussed. The results indicate that the sensitivity of the device is greatest when the incident light is confined within the glass substrate and sensitive layer. The experimentally optimized DO sensor and simplified numerical model provide a foundation for the development of advanced models and new optofluidic devices employing TIR for the continuous analysis of urine samples.

Chapter 4 investigates the relative sensitivity of multilayered optofluidic sensors with respect to the incident angle of light when using different coupling scenarios using 3D ray tracing simulations. The simulation is based on the experimentally tested DO sensor and validated against experimental results. The importance of increasing the path length of light within the sensitive volume is highlighted. Simulation results also predict the shape and size of the fluorescence generation sites. These novel simulations can be applied to the rapid development and optimization of new TIR based optofluidic devices considering the application requirements.

Chapter 5 presents the current progress towards developing an optofluidic sensor for dissolved ammonia. A fabrication method is developed for the optofluidic ammonia sensor. A prototype optofluidic chip reading platform for fluorescence-based sensors is developed enabling the control of light sources, detectors, and automation of fluorescence measurements. The prototype sensing platform can be employed for the continuous measurement of new multilayered optofluidic devices. Future development is expected to enable the continuous remote monitoring of ammonia directly and the indirect analysis of additional compounds of interest in urine samples by employing enzymatic reactions.

Chapter 6 provides the conclusions of the thesis, summarizing the progress made towards the development of a remote monitoring platform for optofluidic urine analysis devices. The direction of future work and next

steps are presented based on the current results and the proposed development roadmap.

1.5.   CONTRIBUTIONS

The research presented in this dissertation is organized as three first-author journal articles from **Chapter 2 - Chapter 4** and a manuscript presented as **Chapter 5**. I prepared the first drafts of content presented in Chapters 1, and 3 - 6. I developed responses to questions from reviewers and made the required changes to the published articles with guidance from Dr. Fang and the approval of all co-authors.

The review paper presented in **Chapter 2** was published based on the combination of literature reviews for urine analysis methods conducted by myself and Ms. Jessica Kun. I prepared a review of methods for detection of dissolved analytes in urine and urination related activities of daily living as I worked to develop an optofluidic device for the detection of ammonia in urine and water. Ms. Jessica Kun prepared the review of imaging-based detection methods for urinalysis as she produced a lensless imaging device for the diagnosis of Urinary Tract Infections. Professor Fang challenged us to prepare a review of methods in urine analysis by combining our respective literature searches and assisted with integrating and reviewing the papers. Dr. Smieja provided insight and feedback from his perspective as a urologist to guide our reviews. The significant contribution of the critical review of urine analysis is the identification of the current landscape of available technology, and the importance of integrating compatible devices to realize remote urine analysis systems.
Eric Mahoney, Jessica Kun, Marek Smieja, Qiyin Fang. **(2020)**. Review—Point-of-Care Urinalysis with Emerging Sensing and Imaging Technologies. Journal of Electrochemical Society. 167(3): 037518. Available from: http://dx.doi.org/10.1149/2.0182003JES

The prototype optofluidic device presented in **Chapter 3** was initially prepared by Ms. Fiona Du for the detection of Dissolved Oxygen. I assisted with final measurements of the DO sensor. I completed the manuscript based on the platform and expanded on the model used to explain sensitivity enhancement in multilayered optofluidic sensors. I also took a lead role in addressing reviewer questions and concerns. The significant contributions of this work include the development of an experimentally optimized fluorescence-based DO sensing platform, and a simplified

numerical model describing the mechanism of sensitivity enhancement.
Eric Mahoney, Huan-Hsuan (Leo) Hsu, Fei Du, Bo Xiong, P. Ravi
Selvaganapathy, Qiyin Fang. **(2019)**. Optofluidic Dissolved Oxygen Sensing
With Sensitivity Enhancement Through Multiple Reflections. IEEE Sensors
Journal. 19(22): 10452-10460. Available from:
http://dx.doi.org/10.1109/JSEN.2019.2932414

I was inspired to develop a 3D ray tracing-based model shown in
Chapter 4 to better describe sensitivity enhancement using different light
coupling scenarios and validated the model by comparison to experimental
results. Mr. Bo Xiong suggested modelling the prism-assisted coupling
situation by adding prisms to the simulation. I conducted each of the
simulations predicting relative sensitivity and the distribution of reflections
in multilayered devices. I prepared the manuscript and took a lead role in
addressing reviewer questions. The significant contributions of this work
include the development of an advanced model describing sensitivity
enhancement in multilayered optofluidic devices, and the discussion of
application-based design considerations for future devices.
Eric Mahoney, Bo Xiong, Qiyin Fang. **(2020)**. Optical Model of Light
Propagation in Total Internal Reflection Fluorescence Sensors. OSA Journal
of Applied Optics. Accepted for publication on Oct. 14, 2020 – In press.

The technical challenges overcome thus far towards the development of
an optofluidic ammonia sensor are presented as a manuscript in **Chapter 5.**
As a result of the DO sensor experiments and simulation results, I modified
the sensor platform to produce an optofluidic sensor for ammonia. I
constructed the optofluidic chip reading platform to measure a variety of
fluorescence-based sensors. I developed the custom python code prepared
to control the prototype optofluidic chip reader, which is presented as a
diagram in **Appendix A**. The significant contributions of this work include
the production of a prototype fluorescence chip reader that can be
reconfigured to measure a range of fluorescent sensors, and detailed
discussion of design challenges identified during the ammonia sensor
module development.
Eric Mahoney, P. Ravi Selvaganapathy, Qiyin Fang. **(2020)**. Fluorescence-
Based Ammonia and Creatinine Sensing for Environmental and Point of
Care Monitoring. Manuscript in preparation for submission to IEEE Sensors
Journal.

During the course of my research I also had the opportunity to develop a smart sensor station with the purpose of collecting sensor data for students to analyze in course assignments. Professor Fang determined the requirements for the sensor station and data management as I developed the prototype. I assisted Ms. Colleen Chau with preparing a manuscript summarizing the initial sensor station results, and its potential for use in teaching and learning with the guidance of Professor Fang. The work was presented at the SPIE Conference on Education and Training in Optics and Photonics. The conference proceedings from the event are presented as **Appendix B**. The smart sensor station has been successfully demonstrated for the continuous transmission of sensor data, and has been applied as an educational tool in an Applied Statistics for Engineering course.

References

[1]   United Nations. World populating ageing 2015 [Internet]. New York; 2015. Available from: https://www.un.org/en/development/desa/population/publications/pdf/ageing/WPA2015_Report.pdf

[2]   Nathan V, Paul S, Prioleau T, Niu L, Mortazavi BJ, Cambone SA, et al. A Survey on Smart Homes for Aging in Place: Toward Solutions to the Specific Needs of the Elderly. IEEE Signal Process Mag [Internet]. 2018 Sep;35(5):111–9. Available from: https://ieeexplore.ieee.org/document/8454407/

[3]   Jayantha WM, Qian QK, Yi CO. Applicability of 'Aging in Place' in redeveloped public rental housing estates in Hong Kong. Cities [Internet]. 2018 Dec;83(July):140–51. Available from: https://doi.org/10.1016/j.cities.2018.06.016

[4]   Saatkamp CJ, Silveira L. Quantifying creatinine and urea in human urine through Raman spectroscopy aiming at diagnosis of kidney disease Quantifying creatinine and urea in human urine diagnosis of kidney disease.

[5]   Fava EL, Silva TA, Prado TM do, Moraes FC de, Faria RC, Fatibello-Filho O. Electrochemical paper-based microfluidic device for high throughput multiplexed analysis. Talanta [Internet]. 2019;203(May):280–6. Available from: https://doi.org/10.1016/j.talanta.2019.05.081

[6]   Kavi Priya S, Shenbagalakshmi G, Revathi T. Design of smart sensors for real time drinking water quality monitoring and contamination detection in water distributed mains. Int J Eng Technol. 2019;7(1.1):47–51.

[7]   Tamura T. Home geriatric physiological measurements. Physiol Meas. 2012;33(10).

[8]   Majumder S, Aghayi E, Noferesti M, Memarzadeh-Tehran H, Mondal T, Pang Z, et al. Smart Homes for Elderly Healthcare—Recent Advances and Research Challenges. Sensors [Internet]. 2017 Oct 31;17(11):2496. Available from: http://www.mdpi.com/1424-8220/17/11/2496

[9]   Gokalp H, Clarke M. Monitoring activities of daily living of the elderly and the potential for its use in telecare and telehealth: a review. Telemed J E Health [Internet]. 2013;19(12):910–23. Available from: http://www.ncbi.nlm.nih.gov/pubmed/24102101

[10]   Charlon Y, Fourty N, Bourennane W, Campo E. Design and evaluation of a device worn for fall detection and localization: Application for the continuous monitoring of risks incurred by dependents in an Alzheimer's care unit. Expert Syst Appl [Internet]. 2013;40(18):7316–30. Available from: http://dx.doi.org/10.1016/j.eswa.2013.07.031

[11]   Zheng YL, Ding XR, Poon CCY, Lo BPL, Zhang H, Zhou XL, et al. Unobtrusive sensing and wearable devices for health informatics. IEEE Trans Biomed Eng. 2014;61(5):1538–54.

[12]   Abbate S, Avvenuti M, Bonatesta F, Cola G, Corsini P, Vecchio A. A smartphone-based fall detection system. Pervasive Mob Comput [Internet]. 2012;8(6):883–99. Available from: http://dx.doi.org/10.1016/j.pmcj.2012.08.003

[13]   Tsukiyama T. In-home health monitoring system for solitary elderly. Procedia Comput Sci. 2015;63:229–35.

[14]   Liu J, Geng Z, Fan Z, Liu J, Chen H. Point-of-care testing based on smartphone: The current state-of-the-art (2017–2018). Biosens Bioelectron [Internet]. 2019;132(November 2018):17–37. Available from: https://doi.org/10.1016/j.bios.2019.01.068

[15]   Sun AC, Hall DA. Point-of-Care Smartphone-based Electrochemical Biosensing. Electroanalysis. 2019;31(1):2–16.

[16]   Cho S, Park TS, Nahapetian TG, Yoon JY. Smartphone-based, sensitive μPAD detection of urinary tract infection and gonorrhea. Biosens Bioelectron [Internet]. 2015;74(January):601–11. Available from: http://dx.doi.org/10.1016/j.bios.2015.07.014

[17]   Lepowsky E, Ghaderinezhad F, Knowlton S, Tasoglu S. Paper - Based Assays for Urine Analysis. Biomicrofluidics [Internet]. 2017;11(051501):1–34. Available from: https://doi.org/10.1063/1.4996768

[18]   Mayer P, Güldenpfennig F, Panek P. Towards smart adaptive care toilets. Stud Health Technol Inform. 2019;260(May):9–16.

[19]   Bae JH, Lee HK. User Health Information Analysis with a Urine and Feces Separable Smart Toilet System. IEEE Access. 2018;6:78751–65.

[20]   Ranjitkar P. Toilet lab: Diagnostic tests on smart toilets? Clin Chem. 2018;64(7):1128–9.

[21]   Ramamoorthy R, Dutta PK, Akbar S a. Oxygen sensors: Materials, methods, designs. J Mater Sci. 2003;38:4271–82.

[22]   Waich K, Mayr T, Klimant I. Talanta Fluorescence sensors for trace monitoring of dissolved ammonia. Talanta. 2008;77:66–72.

[23]   Du F. Development of an Optofluidic Platform Based on Total Internal Reflection- Application of Dissolved Oxygen Sensing for Water Monitoring. 2015;(August):1–86.

[24]   Giannakopoulos X, Evangelou A, Kalfakakou V, Grammeniatis E, Papandropoulos I, Charalambopoulos K. Human bladder urine oxygen content: Implications for urinary tract diseases. Int Urol Nephrol [Internet]. 1997 Jul;29(4):393–401. Available from: http://link.springer.com/10.1007/BF02551103

[25]   Deng S, Doherty W, McAuliffe MAP, Salaj-Kosla U, Lewis L, Huyet G. A low-cost, portable optical sensing system with wireless communication compatible of real-time and remote detection of dissolved ammonia. Vol. 6, Photonic Sensors. 2016.

[26]   Wakida FT, Lerner DN. Non-agricultural sources of groundwater nitrate: A review and case study. Water Res. 2005;39(1):3–16.

Chapter 2

Review—Point-of-Care Urinalysis with Emerging Sensing and Imaging Technologies

Eric Mahoney,[1,=] Jessica Kun,[1,=] Marek Smieja,[2] and Qiyin Fang[1,3,z]

[1]*School of Biomedical Engineering, McMaster University, 1280 Main St. West, Hamilton, Ontario, L8S 4K1, Canada*

[2]*Department of Pathology and Laboratory Medicine, McMaster University, 1280 Main St. West, Hamilton, Ontario, L8S 4K1, Canada*

[3]*Department of Engineering Physics, McMaster University, 1280 Main St. West, Hamilton, Ontario, L8S 4K1, Canada*

[=]*Contributed equally.*

[z]*Corresponding Author qiyin.fang@mcmaster.ca*

Introduction to Review Paper

Chapter 2 includes a review paper written and published in 2019 with Jessica Kun, Dr. Smieja, and Dr. Qiyin Fang. My contribution as an equally contributing first author was to complete the literature review of chemical analysis of urine samples and Activities of Daily Living associated with urinalysis. My review focused on targets of interest, detection methods, and applications. Ms. Jessica Kun completed the review of biological targets and imaging methods in urine analysis. Her review focused on microscopy and imaging techniques for pre-screening urine samples for Urinary Tract Infections. Dr. Smieja contributed by advising our review based on his experience as a urologist, and invited us to see the urine testing facility at St. Joseph's Healthcare. Professor Fang guided our reviews and made significant revisions as we combined our work. He revised the content of the review prior to publication and was the first contact for reviewers. The significance of this critical review involves identifying the current landscape of urine analysis targets and detection methods. Researchers are encouraged to consider the compatibility and integration of future devices towards the realization of effective urine analysis platforms for remote health monitoring applications.

Contents of Review Paper

Abstract of Review Paper

Urine testing is a powerful clinical diagnostic tool. The noninvasive collection of samples and wide range of diagnostic targets found in urine makes urinalysis well suited for point-of-care (PoC) monitoring applications. Complete urinalysis testing faces many limitations due to the large quantity of samples processed, the time required for testing, and the labor involved in sample preparation and processing. Development of PoC urinalysis devices with microfluidic technology can enable the detection of infections and monitoring of chronic disease while reducing the demand on testing facilities. In this article, current approaches in clinical urinalysis are reviewed. Emerging sensing and imaging technologies specifically suitable for point-of-care examination of urine samples are discussed with an outlook on the future of point of care urinalysis devices as well as emerging applications enabled by these technologies such as in situ monitoring of Activities of Daily Living (ADL).

2.1. INTRODUCTION

Urine samples are complex and contain many components that are indicative of patient health. Urinalysis is a valuable noninvasive diagnostic tool in patient care, for example, it aids in the diagnosis of various urologic and renal conditions; and it provides evidence of complications in asymptomatic patients [1]. Many illnesses, such as sexually transmitted infections (STI's) may be asymptomatic and lead to the development of more serious health problems over time if not properly treated [2].

A complete urinalysis includes physical, chemical, and microscopic examination of a urine sample. A physical examination includes visual analysis of the color and odor of the urine, a chemical examination determines the pH and protein/chemical content of the sample, while microscopic examinations focus on the morphology of particles [3]. Different tests have been implemented to detect these biomarkers to aid in patient diagnosis. For example, blood cells and casts are indicative of kidney health and can be used to detect acute kidney injury, and to monitor the progression of chronic kidney disease. A full comprehensive review of urinalysis can be found in Strasinger et al [4].

In general, a complete urinalysis requires trained technicians to operate on complex instruments in central processing facilities which may hold thousands of samples at a time [5]. Many of the microscopy tests are time consuming due to the need to culture and manual examination. Given a large number of the results are negative, this approach requires many resources, labor, and at a high over all system cost. There are challenges with storing and transporting urine samples to testing facilities. Transportation of samples containing test strips can also lead to degradation of targets of interest [6]. To mitigate these issues, point-of-care (PoC) devices can be implemented, either at the clinic or for in-home care. Commonly available PoC urinalysis devices include dip strips for pregnancy testing, and urinary tract infections (UTIs). Urinalysis tests are often performed to diagnose symptomatic illnesses or performed on a routine basis. It is difficult to make clinical decisions based on some test results because there can be a large variability in the contents of a 'normal' sample between individuals, and even for a single person over time [7].

The capability of processing samples directly at the site of collection would significantly reduce the demand on testing facilities and associated cost, while also reducing the risk of improper storage and transportation.

Further development of PoC testing devices would enable the continuous monitoring of an individual patient in order to establish a personalized baseline [8].

For example, a common, rapid, and cost-effective test that can be done on site is the dipstick test, which is often employed in cases where urinary tract infections are suspected. Dipsticks are devices coated with reagents that change color in the presence of an analyte, such as nitrite [3]. The benefit of such a test is that it only takes a few seconds to change color, giving a preliminary diagnosis in real time. Extensive clinical studies and meta-analyses have been done to determine the diagnostic accuracy of the dipstick test. In general, it has been shown that screening by dipstick alone carries the risk of missing infections and other urinary diseases. Urine dipsticks may give false-negative results in the case of dilute urine samples or samples in which the pathogen does not produce nitrite, such as Enterococcus and Staphylococcus [9]. Urinary pH is also tested with a dipstick and is useful for the diagnosis of UTIs, as alkali urine indicates the potential presence of microorganisms breaking down urea. Urinary pH change, however, is not specific to UTIs, but also associated with other conditions [3]. In order to get a more specific diagnosis, microscopic examination is employed. As a result, urine dipsticks are not recommended as the sole diagnostic tool nor a PoC test [9,10] but combined with other methods of urinalysis in clinical laboratories [11].

This review focuses on recently developed point-of-care device technologies that can be applied to urinalysis. It covers the strategies for measuring the contents of urine samples and an outlook on the development of PoC urinalysis devices. We have divided the paper into three distinct sections in order to cover urinalysis from several perspectives. First the assessment of suspended urine sediments using imaging techniques are discussed. Next the assessment of dissolved analytes in urine by chemical analysis methods are covered. Finally, we discuss monitoring daily behaviors associated with urination as useful indicators of health and context for PoC applications. Activities of Daily Living (ADL) such as medication adherence, bathroom frequency and volume can provide additional context to consider when assessing urine samples. Monitoring ADL on a continuous basis becomes possible with the development of PoC devices and is well suited for integration for personalized urinalysis.

2.2.   DETECTION OF URINE SEDIMENTS

Urine sediments can be either organized or unorganized. Organized sediments include cells, casts, bacteria, fungi, parasites and sperm. Unorganized sediments include various types of crystals [12]. These sediments all have a characteristic morphology that can be exploited for identification under a microscope. Flow cytometry has been implemented to screen for urine sediments, and eliminate samples negative for the presence of bacteria to reduce the number of urine samples being cultured. To date, microscopy and flow cytometry are being used as benchtop tools in centralized laboratories. A number of techniques have been investigated to produce compact, low-cost PoC sensing devices. As an example, lensless imaging may be integrated with a microfluidic device to achieve a low-cost image based flow cytometer.

2.2.1.   Microscopic Analysis

Through microscopic urinalysis, casts, cells, crystals, parasites, and bacteria can be identified. A list of urine components and sizes is provided in Table 2.1. Optical microscopy allows for direct visualization of the different urinary sediments to produce morphological and movement characteristics for identification. Brightfield microscopy is the most common method of microscopic urinalysis, though other techniques, like phase contrast, dark field and fluorescence are also employed. Normally, to prepare for microscopic urinalysis, a fresh sample of urine is centrifuged to concentrate particulate matter to ensure a higher limit of detection. Samples are then viewed under the microscope, and scored over 10 fields of view (FOV) [4]. Examined by a trained analyst, these elements can be distinguished from one another. In practice, the quality of these tests strongly depends on the training and experiences of the analyst. In addition, microscopic examination of urine samples is time consuming due to the number of FOVs that must be analyzed for each sample [4]. Laboratories may need to analyze thousands of samples a week and the turnaround time per cultured sample is 1–3 days.

Table 2.1 A list of the different components of urine and their sizes, and the subsequent diagnosis if found. Information was derived from Simerville et al. [3]. For more variations of different components, visit Strasinger et al. [4].

Component	Clinical Significance	Size (um)
Leukocytes (White Blood Cells) Erythrocytes (Red Blood Cells)	- Normally, men have <2 WBC/HPF (high powered field) and women <5WBC/HPF - >3 RBC/HPF in two of three urine samples suggests hematuria - If RBCs are dysmorphic, patient may have glomerular disease.	10-12 6-8
Epithelial cells	- Squamous epithelial cells suggests contamination - Transitional epithelial cells is normal - Renal tubule cells indicates significant renal pathology	15+
Casts	- Casts are used to localize disease to a specific location in the genitourinary tract depending on their composition - Hyaline casts can be associated with pyelonephritis or chronic renal disease. A full list of casts and associated conditions can be found in Simerville et al. [3]	15+
Crystals	- Calcium oxalate crystals are normal - Uric acid crystals are normal - Triple phosphate crystals are associated with UTIs caused by Proteus - Cystine crystals are associated with cystinuria	15+
Bacteriuria	- In asymptomatic females 5 bacteria/HPF (roughly 100,000 colony forming units (CFU) per mL) represents asymptomatic bacteriuria - In symptomatic patients, 100 CFU per mL suggests UTI - In males, the presence of bacteria is abnormal and culture should be obtained	1-2
Parasites	- Although less common, parasitic infections can also be detected in the urine. The two most common parasites that give rise to urological disorders are schistosomiasis (1 mm length) and *Trichomonas vaginalis* (10 μm length). *Trichomonas vaginalis* is estimated to be one of the most common non-viral STIs in the world [123] and often gives rise to renal and lower urinary tract diseases.	10 μm– 1 mm
Yeast	- The presence of budding yeast, *Candida albicans*, can be an indication of a yeast infection. They can be single, budding, or branched based on the severity of the infection.	5-10

Microscopes and specialists qualified to perform microscopic analysis are not commonly found in outpatient clinics or where samples are collected. Instead, samples collected from multiple sites across a region then sent to a centralized clinical microbiological laboratory for processing

[13]. In order to prevent sample contamination, urine specimens must either be refrigerated or examined within two hours as longer delay times often cause unreliable results [3]. Tests for bacteria and parasites often take a few days due to the need for culture, which also requires significant resources for incubation [14]. Furthermore, urinalysis tests are also often requested unnecessarily [15], which adds to the demand. For example, in the case of the diagnosis of trichomoniasis, commonly diagnosed through wet mount microscopy, the test must be read within 10 minutes of collection to avoid false results [16]. Ideally, optical microscopy would be used to detect the samples but with an improvement in throughput. This would allow for a universal instrument to detect any urinary sediment.

2.2.1.1. Sample Amplification

Generally, urine sediments are easily identifiable through microscopy, with the exception being bacteria. Although visible, bacteria remains difficult to examine microscopically due to their small size and semi-transparent nature. The gold standard for bacterial detection is culture, which requires an 18–30 hour incubation time to visualize growth. This is a time consuming process that has become automated, however, there remains the issue of expending resources in the culturing of negative samples. In urine culture, a urine sample is placed on agar plates for growth and identification of present bacteria. Culture positives are generally those which grow $\geq 10^4$cfu/ml of one species of bacteria [17]. Though effective, this approach is time consuming and of all samples being screened 60–80% are negative [18]. Automated culturing, such as the Copan WASPLab (Walk-Away Specimen Processor and smart incubator), has reduced the workload and automated the process, but has not decreased the need for an alternative processing method.

A solution to unnecessary culturing of samples is a screening test prior to culture with a high negative predictive value, ensuring that a sample determined to be negative is truly negative. In an effort to improve the efficacy of urinalysis, several alternative screening methods such as flow cytometry have been developed. These techniques are a preliminary screen that aim to reduce the number of samples cultured, reducing the workload, time, and costs in large laboratories. In addition, negative results are informed earlier which reduces broad spectrum antibiotic prescriptions [19].

A PoC device that would enable the rapid detection of bacteria would enable physicians to determine a treatment plan quicker, and decrease the

time and cost required for culture. Ideally, this device would be able to determine the concentration of bacteria in the sample in order to facilitate the physician's decision, as different concentrations indicate different treatment plans as well. Davenport et al. reviews new and developing diagnostic technologies specifically for UTIs [11].

2.2.2. Flow Cytometry

An alternative to microscopy is flow cytometry, where the sample is examined as it is hydrodynamically focused and continuously flowed through a channel. This can be done to reduce the number of samples that go through culture and increase the throughput of manual microscopy.

2.2.2.1. Non-imaging Flow Cytometry

Fluorescence and scattering flow cytometry is a method by which cells are optically screened to rapidly determine chemical and physical properties of urinary constituents [20]. The urine sample is labeled with fluorescent dyes, which bind to nucleic acids, and sorted to two different chambers: microorganisms and other. This prevents any interference in the analysis. There the hydrodynamically focused samples are illuminated with lasers of appropriate wavelength and the signal of emitted fluorescence and forward and side-scattered light are examined. Fluorescent signal informs on nucleic acid contents. Forward scatter provides information on particle size, while side scatter dictates surface and internal complexity. Red Blood Cells (RBCs), White Blood Cells (WBCs), squamous epithelial cells, casts, bacteria, yeast-like cells, spermatozoa, and crystals can be individually identified and counted. Stained bacteria are determined as gram positive or negative. The software from the cytometer presents the data as identified particles per field of view or particles per microliter [20].

A thorough meta-analysis of the use of flow cytometers as a tool for urinalysis was conducted by Díaz-Gigante et al., where studies using the UF1000i (Sysmex, Hamburg, Germany) as a pre-screening technique for urinalysis were analyzed [13]. They showa28%–60%reduction in the number of processed samples when pre-screened with flow cytometry. Savings of $239-$306 USD per 100 samples have also been reported, indicating the use of a flow cytometer is cost efficient [21]. A significant reduction of turnaround time of negative cultures is noted, which leads to a decrease in empirical antibiotic prescription.

Although there are significant benefits to this pre-screening approach, there are certain caveats to this flow cytometry system. The performance of the screening process strongly depends on the cut off criteria applied to the patients, which is highly dependent on the population being analyzed. Published data recommended adjusting the cut off values of the screens according to the clinical situation of the patients as well as the type of specimen collection in order to implement fluorescence flow cytometry as an effective screen [13].

2.2.2.2. Imaging Flow Cytometry

Image-based flow cytometry is a high throughput alternative to microscopy. The Iris iQ200 (Beckman Coulter, Brea, CA) is an FDA approved automated urine microscopy analyzer. In the Iris iQ200, urine samples are hydrodynamically focused between two layers of fluid in order to create a planar flow. Particles in the urine are analyzed as they are imaged by an objective lens and a camera at 500 frames per sample [20,22,23]. A neural network algorithm analyzes the images and classifies particles based on shape, size, texture and contrast. Particles are classified into the following categories: RBCs, WBCs, squamous epithelial cells, non-squamous epithelial cells, hyaline casts, non-hyaline casts, bacteria, crystals, yeast, sperm and mucus. Images that contain particles that are not identified to be a part of one of these categories are collected separately and are classified by a trained analyst. The lower limit for particle detection and quantification has been reported to be about 20–30 particles/µl [20]. One caveat of the system is that at times, the images may appear out of focus to the analyst, and the image cannot be improved as the sample has already left the flow chamber.

A study analyzing the Iris iQ200 as a urinalysis screen found that the Iris iQ200 results were similar to the result of manual microscopic examination [23]. There were, however, uncertain cases (particularly dysmorphic cells, bacteria, yeasts, casts and crystals), in which images had to be reexamined by trained staff. This indicates that manual examination is still necessary in the implementation of this screen, and the software requires further development to be fully automated. With these modifications, similar to the findings for the UF1000i, ˙Ince et al. [23] concluded that automated systems would be helpful in terms of time saving and standardization.

2.2.3. POC Testing for Urine Sediments

It is evident that urinalysis is a critical diagnostic tool used in health care, although current techniques tend to be time consuming and expensive. PoC devices, used to test patients in real time outside of a laboratory, has the ability to mitigate these issues. PoC testing for urinalysis has the ability to significantly reduce costs and allow physicians to administer earlier and more appropriate treatments to patients. With PoC testing, there can be a significant reduction in the storage and transportation of the samples to a centralized facility, as it would allow for home testing and prescreening. A universal test for a variety of pathogens can also reduce the rate of misdiagnosis in situations where clinical presentations are similar to one another. Lensless imaging is a promising technique for PoC urinalysis.

Lensless, or lens-free, microscopy is beginning to take shape as a competitive alternative to traditional microscopy, offering advantages like low-cost, large field of view, 3D reconstruction, and portability. This technique records the image of the specimen on the detector without any intervening lenses (Figure 2.1. [24]). This allows for a large field of view, limited by the size of the detector, while maintaining sub-micron resolution. Lensless microscopes are also cost effective, where the most expensive component is an image sensor costing a few dollars, and it allows for portability as there is no precise alignment needed.

By integrating a microfluidic channel in a lensless microscopy setup, an imaging flow cytometer is created, which can screen a large volume over a short period of time. One of the main advantages of using lensless imaging is the adaptability and cost effectiveness allowing these devices to be implemented as point-of-care instruments for community clinics and low-resource areas. It can also eliminate the need to culture every sample that comes through the regional microbiology laboratory by evaluating urine samples immediately after the sample was collected, resulting in a quicker turnover time, reduction in the administration of empirical antibiotics, and a lower operational cost. If a sensitive and specific test can be developed for urinalysis it could replace conventional microscopy tests and simultaneously perform trichomoniasis, candida and bacterial vaginosis testing in addition to UTI testing.
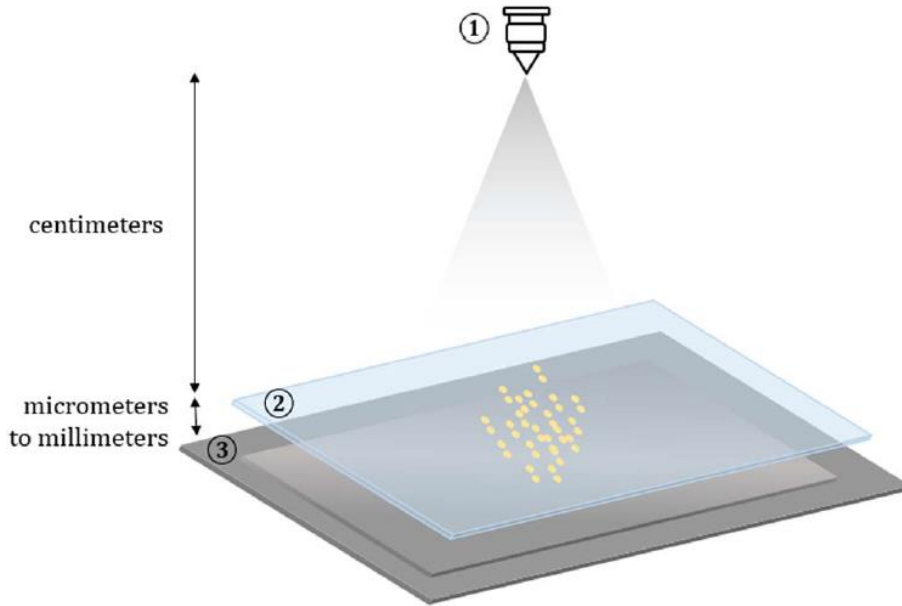
Figure 2.1 Lensless imaging design. A light source (1) illuminates a sample (2) that is placed above the detector (3). The type of light source (coherent/incoherent) and distance from the sensor (far/close) can be adjusted to create a shadow imaging or holographic imaging setup. [24] (Copyright Permission Granted).

There are three main types of lensless imaging: holographic, shadow, and fluorescence. Benefits of holographic imaging include 3D reconstruction and a flexible sensor-sample distance. Holography also allows for phase recovery of the sample, which may be of benefit to imaging bacteria. Although bacteria are transparent and do not significantly affect the intensity of light that pass through them, the phase of the light is affected [23]. Shadow imaging does not require image reconstruction and it is able to attain the same resolution as holographic imaging. Nonetheless, the resolution of shadow imaging is limited by pixel size and sensor-sample distance, which is difficult to attain. For urinalysis, 3D reconstruction is generally not needed; and most of the components can be identifiable by their morphology. Therefore, shadow imaging techniques are attractive options in PoC urinalysis.

Fluorescence imaging of a sample requires either autofluorescence or labeling with a fluorophore. Modern biological research relies on fluorescence microscopy, and as such, lensless modalities have been created as a low-cost alternative [25]. In the case of urinalysis, minimal sample

preparation is highly desired to reduce cost and turnover time, indicating that fluorescence labeling should be avoided if possible. Analyzing the autofluorescence of urine is possible, however the signal is a highly complex mosaic of overlapping signal from multiple microparticles and metabolites [26] making meaningful analysis very challenging.

Lensless imaging can also be used together with pixel superresolution to enhance the resolution of the images. Pixel superresolution is a technique that uses multiple sub-pixel shifted low-resolution images to create a single high-resolution image. Other techniques create a high-resolution image through a training set of low and high-resolution images. Zheng et al. created a lensless optofluidic device with shadow imaging and pixel super-resolution to image several homogenous samples flowing through the channel (Figure 2.2 [27]). In the application of urinalysis, a high resolution is not necessarily critical in order to distinguish between the macroscopic urinary constituents.
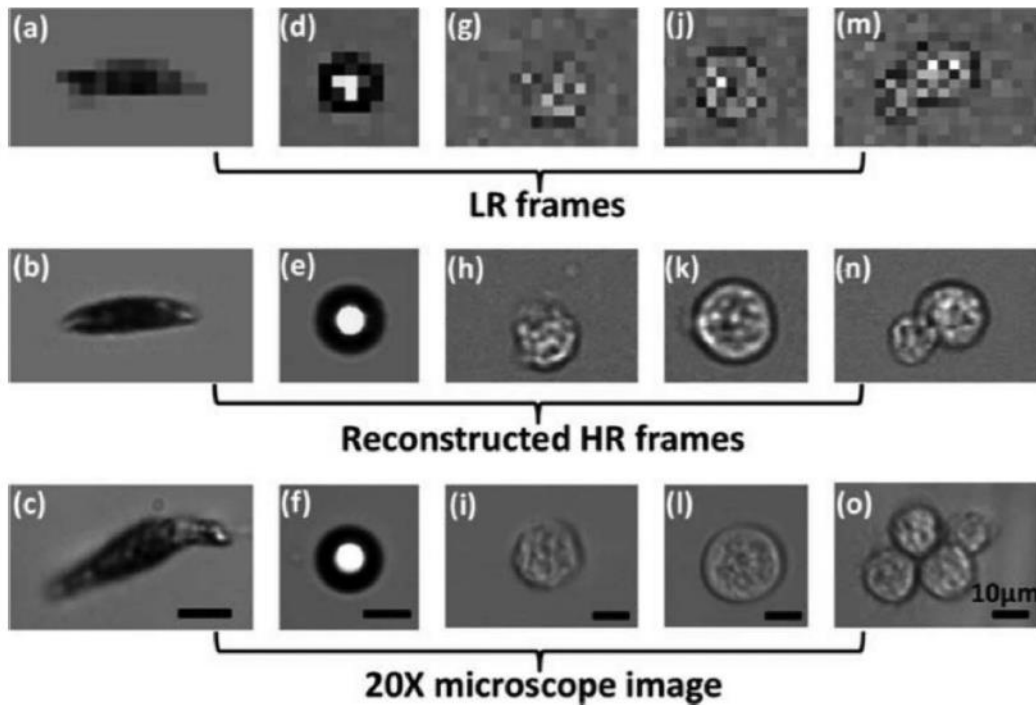
Figure 2.2 Shadow images of Euglena gracilis (a–c), microspheres (d–f), and Entamoeba invadens cysts (g–o). The LR frames (top row) are directly from the device, with reconstructed HR frames below. Brightfield microscopy images taken with 20x objective lens are on the bottom row. Figure and caption derived from Zheng et al. [27] (Copyright Permission Granted).

Though a detailed review of the applications of lensless imaging is beyond the scope of this review, a number of devices have been fabricated as an alternative to standardized health care screens. These include blood counting and analysis [28], pap smear analysis [29], sperm motility analysis (Figure 2.3 [30]), and so on. It is evident that lensless imaging has a lot of potential for health care monitoring. Applications of many of these techniques can be extended to urinalysis.
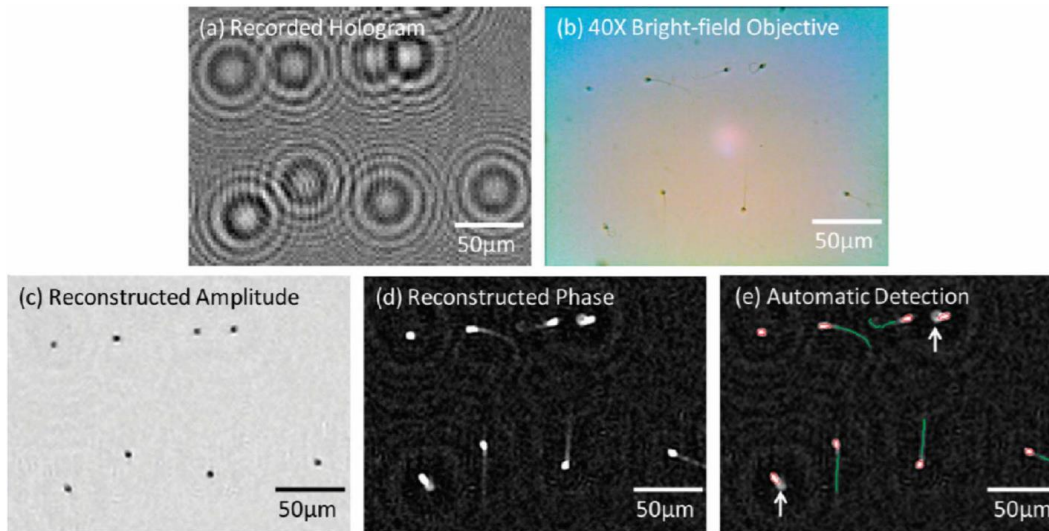
Figure 2.3   (a) Lensfree hologram of an immobilized semen sample (b) A bright-field microscope image of the same FOV as in (a) 40 × objective-lens; NA: 0.65. (c, d) The reconstructed amplitude and phase images from (a). (e) Automatic detection of the sperm. Figure and caption derived from Su et al. [30] (Copyright Permission Granted).

Recently, Zhang et al. developed a lensless holographic imaging device for the analysis of parasites in cerebrospinal fluid [31]. Their device is adaptable to Trichomonas vaginalis detection, though further testing must be done in urine samples. The device uses holographic phase imaging to scan and analyze 3 ml of fluid in 20 minutes. The limit of detection was found to be 10 parasites per milliliter of whole blood, and it costs ~$1850 USD to construct one device. This cost does not include the price of a laptop which is necessary for the short processing time.

Optical microscopic analysis techniques for urinalysis have the potential to detect and analyze different components of urine, thus allowing for a universal testing platform. Flow cytometry is being developed and tested as preliminary screens for urinalysis, and PoC tests have been developed for

the diagnosis of trichomoniasis, bacterial vaginosis and vulvovaginal candidiasis. Though there has been progress in this area, rapid and cost-effective diagnosis is not yet routine. Lensless imaging as a PoC device has the potential to reduce the turnaround time for samples, decrease the health care costs, and decrease the workload in labs. Turnaround time is crucial for the comfort and diagnosis of the patient as well as for the overloaded lab, and prescreening techniques bypass the initial overnight urine culture thereby eliminating the most time consuming step. By filtering out negative samples early from the screening process, unnecessary culturing is avoided, as well as avoiding unnecessary antibiotics. Ideally, this device would be implemented as a point-of-care device in hospital rooms and clinics to reduce the number of samples being sent to the lab, as well as allowing for personalized diagnosis as the clinical situation of the patient is immediately apparent.

2.3.   CHEMICAL ANALYSIS OF URINE

Microscopic methods are mostly used for identifying sediments suspended in urine, while chemical analysis of urine provides opportunities to detect and quantify a wide range of small molecules dissolved in samples. In this section we first discuss test strips as they have been used to measure indicators of infection, physical parameters, and small molecules. Direct measurement of physical parameters are discussed as indicators of sample concentration which is important to consider for quantification. Refractometric methods are optical techniques that can be used to assess specific gravity (SG) and indicators of infection such as cells and proteins. DNA detection techniques and chromatography are also capable of detecting pathogens by genetic markers and bacterial proteins respectively. Several of the target parameters and their indications are summarized in Table 2.2.

Table 2.2 Target parameters of interest in urinalysis testing.

Target	Indications	Notes
Proteins	Infection Kidney Health	Bacterial proteins can be used to identify the organism, and antimicrobial resistances. Protein markers may indicate diabetic nephropathy or cancer [103,105,124].
Cells, DNA, RNA	Infection Antimicrobial Susceptibility	Presence of bacteria, bacterial DNA and RNA indicates infection. Can be identified to determine antimicrobial susceptibility [11].
Leukocyte Esterase	Infection	Indicates presence of WBCs due to infection or arthritis. Can be used to detect prosthetic joint Infections [125].
Nitrites	Infection	Found due to metabolism of Nitrates by bacteria [126].
Osmolality & Specific Gravity	Hydration Status Urolithiasis Kidney Health	Physical measures of the amount of solute in the sample to determine concentration [52,76].
Creatinine	Internal Reference Dilution	Produced from degradation of Creatine. Used normalize measurements for dilution adjustment. Clearance may indicate renal disease [120,127,128].
Glucose	Diabetes	Monitored as indication of Diabetes and progression of disease [129,130].
Ketones	Ketonuria Diabetes Starvation	Ketones accumulate due to metabolism of secondary energy sources caused by insufficient insulin. Low insulin indicates diabetes or starvation [120,129].
Ammonia	Urolithiasis Infection	Ammonia is produced by metabolism of urease producing bacteria. Low ammonia and acidic urine is common in uric acid stone cases [131–133].
Urea	Diet Starvation	Produced by the degradation of protein. Indicates dietary protein intake and starvation [134,135].
Phosphates	Infection Kidney Health	Phosphate levels in combination with other parameters may be used to determine causes of kidney stone formation [131,133,136].
Cholesterol & Lipids	Renal Disease	Elevated levels in nephritic patients [137,138].
Drug Metabolites	Medication Adherence Drugs of Abuse Doping	Monitored in urine to determine medication adherence. Can also be used to detect drugs of abuse and doping in sporting events [100,116,120,139].

2.3.1. Lateral Flow Assays

The lateral flow assay (LFA) is the most common chemical analysis method and has been extensively reviewed [32–37]. Briefly, the LFA uses diffusion to transport the sample to sensing regions along a hydrophilic

strip. Target molecules may be detected by the development of a signal at the sensing region. The technique has received significant interest in the field of point of care diagnostics due to the low cost, high specificity, and simplicity of these devices. Test strips have been developed for a wide range of analytes and have been used to detect indicators of infection, bacteria such as trichomonas vaginalis [38]. Commonly used commercial lateral flow test strips include the pregnancy test, fertility and ovulation tests, and cancer diagnosis [39]. LFA strips are discussed here as Immunochromatographic assays, and reagent based assays. Immunochromatographic test strips rely upon immobilized antibodies to capture and concentrate target biomolecules, where reagent based strips depend on the development of a colorimetric reaction with the target analytes. The diagnostic potential of this method appears to be well established. The more recent developments have generally been in strategies for enhancing the signal from the test strips and in producing portable reagent strip readers.

2.3.1.1. Immunochromatographic Test Strips

Lateral Flow Immunochromatographic Assay (LFIA) strips are often used for the detection of proteins and hormones. E. Coli and N. gonorrhoeae have been detected by Mie scattering as indicator of STI [40]. The LFIA method is based on the Enzyme-Linked Immunosorbent Assay (ELISA) which is considered the gold standard in protein detection. The ELISA relies on capture antibodies to concentrate the target molecule and a labeled secondary antibody binds the captured targets [41]. The concentration of target molecules is determined by a measurement of the rate of color development, fluorescence generated, or magnetic field depending on the label used. A review of lateral flow assay design is provided by Sajid et al. [42]. The strip is placed in a sample and the fluid travels up the strip, through a conjugation pad, toward a reaction zone where color develops to indicate the presence of an analyte. The development of a control line indicates the validity of the test [39]. An example of an LFIA strip design is presented in Figure 2.4.
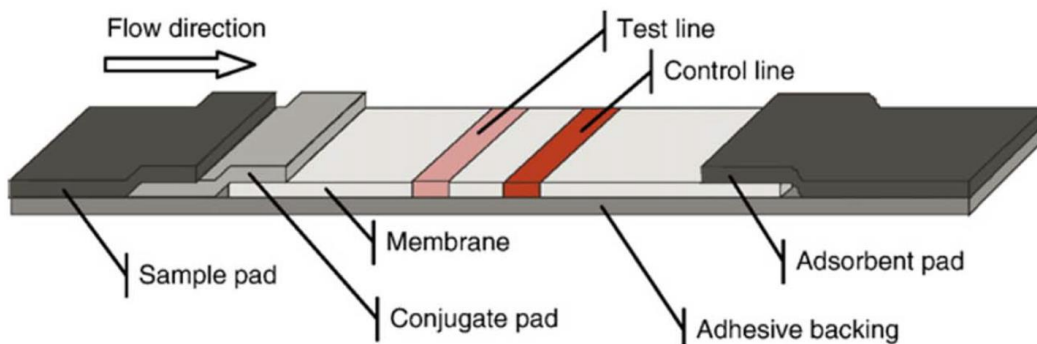
Figure 2.4 Standard layout of a lateral flow test strip [39]. The sample mixes with reagents in the conjugate pad as it travels up the strip. Aggregation of particles at the test and control lines leads to color development. (Copyright Permission Granted).

The lateral flow assay (LFIA) typically uses antibodies deposited in lines along a test strip. The test strip has a higher detection limit compared to the ELISA. A Chemiluminescent LFIA design has been produced for the measurement of serum albumin. Light is generated as a result of a reaction catalyzed by Horseradish Peroxidase (HRP) concentrated at the test and control lines to be detected by a photodiode [43].

Various nanomaterials and structures have been actively studied to enhance the sensitivity and specificity of LFA. Fluorescent nano-spheres, quantum dots (QDs) or Upconverting Nanoparticles (UCNPs) can be used as reporters in LFA strips for more sensitive measurement [44]. An example of a fluorescence based LFIA strip is shown in Figure 2.5. Gold nanoparticle labels can be detected on a LFIA strip due to the color change as the gold particles accumulate on a test line, a strategy recently used to detect phenylethanolamine A [45]. Magnetic nanoparticles have been used in a competitive lateral flow assay for the detection of drugs such as Cocaine [41]. Biosensors employing antibodies to capture human IgG in urine samples have been developed using fluorescence probes [46].

Enzyme Multiplied Immunoassay Technique (EMIT) relies on the use of an antigen linked to an enzyme that competes with the target analyte for binding sites. The enzyme is inactivated by binding and enzyme activity can be monitored as a measure of target concentration [47]. Devices are available for the detection of drugs using EMIT [48]. Multiplexed lateral flow tests are being developed to improve the utility of portable test strips [49].
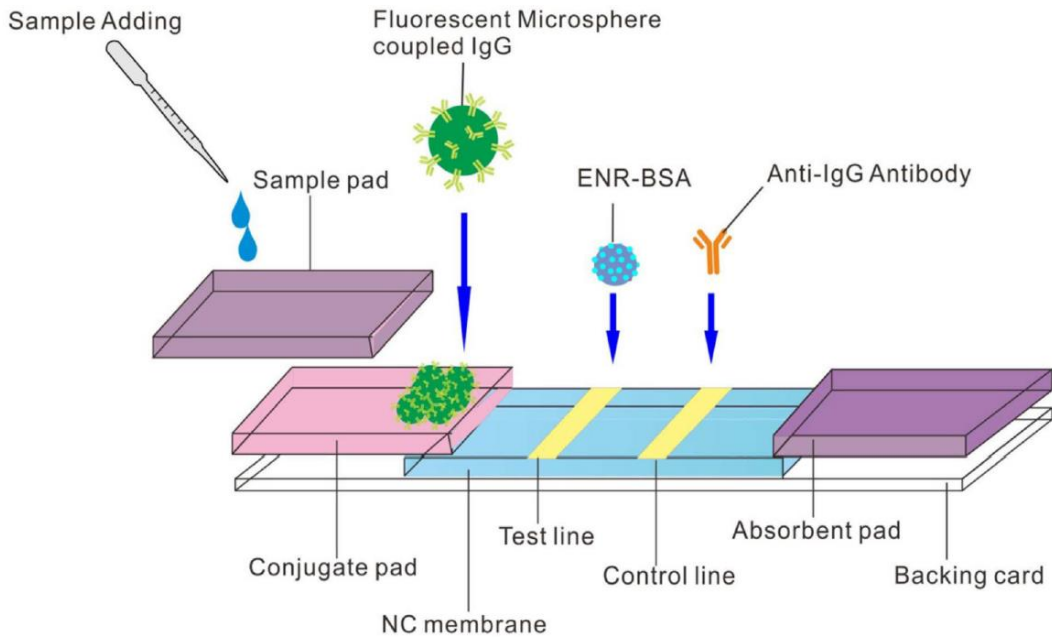
Figure 2.5 Fluorescent probes as reporters in LFIA tests [44]. (Copyright Permission Granted).

2.3.1.2. Urine Reagent Test Strips

Urine test strips have been developed for a wide range of analytes in urine samples including Specific Gravity, Creatinine, Glucose, Ions, Ketones, Lactate, Nitrite, pH, Protein, and Uric Acid (UA) [33,50]. Specific gravity reagent strips have been used for some time but have been found to be less reliable than the refractometric methods [51]. Urine samples may be compared to a urine color chart to predict the specific gravity [52]. SG test strips rely on the development of color by a chemical reaction that is compared to a lookup table [51]. The specific gravity test strips can be influenced by pH and may not be appropriate as a measure of osmolality for some conditions [53]. pH may play a role in the formation of crystals in saturated urine [54]. Interference of test strip results and false negatives may be caused by vitamin [55,56]. An example of a colorimetric urine test strip is shown in Figure 2.6 [50].
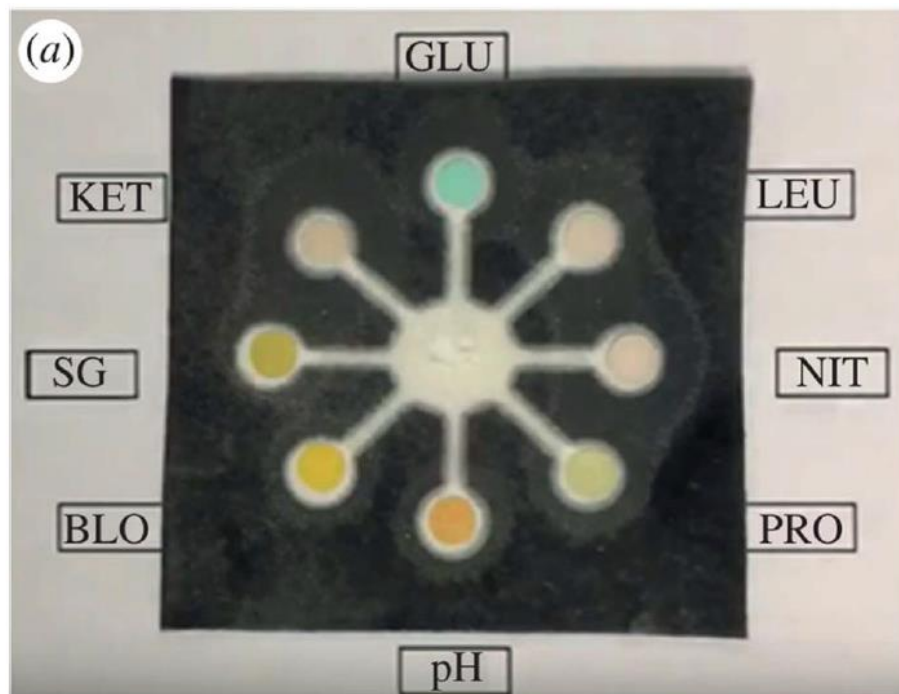
Figure 2.6 Example of colorimetric urine test pad [50]. The sample diffuses radially into various test zones where a colorimetric reaction progresses to quantify targets. (Copyright Permission Granted).

Micro paper based analytical devices (μPADs) employing electrochemical detection have been produced for monitoring Glucose, Lactate, and Uric Acid. Oxidase enzymes immobilized at each of the test zones leads to production of peroxide with the degradation of target molecules. The change in potential can be monitored using cyclic voltammetry [57]. μPADs have been developed to directly sense ammonia in urine samples using printed Pt electrodes [58]. An electrochemical μPAD has been recently developed to simultaneously measure several channels [59]. An example of a paper based electrochemical test strip is shown in Figure 2.7.
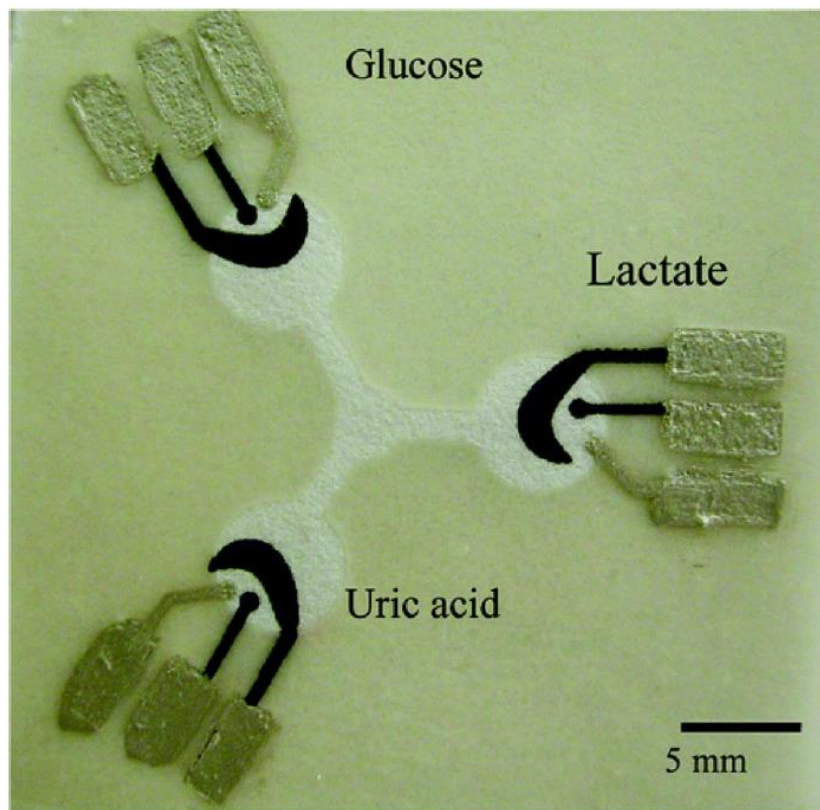
Figure 2.7 Example of electrochemical detection of paper based analytical devices [57]. The sample diffuses radially into the test zones where reactions with target molecules cause changes in electrical potential across electrode pads. Reprinted with permission from (W. Dungchai, O. Chailapakul, and C.S. Henry, Anal. Chem., 81, 5821 (2009)). Copyright (2009) American Chemical Society. (Copyright Permission Granted).

2.3.1.3. Portable Reagent Strip Readers

Reagent strip readers are an effective way to objectively assess colorimetric test strips. They can be designed to read fluorescent tags and could work with cell phone cameras making them particularly useful for diagnosis in low resource settings. Rapid improvements in the quality of smartphone cameras and image processing techniques have enabled low cost devices for quantifying colorimetric test strips. Recently there has been significant interest in the development of portable urinalysis reagent strip readers for point of care testing applications [32,50,60–65]. An example of a smartphone imaging application of urinary pH test strips is provided in Figure 2.8. Aggregation of nanoparticles in test regions have been monitored using Mie scattering as shown in Figure 2.9.

Figure 2.8 Smartphone analysis of urine test strips [140]. Smartphone images of colorimetric test strips are compared against a reference color chart to detect analytes in urine. (Copyright Permission Granted).
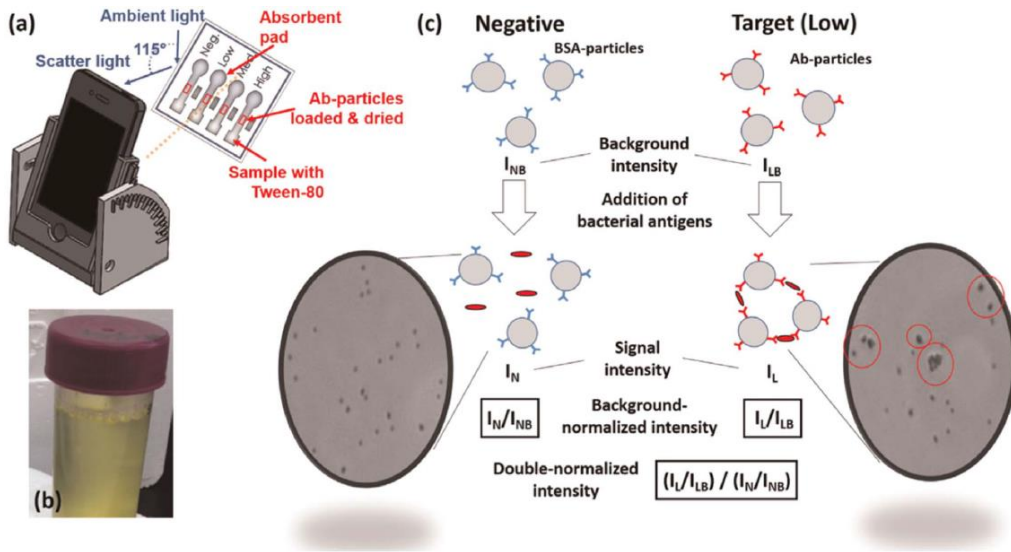
Figure 2.9 Smartphone Mie scattering for bacteria detection [40]. Changes in signal intensity due to aggregation of particles in the sample are used to detect target antigens. (Copyright Permission Granted).

Color development of test and control lines due to accumulation of magnetic nanoparticles has been measured using smartphone imaging as shown in Figure 2.10. The smartphone optical measurement concept can be applied for development of microfluidic devices as well as lateral flow assays.
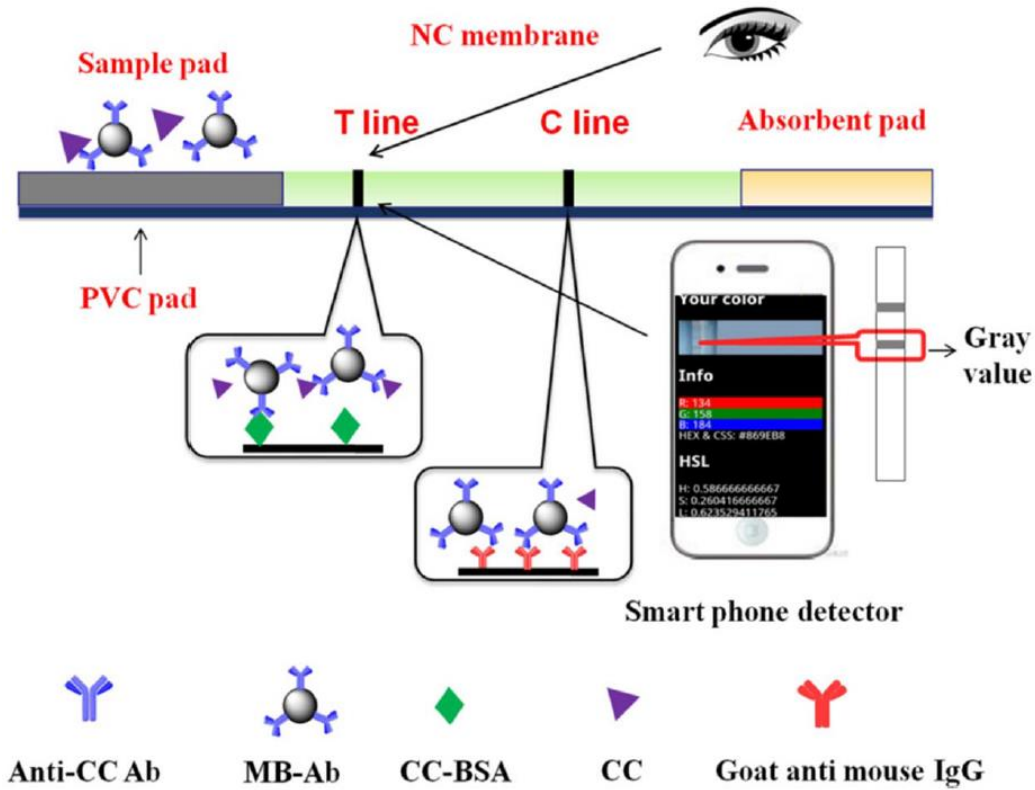
Figure 2.10 Magnetic nanoparticle based LFIA sensor with colorimetric detection [41]. The aggregation of target antigens is monitored by the development of color and magnetic field. (Copyright Permission Granted).

2.3.2. Physical Parameters

Physical measurements of urine samples such as color, specific gravity, and osmolality provide information about the concentration of urine samples and hydration status. Electrical conductivity measurements of urine samples can also be used to predict sample concentration.

2.3.2.1. Color

Color of urine samples is related to sedimentation and hydration status. The color is typically measured by comparison to a color chart. There are positive correlations between the color of samples and electrical conductivity [54]. The urine color chart is used to classify the sample based on a color scale. Color measurements are interfered with by consumption of certain medications, fruits, vegetables, and vitamins [52]. An example color chart is provided in Figure 2.11.
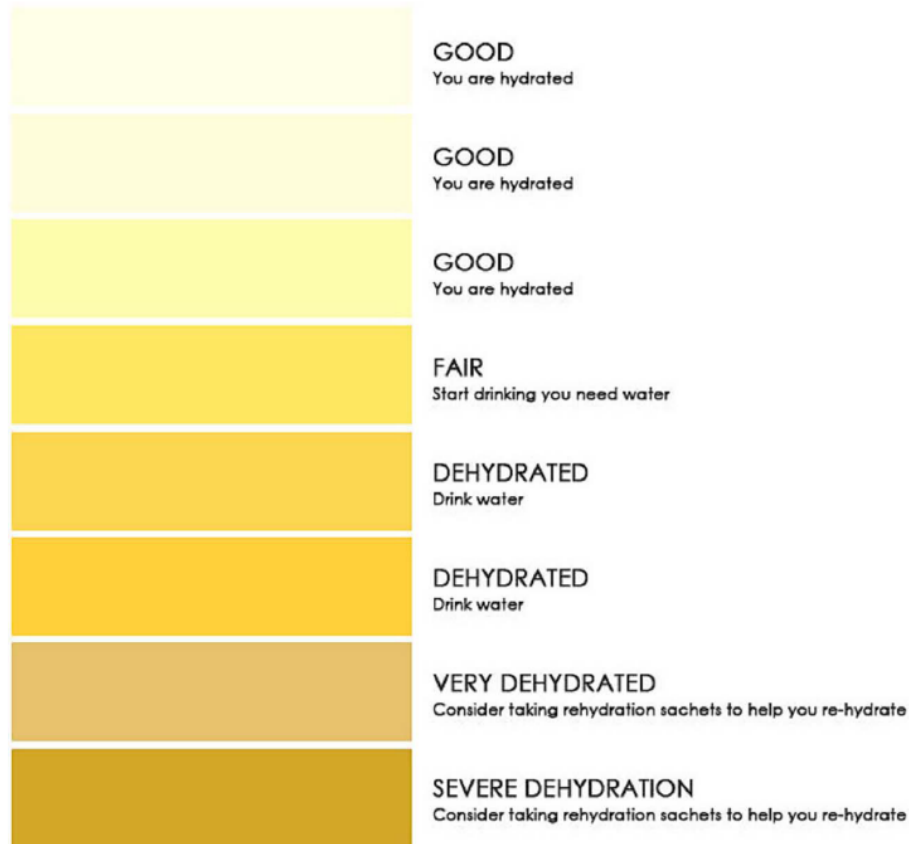
Figure 2.11 Example of a urine color chart for hydration assessment [141]. (Copyright Permission Granted).

2.3.2.2. Hydrometers and Osmometers

Hydrometers rely on the buoyancy of a floating scale to determine the specific gravity of the fluid. Hydrometers are traditionally relied upon, but require a reasonable sample size and are not suitable for continuous point of care application. The result obtained from a hydrometer is subject to error depending on the judgement of the user [66]. Osmometers are commonly used to directly measure the osmolarity of urine samples but they are typically large and expensive and are restricted to lab testing rather than remote measurements [52]. An example of a hydrometer measurement is provided in Figure 2.12.

Figure 2.12 Example of hydrometer for urine specific gravity assessment [142]. (Copyright Permission Granted).

2.3.2.3. Electrical Conductivity

Electrical conductivity of urine samples is measured to predict the development of kidney stones. Conductivity has been shown to positively correlate with SG, and color as indicators of sedimentation [54]. Electrical conductivity also correlates with osmolality [67]. Impedimetric sensors have also been developed for E.Coli in urine samples. The sensor is incubated with the urine sample and changes in the conductivity over time are indicative of bacterial growth and the formation of biofilm [68]. An example of multi-frequency electrical conductivity measurement of urine samples is provided in Figure 2.13.
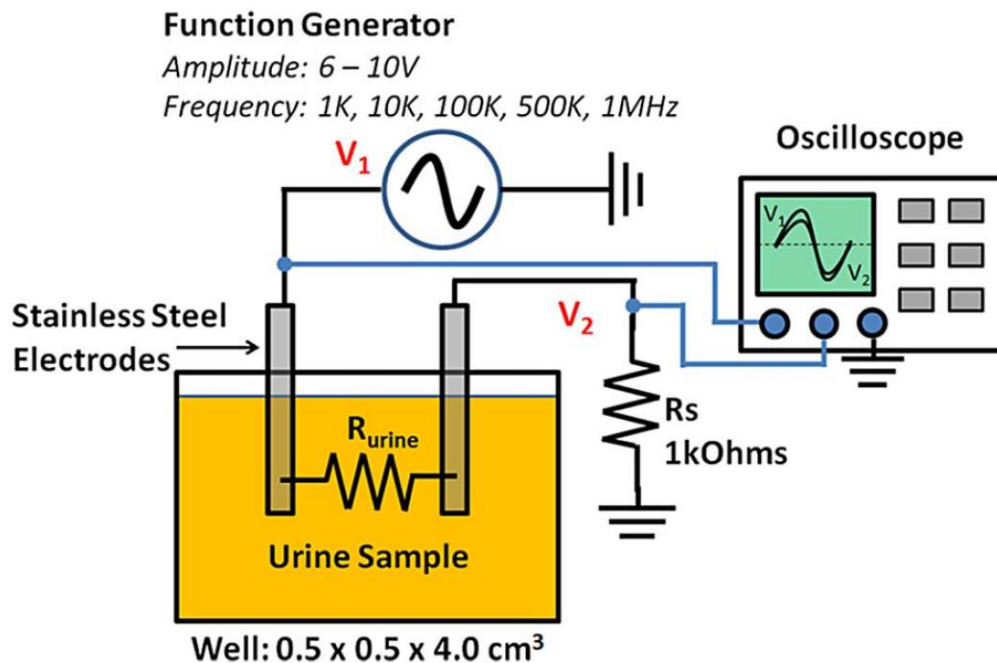
Figure 2.13   Example of urine multi-frequency electrical conductivity measurement [54]. (Copyright Permission Granted).

Modification of electrode surfaces has led to the production of electrochemical sensors for several analytes in urine. Modified glassy carbon electrodes have been used to detect UA in urine with high specificity [69,70]. Ionic liquid modified carbon paste electrodes with ZnO nanoparticles have been used to simultaneously detect the drugs Analgine and Camylofin [71]. Multiwalled carbon nanotube (MWCNT) structures with Zinc nanoparticles have been used for the simultaneous detection of two antidepressant drugs [72]. MWCNTs are also being developed for the simultaneous detection targets with overlapping electrochemical oxidation peaks [73]. Functionalized carbon black and Nickel Sulfide have been used to detect Glucose in a non-enzymatic sensor [74]. Nickel Bromide nanoparticles have also been used for non-enzymatic Glucose detection [75].

2.3.3.   Refractometric Methods

The refractive index of fluids change with the concentration of dissolved components such as salts. Refractometers, fiber optic sensors, and photonic crystals [76,77] can be used to monitor specific gravity to assess hydration. Refractometric methods demonstrate the best linear relationship with osmolality [78,79].

2.3.3.1. Refractometric methods for detection of acute dehydration

The refractometer measures the refraction of light as it encounters an interface of different refractive index between the waveguide material and the sample. The refractive index of the sample is influenced by the concentrations of solutes including salts, glucose, protein, and creatinine. Simple manual and digital refractometers are available for measurement of urine specific gravity [53,78].

2.3.3.2. Surface Plasmon Resonance

Recently Surface Plasmon Resonance (SPR) sensors have been employed for osmolality measurement in urine samples [80]. SPR methods have been developed as sensitive biosensors for fluid samples and are integrated into microfluidic devices. These devices employ prism coupling, grating based, and fiber optic based sensing mechanisms [81]. Excitation light is injected and Surface Plasmon's are generated at the interface of the dielectric material (sample) and a metal (coated coupling element) by optical excitation. An absorbance peak indicates the region where energy is transferred to generation of SPR which is dependent on the refractive index of the sample acting as the dielectric layer [80,82]. The metal coating may be left bare to measure the average RI of the sample, or the coating may be functionalized with antibodies to target a particular molecule. As target molecules bind the antibodies, there is a local change in the refractive index which can be detected as a change in transmission efficiency through the sensor. The SPR sensor and biosensor mechanisms are presented in Figure 2.14.
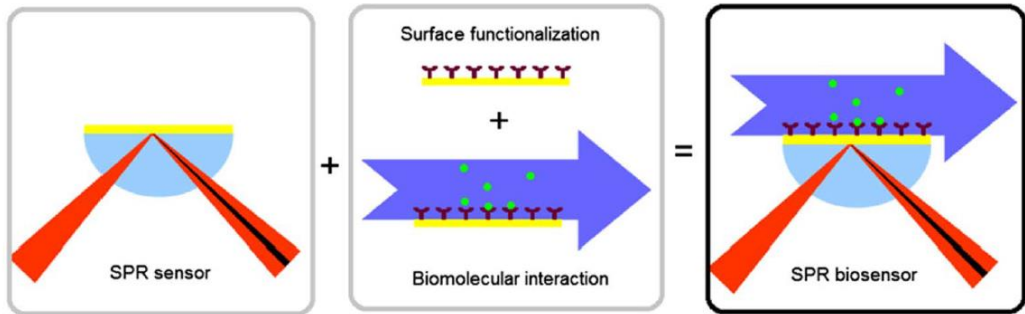
Figure 2.14 Example of SPR sensing mechanism [81]. Analytes binding the sensor surface results in a change of refractive index that is measured to determine concentration of targets. (Copyright Permission Granted).

SPR is well suited for integration into microfluidic devices and may be a powerful detection method for point of care diagnostic devices. Fiber optic

SPR sensors could be of interest for sampling from directly inside the toilet at the point of care. Light is directly injected into the fiber and detected from opposing ends of the fiber. These SPR sensors employ a sensing region made of de-clad fiber, coated in a thin metal layer. The shift in the peak wavelength coupled to SPR generation is monitored as an indication of SG using a spectrometer [80]. An example of a fiber based SPR sensor for urine SG is presented in Figure 2.15. Smartphone based imaging devices are being developed for PoC measurement of plasmonic sensors, and colorimetric sensors [83,84].
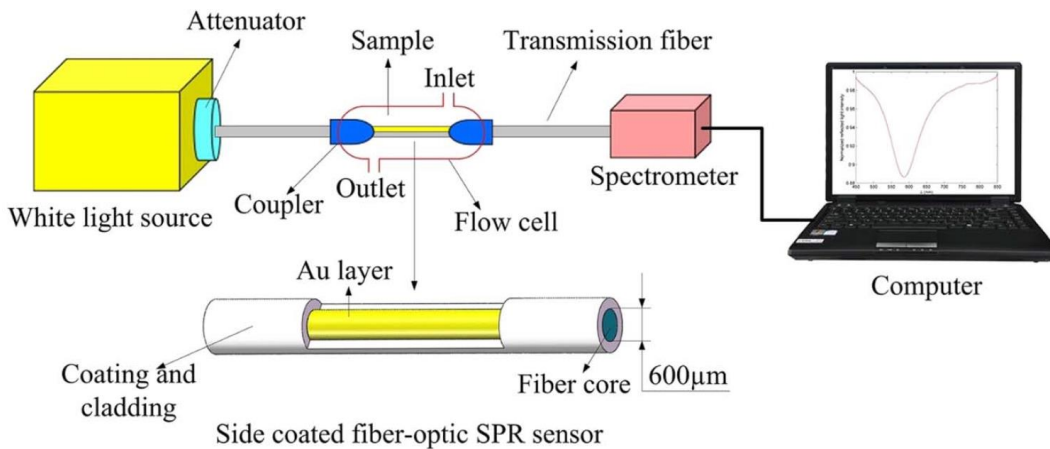
Figure 2.15 Example of fiber based SPR sensor for urine Specific Gravity [80]. Changes of refractive index by SG in the sample are monitored by the peak wavelength coupled to SPR. (Copyright Permission Granted).

Nanoplasmonic microarrays have been developed to detect the presence of bacteria based on surface plasmonics. A gold substrate with a nanohole array is placed above a CCD detector. The transmission spectrum of the nanohole array is sensitive to changes in the refractive index near the gold surface. The surface of the gold array is functionalized with detection spots of capture antibodies. The sensor is illuminated with a broadband source and the transmitted light is detected by the CCD. When target cells bind to the antibodies the change in refractive index is captured as a wavelength shift in the transmission spectrum detected by the CCD. This is a very new and promising technique enabling multiplexed and label free detection of infections in near real time [85].

2.3.4. DNA and RNA Detection

Polymerase Chain Reaction (PCR) is a popular method for amplification and detection of DNA used for the detection and identification of bacteria

based on their characteristic genetic features. Several methods have been developed based on the traditional PCR process [86]. Traditional PCR is a cyclical process that involves the denaturation of double stranded DNA (dsDNA), annealing of DNA primers, and subsequent amplification. The process is conducted in a thermocycler in order to denature the dsDNA to facilitate primer binding and amplification. Traditional PCR was typically used to amplify any target DNA of interest before detection using electrophoretic methods [86].

Quantitative Real-time PCR (qRT-PCR) methods can be used to indicate the concentration of target DNA present after multiple cycles. The reaction tube is measured after each cycle so target pathogens can be quantified based on the number of cycles required to produce a detectable concentration of DNA molecules. Primers are selected to amplify target segments of DNA and can be designed specifically in order to detect the presence and speciation of bacteria [87]. The nucleotides provided for the amplification are labeled with fluorescent reporter [88]. RNA transcripts generated by expressed bacterial DNA may also be monitored using PCR processes. Reverse transcription PCR is used to generate a complementary DNA strand from RNA present in the sample. The concentration of DNA is then monitored as a change in fluorescence signal at the end of each reaction cycle [89].

Isothermic PCR reactions are being developed that can be conducted at a constant temperature to avoid the need of thermocyclers, leading to cost reductions [90]. Recombinase Polymerase Amplification (RPA) is an isothermic method that forms a complex of recombinase and primer [91]. The primer recombinase complex binds the target DNA and causes the strands to dissociate at the primer. Single strand binding proteins adhere to the single stranded DNA. The DNA polymerase then displaces the recombinase and replicates the DNA [90]. The isothermic methods such as RPA are well suited for integration with microfluidic devices due to the simplicity of the method and instrumentation required. Loop Mediated Isothermal Amplification (LAMP) is another effective technique for detection of bacterial and viral DNA [92,93]. Isothermic amplification methods may be used in the detection of hepatitis C. The use of LAMP in future portable diagnostic tests may not be as promising as alternative methods such as RPA due to the complex primer design required for LAMP processes [90].

2.3.4.1. DNA microarrays – DNA and RNA level detection

DNA microarrays may be used to establish the presence of target DNA sequences. Microfluidic DNA microarrays with fluorescence detection enable the simultaneous detection of bacteria species. It is also possible to differentiate between pathogenic and non-pathogenic strains of similar bacteria [94]. DNA microchips have been developed for the detection of sexually transmitted infections such as human papillomavirus (HPV) [95]. Bladder cancer (BC) may also be detected by the presence of tumor cells in urine sediment which are characterized by high degrees of DNA methylation [96]. Monitoring BC is possible using DNA microarrays targeting mRNA by the real time PCR method [97].

Several single stranded DNA probes are bound to the bottom of a reaction chamber in spots such that each spot is specific to a unique DNA sequence. Sample DNA is mixed and if a complementary strand of ssDNA is present in the sample it will hybridize with the DNA probe [86,87]. Fluorescently labeled target DNA has been detected as a change in fluorescence intensity in the hybridization regions with DNA probes in a paper-based microarray [98]. DNA microarrays provide an opportunity for improving the throughput and simultaneous detection of DNA markers in urine [86]. This is particularly useful for detection of pathogens that are difficult to culture and to determine variants of detected species [99]. Probes may also be used to detect single nucleotide polymorphisms in bacterial DNA to detect variants [100]. An example of a smartphone based detection system for a fluorescence based DNA microarray is presented in Figure 2.16.
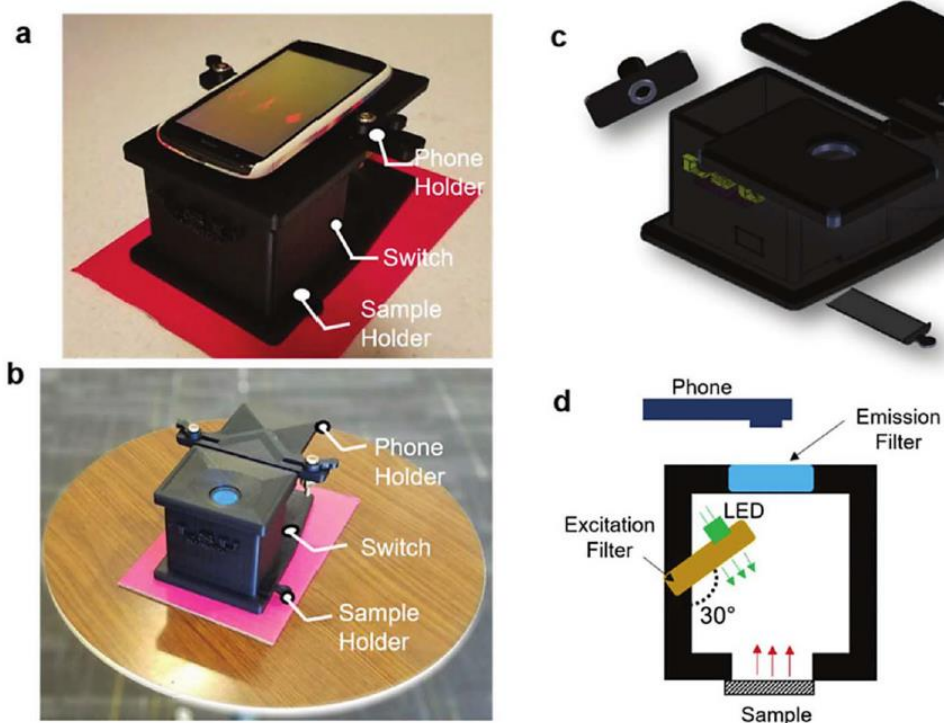
Figure 2.16 Example of portable smartphone reader for fluorescence paper based DNA microarray [143]. An LED is used to excite a fluorescent DNA microarray sample. A smartphone camera images the microarray through an emission filter to measure the sample. (Copyright Permission Granted).

2.3.5. Chromatography

Chromatographic methods such as High performance liquid chromatography (HPLC) and Micellar Liquid Chromatography (MLC) [101] are effective at separating samples based on different affinities between mobile and stationary phase. The sample is analyzed based on the retention time of contents. The sample fractions may then be investigated further using alternative methods such as Mass Spectroscopy (MS). These methods are difficult to employ as point of care diagnostic methods due to the required solvents, and expensive separation columns, pumps, and detectors involved.

Matrix Assisted Laser Desorption/Ionization - Time of Flight – Mass Spectrometry (MALDI-TOF-MS) is used to measure the charge to mass ratio of ionized fragments of analytes [102]. It is well suited to analysis of macromolecules such as proteins. In clinical applications it has been used to identify bacteria in urine samples [103] and to determine antimicrobial

resistance. Chromatographic methods in combination with TOF-MS have been used to demonstrate that changes in urine metabolome may indicate the reappearance of tumors in BC patients [104]. First the samples are mixed and dried to produce a crystalized matrix. Next a pulsed laser is used to desorb and ionize the sample components. The particles are separated by their relative velocity as they are accelerated through an electromagnetic field to a time of flight detector. The particle velocity depends on the charge and mass of the particle [102].

Although it has been suggested that MALDI-MS methods could be useful in daily practice [105] there are still limitations to be overcome in order to further apply MALDI-TOF-MS in point of care urinalysis applications. The results are more reliable for the detection of Gram-negative bacteria than for the detection of Gram positive bacteria and Yeasts [106]. Matrix effects must be considered where sample constituents that are not of interest may influence the efficiency of ionization of components of interest. There is an isobaric effect where components with the same mass to charge ratio are detected simultaneously. The technique still requires expensive detectors and could benefit from miniaturization and cost reduction [103]. New techniques are being developed in order to reduce the incubation time required in order to directly analyze urine samples [107].

2.4. URINALYSIS IN CONTEXT OF ACTIVITIES OF DAILY LIVING

ADL refers to the behaviors, tasks, and routines adhered to on a daily basis. Monitoring ADL on a continuing basis can be used to provide additional context to be considered when analyzing samples. In the conventional urinalysis setting, sample analysis provides information about the sample contents but does not offer information about frequency or volume of urination. This is an emerging application area of urine analysis technologies enabled by the recent advances of PoC urinalysis technologies that allow continuous multi-parameter measurements of urine in a home setting. Several of the ADL parameters of interest associated with urination are presented in Table 2.3.

Table 2.3 Activities of Daily Living associated with urination.

Activities of Daily Living	Indications	Notes
Bathroom Frequency	Chronic Disease Monitoring Nocturia	Bathroom frequency, and times of use can indicate developing Challenges [109,111]. Medication adherence and response to treatment [117,118].
Uroflowmetry	Assessment of Diuretics Volume and flow rate of urination Renal Health	Changes in volume and flow rate may indicate kidney injury [113]. Change in weight indicates the volume of urine [114].
Medication Adherence Monitoring	Adherence to Medication Schedules Context of urine test results	Assist in optimizing medication schedules [117].

2.4.1. Bathroom Frequency

Frequent use of the bathroom at night known as nocturia can be monitored [108–110]. Nocturia is a common symptom experienced by older adults and negatively impacts sleep quality. The more frequent need to urinate can be caused by an increase in urine production due to disease, or as a side effect of diuretic medications [111,112]. Reduced bladder capacity caused by the formation of kidney stones may also cause nocturia [110].

Several strategies have been suggested for monitoring the frequency and timing of bathroom use. These generally involve mechanisms for determining when the bathroom is in use, and in identifying the occupant of the washroom. Indoor positioning strategies such as Radio Frequency Identification (RFID) tracking have been used that rely on a wearable tag to identify the occupant of the bathroom [108]. Ultrasonic range finders have been used to identify the occupant by measuring their height as they enter the bathroom [112]. Ultrasonic flow meters have been employed to track when water starts flowing to refill the toilet bowl as an indicator of bathroom use [108]. Electrodes placed inside of the toilet can be used to measure the change in conductivity of the toilet water during a urination event to indicate use [112].

2.4.2. Uroflowmetry

Uroflowmetry involves the measurement of urine volume, duration, and flow rate. The volume of urine samples can be monitored each time the bathroom is used to establish a daily urine volume. Changes in the volume of urine over time may indicate the development of kidney injuries.

Urine volume has been predicted by the change in weight of an individual before and after they use the toilet. The weight measurements may be conducted by special scales upon which the toilet is installed, or by weight sensors built into the toilet seat [113]. Electrodes can be installed in the toilet bowl to monitor urine volume and average flow rate using fluid models considering the shape and volume of the toilet, and has been shown to correlate with changes in weight to predict volume [114]. Recent preliminary work has demonstrated an array of sensors mounted under the toilet seat have been used to monitor changes in the temperature of water falling into a toilet bowl as an indication of sample volume using thermal models [115]. An optical detection strategy has also been demonstrated to predict sample volume by measuring the change in height of fluid in a special fill container. This technique was not integrated with a smart toilet [116].

2.4.3. Medication Compliance

Drug metabolites may be detected in the urine for several applications. Medication compliance is known to be low and strategies are being developed to monitor and improve adherence to medication schedules. Consequences of non-compliance may lead to preventable medication related hospitalization which comes at a cost of patient comfort and cost to the medical system [117,118]. There are several situations that lead to patients failing to take their prescribed medications which may lead to the development of health issues. Patients may feel that they do not need medication any longer or they may simply get confused and fail to take their medication at the appropriate time [119]. Detection of drugs in urine samples is also used to detect doping for athletic events and the use of drugs of abuse [120].

Strategies for medication compliance monitoring have focused on determining when medications are removed from their containers and to identify which individual removed the medication. Drugs can be detected in urine to monitor drug abuse as well as to monitor drug metabolites to assist in dose control of medication [121]. Typically drug detection relies on chromatographic methods like HPLC, and liquid chromatography with tandem mass spectroscopy (LC-MS) [122]. Microchip electrophoresis followed by UV or electrochemical detection have also been used [121].

2.5. DISCUSSION AND FUTURE OUTLOOK

The current challenges facing urinalysis may be overcome with the development of high throughput integrated sensing systems, and Point of Care devices for personalized medicine. Measurements right at the site of collection reduces the need for sample storage and transportation for testing and may provide more reliable results for patients sending samples far from testing facilities. The results may be available shortly after sample collection enabling more rapid response to results. Additionally, samples may be screened at the site of collection to determine if a more detailed analysis is required to reduce the number of samples sent to testing facilities, reducing the demand and cost of urinalysis testing. By screening for infections and monitoring chronic diseases before they become symptomatic the demand on testing labs may be reduced and potential for early intervention may be improved. The contents of urine samples are highly variable, between individuals and for a given individual over time. Remotely monitoring contents of urine samples over time provides an opportunity to establish normal baselines for individual users. Trends in results over time may be used to identify the development of health challenges before symptoms appear. Integration of new functional components in microfluidic devices such as pumps, mixers, valves, filters may be used to enable automated sample handling, processing, analysis, and disposal, in order to overcome the need for trained technicians to perform analysis. Additionally, many studies focus on validating methods on healthy subjects. Work should be done to investigate the reliability of these methods on subjects with health issues, and to identify behaviors that influence test results.

Continuing development of microfluidic detection methods for the analysis of urine will lead to reliable sensing modules for many diagnostic indicators. Many of these sensing modules may be integrated in a single device to allow for the simultaneous detection of several analytes. The development of new microfluidic microscopies and lensless imaging techniques provide an opportunity to dramatically reduce the size and cost of microscopic examination of samples. High throughput microfluidic microscopy has the potential to detect infections with low concentrations of bacteria without long incubation times, significantly reducing the time for test results.

Point of Care diagnostic devices may be developed that are capable of continuously monitoring urine samples on an ongoing basis, enabling the early detection of diseases and the monitoring of chronic disease. These monitoring devices may be portable units to be deployed, or permanently installed in the home such as smart toilets. Several parameters can be measured from the toilet itself such as the frequency of toilet use, and Uroflowmetry when using the toilet which may provide an indication of a patient's response to medications such as diuretics.

Most of the new PoC urinalysis devices are based on reagent strip readers. The reagent strip design has inspired several chip-based sensors employing a wide range of detection methods. It is not recommended that we should simply develop more test strips to cover a wider range of analytes or concentrations due to the complex nature of the sample and the interactions between different components. Making a device that incorporates redundancy by measuring several parameters using independent methods may provide more reliable information about sample contents. Not all of the methods used in urinalysis testing needs to be translated to microfluidic devices. There are several methods that can be used to detect the presence of bacterial infection. More extensive testing can be performed in lab settings to identify the infecting organism and to determine the effective antibiotic treatment for the infection.

As the methods used to perform urinalysis continue to translate to portable PoC monitoring devices results can be obtained directly from the site of collection, rapidly, and on a continuing basis. The integration of urinalysis devices into smart toilets also allows monitoring of the frequency of urination and volume of urine. This provides an opportunity to detect developing illnesses at an early stage, as well as to monitor ongoing chronic illnesses and response to treatment. The personalized urinalysis may be used to reduce the number of samples sent to large testing facilities to save time and cost by prescreening samples. With the development of lensless imaging devices automated point of care microscopy may also be conducted on urine samples for direct detection of sediment and infectious particles. These sensing strategies may also be applied to alternative remote fluid monitoring applications such as analysis of saliva, environmental water quality monitoring, and process control.

Acknowledgements

References

[1]   G. B. Fogazzi, Kidney Int., 78, 1202 (2010).

[2]   A. Ruettger et al., Mol. Cell. Probes, 25, 19 (2011).

[3]   J. A. Simerville, W. C. Maxted, and J. J. Pahira, Am. Fam. Physician, 71, 1153 (2005) http://www.ncbi.nlm.nih.gov/pubmed/15791892.

[4]   S. K. Strasinger, M. S. Di Lorenzo, and M. Di Lorenzo, Urinalysis and body fluids, 337 (2014).

[5]   J. Liu, Z. Geng, Z. Fan, J. Liu, and H. Chen, Biosens. Bioelectron., 132, 17 (2019).

[6]   M. Haidari et al., Clin. Chim. Acta, 499, 81 (2019).

[7]   G. J. Becker, G. Garigali, and G. B. Fogazzi, Am. J. Kidney Dis., 67, 954 (2016).

[8]   J. Prieto, in Proc. SPIE 10875, Microfluidics, BioMEMS, and Medical Microsystems XVII, vol. 1087510, p. 1, San Francisco, California, United States (2019).

[9]   W. L. J. M. Devillé et al., BMC Urol., 4, 4 (2004).

[10]   G. J. Williams et al., Lancet. Infect. Dis., 10, 240 (2010).

[11]   M. Davenport et al., Nat Rev Urol., 14, 296 (2017).

[12]   A. Bunjevac, N. N. Gabaj, M. Miler, and A. Horvat, Biochem. Medica, 28, 1 (2018).

[13]   P. Mejuto, M. Luengo, and J. Díaz-Gigante, Int. J. Microbiol., 2017, 1 (2017).

[14]   J. Delanghe and M. Speeckaert, Biochem. Medica, 24, 89 (2014).

[15]   M. Chen, S. Eintracht, and E. MacNamara, Clin. Biochem., 50, 88 (2017).

[16]   M. A. Kingston, D. Bansal, and E. M. Carlin, Int. J. STD AIDS, 14 (2003).

[17]   H. A. D'Souza, M. Campbell, and E. J. Baron, J. Clin. Microbiol., 42, 60 (2004).

[18]   W. J. McIsaac et al., Arch. Intern. Med., 162, 600 (2002).

[19]   J. Delanghe, Acta Clin. Belg., 62, 155 (2007).

[20]   K. Yasuma et al., Rinsho Byori., 60, 1070 (2012).

[21]   S. Linko et al., Clin. Chim. Acta, 372, 54 (2006).

[22]   L. Alves, F. Ballester, J. Camps, and J. Joven, Clin. Chem. Lab.Med., 43, 967 (2005).

[23]   F. D. ˙Ince et al., Pract. Lab. Med., 5, 14 (2016).

[24]   A. Ozcan and E. McLeod, Annu. Rev. Biomed. Eng., 18, 77 (2016).

[25]   J. K. Adams et al., Sci. Adv., 3, e1701548 (2017).

[26]   M. Zvarik, D. Martinicky, L. Hunakova, I. Lajdova, and L. Sikurova, Neoplasma, 60, 533 (2013).

[27]   G. Zheng, S. A. Lee, S. Yang, and C. Yang, Lab Chip, 10, 3125 (2010).

[28]   S. Seo, T. W. Su, D. K. Tseng, A. Erlinger, and A. Ozcan, Lab Chip, 9, 777 (2009).

[29]   W. Luo, Y. Zhang, A. Feizi, Z. Göröcs, and A. Ozcan, Light Sci. Appl., 5 (2016).

[30]   T.-W. Su, A. Erlinger, D. Tseng, and A. Ozcan, Anal. Chem., 82, 8307 (2010).

[31]   Y. Zhang et al., Light Sci. Appl., 7, 108 (2018).

[32]   M. Oyaert and J. R. Delanghe, J. Clin. Lab. Anal., 33, 1 (2019).

[33]   E. Lepowsky, F. Ghaderinezhad, S. Knowlton, and S. Tasoglu, Biomicrofluidics, 11, 1 (2017).

[34]   M. Park, B. H. Kang, and K. H. Jeong, Biochip J., 12, 1 (2018).

[35]   J. Li and J. Macdonald, Biosens. Bioelectron., 83, 177 (2016).

[36]   S. Sharma, J. Zapatero-Rodríguez, P. Estrela, and R. O'Kennedy, Biosensors, 5, 577 (2015).

[37]   K. Choi et al., Telemed. e-Health, 22, 534 (2016).

[38]   C. A. Gaydos et al., Sex. Transm. Infect., 93, S31 (2017).

[39]   S. Assadollahi, C. Reininger, R. Palkovits, P. Pointl, and T. Schalkhammer, Sensors, 9, 6084 (2009).

[40]   S. Cho, T. S. Park, T. G. Nahapetian, and J. Y. Yoon, Biosens. Bioelectron., 74, 601 (2015).

[41]   J. Wu et al., Sensors (Switzerland), 17 (2017).

[42]   M. Sajid, A. N. Kawde, and M. Daud, J. Saudi Chem. Soc., 19, 689 (2015).

[43]   M. Zangheri et al., Anal. Bioanal. Chem., 408, 8869 (2016).

[44]   X. Gong et al., J. Mater. Chem. B, 5, 5079 (2017).

[45]   W. Jiang, L. Zeng, L. Liu, S. Song, and H. Kuang, Food Agric. Immunol., 29, 182 (2018).

[46]   B. Della Ventura et al., ACS Appl. Mater. Interfaces, 11, 3753 (2019).

[47]   B. Olivieri, M. Mari´c, and C. Bridge, Drug Test. Anal., 10, 1383 (2018).

[48]   V. Blandino, J. Wetzel, J. Kim, P. Haxhi, R. Curtis, and M. Concheiro, Curr. Pharm. Biotechnol., 18, 796 (2017).

[49]   D. Fodera et al., GHTC 2018 - IEEE Glob. Humanit. Technol. Conf. Proc. (2019).

[50]   V. Suresh, O. Qunya, B. L. Kanta, L. Y. Yuh, and K. S. L. Chong, R. Soc. Open Sci., 5 (2018).

[51]   K. J. Stuempfle and D. G. Drury, J. Athl. Train., 38, 315 (2003).

[52]   A. J. Warren, M. S. O'Brien, and D. B. Smith, Int. J. Sport. Exerc. Heal. Res., 2, 100 (2018).

[53]   G. C. Voinescu, M. Shoemaker, H. Moore, R. Khanna, and K. D. Nolph, Am. J. Med. Sci., 323, 39 (2002).

[54]   A. A. Silverio, W. Y. Chung, C. Cheng, W. Hai-Lung, K. Chien-Min, J. Chen et al., "The potential of at-home prediction of the formation of urolithiasis by simple multifrequency electrical conductivity of the urine and the comparison of its performance with urine ion-related indices, color and specific gravity." Urolithiasis, 44(2), 12734 (2016).

[55]   A. Unic et al., J. Clin. Lab. Anal., 32, 1 (2018).

[56]   W. Lee, Y. Kim, S. Chang, A.-J. Lee, and C.-H. Jeon, J. Lab. Med. Qual. Assur., 39, 76 (2017).

[57]   W. Dungchai, O. Chailapakul, and C. S. Henry, Anal. Chem., 81, 5821 (2009).

[58]   P. K. Sekhar and J. S. Kysar, J. Electrochem. Soc., 164, B113 (2017).

[59]   E. L. Fava et al., Talanta, 203, 280 (2019).

[60]   C. Ongkum, K. Keawmitr, and E. Boonchieng, in 2016 9th Biomedical Engineering International Conference (BMEiCON), p. 1, IEEE, Laung Prabang, Laos (2016).

[61]   M. Ra et al., IEEE J. Transl. Eng. Heal. Med., 6, 1 (2018).

[62]   D.-S. Lee, W. I. Jang, M. Y. Jung, B. G. Jeon, and C. Ihm, in Sensors, 2011 IEEE, p. 1495, Limerick (2011).

[63]   J. L. Robinson, A. A. Venner, and I. Seiden-Long, Clin. Biochem., 71, 77 (2019).

[64]   A. Pal et al., Adv. Mater. Technol., 2, 1 (2017).

[65]   M. Jalal Uddin, G. J. Jin, and J. S. Shim, Anal. Chem., 89, 13160 (2017).

[66]   A. Garifullina, N. Bhalla, and A. Q. Shen, Anal. Methods, 10, 290 (2018).

[67]   Y. M. F. Marickar, Urol. Res., 38, 233 (2010).

[68] K. Settu, C. J. Chen, J. T. Liu, C. L. Chen, and J. Z. Tsai, Biosens. Bioelectron., 66, 244 (2015).

[69] U. Sivasankaran, A. Thomas, A. R. Jose, and K. G. Kumar, J. Electrochem. Soc., 164, B292 (2017).

[70] Y. Baikeli et al., J. Electrochem. Soc., 166, B1171 (2019).

[71] S. A. Atty, O. M. Abdallah, M. A. Abdelrahman, and A. M. Abdel-Megied, J. Electrochem. Soc., 166, B1217 (2019).

[72] M. Rizk, E. A. Taha, M. M. A. El-Alamin, H. A. M. Hendawy, and Y. M. Sayed, J. Electrochem. Soc., 165, H333 (2018).

[73] W. Yao et al., J. Electrochem. Soc., 166, B1258 (2019).

[74] S. Kubendhiran, R. Sakthivel, S. M. Chen, and B. Mutharani, J. Electrochem. Soc., 165, B96 (2018).

[75] Y. Peng, Q. Chen, J. Xie, and W. Lan, J. Electrochem. Soc., 166, B521 (2019).

[76] C. Nayak and A. Saha, Optik (Stuttg)., 127, 5462 (2016).

[77] O. Tokel, F. Inci, and U. Demirci, Chem. Rev., 114, 5728 (2014).

[78] D. M. Minton, E. K. O'Neal, and T. M. Torres-McGehee, J. Athl. Train., 50, 59 (2015).

[79] A. A. Megahed, W. Grünberg, and P. D. Constable, J. Vet. Intern. Med., 33, 1530 (2019).

[80] Y. Chen et al., Sensors Actuators, B Chem., 226, 412 (2016).

[81] E. Wijaya et al., Curr. Opin. Solid State Mater. Sci., 15, 208 (2011).

[82] N. Alim and M. N. Uddin, in 2017 IEEE Region 10 Symposium (TENSYMP), p. 1, IEEE, Cochin (2017).

[83] X. Wang, T. W. Chang, G. Lin, M. R. Gartia, and G. L. Liu, Anal. Chem., 89, 611 (2017).

[84] M. Soler et al., Biosens. Bioelectron., 94, 560 (2017).

[85] G. I. Lee et al., Biochip J., 7, 68 (2013).

[86] A. Gaber, H. Hamed, and E. Elsawy, Genet. Mol. Res., 16 (2017).

[87]   A. P. Demchenko, Introduction to Fluorescence Sensing, Second Edi., Springer International Publishing (2015).

[88]   S. Park, Y. Zhang, S. Lin, T.-H. Wang, and S. Yang, Biotechnol Adv., 29, 830 (2011).

[89]   H. Zaghloul and M. El-Shahat, World J. Hepatol., 6, 916 (2014).

[90]   T. N. T. Dao et al., Anal. Biochem., 544, 87 (2018).

[91]   C. Liu et al., Analyst, 136, 2069 (2011).

[92]   M. G. Cavalcanti, A. F. A. Cunha, and J. M. Peralta, Front. Immunol., 10, 1 (2019).

[93]   L. Geue et al., Microbiol. Immunol., 58, 77 (2014).

[94]   W. young Chung et al., Biosens. Bioelectron., 26, 4314 (2011).

[95]   W. Chung et al., Cancer Epidemiol. Biomarkers Prev., 20, 1483 (2011).

[96]   H. Becker et al., Microfluid. BioMEMS, Med. Microsystems XIII, 9320, 93200S (2015).

[97]   R. Pichler et al., BJU Int., 121, 29 (2018).

[98]   S. M. Yoo et al., Mol. Cell. Probes, 23, 171 (2009).

[99]   H. Peter et al., J. Clin. Microbiol., 50, 3990 (2012).

[100]   J. Esteve-Romero, J. Albiol-Chiva, and J. Peris-Vicente, Anal. Chim. Acta, 926, 1 (2016).

[101]   Y. K. Chong, C. C. Ho, S. Y. Leung, S. K. P. Lau, and P. C. Y.Woo, Comput. Struct. Biotechnol. J., 16, 316 (2018).

[102]   M. Oyaert and J. Delanghe, Ann. Lab. Med., 39, 15 (2019).

[103]   E. Carrick et al., Proteomics - Clin. Appl., 10, 732 (2016).

[104]   A. Loras et al., Sci. Rep., 8, 1 (2018).

[105]   M. Íñigo et al., J. Clin. Microbiol., 54, 988 (2016).

[106]   W. Li et al., Front. Microbiol., 10, 1 (2019).

[107]   T. Tsukiyama, Procedia Comput. Sci., 63, 229 (2015).

[108]   C. Taramasco et al., in 2018 13th Annual Conference on System of Systems Engineering (SoSE), p. 117, Paris (2018).

[109]   A. Yates, J. Community Nurs., 33, 55 (2019).

[110]   A. Trigg, F. L. Andersson, N. V. J. Aldhouse, D. L. Bliwise, and H. Kitchen, Patient, 10, 711 (2017).

[111]   C. Taramasco et al., IEEE Access, 6, 52500 (2018).

[112]   T. Tamura, Physiol. Meas., 33 (2012).

[113]   M. Miyazato et al., Neurourol. Urodyn., 38, 1106 (2019).

[114]   K. Fujita, Y. Kanayama, J. Kim, and K. Nakajima, Adv. Biomed. Eng., 8, 1 (2019).

[115]   K. Wiens, S. Green, and D. Grecov, Measurement, 47, 314 (2014).

[116]   A. Anastasiou, K. Giokas, and D. Koutsouris, IFMBE Proc., 57, 1237 (2016).

[117]   A. C. Small, S. L. Thorogood, O. Shah, and K. A. Healy, Urol. Clin. North Am., 46, 287 (2019).

[118]   J. G. Hugtenburg, L. Timmers, P. J. M. Elders, M. Vervloet, and L. van Dijk, Patient Prefer. Adherence, 7, 675 (2013).

[119]   D. Ryan, K. Robards, P. Prenzler, and M. Kendall, Anal. Chim. Acta, 684, 17 (2011).

[120]   C.-C. Lin, C.-C. Tseng, T.-K. Chuang, D.-S. Lee, and G.-B. Lee, Analyst, 136, 2669 (2011).

[121]   A. R. Watson and A. Roberts, Pain Physician, 21, E167 (2018).

[122]   B. Šoba, M. Skvarǎc, and M. Matiǎciǎc, Acta Dermatovenerologica Alp. Pannonica Adriat., 24 (2015).

[123]   P. Kissinger and A. Adamski, Sex. Transm. Infect., 89, 426 (2013).

[124]   W. Wang, S. Wang, and M. Zhang, Oncotarget, 8, 38517 (2017).

[125]   O. C. Colvin et al., Skeletal Radiol., 44, 673 (2015).

[126]   T. Bhavsar, R. Potula, M. Jin, and A. L. Truant, MLO Med Lab Obs, 47, 8 (2015).

[127]   D. B. Barr et al., Environ. Health Perspect., 113, 192 (2005).

[128]   P. D. Sawant, S. A. Kumar, S. Wankhede, and D. D. Rao, Appl. Radiat. Isot., 136, 121 (2018).

[129]   N. J. Reine and C. E. Langston, Clin. Tech. Small Anim. Pract., 20, 2 (2005).

[130]   M. Mohammadifar and S. Choi, in 2018 IEEE 12th International Conference on Nano/Molecular Medicine and Engineering (NANOMED), p. 244, IEEE (2018).

[131]   N. A. Tufani, J. L. Singh, M. Kumar, and V. S. Rajora, J. Entomol. Zool. Stud., 5, 2354 (2017).

[132]   E. M. Stansbridge, D. G. Griffin, and V. Walker, J. Clin. Pathol., 66, 426 (2013).

[133]   A. Viljoen, R. Chaudhry, and J. Bycroft, Ann. Clin. Biochem., 56, 15 (2019).

[134]   C. J. Saatkamp et al., J. Biomed. Opt., 21, 37001 (2016).

[135]   C. S. Pundir, S. Jakhar, and V. Narwal, Biosens. Bioelectron., 123, 36 (2019).

[136]   M. Gupta, S. Bhayana, and S. K. Sikka, Int. J. Phys. Chem. Math. Sci., 1, 1 (2012).

[137]   J. A. Gardner and H. Gainsborough, Biochem. J., 19, 667 (1925).

[138]   H. Sobotka, E. Bloch, and A. B. Rosenbloom, Am. J. Cancer, 38, 253 (1940).

[139]   S. García et al., J. Clin. Psychopharmacol., 36, 355 (2016).

[140]   L. Shen, J. A. Hagen, and I. Papautsky, Lab Chip, 12, 4240 (2012).

[141]   A. A. S. Gunawan, D. Brandon, V. D. Puspa, and B. Wiweko, Procedia Comput. Sci., 135, 481 (2018).

[142]   Ward's Science, Ward's Sci. (2019).

[143]   A. Prasad, S. M. A. Hasan, S. Grouchy, and M. R. Gartia, Analyst, 144, 197 (2019).

Chapter 3

Research Paper 1 - Optofluidic Dissolved Oxygen Sensing With Sensitivity Enhancement Through Multiple Reflections

Eric James Mahoney[1,=], Huan-Hsuan (Leo) Hsu[1,=], Fei Du[1], Bo Xiong[1], P. Ravi Selvaganapathy[1,2], and Qiyin Fang[1,3,z]

[1]*School of Biomedical Engineering, McMaster University, 1280 Main St West, Hamilton ON, L8S 4K1, Canada*

[2]*Department of Mechanical Engineering, McMaster University, 1280 Main St West, Hamilton ON, L8S 4K1, Canada*

[3]*Department of Engineering Physics, McMaster University, 1280 Main St West, Hamilton ON, L8S 4K1, Canada*

[=]*Contributed equally.*

[z]*Corresponding Author qiyin.fang@mcmaster.ca*

Introduction to Research Paper 1.

Chapter 3 is a published article based on work conducted from 2013 through 2019. The article was written with Dr. Leo Hsu, Ms. Fiona Du, Mr. Bo Xiong, Dr. Ravi Selvaganapathy, and Dr. Fang in 2019. My contribution as an equally contributing first author of this research paper was to complete the work of Ms. Du on optimizing an optical Dissolved Oxygen (DO) sensor. I presented additional mathematical relationships to explain the mechanism of sensitivity enhancement that was observed in Ms. Dus' experiments. I assisted with one of the final measurements of the DO sensor and significantly expanded the draft manuscript prepared by Dr. Hsu. The final article was based on the TIR model and the work presented in Ms. Dus' Masters Thesis. She fabricated the DO sensors and performed the fluorescence measurements to determine the device sensitivity at each test angle and film thickness. Dr. Leo Hsu prepared electrochemical DO sensors and assisted with fabricating the optical DO sensor films and PDMS channel caps. Dr. Ravi supported our work and revised the work. Professor Fang supported and guided our work and revised the content before submission. I took a lead role in responding to questions from reviewers. The significance of this research involves the experimental optimization of a multilayered fluorescence-based sensor for dissolved oxygen in fluid samples and the development of a simplified model describing the sensitivity enhancement mechanism of Total Internal Reflection in multilayered optical devices.

Contents

Abstract

The development of compact and low-cost dissolved oxygen (DO) sensors is essential for the continuous in situ monitoring of environmental water quality and wastewater treatment processes. The optical detection of dynamic and reversible quenching of fluorescent dyes by oxygen has been used for DO sensing. In this paper, we have optimized a multilayer optofluidic device based on the measurement of fluorescence quenching in a Ruthenium-based oxygen sensitive dye by employing total internal reflection (TIR) of the excitation light to achieve sensitivity enhancement for the detection of 0–20-ppm DO in water. The incident angles of light and sensitive layer thickness are optimized experimentally in order to increase the path length of light in the sensitive layer of the device through multiple

reflections. A model is developed to demonstrate how light propagates through different layers of the device at varying angles of excitation and to describe the mechanism of fluorescence generation for each of the types of TIR observed. The design principles identified in this paper may be applied to the development and optimization of new multilayered optofluidic sensors by employing TIR for sensitivity enhancement.

3.1.   INTRODUCTION

Dissolved Oxygen (DO) is essential for the health of water bodies and aquatic life. Many marine organisms require a DO concentration of at least 5 ppm to survive [1]. Contamination of water with organic compounds from Wastewater Treatment Plants (WTPs) and agricultural runoff can promote the growth of microorganisms leading to a reduction in DO. Low DO causes excessive growth of anaerobic bacteria that can permanently damage water bodies [1]. WTPs employ costly energy intensive aeration processes to maintain high DO in water in order to facilitate the growth of microorganisms that remove organic material from wastewater. The energy consumption in WTPs can be optimized if DO levels in the aeration process are assisted by real time DO sensing [2], [3]. Due to the large quantity of sensors required to monitor bodies of water the sensors have to work continuously with high accuracy for an extensive period of time without requiring manual intervention (e.g. battery change, calibration, maintenance etc.). To widely distribute DO sensors in the environment, the system should be compact and low cost. Low power consumption is also a highly desired feature for applications requiring sensors to be deployed without access to the power grid.

Methods for DO monitoring have been extensively investigated over the past few decades. The primary methods that have been developed include chemiluminescence, electrochemical, and optical detection techniques. The Winkler method, which is a chemiluminescence technique, is considered to be the gold standard of DO monitoring [4]–[6]. However, the Winkler method is costly considering the reagents required. The rate of measurement is limited due to the number of steps involved in the Winkler method. Electrochemical DO sensors have also been developed based on the Clark electrode configuration [7], where the DO concentration is calculated from the current measured. Drawbacks of electrochemical sensors include low sensitivity, and limited lifetime due to aging of the catalyst electrode and fouling of the oxygen permeable membrane. The

amount of time water sensors can continuously function is often limited due to bio fouling. To extend the lifetime of the sensor, anti-fouling coatings have been developed. It has been shown that these anti-fouling techniques enable DO sensors to function reliably for longer periods of time compared to those without the coating. [8].

Optical DO sensors measure oxygen by its ability to quench the fluorescence emission of excited oxygen sensitive fluorophores. A Ruthenium (Ru) complex immobilized in an organic polymer matrix has been used as an oxygen sensitive material for DO sensing [9], [10]. The fluorescent Ruthenium dye is collisionally quenched by oxygen present in the ambient which reduces its steady state fluorescence intensity and fluorescence lifetime [11]. The relationship between DO concentration and quenched fluorescence intensity is expressed by the Stern-Volmer equation [12]:

$$\frac{I_{f0}}{I_f} = \frac{\tau_0}{\tau} = 1 + k_q \tau_0 [Q] \qquad \textbf{Equation 3.1}$$

where I_{fo} and I_f are the integrated fluorescence intensities in the absence of oxygen, and in the presence of DO, respectively. τ_o and τ are the fluorophore excited state lifetimes in the absence of oxygen and in the presence of DO, respectively. k_q is the diffusion dependent quenching constant, and Q is the concentration of oxygen. The relative intensity of fluorescence emitted is expressed by:

$$I_{em} = \phi I_0 (1 - e^{-\varepsilon cl}) \qquad \textbf{Equation 3.2}$$

where I_{em} is the intensity of fluorescence emission. Φ is the quantum efficiency of the fluorophore. I_o is the intensity of light exciting the fluorophore. ε is the molar absorptivity of the fluorophore. c is the fluorophore concentration. l is the path length of the excitation light in the sensitive layer [13]. Optical detection methods demonstrate minimum interference with sample constituents, good sensitivity, and long working lifetime (with calibration) compared to the chemical and electrochemical methods [14]–[16]. However, traditional optical sensing designs are large, expensive, and have high power requirements due to integration of components (e.g., free space optics, lamps, spectrometers, and photomultipliers) [17]. Miniaturization can mitigate some of the limitations

of traditional systems making them suitable for a wider scope of applications.

Miniaturized optical DO sensing methods have been developed for cell culture [18], [19], disease detection [20], and microbial research [21]. Often, bench top fluorescence microscopes with a camera [19], [20], spectrophotometers [18], or high sensitivity photodetectors with high voltage power supplies (e.g. photomultiplier tubes or avalanche photo diodes) are required due to low signal levels [18], which are not suitable for environmental applications. Direct coating of the fluorophore onto an optical fiber is another approach to miniaturize the optical DO sensor [22], [23]. However, the optical path through the fiber shared by both excitation and emission light makes it difficult to detect changes in the emission signal since its intensity is much lower than the excitation light, limiting sensitivity. Alternatively, sensitivity can also be enhanced by increasing the path length of excitation light in the sensitive material to improve the absorption by the fluorophore and thereby increase emission intensity.

Total internal reflection (TIR) is a phenomenon that causes incident light to be completely reflected at an interface when traveling to a lower refractive index medium when the incident angle is larger than a critical angle.

When the TIR condition is satisfied, the device becomes a multi-layer waveguide that effectively increases the optical path length in the sensitive layer to achieve high sensitivity [24]. TIR has been used in many applications including surface plasmon resonance detection devices for DNA hybridization [25] and immunoassays [26], [27]; fluorescence imaging [28], [29]; and fluorescence spectroscopy [30]. Several waveguide-based optical monitoring systems for DO and Oxygen gas have been proposed [29]–[31]. However, integration of TIR into sensors to form multilayer design [32] and optical fiber integration [33] require complex fabrication processes and sensitive optical alignment. The complicated manufacturing procedures of these sensors such as multilayer design [32] and optical fiber integration [33] make them expensive and not used in automated sensing applications.

In this paper, we report the design and development of an optofluidic DO sensor integrating a multipoint TIR optical sensing module into Poly (dimethylsiloxane) (PDMS)/glass microfluidic channels. We systematically

studied different TIR regimes when integrating with multi-layer optofluidic devices. Our results lead to a set of optimized designs which are robust and with reduced fabrication difficulty. We have experimentally optimized the optofluidic TIR based DO sensor presented in our earlier work [34], [35] and developed numerical models of the relationship between sensitivity, incident angle, and sensitive layer thickness. These models are also experimentally validated and applied to optimize the sensitivity of this device. The model and associated design principles have broader applicability to multilayer optofluidic sensing devices where TIR may be used to enhance sensitivity.

3.2. SENSOR DESIGN AND MODEL

The fabricated DO sensor consists of two main layers as illustrated in Fig. 3.1. The first layer is a 1.1mm thick 74×25 mm² soda lime glass slide serving as both substrate and total internal reflection waveguide. Glass was selected as the optical waveguide since it is transparent in both excitation (450 nm) and emission (613 nm) of $Ru(dpp)_3$. The second layer is a mixture of Tris(4,7-diphenyl-1,10-phenanthroline) Ruthenium (II) dichloride complex ($Ru(dpp)_3$), and PDMS, in the ratio of 1:200 (w.t.) respectively as a DO sensitive module. $Ru(dpp)_3$ can uniformly mix with PDMS and serves as the DO sensitive fluorophore in this application. The theoretical molar absorptivity of the Ruthenium complex is 29500 $M^{-1}cm^{-1}$ [36]. Sensitive film thicknesses of 10μm, 50μm, and 100μm were tested. PDMS was selected as the main fabrication material due to its high gas permeability making it well suited for gas sensing applications, and it has proven itself to be one of the most commonly used materials in microfluidic devices. A microfluidic channel (3 mm in height) fabricated from PDMS (length: width: height = 60 mm: 2 mm: 2 mm) was attached to this sensing layer such that the water sample that it holds on top of the sensitive layer forms a TIR surface as well. The water sample is injected through tubing inserted into the ends of the channel through inlet and outlet ports in the PDMS cap.
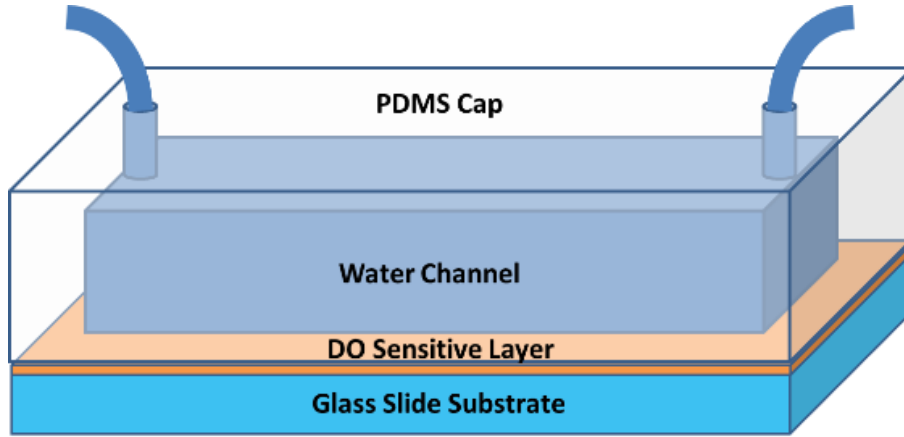
Figure 3.1   Schematics of the Dissolved Oxygen sensing device (not to scale). The bottom layer is a 1.1 mm thick soda lime glass microscope slide. The second layer is a 10 μm thick oxygen sensitive fluorescent film. The third layer is the 2 mm ×2 mm water sample guided through a PDMS channel. The PDMS cap is 3 mm thick.

   Depending on excitation coupling conditions, there are several modes for the excitation light propagating through the sensor structure. First, we assume that the incident light is a collimated source with a uniform intensity distribution. The validity of this assumption will be discussed later. Briefly, the excitation light is delivered to the sensor at the critical angle causing it to reflect internally within the glass slide and propagate along the device beneath the water channel. After the excitation light enters the device some of the optical energy can be absorbed by the DO sensitive material and converted to fluorescence. The observed fluorescence intensity is proportional to the amount of optical energy absorbed and thus becomes the key parameter to determine the sensitivity of the device.

   The sensitivity of the device is optimized by improving the intensity of fluorescence emission from the sensitive layer during DO sensing. The quantum yield, molar absorptivity, and concentration of fluorescent dye in the sensitive layer are constant; however, the intensity and path length of light in the sensitive layer can be optimized. The intensity of incident light, path length, and number of reflection points generated in the sensitive layer are dependent on the incident angle of light, and the sensitive layer thickness. Simulations have been conducted in order to understand the relationship between energy absorption and the incident angle of excitation light. When the incident light reaches the edge of the glass substrate and enters the device the light refracts which can be described by Snell's law:

$$n_i \cdot \sin\theta_i = n_r \cdot \sin\theta_r \qquad \textbf{Equation 3.3}$$

where n_i is the refractive index of material as incident medium and n_r is the refractive index of the refractive medium. θ_i and θ_r are the incident and refraction angles respectively. There are two interfaces of refraction in the device. The first interface is between the air/glass substrate. The second interface is between the glass/PDMS. The path of the total internal reflection can be distinguished into three types depending on the incident angle as shown in Fig. 3.2. When the ideal incident angle is used the light is reflected at the interface of the sensitive layer and the water sample, thus the water layer is neglected as an interface of refraction in this simulation. Based on the calculation, the light is total reflected inside the glass slide when the incident angle of air/glass (θ in Fig. 3.2) is below 33° (type 1); totally reflected inside the glass and sensitive layer when the incident angle is between 33° and 47° (type 2); totally reflected in the whole device when the angle is larger than 47° (type 3).
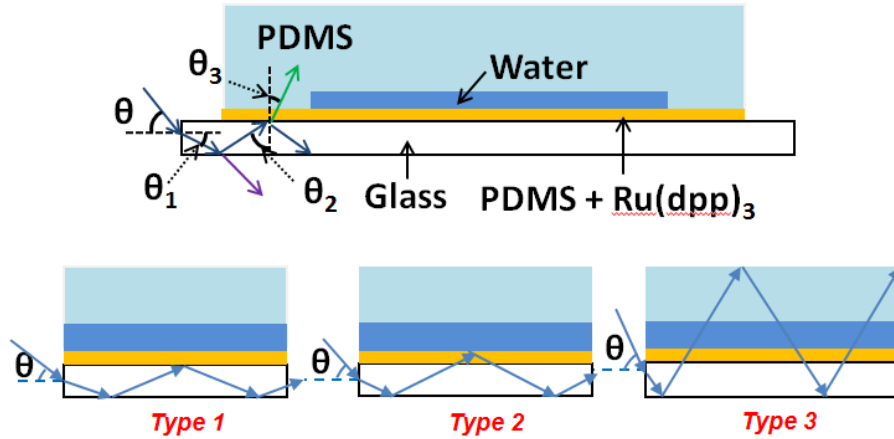
Figure 3.2 Three types of total internal reflections may occur depending on the incident angle of light (θ). Type 1 occurs when $\theta<33°$ and light is reflected within the glass substrate. Type 2 occurs when $33°<\theta<47°$ and light is reflected in the glass and sensitive layers. Type 3 occurs when $\theta>47°$ and light is reflected in the whole device.

In type 1 total internal reflection most of the light is reflected inside the glass and does not transfer into the sensitive layer. In this case the light absorbed by the sensitive layer comes from the evanescent wave extending into the sensitive layer at each site of reflection. The total path length of light in the sensitive volume for type 1 depends on the number of reflections observed at small incident angles and the intensity of the evanescent wave

in the sensitive layer described by eq. 4 and 5. The intensity of the evanescent wave decreases with increasing distance from the interface of the glass and the sensitive layer and can be represented by the evanescent wave equation [37], [38]:

$$\int I(z)\, dz = I \cdot e^{-z/d} \qquad\qquad \textbf{Equation 3.4}$$

where z is the vertical distance of DO sensitive layer from the reflection site. $I(z)$ is the intensity of light at z. I is the intensity of incident light. d is the penetration depth of the evanescent wave which can be calculated by:

$$d = \frac{\lambda_0}{4\pi}(n_{glass}^2\ \sin^2 \theta_2 - n_{PDMS}^2)^{-1/2} \qquad \textbf{Equation 3.5}$$

where λ_0 is the wavelength of incident light which is 450 nm. θ_2 is the incident angle at the glass/PDMS interface (Fig. 3.2). n_{glass} and n_{PDMS} are the refraction indexes of glass (1.52) and PDMS (1.41), respectively. The volume of sensitive material using type 1 reflections is limited by the penetration depth of the evanescent wave leading to low sensitivity compared to type 2 and type 3 reflections.

The number of reflection points along the channel depends on the incident angle, the number of layers in the device, and the refractive index and thickness of each layer. The incident angle will determine which type of TIR propagates in the device, and the angle of light as it travels within different layers. When the type 1 condition is met and the light only travels along the glass slide the average distance between points of reflection can described by:

$$D_r = \frac{2Tg}{\tan(\theta_g)} \qquad\qquad \textbf{Equation 3.6}$$

where D_r is the average distance between reflection points. T_g is the thickness of the glass substrate. θ_g is the angle of light in glass shown as θ_1 in Fig. 3.2. θ_g depends on the incident angle and the refractive index of the glass substrate. At the optimum angle the type 2 condition is met and the light travels within the glass slide and the sensitive film. The distance between reflection points is determined by the distance travelled in glass plus the distance travelled through the sensitive film described by:

$$D_r = \frac{2Tg}{\tan(\theta_g)} + \frac{2Ts}{\tan(\theta_s)} \qquad \textbf{Equation 3.7}$$

where T_s is the sensitive layer thickness, and θ_s is the angle of light in the sensitive layer. θ_s depends on the refractive index of the glass substrate, the refractive index of the sensitive layer, and θ_g. At larger incident angles the type 3 condition is met and the light travels within all layers of the device and the distance travelled in the water layer and PDMS cap must also be considered. The average distance traveled through the sensitive film can be described by:

$$D_r = \frac{2Tg}{\tan(\theta_g)} + \frac{2Ts}{\tan(\theta_s)} + \frac{2Tw}{\tan(\theta_w)} + \frac{2T_{PDMS}}{\tan(\theta_{PDMS})} \qquad \textbf{Equation 3.8}$$

where T_w and T_{PDMS} are the height of the water channel; and the thickness of the PDMS cap respectively. θ_w is the angle of light in the water sample. θ_{PDMS} is the angle of light in PDMS. θ_w depends on the refractive index of the sensitive layer, the refractive index of the water sample, and θ_s. θ_{PDMS} depends on the refractive index of the water sample, the refractive index of PDMS, and θ_w.

Considering type 2 and type 3 reflections, the DO sensitive layer can absorb 28% of energy per reflection site (light penetrates through whole DO sensitive layer). Assuming that all incident light is injected into the device it is expected that the amount of light absorbed by the sensitive layer will increase as the angle between incident light and the normal of the edge of the glass slide increases. However, the collimated laser beam diameter and thickness of the glass slide are both 1 mm; therefore, only part of the light can be effectively coupled into the device. Some light will also be lost due to the partial reflection at the interface between glass and air as the light enters the glass substrate. Due to these losses the energy injected into the device is proportional to the cosine of the incident angle. The calculated absorbed energy before and after cosine correction is shown in Table 3.1.

Table 3.1 Absorbance Efficiency With Respect to Incident Angle

TIR Type	Angle (°)	Predicted Absorbance Efficiency	Cosine Corrected Absorbance Efficiency
I	15	25%	24%
	25	32%	29%
II	34	82%	68%
III	45	83%	59%
	55	92%	53%

A simulation demonstrating the excitation and emission contours and relative intensity for a sensor excited at the critical angle is presented in Fig. 3.3. The intensity of the source light is reduced due to absorbance in the sensitive layer at each point of reflection. At each point of reflection a portion of incident light can be reflected within the sensitive layer. At each point of reflection within the sensitive layer a portion of the incident light may also reenter the glass substrate. The volume within the sensitive material that is excited by incident light generates fluorescence signal dependent on the incident light intensity and DO concentration.
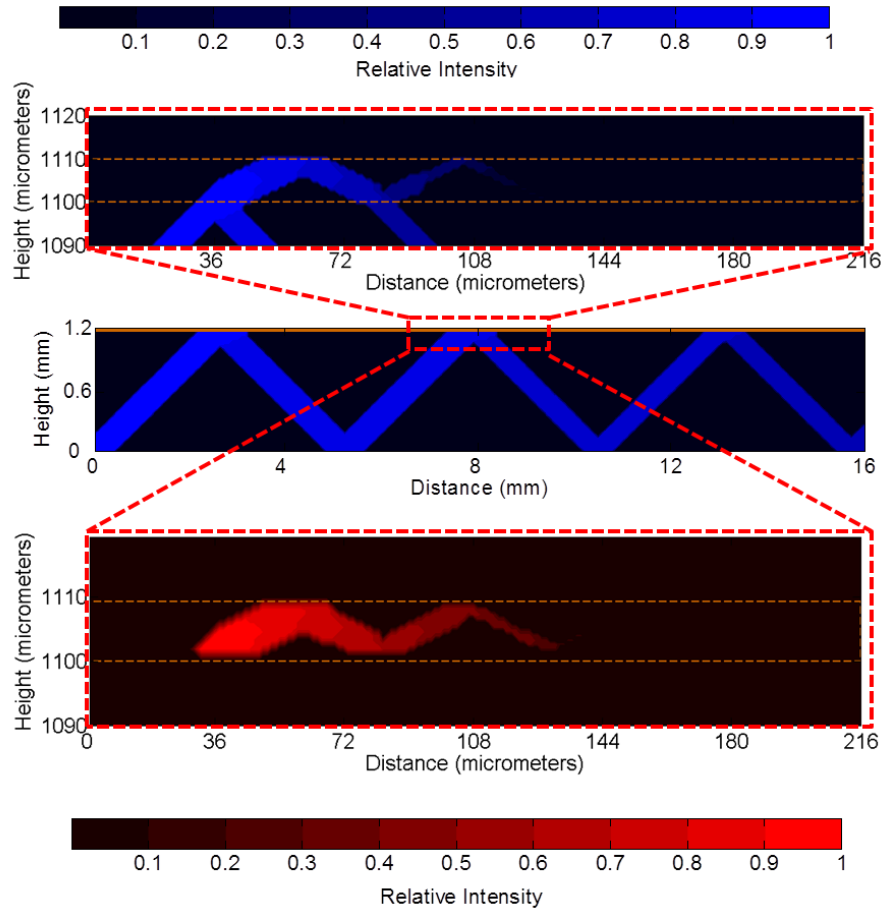
Figure 3.3 Simulated relative excitation (blue) and emission (red) intensity distributions of type 2 TIR inside the sensor at 36° incident angle of excitation. Top figure focuses on the relative intensity of excitation light in the sensitive layer at a single point of reflection. Middle figure shows the propagation of incident light through the glass substrate. Bottom figure focuses on the relative intensity of fluorescence emission from the sensitive layer at a single point of reflection. Orange lines indicate the fluorophore film coated above the glass substrate. Excitation light is total-internal-reflected inside the glass slide and the fluorophore film at this incident angle. The X-axis represents the distance along the water channel length; Y-axis indicates the height.

3.3. MATERIALS AND METHODS

3.3.1. Sensor Fabrication

Prior to fabricating the sensor, the soda lime glass substrate was washed by isopropyl alcohol to remove any impurity. After cleaning, a thin film

mixture of Ru(dpp)$_3$ and PDMS was spin coated onto the soda lime glass. Around 10 μm of Ru(dpp)$_3$/ PDMS thin film was obtained by spinning at 6000 rpm spin rate for 1 minute. After spin coating, the obtained membrane was dried on a hotplate at 100°C for 1 hour. Subsequently, the PDMS microchannel made by conventional soft lithography [39] was bonded on top of the DO sensitive layer by air plasma to support the water sample.

3.3.2. DO Sensing

The fabricated device was first mounted onto a homemade optical stage with adjustable angle as shown in Fig. 3.4. The adjustable angle mount was made using a continuous angle clamp (SWC, Thorlabs, Newton, NJ) and a right-angle plate (AP90, Thorlabs). A transparent protractor was mounted to the optical table next to the sensor with the straight edge parallel to the table surface and the edge of the glass substrate crossing the center. The incident angle was determined by reading the angle where the glass substrate crosses the edge of the protractor. A 150 mW blue laser diode (445–450 nm) (450 Diode, Laserland, Wuhan, China) was used as the excitation source. The intensity profile of the diode laser has an asymmetrical near Gaussian profile, which is typical for diode lasers. The incident light was attenuated through an OD3 filter reducing the power to 150 μW. The light was then focused to a 1mm diameter spot onto the edge of the glass substrate by a 10× microscope objective lens with a NA of 0.25. The cone angle was found to be approximately 15°. Due to the non-Gaussian distribution of light incident upon the objective lens a greater proportion of light will approach the sensor at angles close to the target angle of incidence. The range of angles introduced to the device at each angle tested determined which types of TIR can be generated for each angle of incidence.
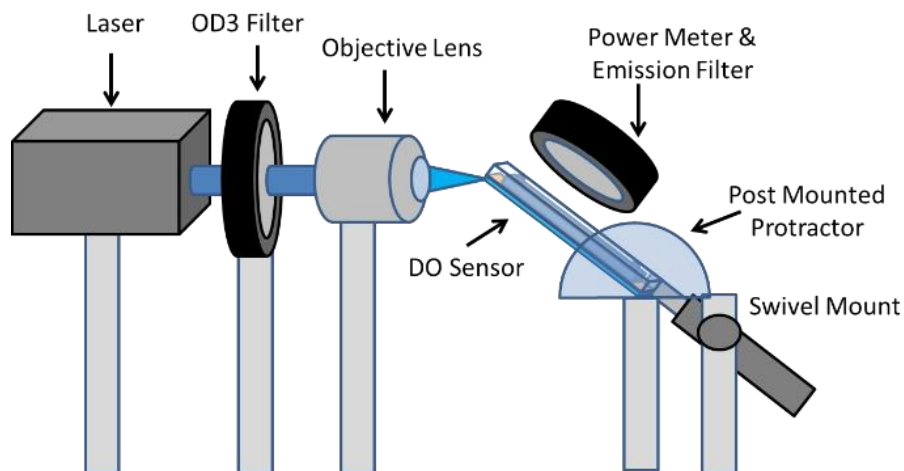
Figure 3.4 Experimental setup of DO measurement. A 450 nm laser is directed through an OD3 ND filter and focused on the edge of the glass substrate using a 10× objective lens (NA 0.25). The angle is controlled using an adjustable mount. A power meter probe with bandpass emission filter (520 – 720 nm) is positioned above the sensor to detect fluorescence. Water samples are injected sequentially and static samples are measured.

Both the power and beam size of the laser were optimized experimentally [34], [35]. The conceptual design of the TIR optofluidic DO sensing device is shown in Fig. 3.5 (a). The incident angle of the laser beam was adjusted to generate the total internal reflection in the DO sensor (as shown in Fig. 3.5 (c) insert). The incident angle was optimized in order to obtain the best sensitivity.

The $Ru(dpp)_3$ DO sensitive layer will emit fluorescence (613 nm) when it absorbs excitation light delivered by the blue laser. The fluorescence emission was collected by an optical power meter (Model 1830-C, Newport, Irvine, CA) mounted above the sensor to provide a measure of fluorescence intensity. The power meter was connected to a 520–720 nm bandpass filter (FF01-609/181-25, Semrock, Rochester, NY) to ensure only the emission light was detected. A syringe is used to inject the water samples onto the chip. The DO measurement is performed after sample injection with a static water sample. During DO sensing, oxygen in the sample can diffuse into the DO sensitive layer following injection into the device thus leading to the quenching of fluorescence. The DO concentration can be calculated by the reduction of fluorescence intensity due to oxygen quenching using the Stern-Volmer equation.
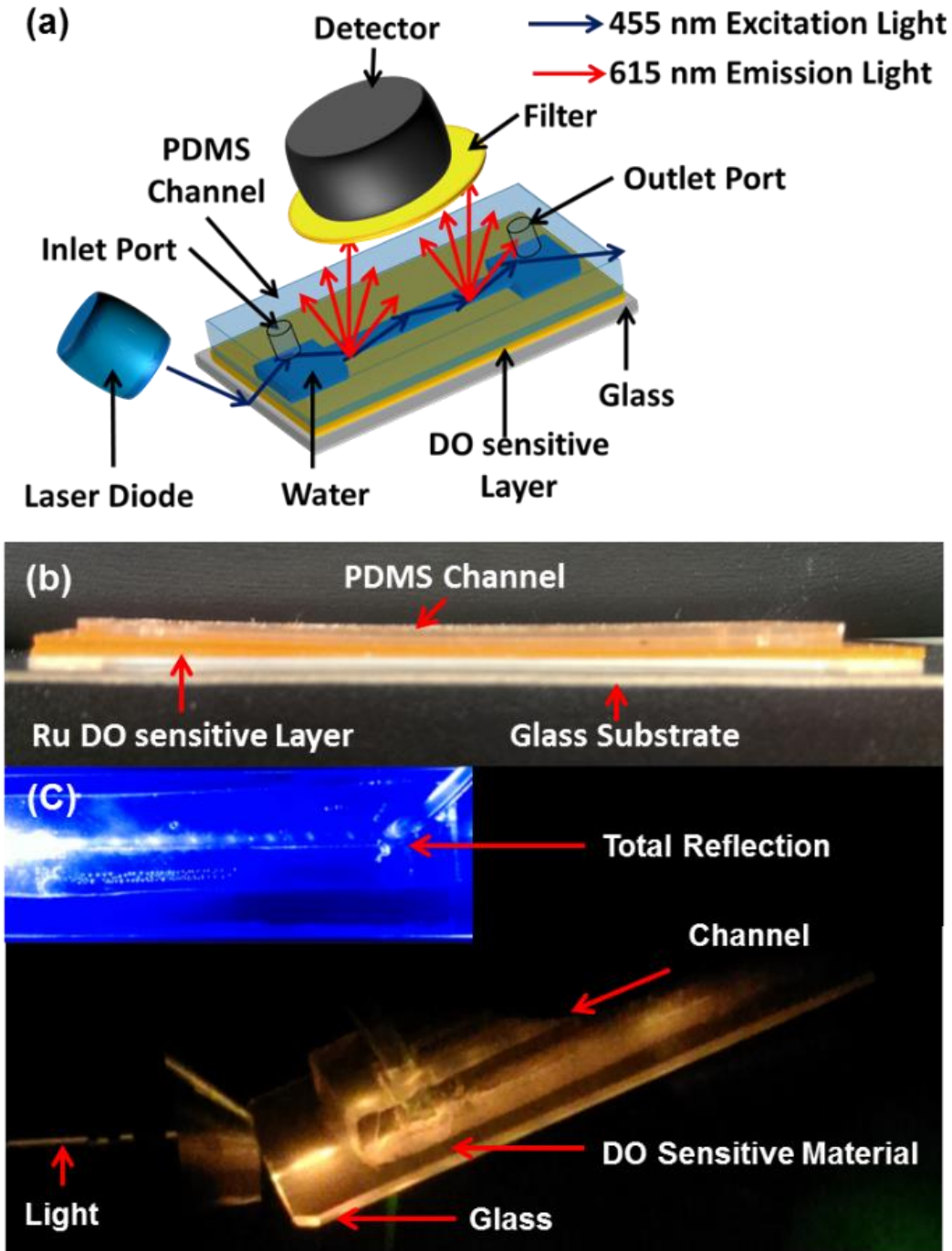
Figure 3.5 (a) Conceptual design of total internal reflection optical DO sensing device; (b) photograph of the side-view of the fabricated total internal reflection optical DO sensing device and (c) photograph of fluorescence emission from the total internal reflection when sensing DO.

3.3.3. Reagents

Tris(4,7-diphenyl-1,10-phenanthroline)Ruthenium(II) dichloride complex (Ru(dpp)$_3$) (99%) was purchased from American element (Los Angeles, CA). Sodium Sulphite (98%) was purchased from Caledon Laboratories (Georgetown, Ontario). Poly(ethylene glycol) dicarboxylic acid (PEGDA) (MW=600, >96%), N,N'-dicyclohexylcarbodiimide (DCC) (>99%), and 3-aminopropyltriethoxysilane (APTES) (99%) were purchased from Sigma-Aldrich (St. Louis, MO). Polydimethylsiloxane (PDMS) Sylgard 184 was purchased from Dow Corning (Midland, MI). All reagents were of analytical grade and were used without further purification. Nitrogen gas (99.9999% pure) and Oxygen gas (99.9999% pure) were purchased from Alphagaz (Montreal, Quebec). Deionized water (18.2 MΩ .cm) was used to prepare all solutions, unless otherwise noted.

3.4. RESULTS

3.4.1. Incident Angle Dependence

The incident angle of the laser beam is one of the main parameters which can determine the occurrence of TIR as well as determine the length of the optical path due to total reflection beam, thus influencing the sensor performance. Five angles (15° 23° 34° 45° and 55°) were tested to understand the influence of incident angle in sensing outcome. The incident angle was set between the glass substrate and the optical table by using a transparent post mounted protractor aligned at the edge of the glass substrate that is exposed to incident light. The emitted light intensity was measured at various DO concentrations in the sample solution at all the incident angles. The results are presented as the conventional Stern-Volmer plot (I_o/I vs. DO concentration) shown in Fig. 3.6(a) where I is the detected intensity, and I_o is the detected intensity when DO is at zero ppm. Sensitivity is determined by the change in fluorescence intensity with respect to DO concentration at each experimental angle, which is shown in Fig. 3.6(b). The resolution of DO measurements is determined by the respective DO concentration associated with the uncertainty in fluorescence intensity measurement. The resolution of fluorescence intensity measurements is judged by the error bars (standard deviation). Measurements of fluorescence generated from the entire device can be achieved using detectors with larger active areas or by focusing light from the device to the detector.
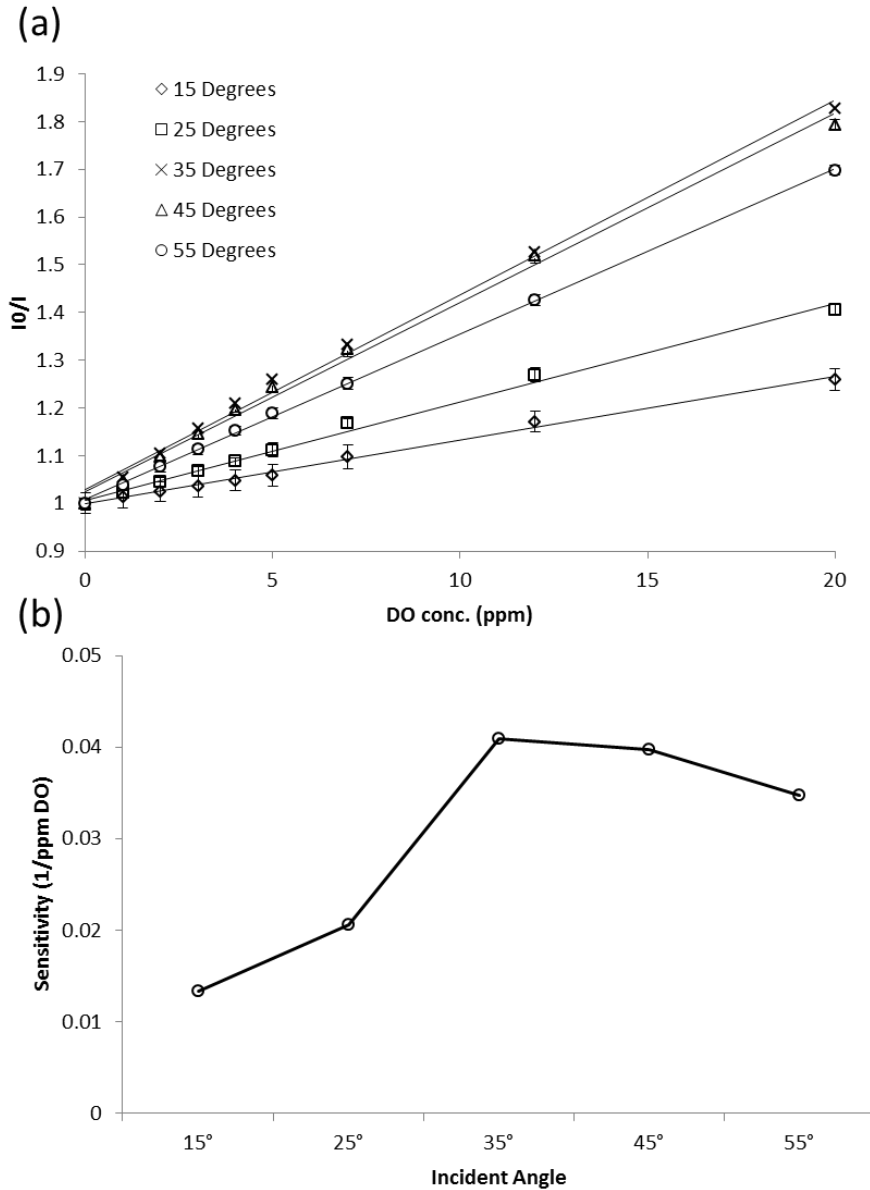
Figure 3.6 (a) Stern-Volmer plot (I_0/I vs. DO concentration) of the TIR optical DO sensing device when different incident angles applied; (b) Sensitivities of the device when different incident angles applied where sensitivity is defined as the slope of the Stern-Volmer plot. Type I (15°, 25°), Type II (34°), and Type III (45°, 55°) TIR conditions are tested.

The experimental results show that at each incident angle a change in fluorescence intensity is observed with respect to changes in DO. The sensitivities represented by the slopes of each Stern-Volmer plot vary with

the incident angle as shown in Fig. 3.6. This trend in sensitivity can be explained as a result of the relationship between the incident angle and the number of total reflection sites within the device which then determines the amount of energy absorbed by the DO sensitive layer. For instance, the total sensing area of the applied power meter probe can be considered to be a circle 3 mm in diameter. In this area, the 45° and 55° incident angles demonstrating predominantly Type III reflections can produce 5 and 7 total reflection sites respectively resulting in higher path length and greater absorption. Overall, the 34° incident angle demonstrates predominantly Type II reflections and exhibits the highest sensitivity among all the test angles followed by 45° 55° 25° and 15° in descending order of sensitivity. The calculated theoretical absorption efficiency of the device determined at each angle also follows this order as shown in table 3.1. The improvement in sensitivity was 3× at optimum angle of 34° compared to the 15° case demonstrating predominantly Type I reflections where most of the incident light is trapped in the glass substrate.

The increase of sensitivity is attributed to the enhancement of light absorption in DO sensitive layer. At the optimum incident angle, the path length of incident light in the sensitive layer is the longest at each point of reflection, which leads to the increase in light absorbed at each reflection. Consequentially the intensity of fluorescence emission is also the highest. Additionally, it must be emphasized that the highest sensitivity of our device ($I_o/I = 1.81$ at 20ppm DO) is comparable with some previously developed miniaturized DO sensing devices ($I_o/I = 2.49$ to 14.37 at 100% O_2) [9], [10], [40]. Moreover, the measurement variability of our DO sensing device is 2% in the range of 0–20ppm DO as determined by the standard deviation which is smaller compared to the sensing results of some previous works demonstrating 2% to 5% variability [22], [40]–[42].

The relatively small measurement variability of our sensing device suggests that our system has better resolution than these previous works. We estimated 95% confidence intervals of DO concentration at 34° by the statistical data of fluorescence intensity in our experiments following (9–11) [43]. The results showed a 0.4 ppm variation at 0 ppm DO and a 0.3 ppm variation at 10 ppm DO.

$$y = y_c \pm t_{v,P} S_{yx} \sqrt{\frac{1}{n} + \frac{1}{N} + \frac{(x - \bar{x})^2}{S_{xx}}}$$

Equation 3.9

$$S_{xx} = \sum_{i=1}^{N} x_i^2 - N\bar{x}^2$$

Equation 3.10

$$S_{yx} = \sqrt{\frac{\sum_{i=1}^{N}(y_i - y_{ci})^2}{N - 2}}$$

Equation 3.11

y_c: estimated value from linear curve fitting

$t_{(v,P)}$: student's t distribution

n: the number of replications for a particular x

N: the number of different x data points

3.4.2. Effect of DO Sensing Layer Thickness

The influence of DO sensitive layer thickness on sensitivity was also studied by using three different thicknesses of DO sensitive layer: 10 μm, 50 μm, and 100 μm. Results indicate that the sensitivity was reduced when the thickness of DO sensitive layer was increased (Fig. 3.7). An improvement in sensitivity of 4× was observed when using the 10 μm film compared to the 100 μm film at a constant angle of excitation at 45°.
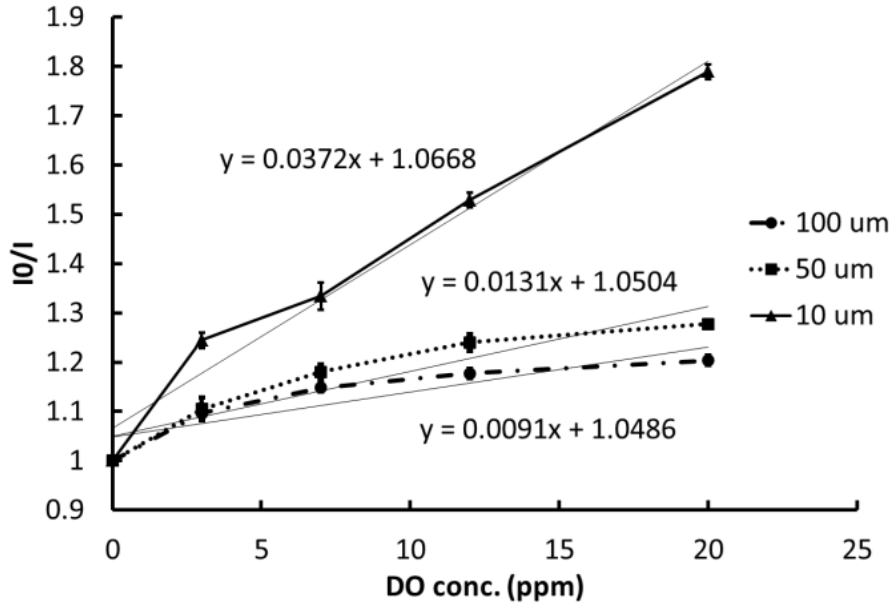
Figure 3.7 Stern-Volmer plot (I_0/I vs. DO concentration) of the total internal reflection optical DO sensing device when different thicknesses of DO sensitive layer applied. A $10\times$ objective lens with a NA of 0.25 is used with an incident angle of $45°$. The sensitivity is defined as the slope of each regression line of the Stern-Volmer line which shows DO sensitive layer with 10 μm thickness obtains highest sensitivity.

In this device, fluorescence is generated within the DO sensitive layer at each point of reflection. Thus, the fluorescence intensity is determined by the DO concentration within this volume which is controlled by the amount of oxygen diffusion (oxygen flux) from the microchannel through the DO sensitive layer. Previous research of Hartmann et al. [44] suggested that the oxygen flux can be estimated by the well-known Fick's law:

$$J_{O_2} = \frac{P}{d}(P_0 - P_1)$$ **Equation 3.12**

where J_{O_2} is the oxygen flux. $(P_0 - P_1)$ is the difference of oxygen pressure which drives the diffusion. P is the permeability. d is the thickness of the diffusion layer. In this design the DO sensitive layer is the diffusion layer. Fick's law suggests that the oxygen flux is inversely proportional to the thickness of the DO sensitive layer. A longer time is required for the DO concentration to equilibrate within thick films. Within a measurement window, the dye that does not come into contact with oxygen from the sample in thicker films will not experience quenching leading to a smaller

difference in emission intensity relative to the DO content in the sample. Devices with 1 μm DO sensitive layer thickness were also tested; however, the results show significant variability and cannot be repeated thus are not presented. The variability was likely due to leaching of $Ru(dpp)_3$ dye caused by sample flow. Nonetheless, the 10 μm or thicker film did not have a significant leaching effect and could be used multiple times without loss of performance.

3.5. DISCUSSION

Overall, the experimental results suggest that this sensing device can obtain the optimum sensitivity at an incident angle of 34° between the light source and the edge of the device. The influence of DO sensitive layer thickness in the sensing performance was also studied. Results suggested that the highest sensitivity can be obtained when the device has a 10 μm DO sensitive layer. Further increasing the sensitive layer thickness leads to reduced sensitivity. The sensitivity also depends on the number of total internal reflection sites. Generally, the sensitivity is enhanced when the number of the total internal reflection sites and path length at each reflection is increased. Thus, longer channels should be able to demonstrate higher sensitivity. These improvements lead to an increase in the amount of incident light that is absorbed in the sensitive layer which in turn increases the intensity of fluorescence emission observed at the detector. It should be noted that accurate modeling of the TIR modes in the devices would require measurements of the light profile as well as divergence angles. In this work, the light was approximated with a collimated uniform profile for qualitative explanation of the results. Work on developing quantitative models for these types of devices is ongoing.

This setup demonstrated the detection range between 0–20 ppm DO. The sensitivity and detection range of this device is adequate to be applied as an environmental based DO sensor with low manufacturing cost (~200 CAD including light source, filter and detector) and high measurement accuracy (± 0.4 ppm).

Total internal reflection has been used in optofluidic devices in waveguides to deliver excitation light to samples and to collect light from samples [45], often in the form of fiber optic probes. It has been employed for imaging in Total Internal Reflection Fluorescence Microscopy (TIRF) [46]. Confocal TIRF systems have been developed for the detection of

Oxygen gas in cell culture applications [47]; however, these have not been employed for the purposes of environmental DO sensing. Optical fibers with cladding omitted have been used to generate evanescent waves for sensing applications [48], yet the multiple reflection sites in optical waveguides have not been widely employed for sensitivity enhancement by producing many excitation regions in fluorescence quenching sensors. The size of the emission detector also needs to be enlarged in order to detect fluorescence from reflections outside of the field of view. Additional optical components may be employed to focus emission to the detector from a larger area.

This device can be used at sites such as wastewater treatment plants and drinking water sources which require highly accurate in-situ DO information. However, there are still improvements to be made to make this sensor suitable for real world application. (i) Experimental DO sensing by this device is performed on an optical setup with separated light source, detector and optical filter. Integration of all components into a compact device should be the next step before the application of this device in field testing. The final alignment requires careful consideration of the light path and sample flow to accurately generate total reflection sites inside the channel and observe the interaction between DO and the sensitive layer. (ii) Microfluidic based sensing devices for water monitoring are always limited from long term usage due to biofouling, which occurs due to the accumulation of organic matter, bacteria, and other biological materials on the surfaces of sensing devices [49]. This biofilm can prevent DO from diffusing into the sensitive layer and interfere with the measurement accuracy. Therefore, a suitable anti-biofouling treatment on the sensor surface is needed. A variety of methods both for electrochemical [8] and for optical sensors [50] are available in the literature which could be used for this purpose.

3.6. CONCLUSION

In summary, we demonstrate a total internal reflection microfluidic device for DO sensing which is inexpensive, sensitive, and exhibits high resolution. In order to optimize the sensitivity of this device, incident angles between the edge of the device and the light source have been investigated and found that 34° is the optimum angle of incidence. Due to the focused coupling method the incident light is a cone of incident angles and all three modes of TIR are observed. At the optimum incident angle

most of the light undergoes type 2 reflections, which agrees with the model. Of the experimentally tested DO sensitive layer thicknesses the ideal thickness was found to be 10 μm. It is possible that the optimum sensitive layer thickness is thinner than 10 μm however it is challenging to produce these films uniformly. Our optimized device showed a comparable sensitivity (as compared to the slope of Stern-Volmer plot of [10]), and sensing range (0–20 ppm) compared to previously developed miniaturized DO sensors, but significantly higher resolution [22], [40]–[42]. We believe our design can provide a low cost and highly accurate miniaturized optical DO sensor to be applied in both natural water quality monitoring and wastewater processing control after accomplishing device integration and biofouling prevention in upcoming studies.

Funding Sources

Acknowledgement

References

[1]   U.S. Environmental Protection Agency, Office of Wetlands Oceans and Watersheds "Chapter 9: Dissolved Oxygen and Biological Oxygen Demand," in Voluntary Estuary Monitoring Manual: A Methods Manual, second edition, EPA-842-B-06-003. Washington, DC, Mar. 2006.

[2]   L. Åmand, L, and B. Carlsson, "The optimal dissolved oxygen profile in a nitrifying activated sludge process - Comparisons with ammonium feedback control," *Water Sci. Technol.*, vol.68, no.3, pp.641-649, Mar. 2013.

[3]   C. Vlad, M. Sbarciog, M. Barbu, S. Caraman, and A. Vande Wouwer, "Indirect control of substrate concentration for a wastewater treatment process by dissolved oxygen tracking," *J. Control Eng. Appl. INFORMATICS*, vol. 14, no. 1, pp. 37–47, 2012.

[4]   G. T. F. Wong, Y.-C. Wu, and K.-Y. Li, "Winkler's method overestimates dissolved oxygen in natural waters: Hydrogen peroxide interference and its implications," *Mar. Chem.*, 122:82-90, 2010.

[5]   U.S. Environmental Protection Agency. (2012). *Water: monitoring and assessment, 5.2 Dissolved Oxygen and Biochemical Oxygen Demand.* Washington, DC. [Online]. Available: https://archive.epa.gov/water/archive/web/html/vms52.html.

[6]   T. O. Mitchell, "Luminescence Based Measurement of Dissolved Oxygen in Natural Waters," Hach Company., Loveland, CO, White Paper, 2006.

[7]   L. C. Clark Jr., and C. Lyons, "Electrode Systems for Continuous Monitoring in Cardiovascular Surgery," *Ann. New. York. Acad. Sci.* Vol. 102, No. 1, pp.29–45, 1962.

[8]   L. Hsu, P. R. Selvaganapathy, J. Brash, Q. Fang, C.-Q. Xu, J. Deen, and H. Chen, "Development of a low-cost hemin-based dissolved oxygen sensor with anti-biofouling coating for water monitoring," *IEEE Sens. J.*, Vol. 14, No. 10, pp. 3400-3407, Oct. 2014.

[9]   A. N. Watkins, B. R. Wenner, J. D. Jordan, W. Xu, J. N. Demas, and F. V. Bright, "Portable, Low-Cost, Solid-State Luminescence-Based O2 Sensor," *Appl. Spectrosc.*, vol. 52, no. 5, pp. 750–754, 1998.

[10]   A. K. McEvoy, C. M. McDonagh, and B. D. MacCraith, "Dissolved oxygen sensor based on fluorescence quenching of oxygen-sensitive ruthenium complexes immobilized in sol–gel-derived porous silica coatings," *Analyst*, vol. 121, no. 6, pp. 785–788, Jun. 1996.

[11]   I. Klimant, and O. S. Wolfbeis, "Oxygen-Sensitive Luminescent Materials Based Silicone-Soluble Ruthenium Diimine Complexes," *Anal. Chem.,* vol. 67, pp. 3160–3166, 1995.

[12]   Y. Amao, "Probes and Polymers for Optical Sensing of Oxygen," *Microchim. Acta*, vol. 143, pp. 1–12, 2003.

[13]   L. Meahcov, and I. Sandu, "Mathematical Equation of Fluorescence Intensity for Polydisperse Sols," *J. Fluoresc.*, 12:259–261, 2002.

[14]   H. Tai, Y. Yang, S. Liu, and D. Li, "A Review of Measurement Methods of Dissolved Oxygen in Water," *Comput. Comput. Technol. Agric.* V, vol. 369, pp. 569–576, 2012.

[15]   R. Ramamoorthy, P. K. Dutta, and S. A. Akbar, "Oxygen sensors : Materials, methods, designs, and applications," *J. Mater. Sci.*, vol. 38, pp. 4271–4282, 2003.

[16]   R. McFarlane and M. C. Hamilton, "A Fluorescence Based Dissolved Oxygen Sensor," *Fiber Opt. Sensors II*, vol. 798, pp. 324–330, 1987.

[17]   *The Dissolved Oxygen Handbook*; YSI Inc., Yellow Springs, OH, Sept. 2009.

[18]   S. M. Grist, L. Chrostowski, and K. C. Cheung, "Optical Oxygen sensors for applications in microfluidic cell culture," *Sensors*, vol. 10, pp. 9286–9316, 2010.

[19]   B. Ungerbock, V. Charwat, P. Ertl, and T. Mayr, "Microfluidic Oxygen imaging using integrated optical sensor layers and a color camera," *Lab Chip*, vol. 13, no. 8, pp. 1593–1601, 2013

[20]   S. Ayyash, Wen-I Wu, and P. Ravi Selvaganapathy, "Fast and inexpensive detection of bacterial viability and drug resistance through metabolic monitoring," in *2014 IEEE Healthcare Innovation Conference (HIC)*, Seattle, WA, 2014, pp. 22-25.

[21]   M. Skolimowski, M. W. Nielsen, J. Emnéus, S. Molin, R. Taboryski, C. Sternberg, M. Dufva, and O. Geschke, "Microfluidic dissolved oxygen gradient generator biochip as a useful tool in bacterial biofilm studies," *Lab Chip*, vol. 10, no. 16, pp. 2162–2169, 2010.

[22]   Z. Rosenzweig, and R. Kopelman, "Development of a submicrometer optical fiber oxygen sensor," *Anal. Chem.*, vol. 67, no. 15, pp. 2650–2654, 1995.

[23]   C. S. Chu, and C. Y. Chuang, "Optical fiber sensor for dual sensing of dissolved oxygen and Cu^{2+} ions based on PdTFPP/CdSe embedded in sol-gel matrix," *Sensors Actuators, B Chem.*, 209:94–99, 2015.

[24]   Q. Fang, J. Xu, Q. Sun, S. Liu, G. Zhang, C. Ma, G. Zhang, and G. Tian,"Multipage storage in a $LiNbO_3$:Fe crystal sheet using the photorefractive light-climbing effect," *Appl. Opt.*, 35(34): 6744-6746, 1996.

[25]   H. J. Lee, T. T. Goodrich, and R. M. Corn, "SPR imaging measurements of 1-D and 2-D DNA microarrays created from microfluidic channels on gold thin films," *Anal. Chem.*, vol. 73, no. 22, pp. 5525-5531, 2001.

[26]   K. S. Phillips and Q. Cheng, "Microfluidic immunoassay for bacterial toxins with supported phospholipid bilayer membranes on poly(dimethylsiloxane)," *Anal. Chem.*, 77(1): 327–334, 2005.

[27]   I. G. Thakkar, K. L. Lear, J. Vickers, B. C. Heinze, and K. F. Reardon, "A plastic total internal reflection photoluminescence device for enzymatic biosensing," *Lab Chip*, vol. 13, no. 24, pp. 4775–83, 2013.

[28]   N. C. H. Le, D. V. Dao, R. Yokokawa, J. C. Wells, and S. Sugiyama, "Design, simulation and fabrication of a total internal reflection (TIR)-based chip for highly sensitive fluorescent imaging," *J. Micromech. Microeng.*, vol. 17, no. 6, pp. 1139–1146, 2007.

[29]   N. C. H. Le, R. Yokokawa, D. V. Dao, T. D. Nguyen, J. C. Wells, and S. Sugiyama, "Versatile microfluidic total internal reflection (TIR)-based devices: application to microbeads velocity measurement and single molecule detection with upright and inverted microscope," *Lab Chip*, vol. 9, no. 2, pp. 244–250, Mar. 2009.

[30]   S.-H. Huang and F.-G. Tseng, "Development of a monolithic total internal reflection-based biochip utilizing a microprism array for fluorescence sensing," *J. Micromech. Microeng.*, vol. 15, no. 12, pp. 2235–2242, 2005.

[31]   Y. Xiong, J. Tan, C. Wang, Y. Zhu, S. Fang, J. Wu, Q. Wang, and M. Duan "A miniaturized oxygen sensor integrated on fiber surface based on evanescent-wave induced fluorescence quenching," *J. Lumin.*, vol. 179, pp. 581–587, 2016.

[32]   D. A. Chang-Yen, and B. K. Gale, "An integrated optical oxygen sensor fabricated using rapid-prototyping techniques," *Lab Chip*, vol. 3, no. 4, pp. 297–301, 2003.

[33]   H. L. T. Lee, P. Boccazzi, R. J. Ram, and A. J. Sinskey, "Microbioreactor arrays with integrated mixers and fluid injectors for high-throughput experimentation with pH and dissolved oxygen control," *Lab Chip*, vol. 6, no. 9, pp. 1229–1235, 2006.

[34]   F. Du, "Development of an optofluidic platform based on total internal reflection-application of dissolved oxygen sensing for water monitoring," M.S. thesis, Biomed. Eng., McMaster Univ., Hamilton, ON, 2015.

[35]   E. Mahoney, F. Du, H. Hsu, R. Selvaganapathy, & Q. Fang, "(Invited) A Frequency Domain Optofluidics Dissolved Oxygen Sensor with Enhanced Sensitivity for Water Monitoring," in *ECS Meeting Absracts*, 2016, pp. 1276.

[36]   M. Dickerson, B. Howerton, Y. Bae, and E. Glazer, "Light-Sensitive Ruthenium Complex-Loaded Cross-linked Polymeric Nanoassemblies for the Treatment of Cancer," *J. Mater Chem B Biol Med*, vol. 4, pp. 394–408, 2017.

[37]   D. Axelrod, "Total Internal Reflection Fluorescence Microscopy in Cell Biology," *Traffic*, vol. 2, no. 11, pp. 764–774, Nov. 2001.

[38]   D. Axelrod, "Cell-substrate contacts illuminated by total internal reflection fluorescence," *J. Cell Biol.*, vol. 89, no. 1, pp. 141–145, Apr. 1981.

[39]   P. Kim, K. W. Kwon, M. C. Park, S. H. Lee, S. M. Kim, and S. Y. Suh, "Soft Lithography for Microfluidics : a Review," *Biochip J.*, vol. 2, pp. 1–11, 2008.

[40]   Y. Tang, E. C. Tehan, Z. Tao, and F. V. Bright, "Sol-gel-derived sensor materials that yield linear calibration plots, high sensitivity, and long-term stability," *Anal. Chem.*, vol. 75, no. 10, pp. 2407–2413, 2003.

[41]   C.-S. Chu, T.-W. Sung, and Y.-L. Lo, "Portable optical oxygen sensor based on Ru(II) complex and dye entrapped core-shell nanoparticles embedded in sol-gel matrix coated on a photodiode," *Opt. Eng.*, vol. 50, no. 5, pp. 54404, 2011.

[42]   Y. Cao, Y.-E. Lee Koo, and R. Kopelman, "Poly(decyl methacrylate)-based fluorescent PEBBLE swarm nanosensors for measuring dissolved oxygen in biosamples," *Analyst*, vol. 129, no. 8, pp. 745–750, 2004.

[43]   P. F. Dunn, *Measurement and data analysis for engineering and science*, 3rd ed., Boca Raton, FL: CRC Press, 2014.

[44]   P. Hartmann, M. J. P. Leiner, and M. E. Lippitsch, "Luminescence quenching behavior of an oxygen sensor based on a Ru(II) complex dissolved in polystyrene," *Anal. Chem.*, 67(1): 88–93, 1995.

[45]   O. Tokel, F. Inci, and U. Demirci, "Advances in plasmonic technologies for point of care applications," *Chem. Rev.*, vol. 114, no. 11, pp. 5728–5752, 2014.

[46]   S. T. Ross, S. Shwartz, T. J. Fellers, and M. W. Davidson. (2016, June). TIRF microscopy: introduction and applications. *Nikon Instruments Inc.* [Online]. Available: https://www.microscopyu.com/techniques/fluorescence/total-internal-reflection-fluorescence-tirf-microscopy

[47]   H. Välimäki, J. Verho, J. Kreutzer, K. D. Rajan, T. Ryynänen, M. Pekkanen-mattila, A. Ahola, K. Tappura, P. Kallio, and J. Lekkala, "Fluorimetric oxygen sensor with an efficient optical read-out for in vitro cell models," *Sensors Actuators B. Chem.*, 249: 738–746, 2017.

[48]   D. A. Woods and C. D. Bain, "Total Internal Reflection Raman Spectroscopy," *Analyst.*, vol. 137, no. 1, pp. 35-48, 2012.

[49]   J. L. Dalsin and P. B. Messersmith, "Bioinspired antifouling polymers," *Mater. Today.*, vol. 8, no. 9, pp. 38–46, 2005.

[50]   Y. Zhang, L. Chen, Z. Lin, L. Ding, X. Zhang, R. Dai, Q. Yan, and X-D. Wang, "Highly Sensitive Dissolved Oxygen Sensor with a Sustainable Antifouling, Antiabrasion, and Self-Cleaning Superhydrophobic Surface," *ACS Omega,.* 4:1715–1721, 2019.

Chapter 4

Research Paper 2 - Optical Model of Light Propagation in Total Internal Reflection Fluorescence Sensors

Eric James Mahoney[1], Bo Xiong[1], and Qiyin Fang[1,2,z]

[1]*School of Biomedical Engineering, McMaster University, 1280 Main St. West, Hamilton, ON L8S 4K1, Canada*

[2]*Department of Engineering Physics, McMaster University, 1280 Main St. West, Hamilton, ON L8S 4K1, Canada*

[z]*Corresponding Author qiyin.fang@mcmaster.ca*

Introduction to Research Paper 2

Chapter 4 has been accepted for publication in the OSA Journal of Applied Optics, and is currently in press. This research article was based on 3D ray tracing simulations conducted using Zemax OpticStudio between 2016-2020 with Dr. Fang and Bo Xiong. My contribution as the first author was to create a simplified Zemax simulation of the experimentally tested optical DO sensor presented in Chapter 3. A series of calculations were conducted to independently predict the outcome of the simulated result for verification. I wrote the complete article and prepared all figures presented. Mr. Bo Xiong introduced the concept of using prisms as an additional coupling strategy and provided a template for 3D models of prisms. Mr. Xiongs' template was used to make simulated prisms that I added to the simulation for the prism-assisted coupling scenario. Dr. Fang supported our work and helped with significant revisions while submitting the article. I took a lead role in addressing the questions of reviewers during the submission process. The significance of this research involves the expansion of the simplified model developed in Chapter 3 to be widely applied to the development and prototyping of future multilayered optical sensors employing TIR for sensitivity enhancement.

Contents of paper

Abstract

In this work we report the development of a three-dimensional optical model to predict the propagation of light though multilayer optical fluorescence sensors employing Total Internal Reflection. The ray tracing-based model visualizes the propagation of light from a light source through the optical sensor allowing optimization of the optical path, optical properties of the materials, and the coupling strategy. The model demonstrates how light can be guided through different layers of the sensor structure by controlling the incident angle of light and the relationship between incident angle and relative sensitivity. Simulation results are compared against experimental data to validate the model in a fluorescence based Dissolved Oxygen sensor. Customization of the light source parameters, coupling optics, sensor optical properties, and sensor dimensions could provide developers an opportunity to refine and optimize TIR sensor prototypes before conducting bench testing.

4.1. INTRODUCTION

Optimization of fluorescence based optical sensing systems is essential in order to improve the sensitivity of these devices while reducing dependence on expensive detectors. Fluorescence based optical sensors have been developed for several fluid analysis [1–6] and imaging applications [7–10]. Widespread distribution of these sensors in an integrated sensing network provides an opportunity for environment monitoring and industrial process control applications [11]. Distributed monitoring enables rapid response to environmental threats and reduction of operating costs through process optimization driven by sensor-based feedback; however, distribution is often limited by overall size and cost of sensing systems [11-13].

One of the challenges of fluorescence-based sensors is the photobleaching effect. After several exposures the fluorescence intensity of the dye is reduced which limits the useful life of these devices before the sensitive element must be replaced [14,15]. To extend the life of these devices very short exposure times can be used for each measurement or the intensity of the light delivered to the device may be reduced at the expense of baseline fluorescence intensity. This leads to a dependence on detectors that demonstrate high sensitivity and a fast response time which also tend to be expensive [15]. Optimization of the sensor structure itself is essential in order to reduce the dependence on expensive detectors.

Total Internal Reflection (TIR) has been recognized as an effective mechanism for optimizing the sensitivity of fluorescence-based sensors by guiding the excitation light through the sensor structure by illuminating the sensor at a critical angle. The critical angle is determined by the refractive indices of different materials in the sensor structure. The angle may be selected in order to generate an evanescent wave at the interface of the sensitive material and the sensor substrate such that the evanescent wave excites the sensitive material [16,17]. Alternatively, the angle can be selected in order to allow the light to transfer completely into the sensitive material in order to excite fluorescence in the entire volume of the sensitive layer along the path of the beam. A glass substrate or optical fiber acting as a base waveguide can be coated in a fluorescent film that acts as a sensitive layer. When light is guided through the device a portion of the energy may be absorbed by the sensitive material generating fluorescence. The fluorescence may be quenched due to collisions with target molecules or

changes in pH leading to a reduction in fluorescence intensity and fluorescence lifetime [18,19]. The fluorescence intensity and lifetime are related to the concentration of quenching molecules through the Stern-Volmer equation [20]

$$\frac{I_{f0}}{I_f} = \frac{\tau_0}{\tau} = 1 + k_q \tau_0 [Q]$$

Equation 4.1

where I_{f0} and I_f are the integrated fluorescence intensities in the absence of quenching, and in the presence of quenching respectively. τ_0 and τ are the fluorophore excited state lifetimes in the absence of quenching and in the presence of quenching respectively. k_q is the diffusion dependent quenching constant and Q is the quencher concentration. If the entire volume of the sensitive layer is capable of interacting with the targeting analyte, then the optimum sensitivity should be achieved in the situation where the most fluorescence is generated within the sensitive material.

The fluorescence intensity can be monitored using optical detectors such as Avalanche Photodiodes (APDs), Photomultiplier Tubes (PMTs), Complementary Metal-Oxide-Semiconductor (CMOS) or Charge Coupled Device (CCD) cameras in conjunction with optical filters that are carefully selected to pass only emitted fluorescent light to the detector. Steady state measurements may be conducted by illuminating the sensor at a constant power and then measuring the steady state fluorescence intensity [15,21]. Alternatively, the fluorescence intensity and lifetime can be measured using frequency domain methods. Frequency domain measurements are conducted by oscillating the light source intensity and measuring the difference in amplitude and phase between the reference signal sent to the light source and the change in fluorescence intensity from the detector [15,22]. A novel frequency domain measurement method based on directly measuring fluorescence emission using the rolling shutter of a CMOS camera has been recently reported [10].

In our previous work, we reported the development of a miniaturized optofluidic Dissolved Oxygen (DO) sensor built on a glass substrate for monitoring changes in DO as changes in steady state fluorescence intensity due to Oxygen quenching in an Oxygen sensitive dye. A numerical model was developed to demonstrate how major design parameters can influence the sensitivity of the DO sensor [21]. It was shown that sensor optimization is a very time consuming and laborious process when conducted

experimentally even when the major design parameters are well understood.

Optical ray tracing has been used to describe TIR in waveguide structures and to compare various coupling mechanisms for applications in fluorescence sensing and microscopy. The 2D models such as those presented by Burghardt [16] and Axelrod [17] are well suited to conceptualize the optical path in TIRF microscopy applications. Although useful to conceptualize propagation in various coupling strategies, 2D models provide limited quantitative information and do not consider the contribution of partially reflected rays at each interface to the overall fluorescence generated. A 3D model has been prepared using a ZEMAX raytracing simulation based on an experimentally tested device and was validated by the experimental measurements [23]. The simulation demonstrates the coupling mechanism employed and to generate quantitative information from ray tracing simulations, however a generalized model was not developed to apply to other device designs. Recently other 3D ray tracing simulations incorporating TIR have been developed for applications in optofluidic device design [24], TIRF microscopy [25], solar concentrator design [26,27], suggesting the value of a generalized 3D TIR simulation validated by experiment results in device design and prototyping.

In this work, a three-dimensional model of the DO sensor is developed using optical ray tracing in order to visualize the optical path within the sensor. The goal is to predict the relative sensitivity changes as a function of the incident angle and other design parameters. The model can be validated by comparing the predicted results to our previous experimental results. Such model will lead to systematic optimization of optical sensing devices for improved sensitivity, reduced cost, and miniaturization [21,28].

4.2. SENSOR DESIGN AND CONCEPT

4.2.1. Sensor Design
The experimentally tested optofluidic DO sensor is a multilayer device fabricated on a glass substrate. The substrate is a 1.1 mm thick standard soda lime glass microscope slide. A Ruthenium based Oxygen sensitive dye (Tris(4,7-diphenyl-1,10-phenanthroline)Ruthenium(II) dichloride complex (Ru(dpp)$_3$)) is dissolved in a Poly DimethylSiloxane (PDMS) polymer and is coated on the surface of the glass substrate. The thickness of the DO

sensitive layer is approximately 10 μm. A water channel is cast in a PDMS block using soft lithography techniques with inlets and outlets for introducing the water sample to the device. The dimensions of the water channel are 2 mm wide by 2 mm tall, and 60 mm long. A hole punch was used to make an opening for inserting tubing into the water channel at the inlet and outlet from the top of the device. The PDMS cap is bonded to the surface of the sensitive layer using air plasma [21]. The TIR fluorescence sensor concept is illustrated in Fig. 4.1.
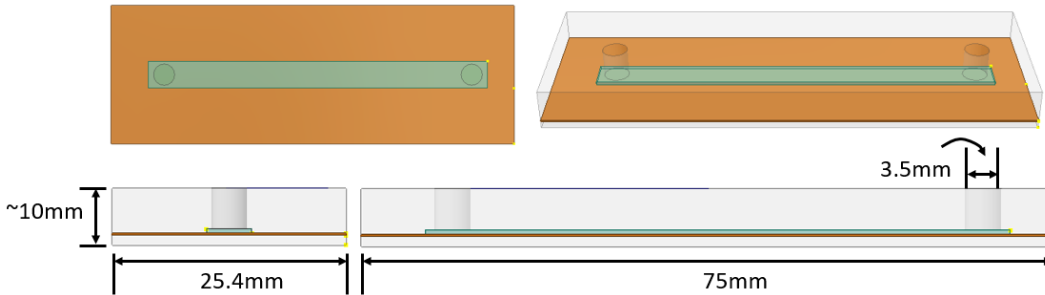
Figure 4.1 Multilayered TIR fluorescence sensor concept. The bottom layer is a 1.1 mm thick glass microscope slide. The slide is coated with a 10 μm film of Oxygen sensitive fluorescent dye. A 2 x 2 x 60 mm rectangular water channel cast in PDMS is the third layer. The final layer is a 3mm thick PDMS cap supporting the water channel and tubing ports.

When the water sample is injected into the sensor, the DO in the water diffuses through the PDMS membrane where it interacts with the Oxygen sensitive dye. The presence of DO leads to the quenching of fluorescence from the sensitive material which can be monitored as a change in the steady state fluorescence intensity or a change in the fluorescence lifetime of the dye with respect to the DO concentration as described by the Stern-Volmer equation [21].

4.2.2.   Experimental setup

The fluorescence based optical sensor developed in house is presented in our earlier work [21]. The light source used was a 150 mW, 445-450 nm laser (450 Diode, Laserland, Wuhan, China) which is attenuated through an OD3 neutral density filter to reduce the power to 150 μW. The incident light is focused onto the edge of the glass substrate of the DO sensor chip using a 10x microscope objective lens with a 0.25 NA. The light propagates through the sensor and can be contained in different layers by adjusting the incident angle between the light source and the edge of the glass substrate. The

incident angle between the objective lens and sensor substrate is controlled by clamping the glass slide to a variable angle mount while referencing a transparent protractor that is mounted to the optical table next to the sensor. The incident light may undergo multiple reflections within the device and fluorescence is generated in the sensitive layer by absorbing the incident light at each site of reflection inside of the sensitive volume. The emitted fluorescence is collected through an emission filter (FF01-609/181-25, Semrock, Rochester, NY) and measured using an optical power meter probe (Model 1830-C, Newport, Irvine, CA). A schematic of the experimental setup used for model validation is shown in Fig. 4.2.
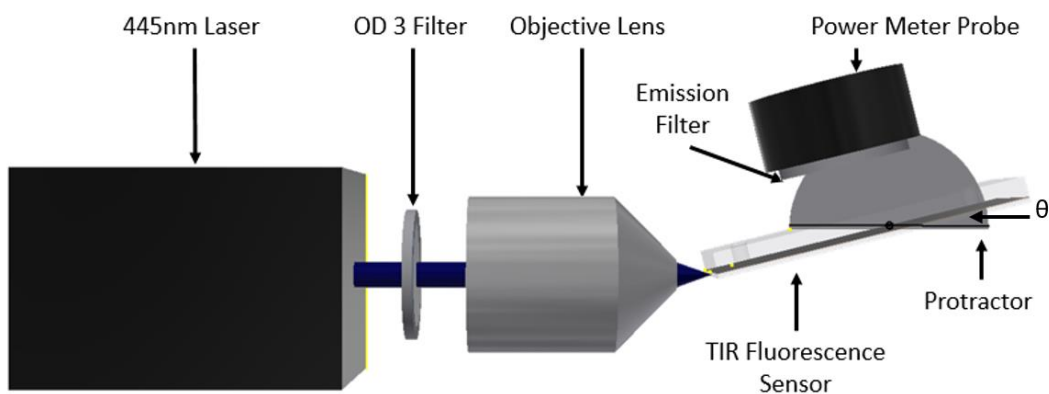
Figure 4.2 TIR fluorescence measurement experiment setup. A 445 nm diode laser is attenuated through an OD3 filter and focused by a 10x microscope objective lens (NA 0.25) onto the edge of a glass substrate. The incident angle between the objective and sensor substrate is controlled using a post mounted protractor. An optical power meter is used to monitor the intensity of fluorescence emission through a 520 – 720 nm band pass filter.

DO standards were measured using the experimental setup over a range of incident angles and the sensitivity is determined by the slope of the Stern-Volmer plot obtained for each set of measurements [21].

4.2.3. Reagents and methods

The reagents and materials used to produce and test the experimentally tested DO sensor are disclosed in the reagents and materials section of our previous work [21]. The fabrication processes detailing sensitive film preparation, spin coating, and soft lithography have also been disclosed [21].

4.3.   SIMULATION

4.3.1.   TIR Simulation Design

   The simulation of the sensor structure and excitation strategies is conducted using a commercial ray tracing software (Zemax OpticStudio, Version 19.4 SP2, Premium (64-bit)). A non-sequential design is developed with consideration of the light source used for excitation, the optical components used to couple the incident light to the sensor structure, and the sensor structure itself including the optical properties of the fluorescent film. The concepts of TIR simulation coupling scenarios are shown in Fig. 4.3.
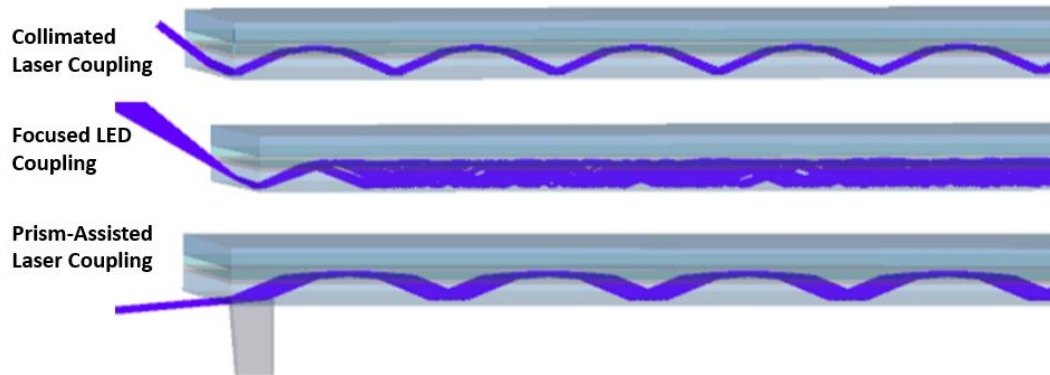
Figure 4.3 Concept of TIR excitation coupling strategies. Direct collimated coupling approach: collimated light enters at the slide edge at the same incident angle (Type II TIR seen at 37° is shown). Focused coupling approach: light enters within a cone of incident angles defined by the beam diameter and objective NA (Type I & II TIR seen at 35° using a 0.25 NA objective is shown). Prism assisted coupling approach: collimated light enters from the bottom of the glass substrate through a prism (Type II TIR seen using an 85° PDMS prism is shown).

   The sensor structure and optical properties of the layers in the device are simulated and the sensor model is used for the relative fluorescence intensity predictions in various coupling scenarios. Each layer in the multilayer device is modeled as a rectangular volume with a known refractive index. The refractive index of each layer determines how the incident light is refracted or reflected as each ray encounters the interface between different layers. The thickness of each layer determines how far each ray will travel for each reflection, which determines the number of reflection spots observed along the sensor for each incident angle. The footprint of each rectangular volume is defined as 25.4 mm wide and

76.2 mm long to approximate the dimensions of the glass microscope slide. The glass substrate is modeled as 1 mm thick with a refractive index defined as the BK7 material (1.5168) from the materials library in OpticStudio. The fluorescent sensitive layer is modeled as 200 μm thick in order to visualize the path of light in the sensitive volume. The refractive index of the sensitive dye and PDMS was assumed to be similar to PDMS by itself (1.416) provided in the OpticStudio materials library in OpticStudio.

The fluorescence properties of the sensitive layer defined in the Phosphors and Fluorescence parameters section determine how much fluorescence is generated in the sensitive material. The absorbance spectrum, emission spectrum, and quantum efficiency parameters are defined as $RuDPP_3$ using the OpticStudio materials library in OpticStudio. The fluorescence properties determine the efficiency of absorption by the sensitive layer, how many rays are emitted isotropically from the site of absorption, and the wavelength of each emitted ray. The refractive index of the dye particles is defined as 1.425 corresponding to a measurement of dye dissolved in gel [29]. The size and concentration properties of dye particles determine the scattering efficiency in the fluorescent layer. The dye particle concentration was set as 104 particles/cm3. The particle radius was set to 10μm.

The water layer is modeled as a 500 μm thick non-scattering surface with a refractive index of water from the OpticStudio materials library in OpticStudio (1.333). The PDMS water channel cap was modeled as 1 mm thick and is defined as a non-scattering volume with a refractive index of PDMS from the OpticStudio materials library in OpticStudio (1.416). Although the thickness dimensions are not the same as the experimental device, they are constant for all simulations allowing relative fluorescence intensity predictions, however absolute fluorescence intensity cannot be directly predicted.

The light source model and strategy for coupling the incident light to the sensor substrate define the optical power coupled to the device, and the distribution of incident angles introduced to the substrate. The excitation light source was simulated as a circular ellipse with random polarization. The wavelength distribution was set between 440-450 nm with a peak at 444 nm. The power was arbitrarily set to 1.0 W. In all simulations 30 layout rays are traced for visual assessment and 500,000 rays are considered for intensity predictions. The light source intensity distribution is adjusted for

each of the coupling scenarios. In the collimated coupling and prism-assisted coupling simulations the light source is modeled as a uniform spot with a radius of 0.08 mm. The small diameter was used to ensure that the entire spot coupled into the glass substrate layer. In the focused coupling simulation, the light source is modeled as a Gaussian spot with a 2 mm radius. The spot is focused to the edge of the glass substrate through a simulated aspheric condenser lens from the OpticStudio components library in OpticStudio (Thorlabs AL2520M). The aspheric lens was used to approximate the 10x objective lens used in the experimental setup by producing a spot easily coupled to the edge of the glass substrate. Where the light source has a Gaussian profile the relative intensity of the light approaching at the principle angle will be greater than the intensity of light approaching from more extreme angles. In the prism-assisted coupling scenario a 3D prism model is inserted between the light source and the glass substrate such that the incident light is perpendicular to the front face of the prism, and the base of the prism is in contact with the bottom of the glass substrate. The prism material and refractive index are defined as PDMS using the OpticStudio materials library in OpticStudio. Many of the significant model parameters are summarized in Table 4.1.

The predicted fluorescence intensity is measured using a detector surface placed 3 mm above the PDMS channel cap over the center of the simulated sensor structure. The circular detector surface is modeled with a 5 mm radius with 16 angular zones and 8 radial zones to observe where fluorescent light hits the detector. The detector surface records the number of ray hits and the peak irradiance of emitted rays. The intensity of emitted fluorescence is directly proportional to the amount of light absorbed, which depends on the incident light intensity, overlap of the wavelength distribution of the source, the absorbance spectrum of the sensitive layer, and the quantum yield of the dye. The fluorescent volume is modelled as a detector volume with 150 pixels wide x 1000 pixels long x 50 pixels depth and can record the incident flux, absorbed flux, and absorbed flux / volume. The detector can be used to visualize the sites of absorption within the sensitive volume from the top view.

Table 4.1 Summarized model variables. Major model variables used in the ray tracing simulation are compiled.

Model		Variable	Collimated	Focused	Prism-Assisted
Light Source	Source	Power		1 W	
		Radius	0.08 mm	2.5 mm	0.08 mm
		Wavelengths		440 – 450 nm, 444 nm Peak	
		Uniformity	Uniform	Gaussian	Uniform
		Polarization		Random	
	Traced Rays	Max Layout Rays		30	
		Max Analysis Rays		500,000	
		Intersections per ray		4,000	
		Segments per ray		500	
		Min relative ray intensity	$1x10^{-5}$	$1x10^{-4}$	$1x10^{-9}$
		Max source file rays in memory		1,000,000	
Sensor	Prism	Base Dimensions	-	-	$1\ cm^2$
		Angle	-	-	5° to 85°
		Material RI	-	-	1.416
	Glass	Dimensions		25.4 x 76.2 x 1.1 mm	
		Material		1.5168	
	Sensitive Film	Dimensions		25.4 x 76.2 x 0.200 mm	
		Matrix RI		1.416	
		Dye RI		1.425	
		Particle Settings		10^4 particles / cm^3, 10 μm diameter	
	Water Layer	Dimensions		25.4 x 76.2 x 0.500 mm	
		Material RI		1.333	
	PDMS Cap	Dimensions		25.4 x 76.2 x 1 mm	
		Material RI		1.416	
Detector	Simulated Probe	Radius		5 mm	
		Angular Zones		16 zones	
		Radial Zones		8 zones	
	Sensitive Layer	Pixels (W x L x H)		150 x 1000 x 50	

Any differences between the model parameters and the actual light source and dye properties will lead to differences in the absolute predicted fluorescence intensity and experimentally measured fluorescence intensities. Therefore, the results are normalized in order to compare between experimental and simulated results. Experimentally the sensitivity of the sensor is determined by the slope of the Stern-Volmer plot for each test condition. In the simulation, it is assumed that the greatest sensitivity occurs when the predicted fluorescence intensity is greatest given that the

entire volume of the sensitive layer is expected to interact with the target analyte such as DO.

4.3.2. Software and Computer Specifications

The software used to produce models used in this work are shown in the Table 4.2.

Table 4.2 System Information. Table of basic computer specifications used to run ray tracing simulations.

	System Specifications	
Computer	**Component**	**Specification**
Lenovo T430s	Operating System	Microsoft Windows 10 Pro
Model: 2356 GPU	Processor	Intel(R) Core(TM) i5-3320M CPU @ 2.60GHz, 2601 MHz, 2 Core(s), 4 Logical Processor(s)
	Virtual Memory	12.4 Gb
	HDD	296 Gb
	Video	Intel HD 4000

4.4. RESULTS

4.4.1. TIR Fluorescence Sensor Model

The accuracy of the light source model has been determined to be an important factor in predicting the performance of an experimental setup. The type of internal reflections observed depends on the incident angle of each ray entering the system. If the light source is uniform and collimated all of the light enters the device at a common angle and will experience the same type of TIR. If a focused light source is employed, then the incident light approaches the sensor structure over a range of incident angles and the relative intensity of light approaching at each angle depends on the uniformity of the light source and the Numerical Aperture (NA) of the lens. Any deviations between the simulated illumination profile of the light source and the actual properties of the experimental light source will impact the accuracy of the fluorescence intensity observed at each incident angle. The difference between the experimental and model results are expected to be the greatest closest to the theoretical optimum incident angle. In this simulation the light source was not perfectly modeled based on the experimental light sources used.

The diameter of the light source can be adjusted to control the range of angles incident on the device without reducing the total input power. The uniformity of the source can be adjusted to control the relative intensity of

light approaching the system from different angles. The intensity of light approaching from different angles was not measured experimentally and is believed to be the main cause for differences between simulated and experimental results for the focused coupling scenario.

The model of the sensor structure is simplified to demonstrate the path of light through the sensor beneath the water channel. In the experimental device, there are water channels cast in the PDMS block that is bonded to the sensitive layer, so there are regions in the chip where there is no water layer. In this simulation the entire volume above the sensitive layer is modeled as a volume of water. The fluorescence quenching effect caused by the interaction of DO and the sensitive dye is not included in the model so changes in fluorescence intensity with respect to quencher concentration cannot be predicted directly. However, it is expected that the sensitivity of the device is maximized under the conditions where the fluorescence generated in the sensitive layer is greatest assuming that all of the excited dye can interact with the target analyte.

The fluorescence intensity is predicted by using a simulated detector surface with dimensions similar to those of the optical power meter probe employed for the experimental measurements. The detector surface can be used to predict the relative fluorescence intensity from the sensor in each test condition. Detector surfaces can also be used to predict where fluorescent photons are emitted from within the sensitive volume. An example of detector volume output showing the distribution of light within different layers of the fluorescent film is shown in Fig. 4.4.
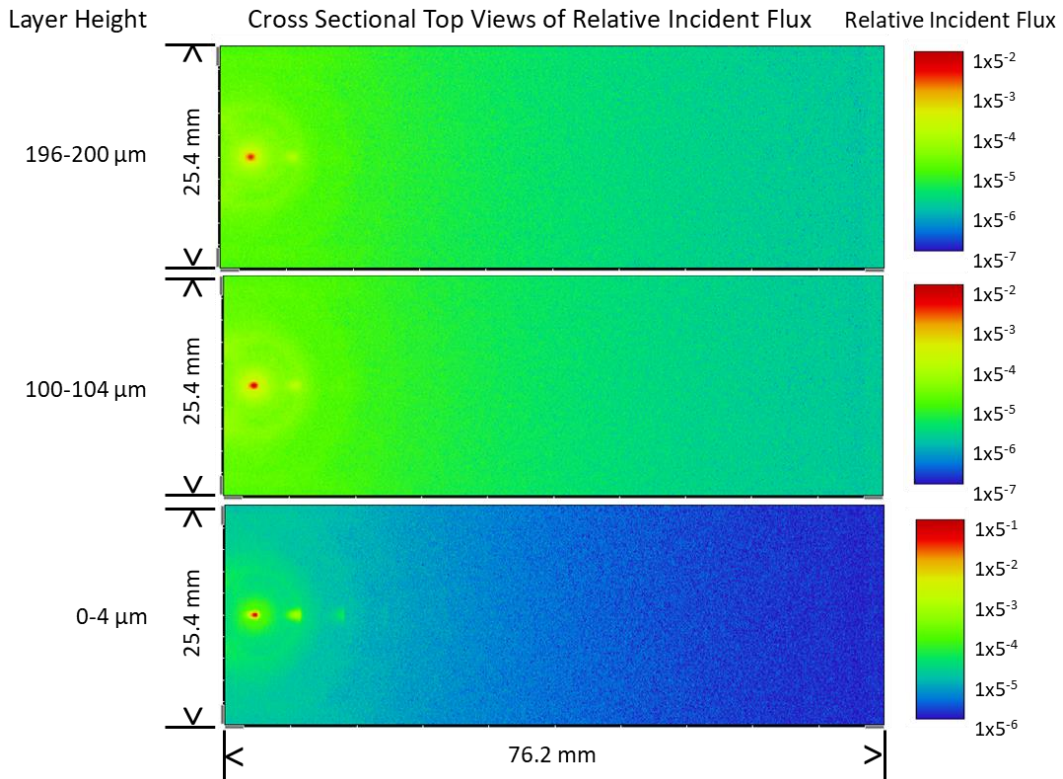
Figure 4.4 Relative intensity of incident light within layers of fluorescent volume. Cross-sectional top views from the detector volume are shown from the focused coupling model using an incident angle of 37°. The intensity and spatial position of incident light is predicted at different heights within the detector volume. The relative intensity of incident light is indicated by the color scale.

The intensity of background fluorescence around the most significant reflection spots is predominantly caused by the lateral dispersion of light in the focused coupling case. The range of lateral angles is introduced determined by the NA of the focused input and intensity distribution of the source. Each of the main rays has the potential to generate significant fluorescent rays. In the collimated coupling case, there is very little lateral dispersion of light. The background fluorescence around the reflection spots is caused by scattering or the reabsorption of a fluorescent ray of sufficient energy. The results suggest that a larger volume of the sensitive film contributes to fluorescence generation in the focused coupling case, however the brightness fluorescence generated at reach reflection is greater when using collimated inputs.

4.4.2.   Collimated Laser Coupling Performance

The simulation of the direct collimated coupling scenario clearly identifies the incident angles where the light transfers between different layers of the sensor structure. For angles smaller than the critical angle the light appears to be completely contained within the glass substrate (Type I TIR). In this case the only fluorescence produced comes from the evanescent wave generated at the interface of the glass substrate and sensitive layer. When the incident angle is optimized the incident, light is able to transfer into the sensitive layer and travels nearly parallel to the sensor surface, maximizing the path length of light in the sensitive layer for each reflection (Type II TIR). As the incident angle increases the light travels through the sensitive layer at a steeper angle so the light is reflected back into the glass substrate earlier and the path length of the incident light in the sensitive layer decreases for each reflection. As the angle continues to increase beyond a boundary angle the incident light is transmitted through the sensitive layer and transfers into the water layer and PDMS cap (Type III TIR). In this case the distance between reflection points increases and number of reflections along the length of the sensor are reduced resulting in a drop in fluorescence intensity due to the increase in the distance travelled by the incident light for each reflection. As the angle continues to increase the distance between reflection points is reduced and more reflection points are observed along the length of the chip and the fluorescence intensity increases. The computation time of the model can vary considerably depending on the ray tracing settings, detector settings, and other tasks performed by the computer during simulation. The type I simulations typically take less than 1.5 minutes, Type II simulations take between 15 and 35 minutes, and Type III simulations take roughly 10 to 15 minutes. The collimated coupling simulation results are presented in Fig. 4.5.
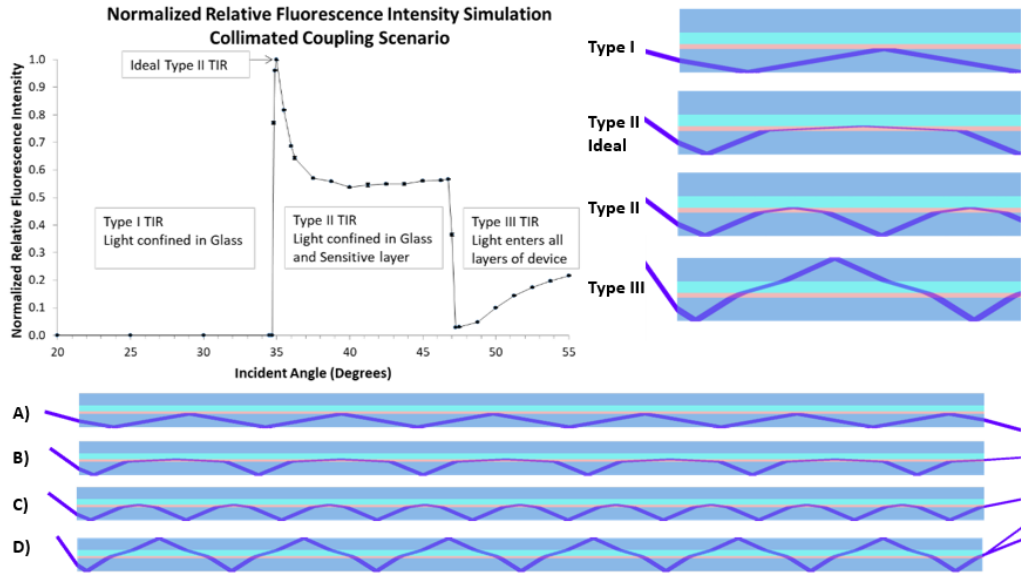
Figure 4.5 Collimated coupling simulation results. The plot indicates the normalized fluorescence intensity predicted with respect to incident angle given a uniform collimated input to the edge of the glass substrate. A) Type I TIR seen using a 15° incident angle. B) Ideal Type II reflections observed at the critical angle of 35°. C) Type II reflections seen when the incent angle is between the critical angle and the Type III boundary angle (37° case is shown). D) Type III reflections observed when the incident angle exceeds the boundary angle (55° case is shown).

4.4.3. Focused Coupling Performance

In the focused laser coupling scenario, a range of angles is introduced to the sensor, and the relative intensity of the light approaching at each angle depends on the uniformity of the light source. The greatest fluorescence intensity is observed close to the critical angle but the change in fluorescence intensity observed with changes in incident angle appear to be smoothed. This situation is the most similar to the experimental setup used.

The relative sensitivity is predicted by normalizing the predicted fluorescence intensity observed for each simulated incident angle. The sensitivity of the experimental results is defined as the slope of the Stern-Volmer plot obtained for measuring DO concentrations in the range of 0-20ppm at various incident angles using a focused laser for excitation [21]. In order to compare the simulated and experimental sensitivities to validate the model the results are plotted together in Fig. 4.6. The simulated fluorescence intensity results are normalized such that the maximum

relative sensitivity is 1 as shown by the green points in Fig. 4.6. The normalized simulation results are rescaled further by matching the minimum relative sensitivity to the experimental minimum as shown in the red curve in Fig. 4.6. It can be seen that the experimental results and the simulated results are in close agreement where the results deviate the most at the critical angle. This is expected because any differences between the simulated and experimental results should be the most significant at the critical angle. The differences between the real excitation setup used and the simulated light source such as range of angles and uniformity of the light source are significant. The computation time required for Type I reflections is typically between 2 and 4 minutes, Type II simulations require 17 to 23 minutes, and Type III simulations require 8 to 17 minutes.
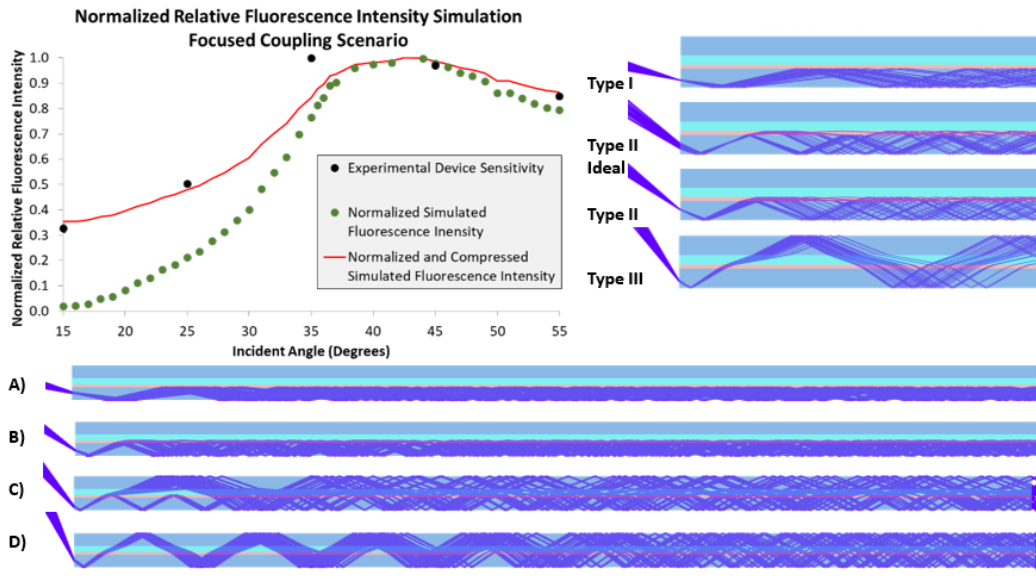
Figure 4.6 Focused coupling simulation results and experimental comparison. Ray trace simulations of a Gaussian light source focused through a 10x objective with 0.25NA are used to predict relative fluorescence intensity. Black points are the normalized experimental device sensitivity values. Green points are the normalized fluorescence intensity simulation results with respect to incident angle. The Red curve represents the normalized fluorescence intensity simulation results rescaled to match the experimental and simulation minimum values for comparison. A) Type I TIR seen using a 15° incident angle. B) Type I and Type II reflections seen at the critical angle of 35°. C) Type II and Type III reflections seen when the incent angle is between the critical angle and Type III boundary angle (50° case is shown). D) Type III TIR seen when the incident angle exceeds the boundary angle (65° case is shown).

4.4.4. Prism-Assisted Coupling Performance

In the prism coupling situation a right angle PDMS prism is produced and adhered to the bottom of the glass substrate of the sensor. The right-angle prism is constructed with different angle dimensions. The incident light is directed to the face of the prism such that it is perpendicular to the first surface of the prism. The light does not refract as it enters the prism from air due to the perpendicular beam, and the angle of the prism determines the angle with which the incident light reaches the base of the glass substrate. Prism-assisted coupling can be an effective method for improving the coupling efficiency of these devices as less light is lost as a partial reflection at the first surface. If the light is incident on the edge of the glass substrate directly the spot size of the beam can be larger than the glass thickness so only a portion of the incident light could be coupled. The incident light is often focused onto the edge of the slide in order to reduce the spot size and increase the amount of light injected, however this leads to the range of angles introduced to the device, smoothing the angular sensitivity profile of the device so the perceived enhancement observed at the critical angle is reduced. The prism coupling scenario enables the entire spot of light to be introduced to the device at a constant angle. Prisms with small angles are capable of producing Type II and Type III reflections as the angle increases. As prism angles become more significant, the incident light is able to escape the device and fluorescence is only produced by single-pass excitation. The computation time required for both single pass conditions and Type II reflections are typically between 30 and 90 seconds, Type III reflections require 1 to 4 minutes. The prism-assisted coupling simulation results are shown in Fig. 4.7.
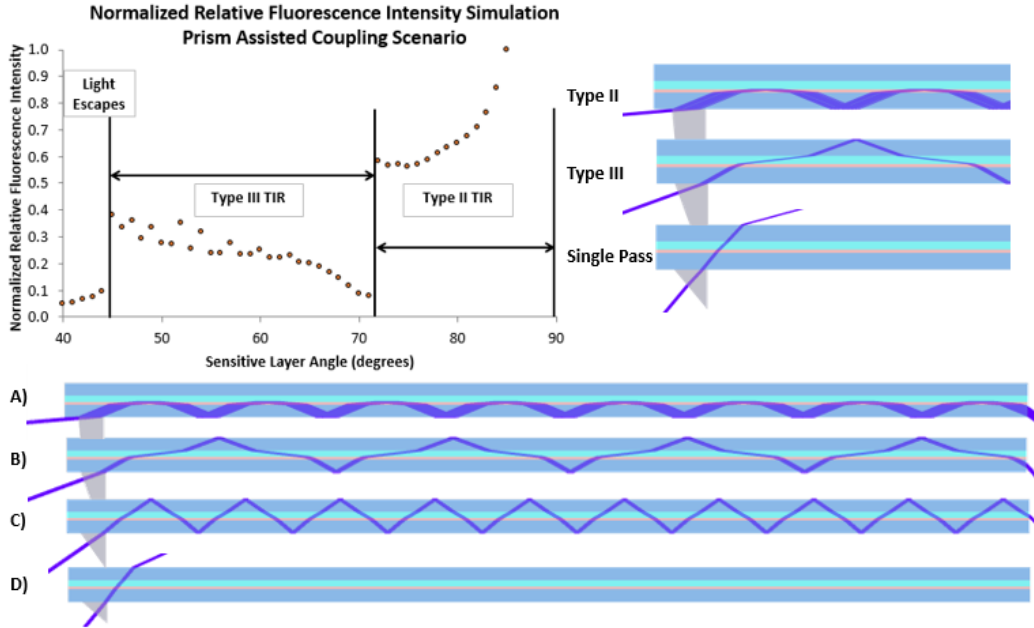
Figure 4.7   Prism assisted coupling simulation results. The collimated incident light is coupled through the base of a prism modelled with the same RI as the sensitive volume. Normalized relative fluorescence intensity simulation results are presented. A) Type II TIR seen using an 85° PDMS prism. B) Type III reflections seen using a 70° PDMS prism. C) Type III reflections seen using a 55° PDMS prism. D) Single pass excitation scenario seen using a 40° PDMS prism where incident light no longer experiences TIR and escapes the device.

4.5. DISCUSSION

The multilayered waveguide structure of the TIR fluorescence sensor makes it well suited for integration in optofluidic sensing systems. The fluorescence intensity measurement module could be easily miniaturized to monitor fluorescent film brightness periodically over time. Fluorescent sensitive modules may be developed for a variety of analytes in water samples and bodily fluids such as DO, pH, Ammonia, and Creatinine for example [4,21,30]. The sensitive devices themselves are easily fabricated using standard low-cost manufacturing methods. Although the TIR mechanism has been employed in sensing applications, the results presented here highlight important design considerations depending on the application of the TIR sensor.

The collimated coupling simulation demonstrates that Type II TIR conditions should provide the best sensitivity. For desktop sensing

applications where calibration is easily performed and the greatest sensitivity is required the Type II reflections approaching the critical angle are the most ideal. However, frequent calibration may be required due to the sharp change in sensitivity close to the critical angle. Slight misalignment of the incident angle could lead to poor accuracy. Type II reflections closer to the boundary angle are more stable and less sensitive to misalignment. Although less sensitive than the ideal Type II TIR condition, the reduced requirement for calibration could allow these devices to function with consistent accuracy in more rugged conditions. The coupling efficiency in the direct coupling case may be limited by matching the light source diameter to the thickness of the glass substrate. Intense beams of small diameter could lead to damaging the sensitive layer and photobleaching.

The focused coupling simulation demonstrated an agreement with the experimental sensitivity of the DO sensor we developed previously. The differences between the simulated and experimental results are the most significant at the critical angle. This is most likely due to the differences between the model of the light source intensity distribution and the actual intensity distribution of the experimental light source. Even small differences between experimental and simulated results should be the most significant at the critical angle due to the sharp increase in sensitivity. The results indicate that when focused input is used the critical angle provides the best sensitivity. Again, the change in sensitivity close to the critical angle suggests longer Type II reflections could be less sensitive to misalignment. The distribution of incident angles depends on the NA of the objective lens, light source beam diameter, and light source intensity distribution. Although a smaller spot size may be achieved from a larger beam diameter to couple more light into the glass substrate, only a proportion of the incident light can enter the device at the ideal critical angle.

The prism assisted coupling simulation results indicate that the Type II TIR condition should provide the best sensitivity. The incident light beam is always perpendicular to the front face of the prism so alignment is less complicated. In this situation the light must enter the glass substrate from the face of the prism. In the ideal situation where the prism angle is slight, the challenge to coupling becomes matching the spot size of the incident light at the device interface to the thickness of the prism. Where larger

beam diameters are used the prism angle may need to be reduced to effectively couple the light.

4.6. CONCLUSION

A ray tracing-based model has been developed in order to demonstrate the propagation of light through fluorescence-based water sensors employing the Total Internal Reflection mechanism to achieve sensitivity enhancement. The source of incident light has been approximated in the model to demonstrate the propagation of light in the device when receiving direct collimated input, focused input, and prism-assisted input. The structure of our previously tested TIR Fluorescence DO sensor [21] has been constructed with consideration of the refractive index of the different layers in the device, and the fluorescent properties of the dye used in the sensor. A detector surface is employed in order to predict the relative intensity of the fluorescence generated in the sensor when using different coupling mechanisms and incident angles. The model demonstrates how incident light transfers between layers of the device as the incident angle changes.

The results indicate that the sensitivity of the device is optimized when the path length of the incident light in the sensitive later is maximized. The path length of incident light increases as the incident angle approaches the critical angle. The model is validated by comparing the focused light source scenario with the similar experimentally measured DO sensor. Results suggest that devices using the critical angle could have the best sensitivity but may also be subject to misalignment. Devices employing Type II reflections closer to the Type III boundary angle could demonstrate a balance of sensitivity enhancement and less stringent alignment and calibration requirements. Although the model has not been used to directly determine the absolute fluorescence intensity observed, it can be used to predict the relative fluorescence intensity using different coupling schemes. The relative sensitivity of the experimental sensor presented previously exhibits a similar profile to the normalized relative fluorescence intensity predicted by the model. The model serves as a foundation for simulating TIR fluorescence sensors and can be customized depending on the sensor structure, the light source, and coupling optics which could prove useful for device design and rapid prototyping applications.

Funding Sources

Acknowledgement

Disclosures

The authors declare no conflicts of interest.

References

[1]   C.-S. Chu, T.-W. Sung, and Y.-L. Lo, "Portable optical oxygen sensor based on Ru(II) complex and dye entrapped core-shell nanoparticles embedded in sol-gel matrix coated on a photodiode," Opt. Eng., vol. 50, no. 5, pp. 54404–54406, 2011.

[2]   C. S. Chu and C. Y. Chuang, "Optical fiber sensor for dual sensing of dissolved oxygen and Cu2+ ions based on PdTFPP/CdSe embedded in sol-gel matrix," Sensors Actuators, B Chem., vol. 209, pp. 94–99, 2015.

[3]   J. F. Fernandez-Sanchez et al., "Fluorescence optosensors based on different transducers for the determination of polycyclic aromatic hydrocarbons in water," Anal. Bioanal. Chem., vol. 377, no. 4, pp. 614–623, Oct. 2003.

[4]   K. Waich, T. Mayr, and I. Klimant, "Talanta Fluorescence sensors for trace monitoring of dissolved ammonia," Talanta, vol. 77, pp. 66–72, 2008.

[5]   V. M. C. Rerolle, C. F. A. Floquet, M. C. Mowlem, R. R. G. J. Bellerby, D. P. Connelly, and E. P. Achterberg, "Seawater-pH measurements for ocean-acidification observations," TrAC - Trends Anal. Chem., vol. 40, pp. 146–157, 2012.

[6]   M. Li, H. Gou, I. Al-Ogaidi, and N. Wu, "Nanostructured sensors for detection of heavy metals: A review," ACS Sustain. Chem. Eng., vol. 1, no. 7, pp. 713–723, 2013.

[7]   Shanmugam and C. Salthouse, "Lensless fluorescence imaging with height calculation.," J. Biomed. Opt., vol. 19, no. 1, p. 16002, 2014.

[8]   W. Il Lee, S. Shrivastava, L. T. Duy, B. Yeong Kim, Y. M. Son, and N. E. Lee, "A smartphone imaging-based label-free and dual-wavelength fluorescent biosensor with high sensitivity and accuracy," Biosens. Bioelectron., vol. 94, no. March, pp. 643–650, 2017.

[9]   M. L. Martin-Fernandez, C. J. Tynan, and S. E. D. Webb, "A 'pocket guide' to total internal reflection fluorescence," J. Microsc., vol. 252, no. 1, pp. 16–22, 2013.

[10]   Xiong, E. Mahoney, J. F. Lo, and Q. Fang, "A Frequency-domain optofluidic dissolved oxygen sensor with total internal reflection design for in situ monitoring," IEEE J. Sel. Top. Quantum Electron., vol. 27, no. 4, pp. 1–7, 2021.

[11]   S. Kavi Priya, G. Shenbagalakshmi, and T. Revathi, "Design of smart sensors for real time drinking water quality monitoring and contamination detection in water distributed mains," Int. J. Eng. Technol., vol. 7, no. 1.1, pp. 47–51, 2019.

[12]   L. Amand and B. Carlsson, "The optimal dissolved oxygen profile in a nitrifying activated sludge process - Comparisons with ammonium feedback control," Water Sci. Technol., vol. 68, no. 3, pp. 641–649, 2013.

[13]   Vlad and M. Sbarciog, "Indirect control of substrate concentration for a wastewater treatment process by dissolved oxygen tracking," J. Control Eng. Appl. INFORMATICS, vol. 14, no. 1, pp. 37–47, 2012.

[14]   Z. Rosenzweig and R. Kopelman, "Development of a submicrometer optical fiber oxygen sensor.," Anal. Chem., vol. 67, no. 15, pp. 2650–2654, 1995.

[15]   S. M. Grist, L. Chrostowski, and K. C. Cheung, "Optical oxygen sensors for applications in microfluidic cell culture.," Sensors (Basel)., vol. 10, no. 10, pp. 9286–9316, 2010.

[16]   T. P. Burghardt and N. L. Thompson, "Total Internal Reflection Fluorescence," Ann. Rev. Biophys. Bioeng., vol. 13, no. 17, pp. 247–268, 1984.

[17]   Axelrod, "Total internal reflection fluorescence microscopy in cell biology," Traffic, vol. 2, no. 11, pp. 764–774, 2001.

[18]   K. Shinohara et al., "Measurement of pH field of chemically reacting flow in microfluidic devices by laser-induced fluorescence," Meas. Sci. Technol., vol. 15, no. 5, pp. 955–960, 2004.

[19]   Klimant and O. S. Wolfbeis, "Oxygen-Sensitive Luminescent Materials Based on Silicone-Soluble Ruthenium Diimine Complexes," Anal. Chem., vol. 67, no. 18, pp. 3160–3166, 1995.

[20]   Y. Amao, "Probes and Polymers for Optical Sensing of Oxygen," Microchim. Acta, vol. 143, no. 1, pp. 1–12, 2003.

[21]   E. Mahoney, H.-H. (Leo) Hsu, F. Du, B. Xiong, P. R. Selvaganapathy, and Q. Fang, "Optofluidic Dissolved Oxygen Sensing With Sensitivity Enhancement Through Multiple Reflections," IEEE Sens. J., vol. 19, no. 22, pp. 10452–10460, Nov. 2019.

[22]   H. Tai, Y. Yang, S. Liu, and D. Li, "A Review of Measurement Methods of Dissolved Oxygen in Water," Comput. Comput. Technol. Agric. V, vol. 369, pp. 569–576, 2012.

[23]   N. C. H. Le, D. V. Dao, R. Yokokawa, J. Wells, and S. Sugiyama, "Design, simulation and fabrication of a total internal reflection (TIR)-based chip for highly sensitive fluorescent imaging," J. Micromechanics Microengineering, vol. 17, no. 6, pp. 1139–1146, 2007.

[24]   Llobera, S. Demming, R. Wilke, and S. Büttgenbach, "Multiple internal reflection poly(dimethylsiloxane) systems for optical sensing," Lab Chip, vol. 7, no. 11, pp. 1560–1566, 2007.

[25]   J. Sinkó, G. Szabó, and M. Erdélyi, "Ray tracing analysis of inclined illumination techniques," Opt. Express, vol. 22, no. 16, p. 18940, 2014.

[26]   P. Xie, H. Lin, Y. Liu, and B. Li, "Total internal reflection-based planar waveguide solar concentrator with symmetric air prisms as couplers," Opt. Express, vol. 22, no. S6, p. A1389, 2014.

[27]   N. ur Rehman, "Optical-irradiance ray-tracing model for the performance analysis and optimization of a façade integrated solar collector with a flat booster reflector," Sol. Energy, vol. 173, no. June, pp. 1207–1215, 2018.

[28]   Derkus, "Applying the miniaturization technologies for biosensor design," Biosens. Bioelectron., vol. 79, pp. 901–913, 2016.

[29]   L. Polerecky, "Optimisation of multimode waveguide platforms for optical chemical sensors and biosensors," p. PhD Thesis, 2002.

[30]   S. Wang, X. Li, J. Yang, X. Yang, F. Hou, and Z. Chen, "Rapid determination of creatinine in human urine by microchip electrophoresis with LED induced fluorescence detection," Chromatographia, vol. 75, no. 21–22, pp. 1287–1293, 2012.

Chapter 5

Research Paper 3 - <u>*Manuscript*</u> – Fluorescence-based Ammonia and Creatinine Sensing for Environmental and Point of Care Monitoring

Eric James Mahoney[1], Bo Xiong[1], Herb. E. Schellhorn[2], P. Ravi Selvaganapathy[1,3] and Qiyin Fang[1,4,z]

[1]*School of Biomedical Engineering, McMaster University, 1280 Main St. West, Hamilton, ON L8S 4K1, Canada*

[2]*Department of Biology, McMaster University, 1280 Main St. West, Hamilton, ON L8S 4K1, Canada*

[3]*Department of Mechanical Engineering, McMaster University, 1280 Main St. West, Hamilton, ON L8S 4K1, Canada*

[4]*Department of Engineering Physics, McMaster University, 1280 Main St. West, Hamilton, ON L8S 4K1, Canada*

[z]*Corresponding Author qiyin.fang@mcmaster.ca*

Introduction to Optofluidic Ammonia Sensing

Chapter 5 is currently a manuscript based on work conducted from the end of 2018 to present, in preparation for submission to the IEEE Sensors Journal. I have conducted experimental work and extensive troubleshooting to produce the current prototype ammonia sensors. I have prepared an experiment plan for sensing Creatinine using a modified ammonia sensor. A portable optofluidic fluorescence chip reader has been developed enabling complete detector and light source control by the user over a wireless network. The significance of this research involves the development of a prototype remote monitoring platform for fluorescence measurements with a discussion of extensive troubleshooting and identified design challenges.

Contents of paper

Abstract

Detection of ammonia in fluid samples has been demonstrated as an important diagnostic test for environmental and medical diagnostic applications. Optofluidic ammonia sensors have the potential for use as remote monitoring and Point of Care diagnostic devices; however, these remote monitoring networks have not been realized. Fluorescence-based pH sensitive dyes have been used for quantification of ammonia in water samples. In this paper, we present our work towards the development of an optofluidic device for the measurement of ammonia in water samples using pH-sensitive fluorescent Eosin dye. A multilayered sensor design is employed to use Total Internal Reflection for sensitivity enhancement. As the ammonia sensor module is refined a prototype portable optofluidic chip reader is developed that can be used to measure other fluorescence-based sensors. With further development the portable remote monitoring device may be deployed for the assessment of environmental groundwater and analysis of urine samples for Point of Care diagnostics. Additional ammonia-containing analytes may be detected indirectly as ammonia using this remote monitoring platform using enzymatic methods in future versions of this platform.

5.1. INTRODUCTION

Ammonia sensing is useful for several fluid monitoring applications including environmental water quality monitoring and point of care (PoC)

diagnostic devices. Typically, it is unusual to find large concentrations of ammonia when assessing the quality of environmental water. The ammonia present often comes from agricultural runoff or from the contamination of groundwater near landfill sites (1–3). Natural rainfall tends to wash contaminants from landfill sites into the ground, where they eventually leach into the ground water. Ground water may contain significant levels of ammonia for several years after a landfill is closed (3). Periodic monitoring of ammonia in groundwater is essential for determining the safety of water supplies. Ammonia is also commonly found in urine samples and can be sensed directly or as an indirect measurement of health-indicative metabolites in urine (4). PoC diagnostic testing could significantly benefit from the development of ammonia sensing systems. Creatinine (Crn) is particularly interesting in the context of urine analysis testing due to its relatively constant rate of production in the human body and rate of excretion by the kidneys. Creatinine is a metabolic product of Creatine (Cr) metabolism that primarily occurs in muscles, liver tissues, and the brain (5). The mass of these tissues in the body is relatively stable over short periods of time, so the quantity of Creatinine produced in the human body can be consistent for an individual over the course of a day (6,7). The rate of Creatinine production during the day may change according to the Circadian rhythm (5).

The detection of ammonia is often achieved by monitoring changes in the pH of the sample environment. Changes in the absorbance of optical films caused by pH changes induced by ammonia gas in air have been investigated using spectrometers (8), photodiodes (9,10), and Paired Emitter-Detector Diodes (PEDDs) (11). The use of photodiodes as optical detectors provides significant cost advantages for the development of remote monitoring devices, however they still require a sensitive analog to digital converter (ADC)(10,11). The PEDD technique employs a reverse biased LED as a detector paired with an LED emitter. The light transmitted through the sample or sensitive film to the detector charges the LED. The time required to discharge the LED below a threshold voltage is related to the intensity of light reaching the detector through the sample. As the intensity of light reaching the detector increases, the photocurrent induced reduces the time required to discharge the LED (11). The PEDD method has also been demonstrated for the detection of ammonia in water samples using the Berthelot reaction, however this technique requires the use of

reagents (12). Alternatively, reagent-free strategies have been developed for the detection of ammonia using pH sensitive fluorescent films (13,14).

The methods identified by previous studies demonstrate the potential of ammonia sensors beyond direct ammonia detection. We consider three generations of optical ammonia sensors distinguished by the sensing mechanism and the complexity of the multilayered device structure. The first generation of ammonia sensors employ ammonia sensitive fluorescent films for the direct detection of ammonia. The detection of ammonia is achieved with the use of pH sensitive dyes. This is achieved by coating a sensitized pH-sensitive film with a protective silicone layer. The protective silicone layer prevents the diffusion of ions while remaining permeable to charged gasses such as ammonia (15). The ammonia diffuses into the pH-sensitive film, leading to an ion exchange with dye molecules. The fluorescent dye demonstrates a change in fluorescence intensity depending on the charge of the dye. These devices are well suited for quantifying background ammonia in urine samples for PoC health monitoring applications, as well as for monitoring the quality of ground water.

The pH-sensitive Eosin dye demonstrates low fluorescence when protonated and high fluorescence when deprotonated, and an equilibrium is reached depending on the local pH (13). When applied to ammonia sensing, the equilibrium depends on the concentration and pKa of ammonia as shown in equations 1 to 3 (14). If the pKa is constant, then the concentrations of NH_3 and NH_4^+ can be determined using the Henderson-Hasselbalch equation, shown in equations 4 and 5 (14).

$$NH_3 + IndH \; \rightleftharpoons \; NH_4^+ + Ind^- \qquad \text{(Eq. 1)}$$

$$NH_3 + H^+ \rightleftharpoons \; NH_4^+ \qquad \text{(Eq. 2)}$$

$$Ka = \frac{[NH_3][H^+]}{[NH_4^+]} \qquad \text{(Eq. 3)}$$

$$[NH_4^+] = [NH_3] x 10^{(pKa-pH)} \qquad \text{(Eq. 4)}$$

$$[NH_3] = [NH_4^+] x 10^{(pH-pKa)} \qquad \text{(Eq. 5)}$$

The second generation of ammonia sensors rely on the indirect measurement of alternative sample constituents based on ammonia generated from a chemical or enzymatic reaction. These sensors may be applied to the detection of a range of compounds containing ammonia. These devices have added complexity due to the requirement to conduct a

reaction before injecting the sample into the sensor, or performing the reaction on the chip. In the case where an enzymatic reaction is used, the enzyme is immobilized in a hydrogel coated above the sensitive film. The hydrogel allows the diffusion of analytes in the fluid sample into the matrix, where it can react with the embedded enzyme to produce ammonia. The enzyme to be immobilized can be selected based on the metabolic pathway of creatine and creatinine. Ammonia can be generated from creatinine by reaction with the Creatinine Deaminase/Deiminase enzyme (4,13,14), as shown in equation 6 (4). Additionally, background measurements must be made to differentiate between background ammonia and ammonia generated from target analytes. With the use of Creatinine Deiminase, a second-generation ammonia sensor for the indirect detection of creatinine can be produced. Ammonia can also be generated from urea by the Urease enzyme, as shown in equation 7 (4). Urea may naturally be present in the sample or may be the product of another enzymatic reaction.

$$Creatinine + \; H_2O \; \xrightarrow{Creatinine \; deiminase} \; NH_4^+ + N - methlyhydantoin \;\;\; (6)$$

$$Urea + \; H_2O \; \xrightarrow{Urease} \; NH_4^+ + CO_2 \;\;\;\;\;\;\;\; (7)$$
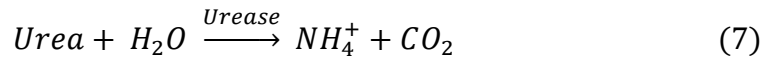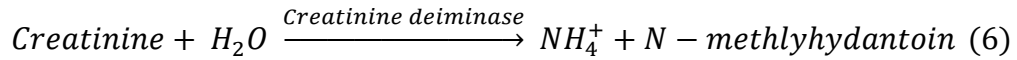
The third generation of ammonia sensors relies on the detection of ammonia produced from a known compound that is generated from a target molecule. These devices are similar in complexity to the second-generation sensors. The most significant difference between the second and third generation ammonia sensors is the composition of the hydrogel layer, which must contain a cocktail of enzymes. For example, urea can be generated from creatine by an enzymatic reaction catalyzed by Creatinase as shown in equation 8 (4). The urea produced can then be converted to ammonia and detected similarly to the second-generation method. The background corrections become more complicated as well, as the ammonia and intermediate analyte need to be quantified.

$$Creatine + H_2O \; \xrightarrow{Creatinase} \; Urea + Sarcosine \;\;\;\;\;\;\;\; (8)$$

Although multilayered ammonia-sensitive fluorescent sensors have been developed, they are still produced with applications in commercial medical testing in mind. Duong et. al. (2017) report all three generations of ammonia sensors working together, coated on the bottom of wells in a 96-well plate, and measured using a microtiter plate reader (4). Waich et. al. (2008) and Deng et. al. (2016) have demonstrated first and second-

generation ammonia sensors in an optofluidic chip format, but these methods still relied on benchtop measurement systems (13,14). The power of portable ammonia sensing systems reaches beyond the ability to directly determine ammonia concentrations in fluids. Our novelty is in applying the methods identified by previous studies to our automated remote monitoring fluid-sensing platform. In our project, we work to integrate the optofluidic ammonia sensing chip with a prototype remote measurement chip reader to realize continuous PoC diagnostics and water quality monitoring. We take advantage of Total Internal Reflection (TIR) to improve the sensitivity of the sensor module, to reduce the dependence on expensive detectors and light sources. The integrated sensing system is able to capture measurements continuously directly from the site over time, enabling analysis of trends for diagnostic and predictive purposes, rather than relying on the assessment of sparsely collected single measurements.

5.2. SENSOR DESIGN

The design of the optofluidic fluorescence sensor for dissolved ammonia is based on a multilayered structure built upon a glass substrate. The device fabricated here is based on the platform for fluorescence based Dissolved Oxygen (DO) sensing developed in our previous work (16) and the ammonia sensing methods reported by other studies (13,14). The novelty in our approach is to leverage TIR of excitation light within the sensor structure to enhance the sensitivity of the sensor module. The dependency on expensive sensor modules and light sources is significantly reduced by optimizing the sensitivity of the sensor module.
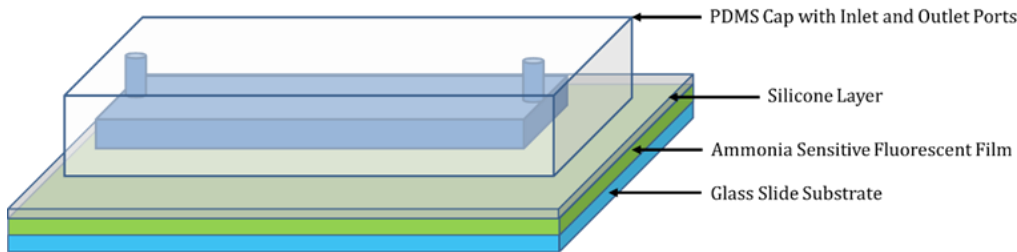
Figure 5.1 Dissolved Ammonia sensor structure. The base of the device is a 1.1mm thick glass substrate. The sensitive layer consisting of Eosin dye in a polymer matrix is coated above the glass. The sensitive layer is protected by a RG01 silicone membrane applied by spin coating. A PDMS water channel is bonded to the top of the device to contain the fluid sample for analysis.

The device is fabricated on a 1.1 mm thick cleaned glass substrate. The glass is coated with an ammonia sensitive Eosin dye dissolved in a polymer matrix. Eosin dye mixtures in Cellulose Acetate (Cac) and Cellulose Acetate Propionate (Cacp) were tested. Cac films were produced using a paint on method where Cacp films were prepared by spin coating (<100 μm). A protective silicone layer is applied above the Eosin film to prevent the device from responding to bulk pH changes while still allowing the ammonia to diffuse to the sensitive film (<100 μm). A water channel (8 mm wide x 2 mm tall x ≤ 5 cm long) prepared by conventional soft lithography in Poly-Dimethylsiloxane (PDMS) is then bonded to the top of the device to contain the fluid sample for analysis. Various channel lengths were used, but the channel width and depth were consistent. Tubing ports are punched into the top of the water channel to allow the sample to be injected and drained to waste after measurement. In future versions of this device, a hydrogel layer may be applied above the silicone membrane to immobilize enzymes, enabling the indirect detection of alternative analytes by generating ammonia.

5.3. MATERIALS AND METHODS

5.3.1. Reagents and Materials

All water used was deionized (18.5 Mohm) unless otherwise specified. HPLC water purchased from Caledon (CAS:7732-18-5, 8801-7-40) was used in many final experiments when 18.5 Mohm Deionized (DI) water was unavailable. The acetone used to prepare the fluorescent films was purchased from Sigma Alderich (CAS:67-64-1, 179973-1L) 99.99%. The Eosin Ethylester dye was purchased from Sigma Alderich (CAS:6359-05-3, 199540-5G). Cellulose Acetate and Cellulose Acetate Propionate used to prepare the sensitive membrane were purchased from Sigma Alderich (CAS:9004-35-7, 419028-500G [~50000 MW], CAS:9004-39-1, 340642-250G [~15000 MW]). Glass microscope slides used as sensor substrates were purchased from VWR (VWR Gold Slide). The slides were cleaned using isopropyl alcohol 99.9% purchased from Sigma Alderich (CAS:67-63-0). The Methanesulfonic Acid (MSA) used to clean slides and sensitive the film was purchased from Sigma Alderich (CAS:75-75-2, 471356-25ML). Heptane used to prepare spin coated Cacp coatings was purchased from Sigma Alderich (CAS:142-82-5, HX0080-6). The PDMS was purchased from Corning (Sylgard 184, Corning). Phosphate Buffered Saline (PBS) concentrate was purchased from Sigma Alderich used to prepare the pH standards (P5368-10PAK). The RG-01

reprographic silicone was purchased from Gelest (PP2-RG01). The ammonium chloride used to prepare ammonia standards was purchased from Sigma Alderich (CAS:12125-02-9, A9424-500G).

5.3.2.   Preparation of Standards and Sensors

The sensitive dye mixture was prepared by dissolving 0.007 g Eosin dye powder per 10mL of acetone. A clean dry 15 mL Falcon tube was covered in a thin film of tin foil to prevent photobleaching of the dye mixture by reducing exposure to ambient light. The dye was weighed directly in the tube using an analytical balance. 10 mL of acetone is transferred to the tube containing the dye. The dye was completely dissolved in the solvent by inverting the tube several times. 0.50 g of Cellulose Acetate or Cellulose Acetate Propionate was weighed in a weigh boat, transferred slowly to the tube, and dissolved using a vortex mixer. The resulting mixture of Cac or Cacp and Eosin was used to coat the glass substrate to prepare the sensitive film. The pH standards were prepared in PBS. A 10x concentrate was prepared and adjusted to different pH values by adding concentrated sodium hydroxide. The pH values were recorded using a benchtop pH meter (HANNAH HI-223) and verified later using a portable pH meter (OHAUS ST-20). Ammonia standards were prepared in DI water and pH 7.3 PBS buffer. A serial dilution was conducted in order to prepare the remaining standards of ammonia.

5.3.3.   Device Fabrication Methods

5.3.3.1. *Method 1 Cac painted-on without Sensitization or Silicone Layer*

The first fabrication method tested was based on Waich et al. (2008) (13). In this method they compared the sensitivity of ammonia sensors by immobilizing the Eosin dye in various polymers. At this stage the Cellulose Acetate (Cac) was identified as an ideal polymer to start with. After gaining experience working with Cac and Cacp it appears that the Cac films are more rigid and take longer to sensitize. The mixture of dye and polymer is very fluid and difficult to apply by spin coating. Instead of following the spin coating procedure recommended by Waich et al. (2008) (13), the film is applied using a pipette and spread using a wooden stir stick instead of using a knife coating method. The surface tension supports the dye mixture on the surface of the glass slide and it quickly solidifies as it dries on the surface, due to the evaporation of acetone solvent.

Table 5.1 Method 1

Layer		Waich et. al. (2008) (13)	
Substrate	Preparation	Polyester Films	175 µm thickness
Sensitive Film Coating	Preparation	Cellulose Acetate	100000 MW Cac for most sensitive 5% (W/W)
		Cellulose Acetate Propionate	15000 MW
			0.6 µM MSA
		Acetone	Merck
		Eosin Ethylester - Sigma	Sigma Alderich
	Coating	Custom Knife Coating	
		Concentration	
		Thickness	1-5 µm
	Sensitization	NA	
Protective Membrane	Preparation	Silicone	5% (W/W) in n-hexane
			PP2-RG01, 2part reprographic Silicone from ABCR
	Coating		1 µm
			175 µm for suspension of nanospheres
			Spread down to 1 µm
			Coated in 1 µm of silicone
Channel Cap	Preparation	NA	

The painted coating devices were initially used without sensitization or a protective top coat for characterizing the fluorescence of the sensitive coating, optical filters, and light sources. Following the characterization of the Eosin dye and light sources, the sensitization step was implemented. Photographs of the Eosin-coated slides prepared by the paint-on method before and after drying are presented in the following figure.
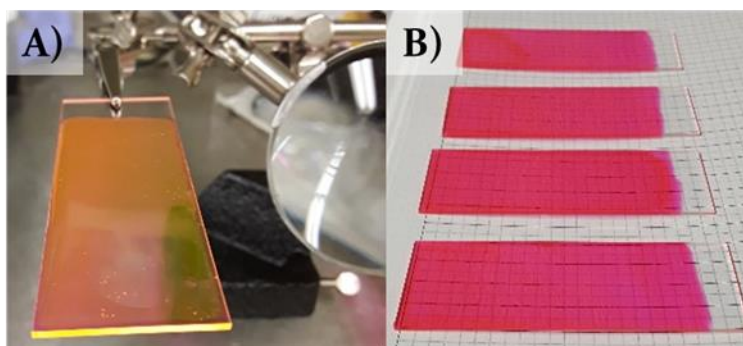
Figure 5.2 Paint-on coating method images. A) A freshly applied Eosin dye mixture in Cac and acetone. B) A batch of dried sensitive coatings on glass.

5.3.3.2. Method 2 Cac with Sensitization and without Silicone Layer

This method is similar to Method 1, but the slides are immersed in an acid bath of MSA in order to protonate the dye and improve sensitivity after curing the sensitive film. It was found that the sensitive films can delaminate and wrinkle, causing the film to peel away from the glass substrate. In order to determine if the films could still be used, PDMS was used to reattach the films to the glass substrate. Once the PDMS had solidified, the films were reattached to the substrate but it was unknown if these recovered devices could be used.

Table 5.2 Method 2

Layer			Deng 2016 (14)
Substrate	Preparation	Glass Microscope Slides	No details provided
Sensitive Film Coating	Preparation	Microcrystalline Cellulose	5% (W/W) MCC, no details provided
		Methanesulfonic Acid	0.7 µM MSA
		Acetone	99.5:1, Acetone: Water Mix
		Eosin Dye	1 mM Eosin, no details provided
	Coating	Spin Coating	
		Thickness	70 µm
		Method	600 RPM 50 s
	Sensitization		0.7 µM MSA to protonate dye
			Overnight soak in MSA
Protective Membrane	Preparation	Silicone	25% (W/W) in n-heptane
	Coating	Spin Coating	
		Thickness	100 µm
		Method	1200 RPM - 50 s
Channel Cap	Preparation		**NA**

When the sensitization step with MSA was implemented with the painted-on Eosin-Cac films, they often wrinkled and delaminated. When the fabrication method was adjusted to use the Eosin-Cacp films they would delaminate but not wrinkle. The delaminated films could be reattached to the glass substrate using PDMS. It was determined that pipetting the sensitization solution out of the dish would prevent the films from delaminating.
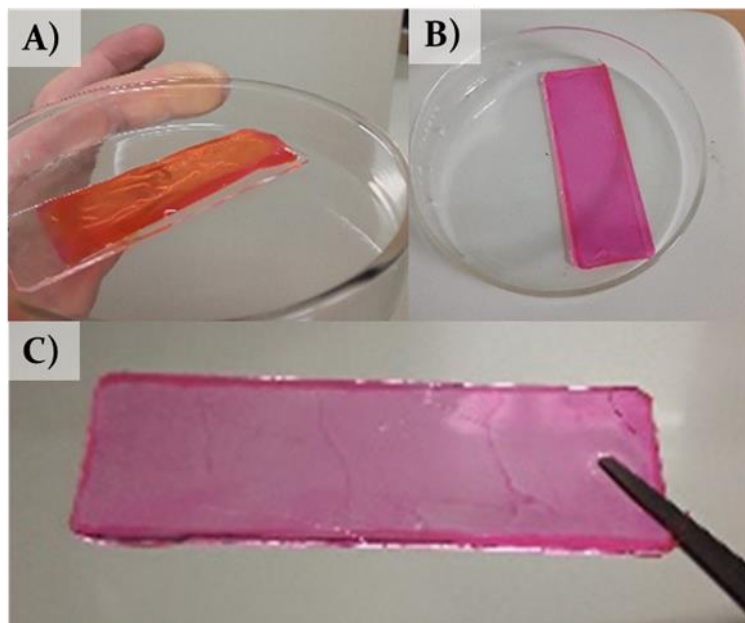
Figure 5.3 A) A wrinkled delaminated sensitive film after sensitization. B) A spin coated device soaking in MSA for sensitization. C) A device recovered by reattaching the film using PDMS.

5.3.3.3. Method 3 Cacp with Sensitization and without Silicone Layer

 The fabrication method was adjusted to follow the protocol of Deng et. al (2016) (14). This method clarifies many of the fabrication details that are omitted from the original publication and is easier to follow. Cacp was used instead of Cac as the polymer matrix. It was found that the Cacp polymer is more flexible than the Cac, and also appears to be more susceptible to sensitization. The films can delaminate when the MSA dish is disturbed during sensitization and the films can tear, but the films rarely wrinkle. The solvent is removed using pipettes to avoid disturbing the film and it remains laminated. The method is refined to produce films uniformly.

Table 5.3 Method 3

Layer			Custom – 2019
Substrate	**Preparation**		Washed in 7 µM Methanesulfonic Acid
Sensitive Film Coating	**Preparation**	Cellulose Acetate	5% W/V, Cac in Acetone, 50000 mW (CAS:9004-35-7), Sigma 419028-500g
		Methanesulfonic Acid	0.7µM MSA (CAS: 75-75-2), Sigma 471356-25mL
		Acetone	99% Reagent grade Acetone (CAS:67-64-1, Caledon, 1200-1-10)
		Eosin dye	1 mM Eosin Ethylester dye (CAS:6359-05-3), Sigma 199540-25g
	Coating	Spin Coating	
		Thickness	70-100 µm
		Method	0 - 600 RPM for 10 s
			Hold 600 RPM for 50s
			Remove immediately and place in glass dish
			Cover Glass dish in foil to protect from light
	Sensitization	Methanesulfonic Acid	0.7 µM MSA soak
		Method	Soak in glass dish 24H (Covered)
Protective Membrane	**Preparation**	RG01 Silicone 10:1, Base: CA	100% RG01
	Coating	Spin Coating	
		Thickness	100 µm
		Method	0-1200 RPM for 10 s
			Hold 1200 RPM for 50 s
			Remove immediately and place in glass dish
			Cover glass dish in foil
			Cure the PDMS by heating at 60 °C for 4 hours
Channel Cap	**Preparation**	PDMS 10:1, Base: CA (Sylgard 184, Corning)	
		Method	Pour 15 g into a 3D printed mold
			Cure overnight at 60 °C
			Punch 2.5 mm holes at channel ends
			Remove from mold and paint the bottom with fresh PDMS
			Place over membrane on sensor and press together
			Cure overnight at 60 °C
			Plug holes with more painted PDMS - and cure
			Insert rubber tubing into the holes

5.3.3.4. Method 4 Cacp with Sensitization and Silicone Layer

The method is refined to the point where it more accurately follows the procedure of Deng et al. (2016) (14). The films can be prepared uniformly and sensitized reliably without damage. At this point, I was able to spin coat a protective topcoat of RG-01 silicone for a complete prototype device.

It was found that the dye layer is digested if the MSA concentration is too high, or if the sensitization incubation is too long.
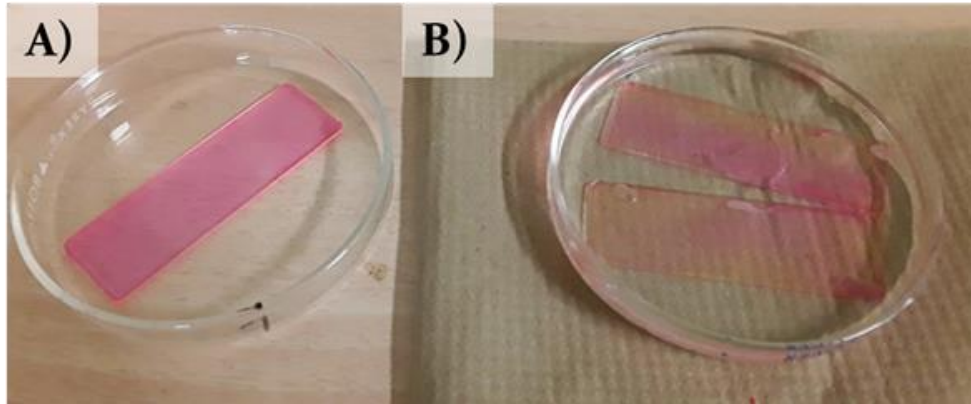
Figure 5.4 A) Unsensitized Cacp device. B) Sensitizing Cacp membranes. The change in color is observed as the dye becomes protonated.

Table 5.4 Method 4 – Current Method

Layer			Current Method
Substrate	Preparation		Washed in 7 μM Methanesulfonic Acid in Acetone
Sensitive Film Coating	Preparation	Cellulose Acetate Propionate	5% Cacp in Acetone
		Methanesulfonic Acid	0.7 μM MSA (CAS: 75-75-2), Sigma 471356-25mL
		Acetone	99% Reagent grade Acetone (CAS: 67-64-1, Caledon, 1200-1-10)
		Eosin dye	1 mM Eosin Ethylester dye (CAS:6359-05-3), Sigma 199540-25g
	Coating	Spin Coating	
		Thickness	Cover completely in solution with dropper
		Method	0 - 600 RPM for 10 s
			Hold 600 RPM for 50 s
			Remove immediately and place in glass dish
			Cover Glass dish in foil to protect from light
	Sensitization	Methanesulfonic Acid	0.7 μM MSA soak
		Method	Soak in glass dish 24 H (Covered)
			Slides turn light orange over time
Protective Membrane	Preparation	RG01 Silicone 10:1, Base: CA	25% in heptane
	Coating	Spin Coating	
		Thickness	100 μm - 1 μm
		Method	0-1200 RPM for 10 s
			Hold 1200 RPM for 50 s
			Remove immediately and place in glass dish
			Cover glass dish in foil
			Cure the PDMS by heating at 50 °C for 4 hours
Channel Cap	Preparation	PDMS 10:1, Base: CA (Sylgard 184, Corning)	
		Method	Pour 15 g into a 3D printed mold
			Cure overnight at 60 °C
			Punch 2.5 mm holes at channel ends
			Remove from mold and paint the bottom with fresh PDMS
			Place over membrane on sensor and press together
			Cure overnight at 60 °C
			Plug holes with more painted PDMS and cure
			Insert rubber tubing into the holes

5.3.3.5. *Water Channel Preparation and Bonding*

In order to contain the fluid sample on the sensor, a PDMS water channel was prepared. The fabrication method is the same as for the optofluidic DO sensor reported earlier (16). Soft lithography is used to prepare the channels using a 3D printed mold. Tubing ports are punched into the PDMS channel cap and then the cap is bonded to the sensor using air plasma. Tygon tubing is then inserted into the ports to transport fluid samples.
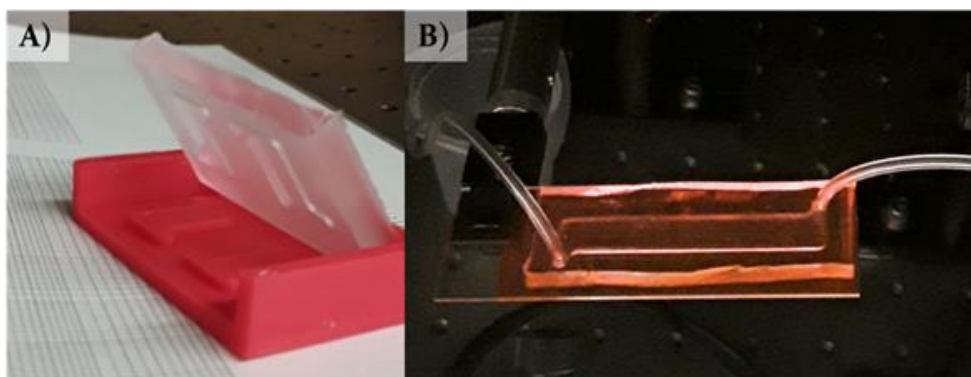
Figure 5.5 A) A 3D printed mold used to prepare PDMS fluid channels using soft lithography. B) Completed optofluidic ammonia sensor prepared using the paint on coating method.

5.3.4. **Experimental Setups**

The experiment setups were prepared within a dark box enclosure. A computer monitor with a keyboard and mouse was set next to the dark box to control computer modules within without opening the enclosure during measurements. The experimental setup was designed to be portable and powered by a 12V 5A DC power supply. The measurement system was comprised of an illumination module, a sensing module, and a detection module. The device was remotely controlled using a Raspberry Pi Model 3B+ computer using a custom Graphical User Interface developed in Python. A prototype of a portable version of the experimental setup was produced, but the benchtop setup within the dark box was used for the experimental results presented here.

Figure 5.6 The dark box enclosure containing the experimental setups and the adjacent workstation.

5.3.4.1. Eosin Emission Spectrum Measurements

In order to experimentally determine the emission spectrum of the Eosin-Cac film, a coated slide was measured when excited by a 470 nm LED from Thorlabs. A lens relay assembled in a 1" lens tube was used to focus the divergent source to the edge of the coated glass slide. Two pinholes were added to the end of the lens tube in order to eliminate the image of the LED emitter from the incident light.
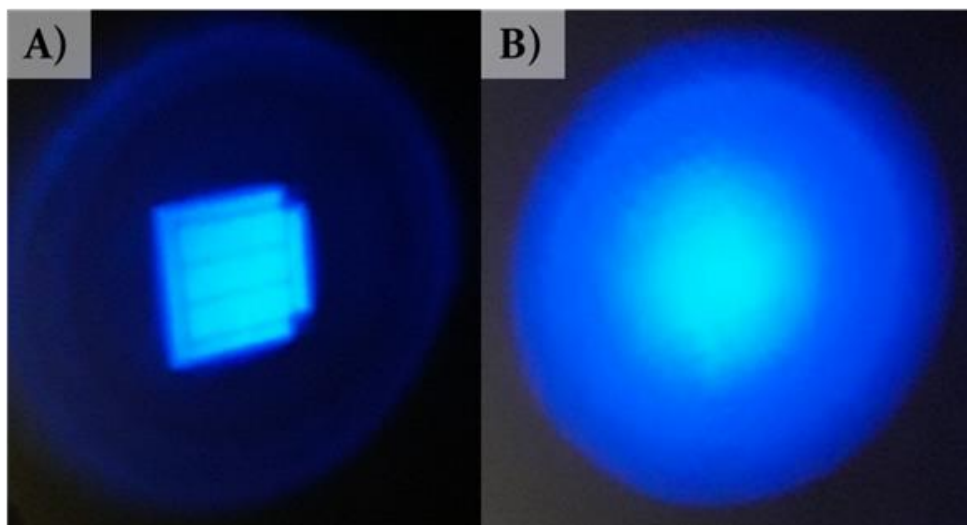
Figure 5.7 The focused 470 nm LED spot projected onto the wall of the dark box before (A) and after pinholes are installed (B).

A fiber optic probe was mounted behind an emission filter from Semrock (609-181) to reject the excitation light while passing the fluorescence emitted from the film. The signal from the optical fiber was measured using the Newport OSM 400 spectrometer. The spectrum of the excitation light was determined without the coated slide installed.
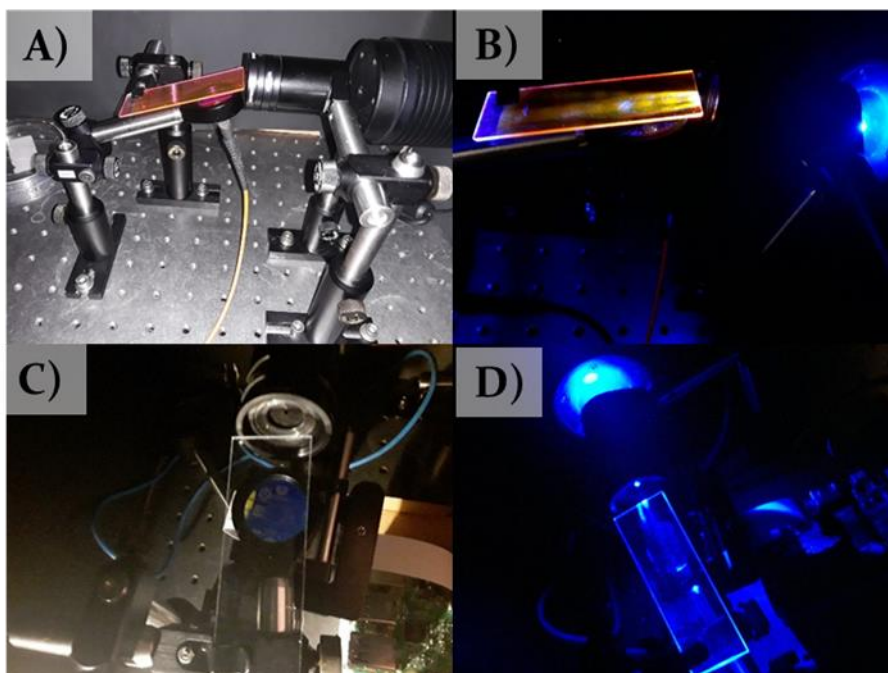
Figure 5.8 Experimental setup for the measurement of fluorescence emission from Eosin dye in Cac. A) Setup of the clamped Eosin-coated slide, fiber probe mounted with an emission filter, and the focused 470 nm LED source. B) An Eosin coated slide excited by the focused LED using edge coupling at approximately 10 degrees. C) An uncoated glass slide installed in the enclosure for uncoated glass control measurements. D) An uncoated glass slide while exposed to 470 nm LED without an emission filter.

5.3.4.2. Eosin Emission Measurements using Raspberry Pi Camera Module

The Illumination module consisted of a blue laser diode (450 nm, 150 mW) that was attenuated through an OD3 Neutral Density (ND) filter to achieve 150 µW peak power. The laser was powered through a dedicated circuit board and can be operated in a continuous wave mode or with frequency modulation. The incident light was directed to the edge of the sensor module that is held by an adjustable angle clamp. The design of the mount enables the user to carefully adjust the incident angle and alignment between the sensor and the excitation beam.

Figure 5.9 Experimental setup for exciting an Eosin-coated slide from the edge using a 450 nm laser line profile through a slit.

   The detection module consists of a Raspberry Pi NoIR camera V2.1, a high magnification smartphone camera lens, and a band pass emission filter from Semrock (609-181). The smartphone camera lens was attached to the front of the camera module using a spring-loaded clip. The emission filter was placed in front of the camera lens and held into place using a thin strip of sticky tack along the edge of the filter mount. The detector assembly was attached to a metal post that is held by the sensor module mount to align the detector with the sensor.
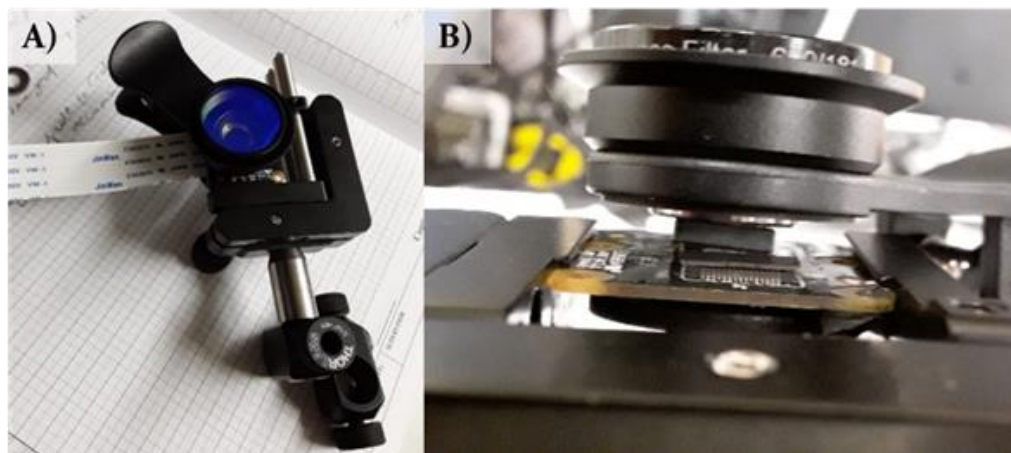
Figure 5.10 A) The modified camera mount with an additional cell phone lens installed above the camera module. The emission filter is moved above the camera lens. B) A side view of the modified camera mount with cell phone lens. A spring-loaded clamp keeps the lens and filter fixed to the front of the Raspberry Pi camera module.

Tubing was used to deliver fluid samples to the sensor module and to drain the spent sample to a waste container from outside of the system enclosure using a 5 mL syringe. The light source and detector modules were controlled by the Raspberry Pi through the user interface.
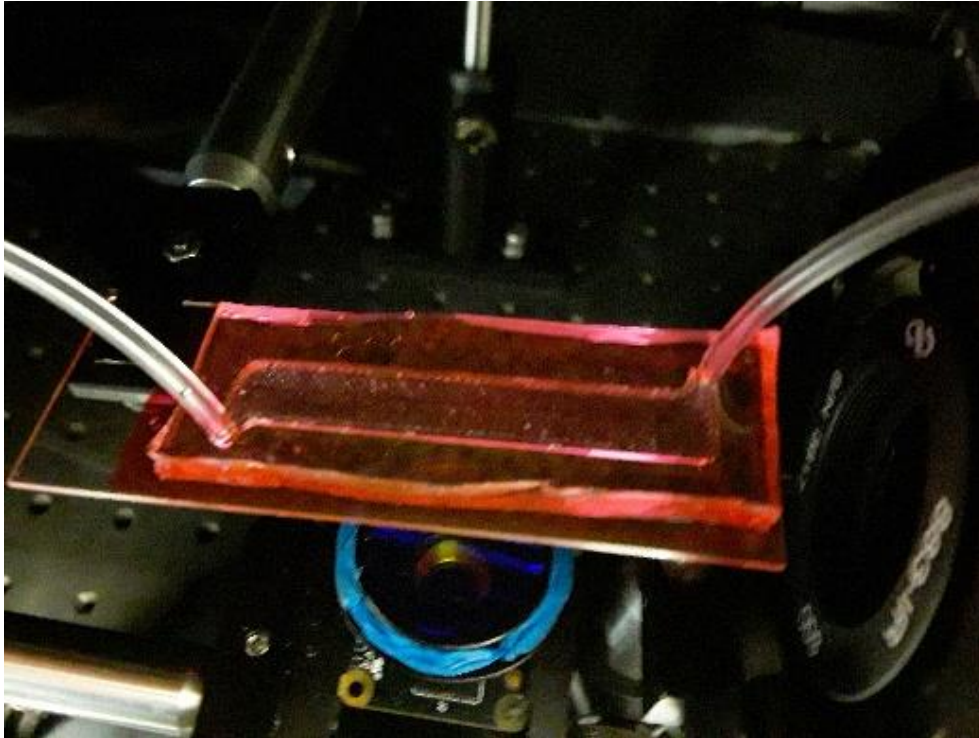
Figure 5.11 A completed sensor prepared using the paint-on coating method. The modified camera mount with the emission filter installed can be seen beneath the slide with blue sticky tack securing the emission filter in place.

A schematic view of the benchtop setup using the Raspberry Pi camera for fluorescence measurements while using the edge coupling setup is shown in the figure below. The setup can also be used in a bottom coupling scenario by raising the clamp holding the slide, allowing the light to partially reflect off the bottom of the glass substrate.
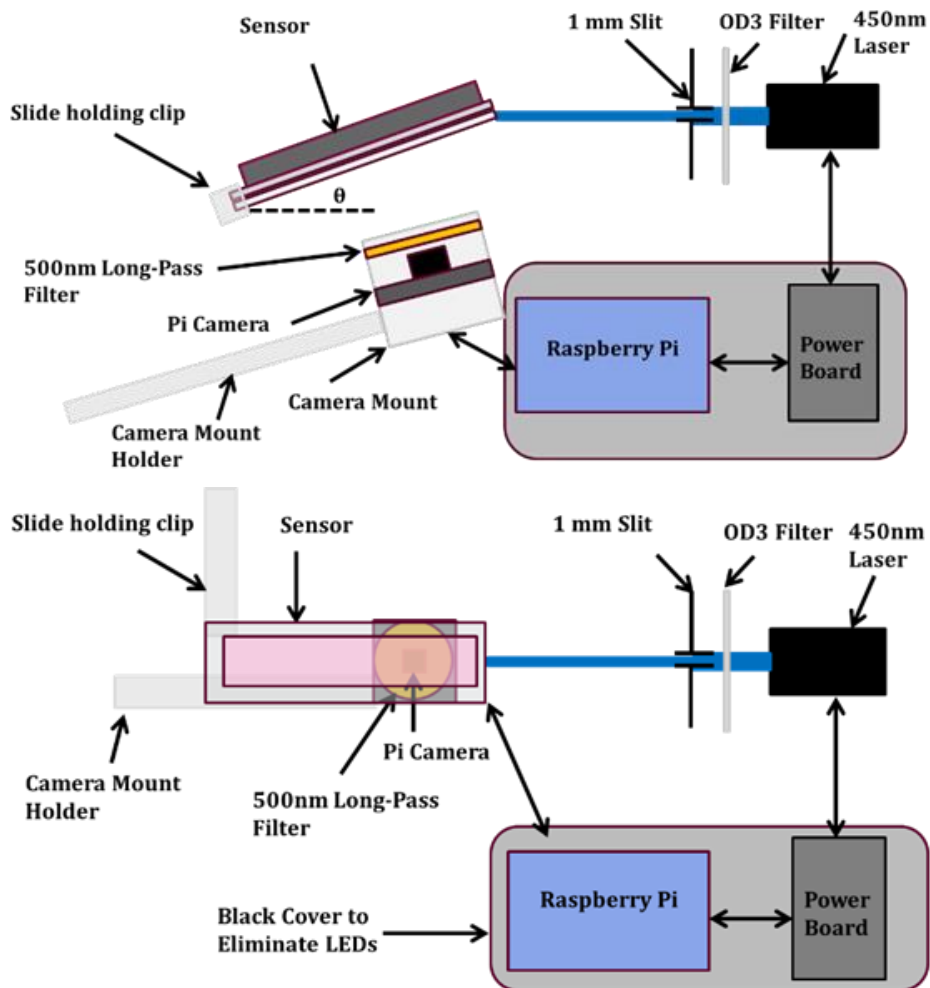
Figure 5.12   Schematics for the experimental setup used to capture fluorescence images using a Raspberry Pi camera as a detector and a 450 nm laser as the excitation source. Top) Side view schematic. Bottom) Top view schematic

5.3.4.3. pH Measurements in Eosin solutions

The measurements of pH standards in cuvettes of Eosin dye solution were conducted using the Raspberry Pi based fluorescence imaging system. The 445 nm laser was used to illuminate a mixture of Eosin-Cac in pH standards prepared in PBS in a standard 1 cm cuvette. The cuvette was held in a cube, allowing excitation from one direction and imaging from the orthogonal direction. The Raspberry Pi camera module was used as the imaging module, with a custom lens assembly incorporating the cell phone lens and emission filter.
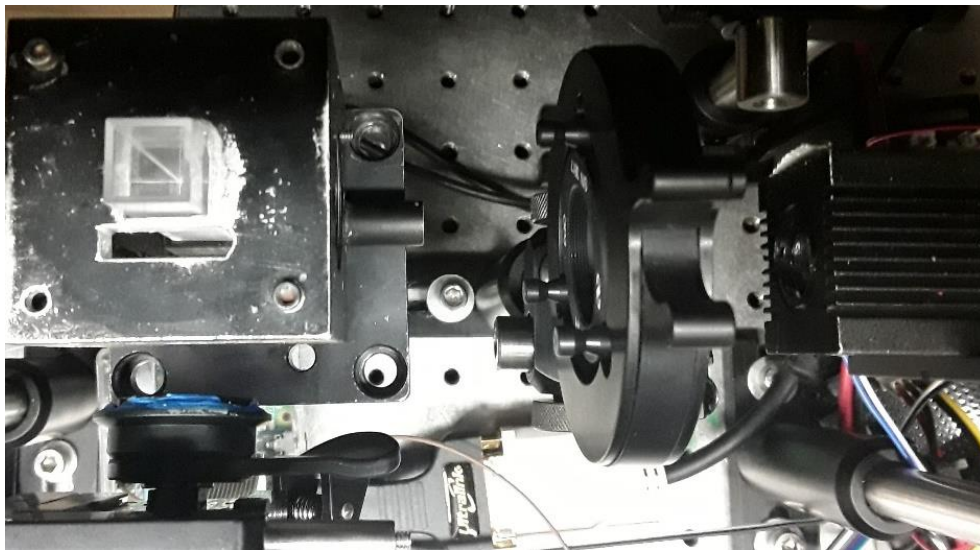
Figure 5.13   Top view of the experimental setup used to measure the fluorescence of Eosin dye mixtures directly injected into cuvettes of pH standard solutions. The cuvette of solution was covered in parafilm to prevent evaporation of solvent. The Raspberry Pi camera with the modified camera mount was used to capture the fluorescence measurements. A 450 nm laser was used to excite the dye through an OD3 filter.

A series of cuvettes were prepared, each containing a different pH standard in PBS. Initially an aliquot of Eosin dye mixture in Cac and acetone was injected into each cuvette. Each cuvette was then capped in parafilm to prevent evaporation and to allow mixing. The cuvettes were measured at the moment of dye injection and each following hour for two hours. It was found that for basic solutions the mixture of Eosin dye and Cac would gel in the cuvette, preventing accurate measurements.

Figure 5.14 A gelled Eosin dye mixture when directly injected into a cuvette of basic solution (pH > 10.5).

5.3.4.4. Direct Beam Stability Monitoring

An experiment monitoring the stability of the beam was conducted within the dark box in order to determine if the laser's stability would change over time. A photodiode (DFR-0026) was installed in the dark box and the fluorescent slide is removed. The laser was aimed directly at the photodiode through an OD3 attenuator. A sheet of kimwipe was placed over the photodiode to scatter the incident light, reducing the dependence on alignment while preventing saturation of the detector. The Raspberry Pi used to trigger the laser and the laser itself ran on separate power supplies. An Arduino UNO connected to a separate laptop computer monitored the photodiode at a rate greater than 73 Hz. The analog voltage measurement received from the photodiode over time was used as an indicator of beam stability.
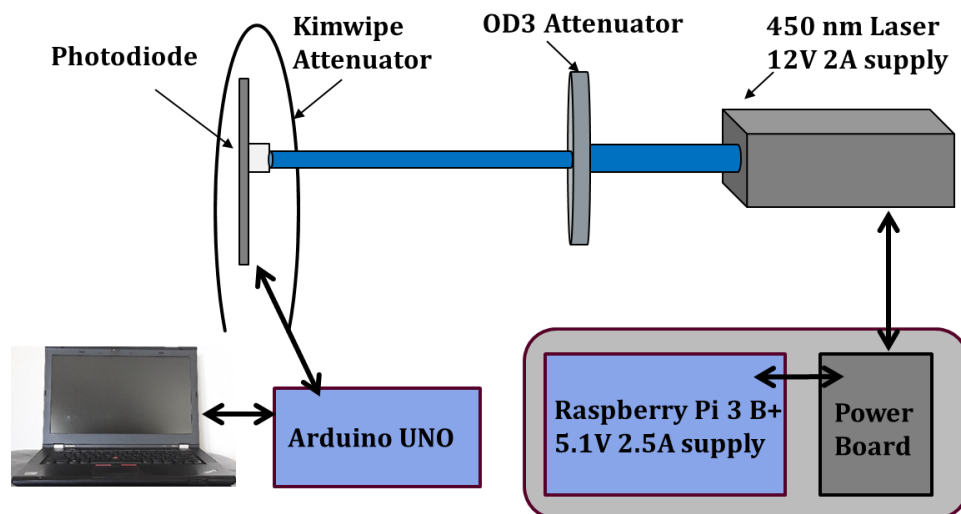
Figure 5.15   A schematic view of an experimental setup for the direct measurement of the laser's beam stability using a photodiode and a kimwipe as an attenuator.

5.3.4.5. Ammonia Standard Measurements and Optional Beam Monitoring

When measuring the ammonia standards on the optofluidic sensor a bottom edge coupling scenario was used. In this configuration, the light source produces one large spot that occupies most of the FOV of the camera module with the lens installed. The light source used was the 450 nm diode laser module triggered by the Raspberry Pi. There was a partial reflection of the light source from the bottom edge of the glass substrate that could be captured by a photodiode as an indicator of beam stability. In these measurements, the photodiode was mounted to the optical table behind a 1" lens mount supporting a kimwipe as a diffuser. An analog voltage was monitored by an Arduino UNO sampling at a rate greater than 73 Hz which is connected to a separate laptop computer. After capturing a bright calibration image and a dark image, the samples can be sequentially injected for measurement. The first injection was usually a 0 ppm ammonia control solution, such as PBS pH 7.3 or DI water. Ammonium chloride standards were injected subsequently for measurement.
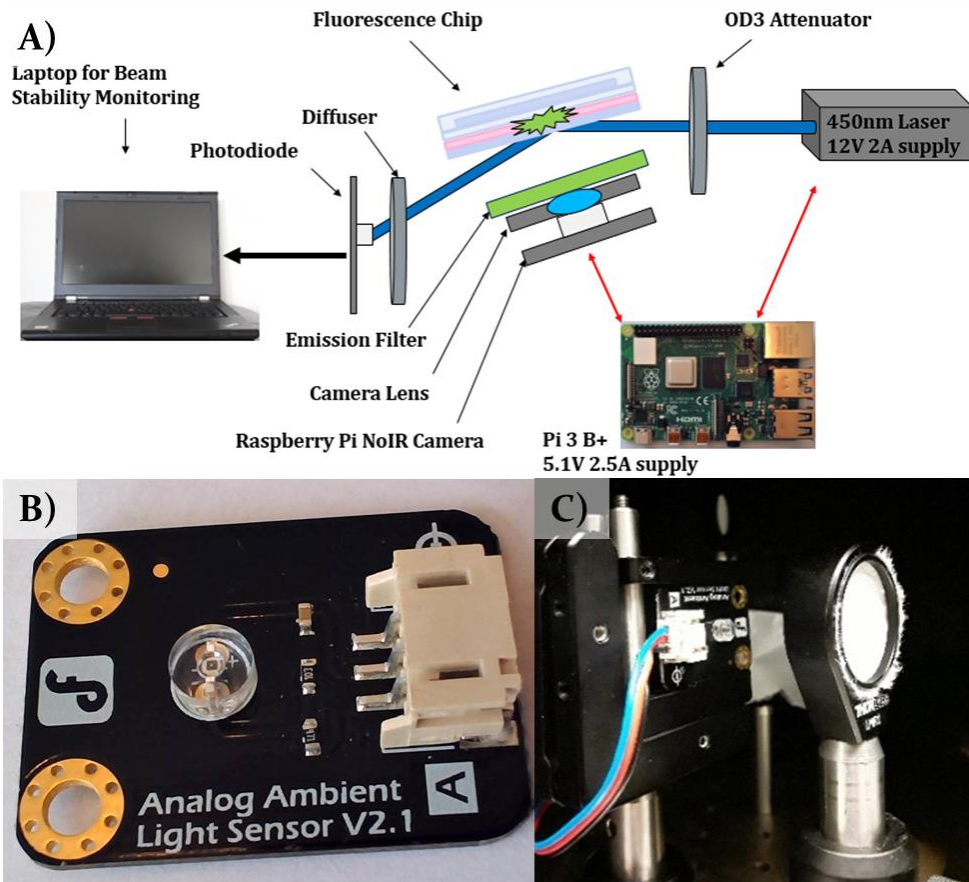
Figure 5.16   A) A schematic view of the experimental setup used to simultaneously measure the fluorescence spot and beam stability. Bottom side coupling was used while monitoring the intensity of the partial reflection from the bottom surface of the glass. B) The photodiode used to measure the laser beam stability. C) The photodiode mounted behind a lens mount with a sheet of kimwipe paper used as an attenuator / diffuser to prevent photodiode saturation during measurements.

5.3.4.6. Measurement Procedure

Exposure settings are set to obtain reasonable signal to noise ratio and relatively low dark noise. Future optimization of detector settings could further improve sensitivity. A custom python script was used to capture test images in YUV format. The Y (brightness) data was used to create a grayscale pixel intensity image for analysis. The average intensity of all pixels was calculated and stored as a measure of image brightness with respect to fluorescence intensity, effectively operating the camera as a power meter. The value of the brightest pixel was also recorded as an

indicator of saturation in the image. The user may define laser power, ISO, desired frame rate, or exposure time, and the number of exposures to average per measurement. For an exposure series the user can also define the number of measurements and the time interval between measurements.

A bright image was captured in air with the laser power settings fixed by the user. Five exposure cycles were performed until the camera white balance gain settled and exposure settings were fixed. In this way, air may always be used as the standard to calibrate the exposure settings; however, there was a risk that the location of the fluorescent spot would move when a sample was injected due to the difference in the refractive index of the sample and air. A dark image is captured in air. The average pixel intensity may be subtracted as average dark noise from subsequent exposures.

A standard background water sample was measured, usually DI water with a neutral pH, or PBS pH 7.3. This value was used as the reference intensity (Io) value. The sample was injected into the tubing inserted in one of the holes of the PDMS channel cap. Approximately 2 mL of sample was injected using a syringe to flush the chamber and clear the tubing. Subsequent sample measurement intensities were reported as Io/I, the relative change in fluorescence intensity with respect to sample concentration. Sample measurements may be captured over time to record the amount of time required to reach a steady state measurement.

5.4. FLUORESCENCE CHIP READER PROTOTYPE

The optofluidic chip reader prototype was built inside of a prefabricated plastic carrying case. The dark walls of the enclosure prevent the ambient light from interfering with measurements and also protects potential observers from accidentally viewing the light source. The interior of the enclosure is separated into two compartments by black foam board, cut to fit the profile of the walls to remove gaps where light can leak between compartments. In the current prototype, laser safety glasses are included within the case with the power supply, required syringes, and waste containers. In the electronics compartment, the laser module, computer module, voltage regulators, and custom circuit board are housed. The Raspberry Pi computer module was installed such that it can easily be connected to a monitor and keyboard for direct control when troubleshooting or updating the system manually.
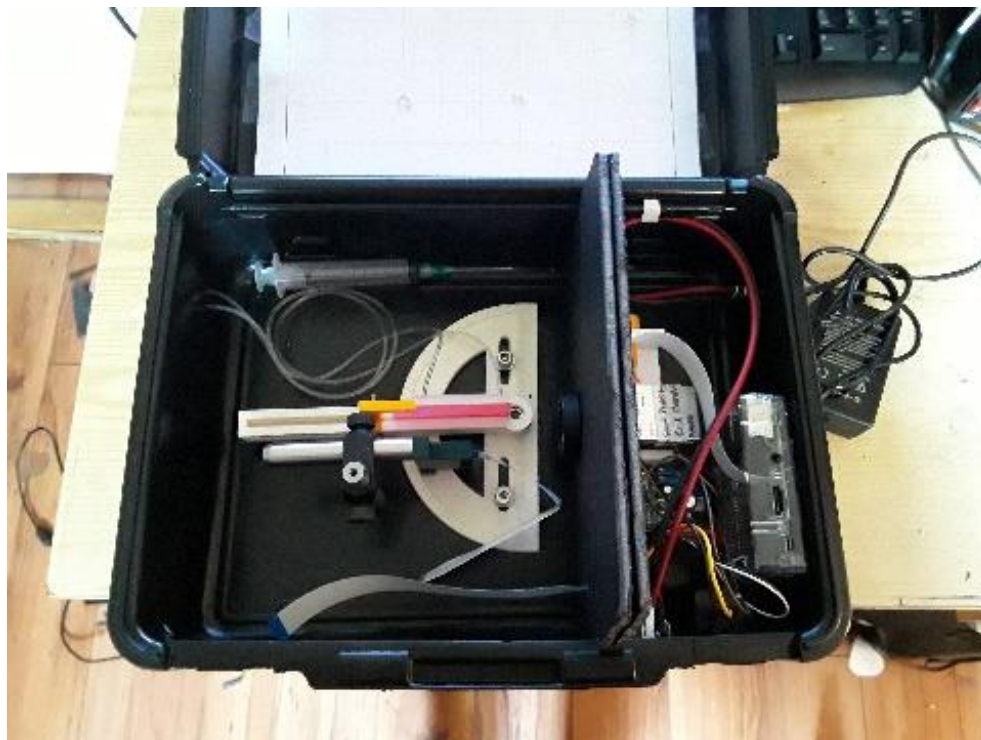
Figure 5.17   The prototype fluorescence chip reader interior with a measurement compartment (left), and an electronics compartment (right).

The measurement compartment houses the optofluidic fluorescence sensor to be measured, the alignment clamp, and the camera module. Tubing connected to the inlet and outlet ports of the installed fluorescence sensor module are routed out of the back of the enclosure, so that samples can be injected from outside of the device when prompted by the software during measurements. The angle on the clamp can be adjusted to control the incident angle of light and the sensor to select the ideal angle of incidence for each sensor module installed. The clamp can also translate laterally allowing the user to switch between edge coupling and bottom side coupling as desired. A camera mount was used to align the camera with the fluorescence sensor. An OD3 filter is currently installed between the light source port and the sensor to reduce the intensity of the laser. In future versions of the device, stable laser dimming can be achieved and the filter can be removed or replaced with a less expensive alternative.

Figure 5.18 The measurement compartment inside of the portable prototype fluorescence chip reader.

In future versions of the device, additional safety features including an interlock switch on the lid and a high moisture interlock should be added. The fluid management components can be modified with pumps and valves to automate the sample collection and injection. A battery pack can be added to allow the system to run without access to mains power, given the occasion to recharge the system. The current software developed may be modified to make remote control of the system easier. With these changes, the next version of the optofluidic chip reader should only need to be opened to replace the sensitive chip, to conduct periodic maintenance, and to perform calibration.

Figure 5.19 The closed portable prototype fluorescence chip reader.

5.5.   RESULTS

5.5.1. Eosin Emission Spectrum and Orange Glow

A portable spectrophotometer (Newport OSM 400) was used to experimentally characterize the light sources employed and the emission spectrum of the Eosin dye films. The investigated films were not sensitized or coated in a silicone membrane for these measurements. The emission filter from Semrock (609-181) was determined by measuring a halogen lamp with and without the filter in place. The edge of the filter was found to be 515 nm. The measured spectrum of the 470 nm LED from Thorlabs (DC3100) had a peak at 461.4 nm with a full width at half maximum (FWHM) of 19.1 nm and did not appear to have any significant output in the pass band of the Semrock emission filter. The 470 nm LED was used as the excitation source for the Eosin film measurements. After measuring the Eosin film, the 470 nm LED was measured as a reflection from an uncoated glass slide to measure the transmittance of the LED through the emission filter. The peak emission of the Eosin dye in Cac was measured as 559 nm. It should be noted that there appeared to be at least two narrow spikes in the measured emission spectrum at 571.6 nm and 633.5 nm. The very narrow profile

suggests it may be contamination from the light source or an LED indicator rather than characteristic features of the dye. The measurements of the 470 nm source through the emission filter demonstrate the same sharp peak at 633.5 nm; however, the 561.6 nm spike cannot be seen. After, the 445 nm laser diode was obtained and measured over a narrower range of wavelengths, extending to 450 nm, and was not used to characterize the fluorescence emission of Eosin dye. The measured spectrum of the 445 nm laser diode has a peak at 442.7 nm with a FWHM of 1.5 nm.
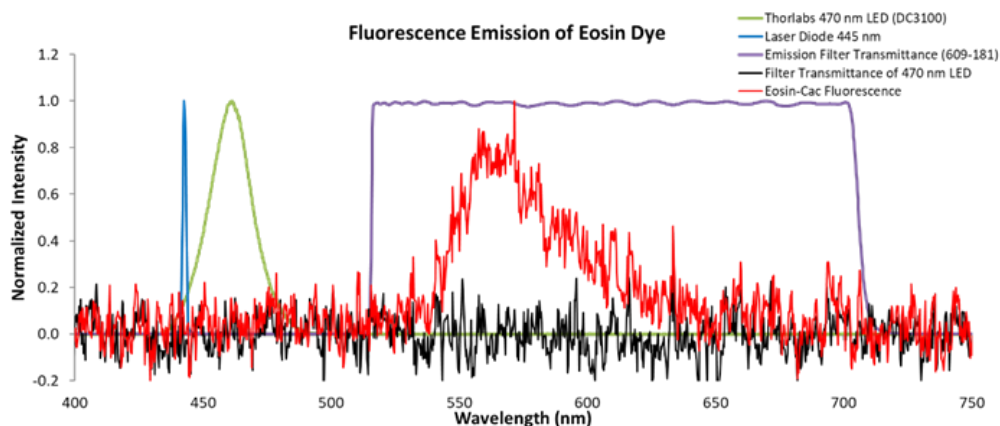
Figure 5.20   Spectral profiles of light sources, filters, and dyes. Measurements were conducted using the Newport OSM 400 fiber spectrometer. The 470 nm LED spectrum has a peak of 461 nm and FWHM of 19 nm. The 445 nm laser has a peak at 443 nm and a FWHM of 1.5 nm. The Semrock emission filter (609-181) was measured through a broadband halogen light source. The emission spectrum of the Eosin dye was measured with a peak emission between 559 and 569 nm. The glass slide control was measured. Note: the two very narrow peaks at 571 and 633 nm in the dye spectrum are not likely fluorescence and could be the light source contamination.

   It was noticed during measurements of Eosin-coated slides that there was an orange glow at the edges of the slide. The glow was seen due to the TIR of light within the slide that is focused out of the edges. The orange glow is visible in room lighting, indicating that the color is likely source light after the absorbance of blue wavelengths by the Eosin film, rather than fluorescence generated by a contaminant. This would indicate that the orange observed in measurement images is likely contamination from the light source used or other indicators that are not completely shielded within the enclosure.
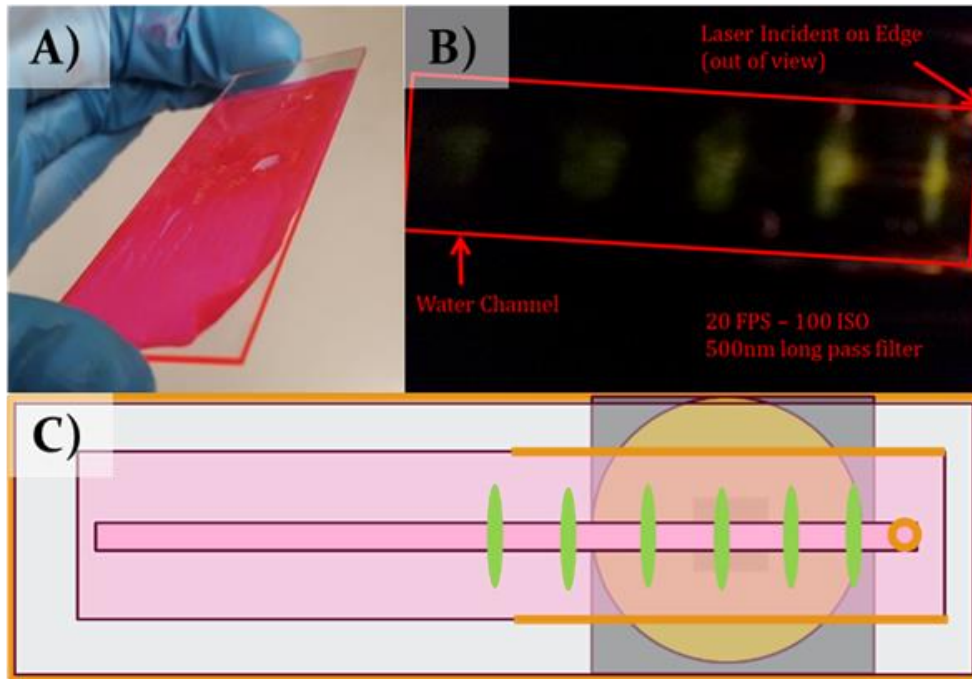
Figure 5.21 A) Delaminated Eosin film after sensitization. The pink and orange glow observed at the edge of the slide is likely internally reflected room lighting after absorbance of blue wavelengths by the Eosin film. B) Fluorescence from complete sensor structure with Eosin coating and water channel cap. C) A schematic view demonstrating relative position and FOV of the camera with respect to the sensor module. Regions where an orange glow were observed during excitation are highlighted.

If the cause of the orange glow is a low intensity undesired wavelength from the light source then it is expected to be a steady state contributor to the background image intensity. Without eliminating the wavelength from the image, its influence on image brightness calculations can be reduced by focusing on regions of the image that do not demonstrate significant scattering. With the addition of the camera lens on the Raspberry Pi camera module features are more easily resolved from the bottom of the slide. Using image segmentation, a region of interest can be selected that excludes the slide and channel edges from calculations.
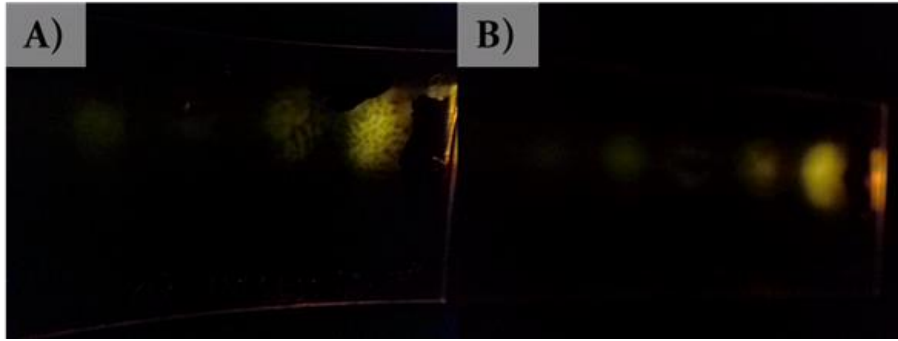
Figure 5.22 Eosin-coated glass fluorescence after adding the camera module with an additional lens (A), and before adding the lens (B).

5.5.2. Eosin Emission Intensity

A power meter probe was used to determine the linearity of the Eosin film emission intensity with respect to the intensity of the 470 nm LED (Thorlabs DC3100). The Semrock emission filter was installed in front of the power meter probe. A dark measurement was recorded before each exposure of the slide. The optical power observed with respect to the current used to drive the light source is used to determine the linearity of the response. Earlier, it was determined that the 470 nm LED brightness was linearly proportional to the driving current. The 470 nm LED was measured through the emission filter with a piece of uncoated glass installed in place of the Eosin film. It was found that there was a small amount of source light that can be transmitted through the emission filter from the 470 nm LED.
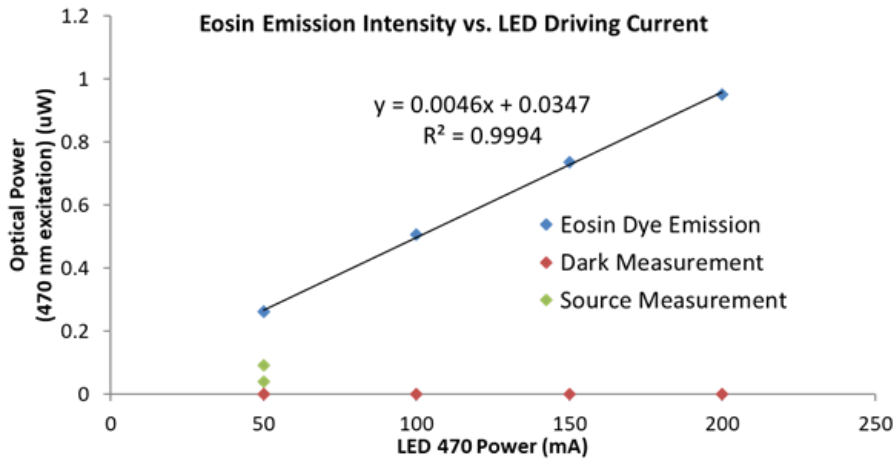
Figure 5.23 Optical power meter measurements of filtered excitation light and Eosin dye mixture fluorescence. Dark measurement is the average optical

power within the dark box with the source light turned off. Source measurement is the average optical power through the emission filter with an uncoated glass slide installed. Eosin dye emission is the optical power observed through the emission filter with the coated glass slide installed.

5.5.3. Scientific Imaging and YUV Images

A Raspberry Pi camera module was used for the fluorescence intensity images of the Eosin-coated slides. This camera module was selected because several pixels can be averaged in a single image providing a measure of intensity and standard deviation in each exposure. In theory, the camera module would provide advantages by extending the device lifetime by reducing the exposure time required for each measurement, while also preserving the spatial information that can be used for image segmentation. Recently, the use of Raspberry Pi cameras has become more common for experimental measurements (17). It is critical that the gains are fixed when performing scientific imaging with a low-cost camera module. Adjustment of gains will influence the sensitivity of pixels to various wavelengths, affecting the color of captured images and image brightness estimates.

Figure 5.24 Examples of white balance gain adjustment and influence on images (18).

Initially, a test is performed to see how the gains drift when free to adjust while the camera is viewing Eosin fluorescence. For longer exposure times, the FOV of the camera changes as a larger number of pixels are used. The gains appear to converge for longer exposure times where the frame brightness is greater. The FOV is reduced and the image becomes size 640 x 480 pixels for framerates greater than 45 FPS. As the exposure times are reduced and the frame brightness decreases, the gains appear to diverge.
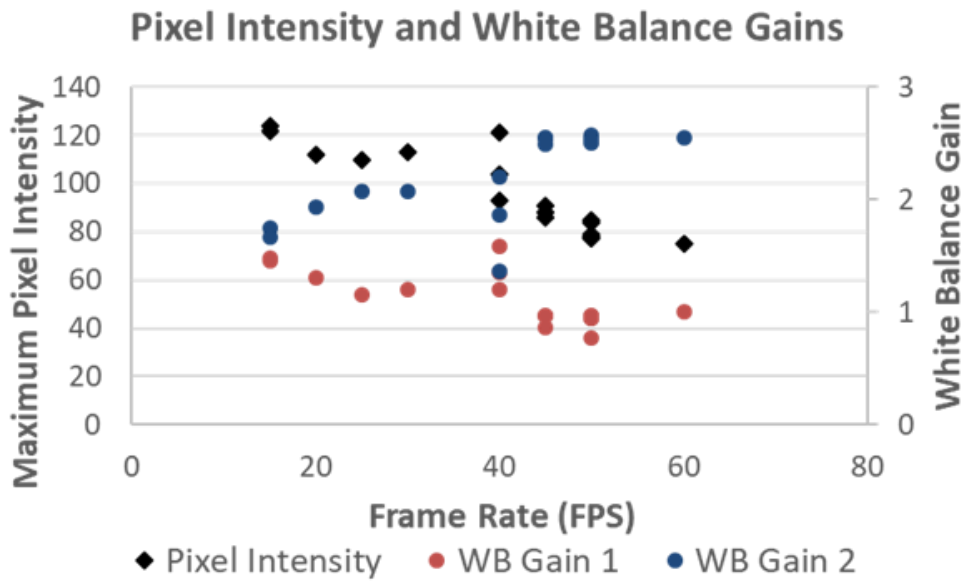
Figure 5.25 Observations of gain adjustment with respect to exposure time settings. The FOV of the camera is reduced for framerates greater than 40 FPS. The brightest pixel intensity and white balance gains are shown with respect to frame rate.

In order to measure the frame brightness independently of the color of the image, the YUV format is considered. The YUV color space separates the brightness (Y-dimension) from the chrominance (U, V dimensions) (19). An array is sized to store the Y data while rejecting the UV data. An example of a Y-dimension array captured from an Eosin fluorescence image is shown as a relative intensity heat map in the following figure. From the Y-dimension the relative intensity of the image can be determined while preserving the spatial information in the image without being influenced by the color of the image. This method captures a standard RGB image, a complete YUV image, and the Y data array, so that the color information is still available for each measurement if required.
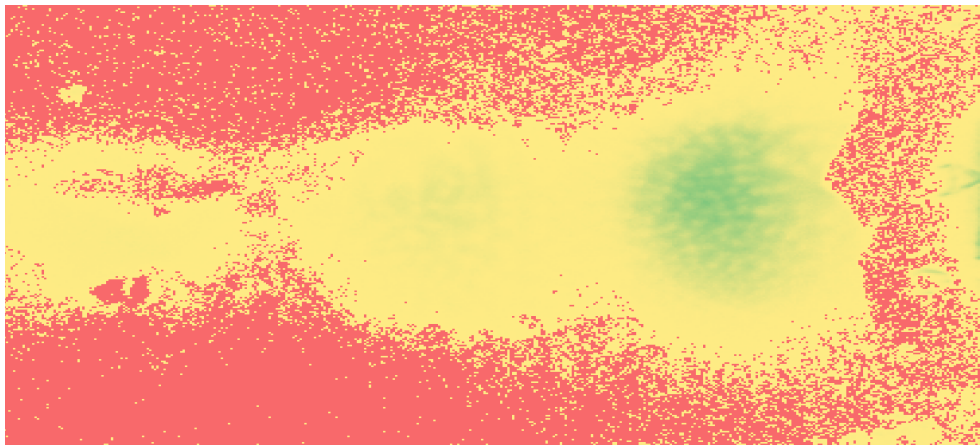
Figure 5.26 A heat map of raw pixel intensity measurements captured by the Raspberry Pi camera module when using an edge coupling setup. Red pixels indicate low intensity values and green pixels represent high intensity values. The incident light is injected from the right edge of the device.

5.5.4. pH Measurements using Eosin Dye Solutions

Eosin dye mixtures with Cac were mixed with pH standard solutions prepared in PBS to assess the change in fluorescence intensity with respect to pH. The Raspberry Pi camera module was used to capture the fluorescence intensity images. Solutions with pH greater than 10.5 gelled when the dye mixture was added and could not be measured. The results do not indicate a significant change in fluorescence intensity until the most basic solutions were measured. There appears to be a positive slope relating pH to frame brightness, but the images were not consistent enough to predict pH with acceptable accuracy. It was determined that measurements of sensitized Eosin films would be the most effective to observe an increase in fluorescence intensity with the deprotonation of the Eosin dye.
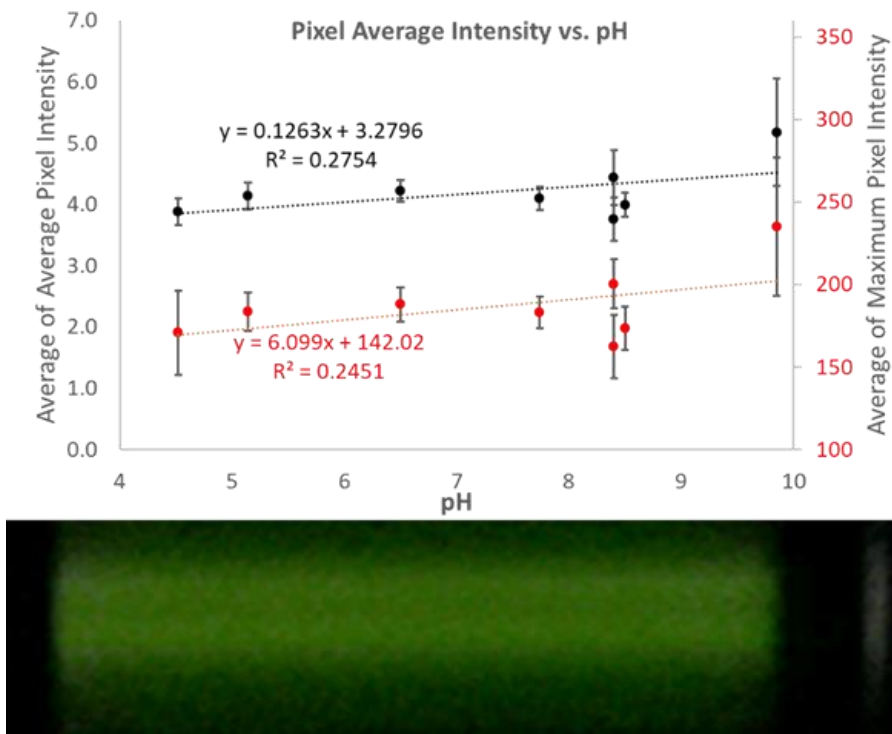
Figure 5.27 Top) Fluorescence intensity measurements of pH standard solutions with Eosin dye mixtures over time. Exposures were captured initially and each hour for 2 hours. The average of measurements over 2 hours are presented. Bottom) Fluorescence from a 1 cm cuvette of Eosin dye mixture in pH standards using the Raspberry Pi camera module.

5.5.5. Eosin Exposure Testing

An exposure test was conducted to determine if the brightness of the Eosin dye changes significantly due to photobleaching over the course of an experiment. Over a course of approximately 40 minutes of continuous exposure to the 445 nm laser, the fluorescence intensity images had not changed significantly. The results indicate that when performing measurements where the laser brightness is stable, the fluorescence intensity of the dye should not be affected by accumulated exposure to the light source over the course of an experiment.
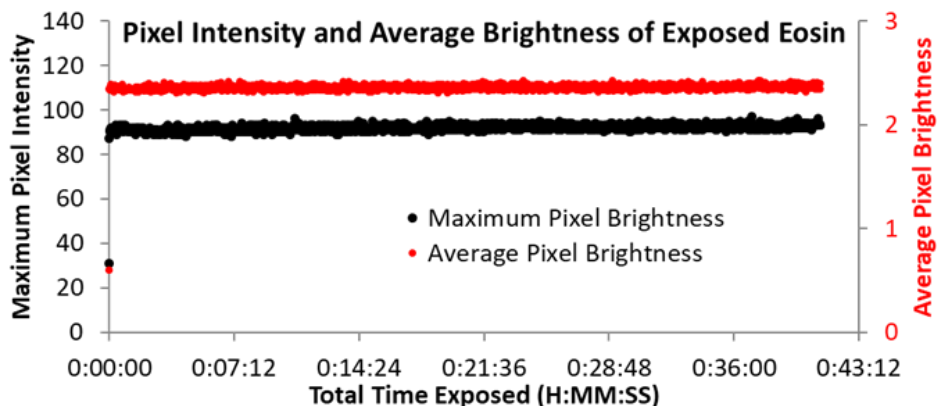
Figure 5.28   The average and maximum pixel intensity observed over continuous exposure.

5.5.6. pH Measurements with Eosin-coated Slides

pH standard solutions were measured on an unsensitized Eosin-coated slide. The difference between the measurements with air and water samples were clearly visible, and an air bubble developing in the channel was identified during measurements of tap water. Although a relationship between image brightness and pH could not be established, the brightest pixel did appear to increase significantly upon the injection of the most basic solution. The earlier result of measurements of Eosin solutions suggested that with an unsensitized coating the device may only respond to the most basic solution. The result may indicate that the brightest point in the image remains in the field of view, but the number of pixels detecting fluorescent light may not be consistent. This may occur if the incident angle is not set appropriately, allowing the incident light to couple to the water channel, causing the measurement to become sensitive to changes in the refractive index of the sample.
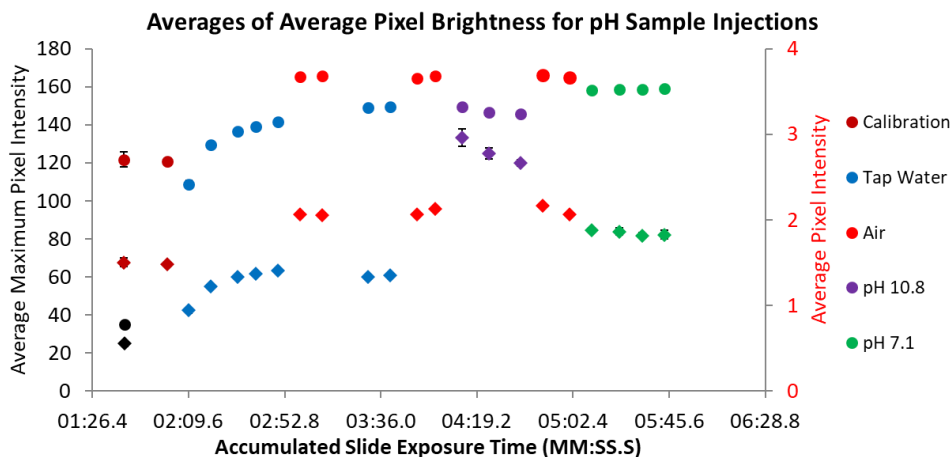
Figure 5.29 The average image brightness from Eosin dye over a series of sample injections. Circular markers represent average frame intensities, and diamond markers are average maximum pixel values. Error bars are shown as the standard deviation of exposures at each time point. The device was not sensitized nor protected with a silicone membrane.

   The experiment is repeated with a series of injections while also comparing single exposures, accumulated exposures, and different exposure times. The series of injections were pH 6.3, pH 10.5, pH 6.3, pH 8.5, and Air. The results for single exposures with a short exposure time do not indicate a change over time with respect to pH, but the measurement in air was significantly more intense. With accumulations of exposures, there also does not appear to be a change in average pixel intensity with respect to pH.
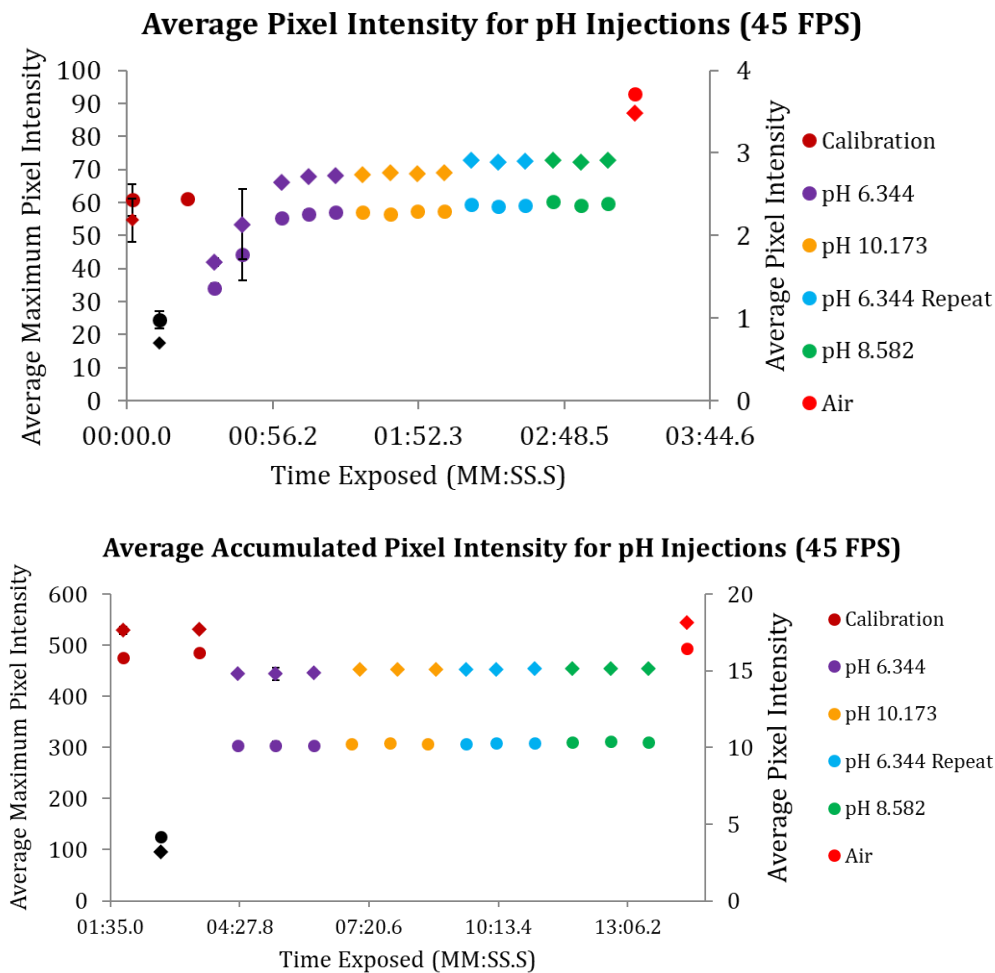
Figure 5.30 The average pixel intensities for pH samples. pH samples are measured every five minutes over a series of injections. The average maximum pixel intensities are shown as points, and the average pixel intensities are shown as diamonds. Top) The average maximum and average pixel intensities calculated over five exposures for each measurement. Vertical error bars are displayed with one standard deviation of five measurements. Bottom) The average image brightness and brightest pixel intensity of Eosin fluorescence images for a series of pH injections. Accumulations of 5 exposures are used with a frame rate of 45 FPS for each exposure.

When the experiment is repeated with longer exposure times, there still does not appear to be a relationship between frame brightness and pH.
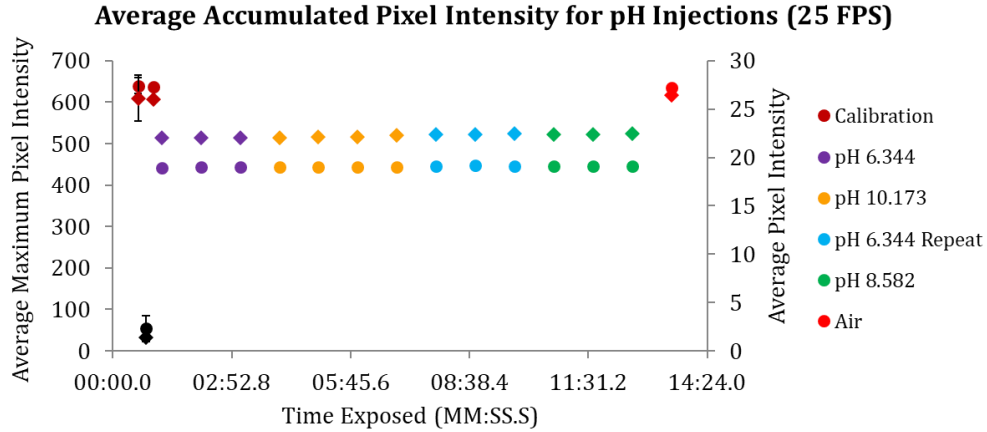
Figure 5.31 The average image brightness (diamond) and brightest pixel intensity (points) of Eosin fluorescence images for a series of pH injections. The accumulations of five exposures are used with a frame rate of 25 FPS for each exposure.

5.5.7. Laser Dimming Frequency and Image Stability

Instead of running the light source at full power and attenuating the source through a filter, laser diming should be applied in the final remote monitoring platform to optimize power consumption and reduce cost. The laser brightness must be stable during the series of exposures for measurements to be consistent. To prevent variations in brightness from appearing in measurement images, the frequency of the signal sent to the laser must be greater than the frame rate. The minimum required frequency to switch the laser to capture a desired number of cycles in each exposure depends on the desired exposure time or framerate for each measurement.
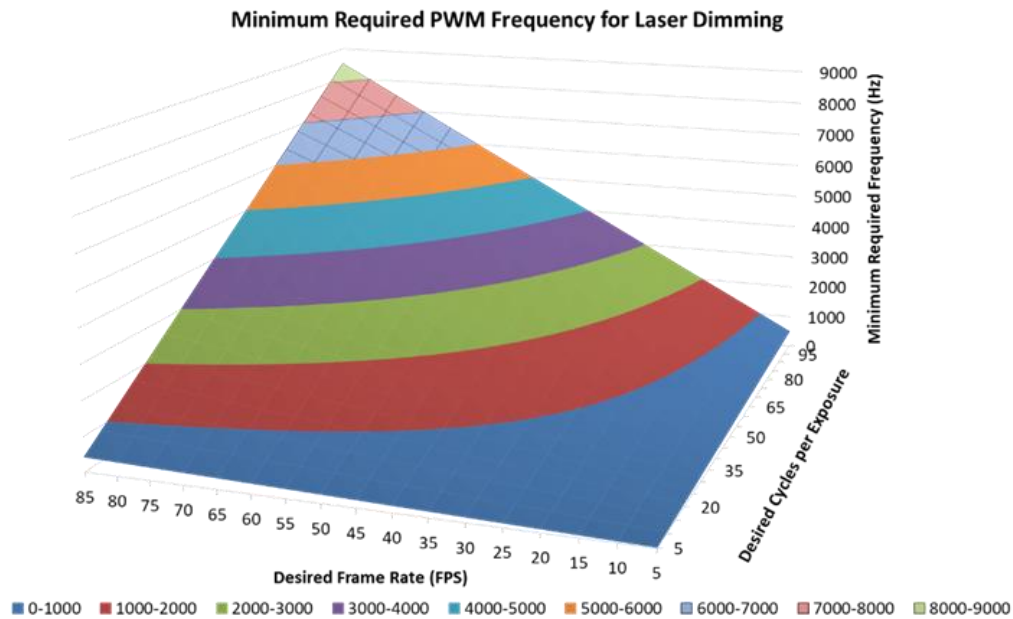
Figure 5.32 A surface plot demonstrating the minimum required PWM frequency to avoid observing ripples in light source intensity. The minimum required frequency depends on the measurement exposure time and the number of pulse cycles to sample per exposure.

The maximum usable frequency of the PWM signal sent to the laser, without visible fluctuations in brightness, is dependent on the duty cycle of the laser. The brightness of the laser appears to be linearly proportional to the average voltage of the PWM signal sent to the laser. The duty cycle and driving frequency can be set to achieve the desired level of laser dimming, while preventing the oscillations from being captured by the camera module.
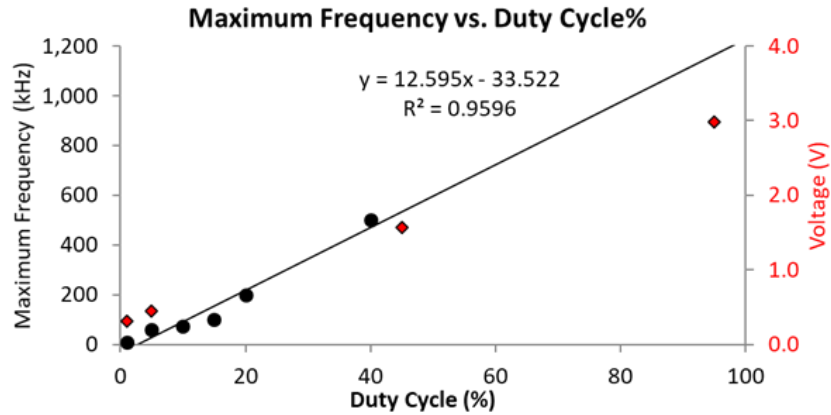
Figure 5.33 The maximum usable frequency with respect to duty cycle for software-based laser dimming is shown in black. The DC Voltage measurement of the PWM signal sent to laser driver from Raspberry Pi with respect to duty cycle is shown in red.

5.5.8. Ammonia Measurements with Eosin-coated Slides

An Eosin-coated slide was used to measure a series of ammonia standards. The slide was sensitized but not protected with a silicone membrane. The measurements were performed in the dark enclosure. No correlation was found between the frame brightness and the pH, but an oscillation may be evident in the background. The result may have suggested that the sensor was only sensing the bulk pH because a protective silicone membrane was not used.

Figure 5.34 The average maximum pixel intensity (circular markers), and average pixel intensity (diamond markers) observed from Eosin dye
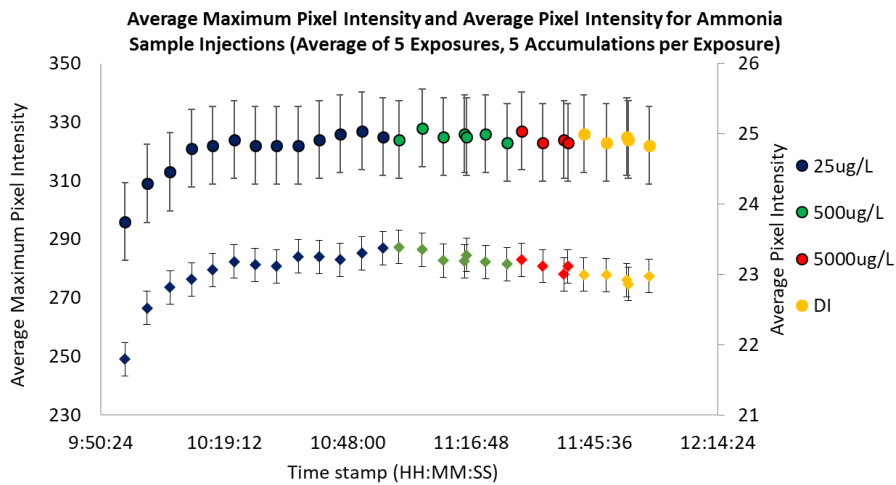
fluorescence for a series of ammonia standard solution measurements. Five exposures are accumulated and the average is reported with a standard deviation rather than as the accumulated values.

A sensitized Eosin-coated slide with a thin film of PDMS as a protective layer was used to test the ammonia standards. This device was sensitized in a 1x MSA solution and top coated in a thin film of PDMS. The device did not respond to ammonia standards and there were observations of changes in the position of the fluorescence spot within the water channel. The results possibly indicate an unstable light source (flickering), or that the film was not permeable to ammonia and another polymer matrix should be tested.
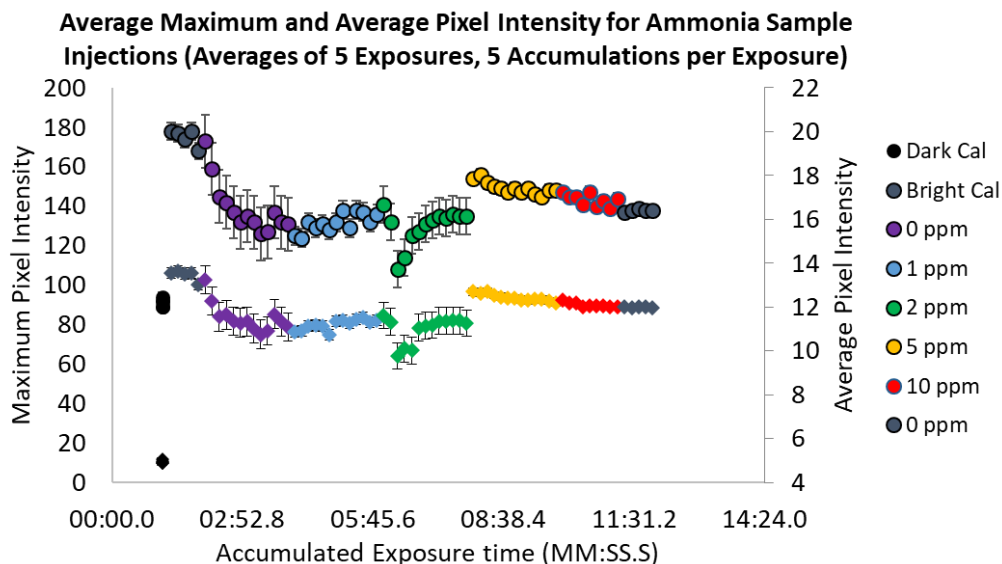
Figure 5.35 The average maximum pixel intensity (circular markers) and average pixel intensity (diamond markers) observed from Eosin dye fluorescence for a series of ammonia standard solution measurements. Five exposures were accumulated and the average is reported with a standard deviation rather than as the accumulated values.

The previous experiment was repeated with the cleanest unused fabricated device, sensitized in a 1x MSA solution. The frame rate was reduced to 45 FPS to increase the frame brightness while maintaining the FOV and spatial resolution. Once again, the results were inconclusive and there may have been evidence of an oscillation in the background.
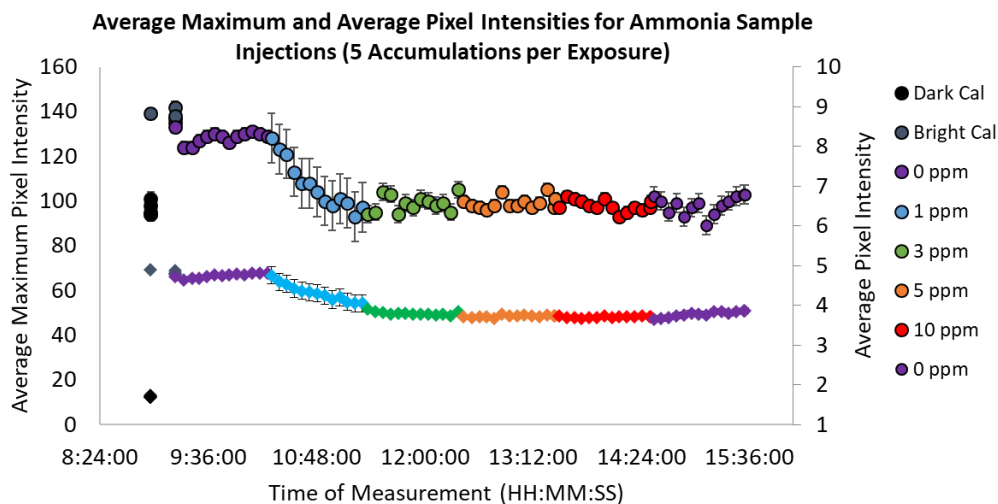
Figure 5.36 The average maximum pixel intensity (circular markers) and the average pixel intensity (diamond markers) observed from Eosin dye fluorescence for a series of ammonia standard solution injections. Five exposures were accumulated and the average is reported with a standard deviation rather than as the accumulated values.

Once the final fabrication method with the new materials is implemented, new optofluidic devices were prepared. The Eosin dye was immobilized in a Cacp polymer instead of Cac, and the sensitized films were protected by a thin film of RG01 silicone diluted in heptane. These devices were measured with a 100 ms delay between the laser activation and measurement. The measurement results did not indicate a relationship between the frame brightness and pH, but the variation in frame intensity values for each scene indicates a measurement error. The error may be caused by the refractive index of the sample, causing movement of the fluorescent spot, or instability of the light source.
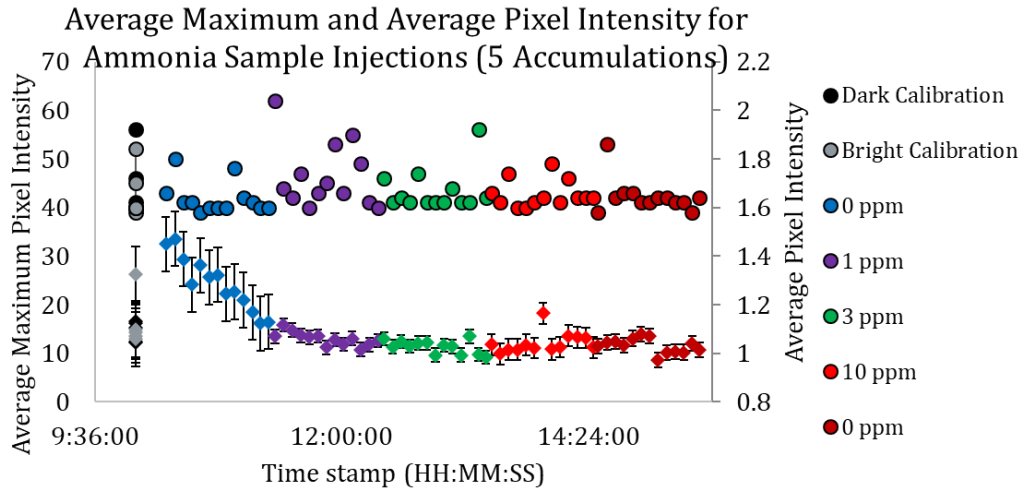
Figure 5.37 The average maximum pixel intensity (circular markers) and the average pixel intensity (diamond markers) observed from Eosin dye fluorescence for a series of ammonia standard solution injections. Five exposures were accumulated and the average is reported with a standard deviation rather than as the accumulated values.

5.5.9. Investigating Beam Stability During Measurements

A photodiode was installed within the enclosure to monitor the stability of the laser over time using an Arduino UNO. The Arduino was able to report analog voltage measurements from the photodiode at a rate greater than 73 Hz at a baud rate of 9600. The result indicates that at a measurement frame rate of 45 FPS the photodiode should be able to detect any flicker in the laser stability during the exposure.
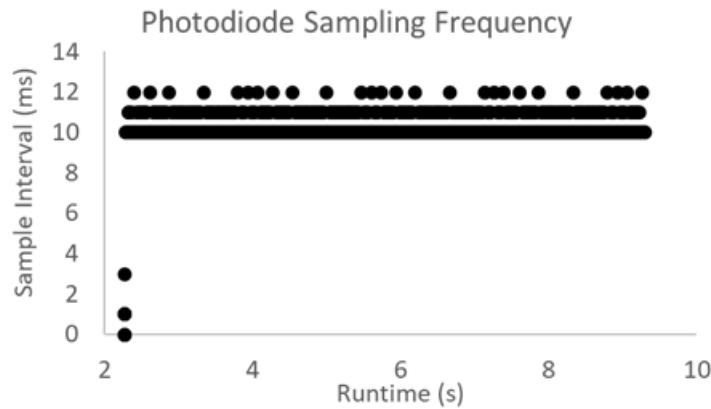
Figure 5.38   The photodiode measurement rate from an Arduino UNO running at the maximum speed while reporting with a baud rate of 9600. The largest time between measurements is less than 13 ms.

The laser was monitored when left on at 100% power for 1 H continuously. The output power of the laser did not appear to increase significantly over a 1 H period. At the beginning and end of the experiment, a series of pulses were sent to the laser to determine the time it takes to reach a steady state output. The results indicate that the laser can take up to 1 second to reach a steady state brightness. Until now, the laser delay setting in the software had been limited to 100 ms, indicating that the laser would not have been stable for any measurements conducted thus far using the current software.
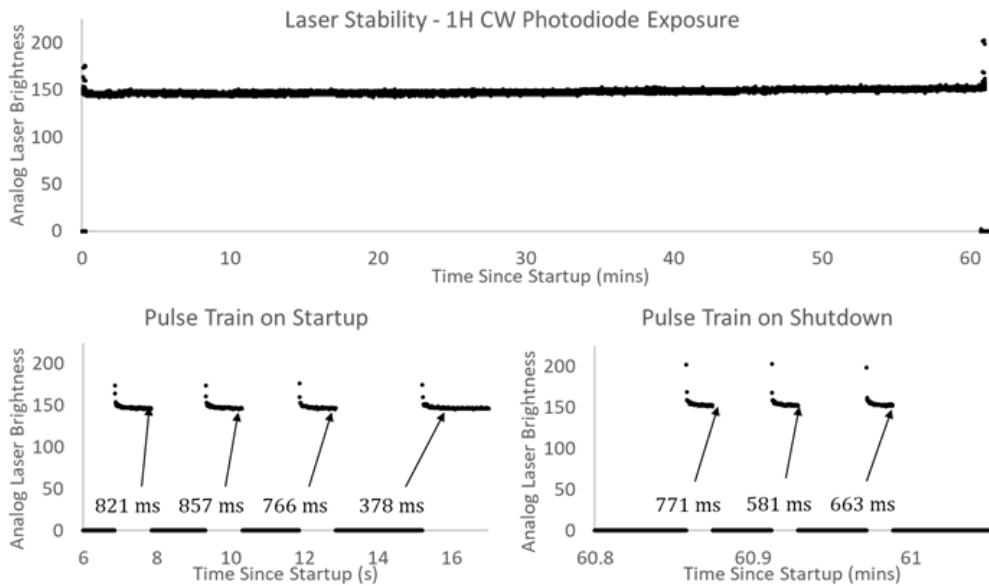
Figure 5.39 Laser stability observed by a photodiode for a continuous exposure over one hour at the maximum frame rate. Bottom) Laser stability observed during a train of pulses at the start and end of the exposure series. The result indicates that even after an hour, the laser has a stable output after ~1 second of activation.

The laser delay was updated to 2 seconds and the ammonia exposure series was repeated while monitoring the laser beam stability from a partial reflection at the bottom of the glass slide. The result from the beam monitor indicates that the laser should now be stable when the sample measurements are captured. It is interesting to see the oscillating pattern in the initial peak detected from the laser as it turns on, which is similar to the pattern seen in the earlier experimental measurements.
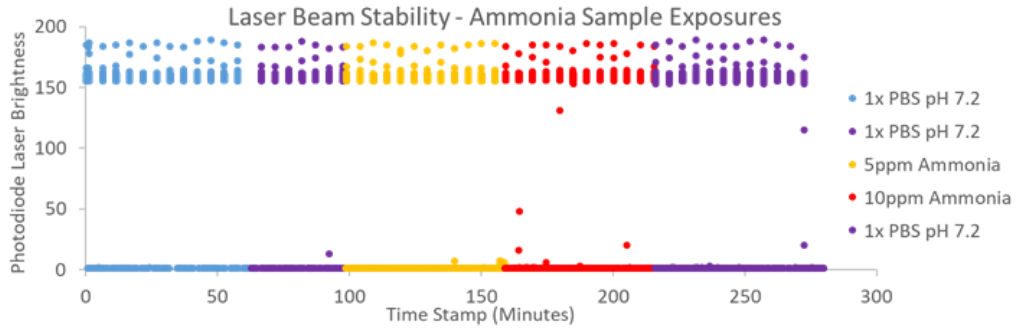
Figure 5.40 Laser brightness over time during a series of injections of ammonia standards. A spike is observed from the laser that decays to a stable brightness within ~1 second of activation. Interestingly, the brightest peak observed during the spikes appear to be oscillating.

When focusing on the beam stability monitor during each of the measurements, the average beam intensity did not change significantly over the course of the experiment. The only point where the beam stability monitor detected a slight increase in the beam intensity was during the most concentrated ammonia sample injection. The result suggests that the photodiode may actually be able to detect an increase in brightness due to the generated fluorescence.
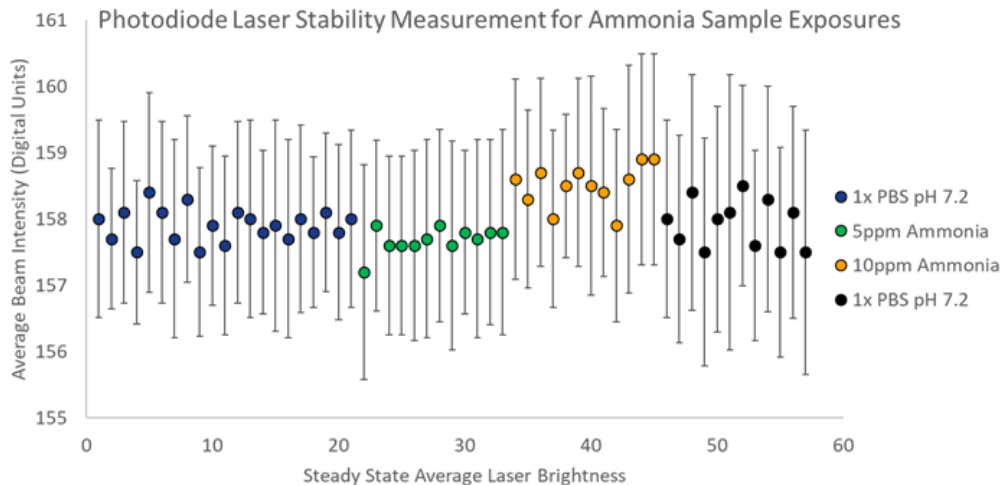
Figure 5.41 Laser stability observed by a photodiode capturing the partial reflection of the laser from the bottom of a sensor during a series of injections of ammonia standards through a kimwipe. The laser brightness does not change by more than 5% over the period of an hour. The photodiode may have captured fluorescence emission from the sensor during the injection of the most concentrated ammonia standard.

156

5.5.10. Final Ammonia Testing and Moving Spot

The ammonia standard measurements were conducted again after extending the laser delay time to two seconds to ensure that the beam was stable before capturing a measurement. A new device prepared using Eosin in Cacp was sensitized and coated in a protective membrane of RG01 silicone. Unfortunately, the camera module was not able to detect a change in frame brightness with respect to ammonia concentration. The results either suggest that the sensor was not sensitive to ammonia, or that the position of the spot was not consistent between sample injections.
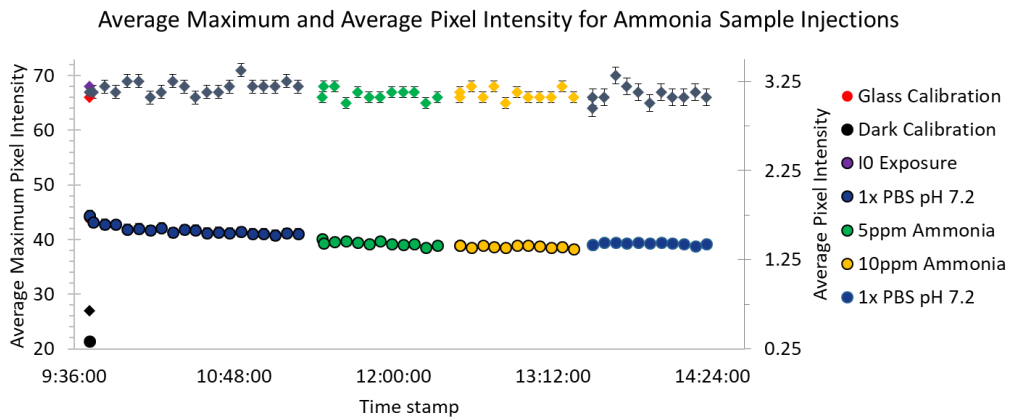
Figure 5.42   The average pixel intensity (circular markers) and average maximum pixel intensity (diamond markers) observed from Eosin film fluorescence for a series of injections of ammonia standards.

The standard RGB images were investigated to determine if there were differences in the scene between measurements. It was determined that the spot that is in focus when there is air in the channel during calibration shifts when a sample is injected due to the difference in refractive index (RI). If the incident angle is not set while a calibration solution is in the water channel, then the type of TIR observed can change once a sample is injected. The results indicate that the incident angle should be carefully selected based on the RI of the sample, or the coupling mechanism should be adjusted to increase the coupling efficiency from the bottom side of the slide to increase intensity while reducing spot movement.
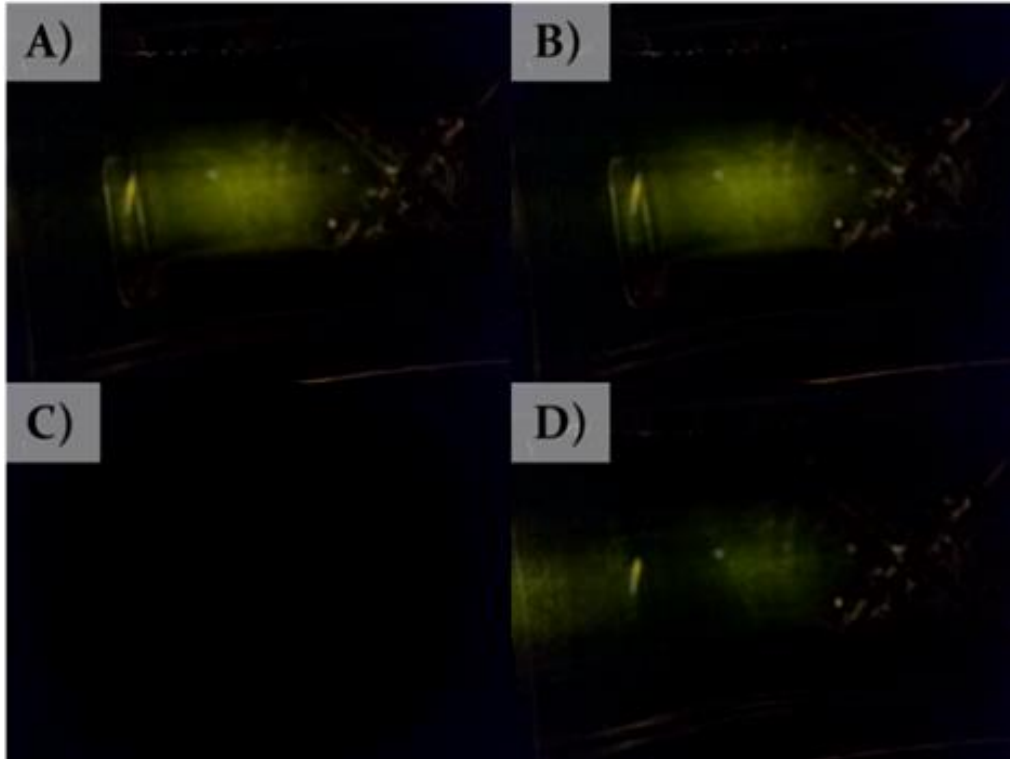
Figure 5.43 Comparison of Eosin dye fluorescence measurement images during bottom side coupling. A) I_0 image captured in air. B) Source calibration image in air. C) Dark calibration image. D) Measurement after injection of 1x PBS pH 7.2. It can be seen that the location of the spot moves when the sample is injected. The change in the RI at the interface of the silicone layer and the water sample allows the type of TIR observed to change at this angle of excitation, resulting in a reduction of frame intensity.

5.5.11. TIR Model Applied to Ammonia Sensor

In our earlier work, a 3D model was developed to predict the optical path of incident light in multilayered TIR sensors using different coupling scenarios. The model was validated by comparison with experimental results. A series of equations were produced in Excel to independently check the model explaining the relationship between sensitivity enhancement and the path length of incident light in the sensitive volume. It was determined that the model of the incident light source significantly influences the relative sensitivity observed at each incident angle, particularly in cases where the incident light was focused into the sensor substrate. The variability was caused by the range of incident angles introduced into the device, and the relative intensity of each incident angle.
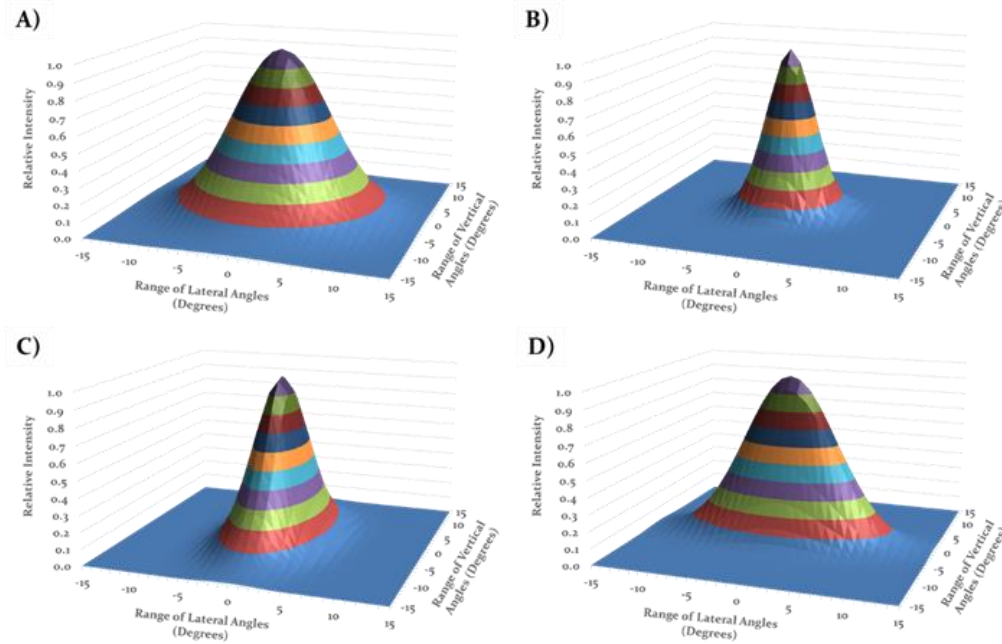
Figure 5.44 Examples of normalized relative light source emission profiles for a circular and an elliptical spatial profile. The spatial profile of the light source and intensity distribution across the spatial profile determines the range of incident angles introduced to the sensor and the relative intensity of light entering at each angle. A) Gaussian spot, B) Compressed Gaussian spot, C) Gaussian ellipse compressed in the lateral axis, D) Gaussian ellipse compressed in the vertical axis.

The Excel calculations were adjusted to consider the optical properties of the multilayered ammonia sensor structure. The sensitivity of the device was expected to be the greatest when the path length of incident light in the sensitive volume was optimized. Four types of TIR were identified by the model depending on the incident angle and coupling scenario used. Type I TIR occurred where the incident light is confined within the glass substrate and only evanescent waves can contribute to fluorescence generation. Type II TIR occurred where the light is confined within the sensitive volume and glass substrate, and the greatest device sensitivity was expected. In Type III TIR, the incident light can escape the sensitive volume into the silicone membrane but it will not couple to the water channel. In Type IV TIR, the incident light was confined within all layers of the device and can reflect within all layers between the glass substrate and PDMS channel cap.
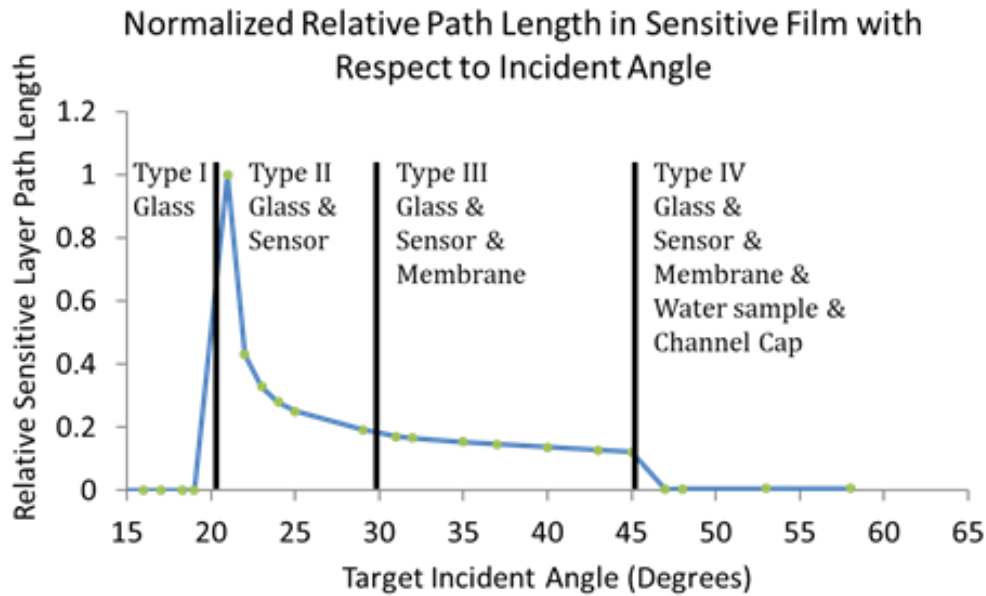
Figure 5.45 Observable types of TIR based on model results. Type I TIR occurs where the excitation light is contained in the glass substrate resulting in excitation by evanescent wave only. Type II TIR contains the light within the sensitive volume and glass and results in the greatest sensitivity. Type III TIR allows the light to enter the protective silicone membrane but prevents coupling to the water sample. Type IV TIR allows the light to enter the water channel and channel cap.

5.6. DISCUSSION

The multilayered sensor design for ammonia sensing is similar to the previously tested optofluidic dissolved oxygen sensor (16), with different optical properties and an additional silicone membrane between the sensitive film and the water sample. Calculations based on the TIR model developed in recent work (16) indicates that Type II reflections should produce the greatest device sensitivity when the incident angle is above 21°, when using the edge coupling method. Measurements of the 470 nm light source reflecting off an uncoated glass through the emission filter show a narrow peak at 633 nm in the pass band of the emission filter. The 450 nm laser was not measured over a large enough dynamic range to capture output in the pass band of the filter. The Eosin dye dissolved in Cac had a strong green emission with a narrow peak at 571 nm, indicating possible contamination in the light source or a bimodal emission due to protonated and non-protonated dye. Observations of orange glow at the slide edges in

room lighting suggest that the color is from ambient lighting after absorbance of blue wavelengths rather than fluorescence. If the orange is from the light source, then it should have a constant contribution to the background of the measurement. The brightness of the fluorescence emission from the dye was found to increase linearly with light source intensity.

A Raspberry Pi camera module was employed as a detector for fluorescence intensity measurements. The motivation for using the Raspberry Pi camera was the capability to configure and capture consistent images, and the suitability for controlling the remote monitoring system with the computer module. The Raspberry Pi Camera module can be configured and controlled easily using a python code that can be iteratively improved. The Raspberry Pi computer is well suited for remotely controlling experimental setups and for integrating devices into remote monitoring networks. Upon experimenting with the Raspberry Pi camera module, it was found that the maximum resolution and FOV depend on the frame rate or exposure time used. The white balance gains can be fixed to prevent adjusting the image brightness during measurements. To demonstrate the capability of the setup for scientific imaging, the system is set to capture RGB images (color information), YUV images (brightness and color), and arrays of pixel intensity values (brightness).

A prototype portable optofluidic chip reader was developed based on the experimental setup with the Raspberry Pi camera module. The system was built into a portable case with a measurement compartment and an electronics compartment. The entire device can be operated over a wireless network. Fluid management components including valves and pumps should be added in future versions for automated sampling capability.

The initial measurements of pH standards on the Eosin-coated slides was not successful and led to a series of troubleshooting tests to improve the light source module, sensor module, and detector module. The sensor module was improved by refining the fabrication method, leading to far more consistent devices.

The detector module was refined by adding a camera lens to better resolve the fluorescence spots in the measurement images, and the code was adjusted to allow the user to average a series of accumulations for each measurement. Significant issues persisted with the light source module,

including power management problems causing flickering, and inconsistent brightness during measurements. The frame intensity estimates of the same scene reported by the custom software was different when the measurement was triggered from a different button, revealing that the delay time between laser activation and camera exposure was not the same. Further investigation revealed that the laser requires about one second to stabilize. Fortunately, the additional tests also suggest that the laser stability does not change significantly once it is turned on for extended periods of time.

The Eosin dye was investigated by measuring dye mixtures with pH standards prepared in cuvettes. Only a 100 ms delay was used when capturing these images, and it is now known that the laser would not have been stable during these measurements. Nevertheless, it is interesting to see that the final sample with the greatest pH demonstrated the greatest frame brightness result. Once the laser delay was adjusted to two seconds to ensure the laser was stable before capturing images another series of ammonia standards were measured on a newly refined device. Although the camera module did not detect an increase in fluorescence with respect to ammonia concentration, the beam stability monitor did detect a slight increase in brightness when the greatest concentration of ammonia was injected. A closer inspection of the RGB images taken from the series of measurements indicated that the location of the spot moved after calibration, such that the brightest pixels were no longer in the field of view. A video captured during a sample injection shows the movement of the spot in real time as the sample is injected and removed. The moving spot may be addressed by adjusting the incident angle or changing the coupling strategy to employ a prism.

The demonstration of direct detection of ammonia in water samples based on the fluorescence of Eosin-coated glass slides would suggest that the sensor module could be used for the assessment of ammonia in ground water. The device should also demonstrate insensitivity to sample background pH. Enzymatic sensors could be developed to measure other potential targets by generating compounds that can be detected using sensitive fluorescent films. Such future designs could be applicable to urine analysis towards improving Smart toilets for PoC diagnostics.

5.7. CONCLUSIONS

To conclude, progress has been made towards the development of an optofluidic fluorescence sensor for the detection of ammonia in water samples. The structure of the multilayered sensor is based on the optofluidic dissolved oxygen sensor presented in earlier work. A prototype portable optofluidic chip reading platform was developed for remotely conducting fluorescence measurements of TIR sensors. A Raspberry Pi, camera module, and diode laser are employed to reduce the cost of the complete sensing system. The Raspberry Pi camera is configured to capture consistent scientific images in order to use the frame brightness as a measure of fluorescence intensity. With the addition of a low-cost cellphone camera lens, the fluorescence spots can be magnified to occupy more pixels on the detector while preserving the spatial information. Initial measurements of pH standards and ammonia standards were unsuccessful; however, two significant causes have been identified. First, it was discovered that the laser delay time was not consistent between calibration and measurement functions. Furthermore, it was found that the laser required almost one second to reach a stable output, while the measurement function only allowed the laser to stabilize for 100 ms. After correcting the laser delay time to two seconds and implementing a beam stability monitor to detect any fluctuations, it was determined that the light source should be stable during measurements. The second contributor to the poor signal intensity was the excitation scenario and incident angle. Once the camera lens was added to the detector, the bottom edge coupling configuration was used instead of the side edge coupling to produce one large spot as opposed to several smaller spots. The concept was to improve sensitivity by causing a greater number of detector pixels to observe the fluorescence at the expense of spot brightness due to a large partial reflection lost at the bottom edge of the glass substrate. To compensate for the low intensity of the single large spot, the incident angle was altered to reduce the partial reflection and improve brightness. When the sample was injected, the light was able to couple to the water channel at this incident angle, causing the spot brightness to change and the spot position to move. The effect of the moving spot was captured in a video during sample injection in real time. It is suggested to use a prism to improve the bottom edge coupling setup in future experiments. The combination of improving light source stability and maintaining Type II reflections in the device should result in consistent quantitative fluorescence intensity images.

Interestingly enough, during this final experiment the laser stability monitor registered a slight increase in intensity during the injection of the strongest ammonia standard. Alternative detectors that are less sensitive to the location of fluorescence generation may be employed in future experiments to validate quantitative fluorescence intensity images.

With the successful demonstration of sensitivity to ammonia, in future work this technology has great potential in several fluid-sensing applications. The method is compatible with several microfluidic technologies, including lensless microscopy and algae detection with particle tracking. The ability to integrate this method with several other modules gives it great potential towards enabling environmental and point of care diagnostic sensing. With the integration of pumps and valves for automated sampling, the system may be used to assess water samples during field tests.

5.8.   NEXT STEPS

Employing a prism-assisted coupling scheme is expected to improve the coupling efficiency by reducing partial reflection losses, resulting in a brighter fluorescent spot that will not couple to the water channel. The stability of the light source can be improved during activation by implementing a soft start and limiting the current available to the laser. Improvements in light source stability will prevent damage to the laser while enabling PWM dimming to reduce dependence on ND filters. The laser source may also be replaced with an LED for further cost reduction. The LED may need to be transmitted through an optical filter to prevent the detector from sensing the excitation light directly. Greater device sensitivity and improved response times may be achieved by employing thinner films for the sensitive layer and protective silicone membrane if they can be reproduced uniformly and reliably. Using the current coating procedures films prepared with a target thickness less than $10\mu m$ were susceptible to tearing and could not be reliably reproduced. Adjusting the composition of the polymer containing the sensitive dye may also lead to further reduction of sensitive film thickness and improved response times. Adjusting the pH of the sensitive film during the sensitization stage using different concentrations of MSA may influence the sensitive range of the sensor, where greater concentrations of ammonia will be required to influence the local pH of a more acidic sensitive film. The relationship between sensitized film pH and sensitive range should be established. The gains for the camera

module may be optimized rather than fixed in future versions of the device to provide greater sensitivity to changes in scene brightness without introducing noise into the image. The camera should be aligned such that the fluorescent signal occupies as much of the field of view of the sensor as possible. If spatial information is not required, the camera module may be replaced with a photodiode or power meter for cost reduction. The detector selected should demonstrate high sensitivity to the wavelengths of light emitted by the fluorescent dye, and should have a large active area and acceptance angle in order to improve the collection of fluorescence by the detector. Future versions of the water channel design should implement a reference channel for calibration, and additional measurement channels that can be accessed when biofouling or photobleaching occurs to extend the time required between maintenance periods.

In the next experiments, ammonia standards will be monitored after installing a prism for bottom side coupling. The measurements will verify that the spot is not moving as samples are injected and that the light source is stable. The frame brightness measurements will be verified using a photodiode or similar filtered detector. Once ammonia standards are measured in water, they can be measured as standards in a range of pH buffers. This would show the influence of background pH on ammonia sensor response or verify that background pH does not interfere with measurements. The portable optofluidic chip reading device can be modified to include a prism and used for field testing demonstrations once the measurement method is refined.
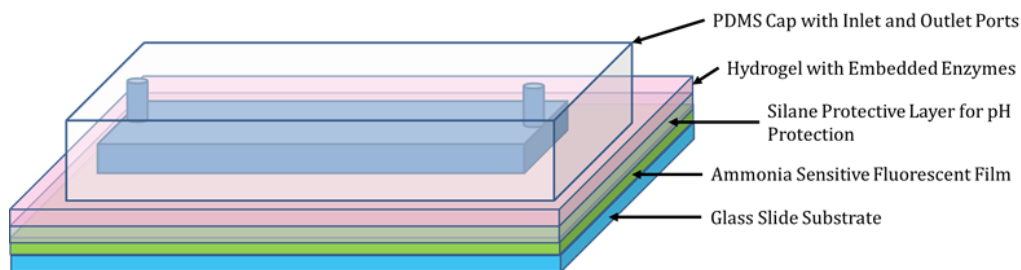
Figure 5.46 Future structure of the next generation of optofluidic fluorescence sensors. A hydrogel layer entrapping enzymes is applied between the fluid channel and the ammonia sensitive film.

Additional analytes can be indirectly detected as ammonia in future versions of these devices. Films incorporating an enzyme immobilized in a hydrogel can be prepared to generate compounds such as urea, that can be

indirectly determined as ammonia. In situations where a hydrogel layer is coated above the silicone membrane the refractive index difference at the interface of the membrane and hydrogel. At the ideal incident angle the light is confined within the sensitive volume and reflects at the interface of the sensing layer and silicone membrane. If the light does not couple to the hydrogel layer, then it is not expected to contribute to the attenuation of excitation light or the distance between reflection points. Alternatively, an enzymatic reaction generating ammonia can be conducted outside of the channel before sample injection. In this remote sensing platform, the next generation of sensitive films are demonstrated as a concept figure.
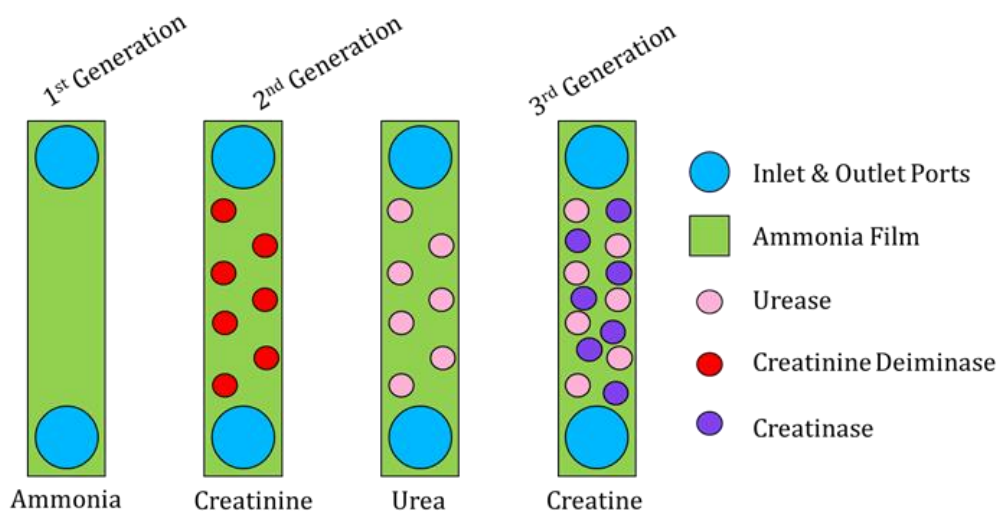
Figure 5.47 A concept of the next generation of sensitive films for remote monitoring platforms. In future versions of this device, the enzymes will be immobilized in a hydrogel layer coated above the protective silicone layer.

Funding Sources

Acknowledgements

Disclosures

References

[1]   Koda E, Osinski P, Sieczka A, Wychowaniak D. Areal distribution of ammonium contamination of soil-water environment in the vicinity of old municipal landfill site with vertical barrier. Water (Switzerland). 2015;7(6):2656–72.

[2]   Wakida FT, Lerner DN. Non-agricultural sources of groundwater nitrate: A review and case study. Water Res. 2005;39(1):3–16.

[3]   Vodyanitskii YN. Biochemical processes in soil and groundwater contaminated by leachates from municipal landfills (Mini review). Ann Agrar Sci [Internet]. 2016;14(3):249–56. Available from: http://dx.doi.org/10.1016/j.aasci.2016.07.009

[4]   Duong HD, Rhee J Il. Development of ratiometric fluorescent biosensors for the determination of creatine and creatinine in urine. Sensors (Switzerland). 2017;17(11).

[5]   Wyss M, Kaddurah-Daouk R. Creatine and Creatinine Metabolism. Physiol Rev. 2000;80(3):1107–213.

[6]   Clark JF. Creatine and phosphocreatine: A review of their use in exercise and sport. J Athl Train. 1997;32(1):45–51.

[7]   Wang S, Li X, Yang J, Yang X, Hou F, Chen Z. Rapid determination of creatinine in human urine by microchip electrophoresis with LED induced fluorescence detection. Chromatographia. 2012;75(21–22):1287–93.

[8]   Grady T, Butler T, MacCraith BD, Diamond D, Anthony McKervey M. Optical Sensor for Gaseous Ammonia With Tuneable Sensitivity.

Analyst [Internet]. 1997;122(8):803–6. Available from: http://xlink.rsc.org/?DOI=a701343d

[9]   Tymecki Ł, Pokrzywnicka M, Koncki R. Paired emitter detector diode (PEDD)-based photometry - An alternative approach. Analyst. 2008;133(11):1501–4.

[10]   O'Toole M, Diamond D. Absorbance Based Light Emitting Diode Optical Sensors and Sensing Devices. Sensors [Internet]. 2008 Apr 7;8(4):2453–79. Available from: http://www.mdpi.com/1424-8220/8/4/2453

[11]   Shepherd RL, Yerazunis WS, Lau KT, Diamond D. Low-Cost Surface-Mount LED Gas Sensor. IEEE Sens J [Internet]. 2006 Aug;6(4):861–6. Available from: http://ieeexplore.ieee.org/document/1661564/

[12]   Lau KT, Edwards S, Diamond D. Solid-state ammonia sensor based on Berthelot's reaction. Sensors Actuators, B Chem. 2004;98(1):12–7.

[13]   Waich K, Mayr T, Klimant I. Talanta Fluorescence sensors for trace monitoring of dissolved ammonia. Talanta. 2008;77:66–72.

[14]   Deng S, Doherty W, McAuliffe MAP, Salaj-Kosla U, Lewis L, Huyet G. A low-cost, portable optical sensing system with wireless communication compatible of real-time and remote detection of dissolved ammonia. Vol. 6, Photonic Sensors. 2016.

[15]   Levinský P, Kalvoda L, Aubrecht J, Fojtíková J. Diffusion of ammonia gas in PDMS characterized by ATR spectroscopy. Photonics, Devices, Syst VI. 2015;9450(January 2015):94500D.

[16]   Mahoney EJ, Hsu H-H (Leo), Du F, Xiong B, Selvaganapathy PR, Fang Q. Optofluidic Dissolved Oxygen Sensing With Sensitivity Enhancement Through Multiple Reflections. IEEE Sens J [Internet]. 2019 Nov 15;19(22):10452–60. Available from: https://ieeexplore.ieee.org/document/8786822/

[17]   Pagnutti M, Ryan RE, Cazenavette G, Gold M, Harlan R, Leggett E, et al. Laying the foundation to use Raspberry Pi 3 V2 camera module imagery for scientific and engineering purposes. J Electron Imaging. 2017;26(1):013014.

[18]   Theilr. unbalanced quartet [Internet]. 2008. Available from:
        https://www.flickr.com/photos/theilr/2439734701/in/photostream/

[19]   Ozcan A, Mcleod E. Lensless Imaging and Sensing.
        2016;(January):77–102.

Chapter 6

Conclusions and Next Steps

6.1. SUMMARY

Fluorescence-based optofluidic sensors have been demonstrated for the detection of dissolved analytes for applications in point of care diagnostics (1–3) and water quality monitoring (4–7). Sensitivity enhancement techniques such as Total Internal Reflection have been proven effective at improving the signal from fluorescence-based sensors (8,9). In this dissertation, an optical dissolved oxygen sensor was experimentally optimized and used as the foundation for a simplified numerical model to explain the mechanism of sensitivity enhancement. A 3D optical model was developed and validated based on the experiment results to identify significant design parameters impacting TIR in sensitivity enhancement. The model was applied to the ongoing development of an optofluidic ammonia sensor.

Efforts to assist the aging in place of older adults are expected to improve health and quality of life while reducing the demand for medical resources. Longitudinal health monitoring is particularly useful in order to identify the development of chronic disease and monitor response to treatment. The successful development of point of care (PoC) diagnostic devices capable of continuous non-invasive monitoring could provide an alternative to routine diagnostic testing from medical centers. Urine analysis devices are well suited to deployment as PoC testing such as smart toilets as urine samples are usually available in sufficient quantities, they can be collected non-invasively, and they contain several analytes with diagnostic potential.

We provide a critical review of urine analysis in **Chapter 2** including the analytes of interest found in urine samples and methods to detect these

analytes. The goal of the review was to draw the attention of researchers to targets of interest in remote urinalysis and unconventional monitoring of activities of daily living related to urination that may be indicative of health. Researchers are encouraged to consider the compatibility and integration of sensors when developing new sensor modules to enable the detection of several analytes from each measurement platform.

An approach was taken to improve the sensitivity of fluorescence-based optofluidic sensing devices to improve device sensitivity using TIR. Sensitivity enhancement serves to lower cost by enabling the use of less expensive light sources and detectors. An optofluidic DO sensor was experimentally optimized and the design parameters influencing sensitivity were identified in **Chapter 3**. The sensitivity of the sensor module is determined experimentally by measuring 0-20 ppm DO standards prepared by sparging over a range of incident angles. The limit of detection observed for the experimentally tested device was found to be 0.2 ppm based on the standard deviation of 0 ppm DO standard measurements, which is similar to the accuracy of the instrument used for calibration. The importance of increasing the path length of light used to excite the fluorescent sensitive film to improve signal intensity was highlighted. A simplified series of equations were produced to demonstrate how the average distance between reflection sites within the sensor changes with the type of TIR observed.

A 3D ray tracing model was developed in Zemax OpticStudio based on the experimentally tested DO sensor in **Chapter 4** to expand on the simplified model. The model was then validated using experimental results and applied to additional untested situations. The resulting model explained the TIR sensitivity enhancement mechanism under various coupling strategies that can be applied to a wide range of fluorescence-based optical sensors. In particular, the specifications of the light source used are identified as an important consideration in designing optical sensors and in the accuracy of the optical model. The implications of the model on the design of future optofluidic sensing platforms were speculated.

The design considerations identified in the model were applied to develop an optofluidic ammonia sensor for water and urine samples in **Chapter 5**. The current results for the optofluidic ammonia sensor testing were disclosed with a discussion of current challenges and future work to overcome these challenges. Although the current ammonia sensor

prototype has not demonstrated sensitivity to ammonia, strategies have been identified to overcome current design challenges. A portable fluorescence measurement platform prototype has been developed that can be applied to measurements of fluorescent optofluidic chips.

6.2. DISCUSSION AND FUTURE DEVELOPMENTS

As the discussions for the content of each of the individual chapters are included within each respective chapter, the discussion here will focus on the underlying significance of the contributions to optofluidic sensor design. The relationship between earlier chapters and the significance of overall contributions are discussed in **section 6.2.1**. Speculations are made regarding the application of these contributions to future developments. Future developments and next steps are discussed in **section 6.2.2**.

6.2.1. Discussion

Initially, the motivation for this research project began with an underlying interest in remote monitoring networks for longitudinal health monitoring to assist the aging in place of older adults. The development of point of care fluid monitoring was identified as an effective approach to continuous health monitoring. Many challenges associated with the remote monitoring of bio-fluids are also common to many remote environmental water quality monitoring applications. Although these applications may seem to be very different, the challenges facing these technologies are similar regarding power requirements, cost, and sensitivity. Water pollution has been identified as a significant issue as a result of contamination from industry and agriculture. As a result of water pollution, there are devastating consequences for the health of humans and the natural ecology (10). Water quality issues also have a significant impact on the economy and society (10). The successful development of remote health monitoring networks may also enable further developments towards environment monitoring systems.

As the population continues to age, we are also driven to focus more intently on the health of older adults. There has been interest in promoting aging in place to improve the health and quality of life of older adults while minimizing dependence on hospitals and care centers (11). The successful development of remote monitoring networks for the health of humans and the environment may enable rapid intervention to identified challenges (12,13). Reducing the size and cost of these sensing systems while improving

sensitivity was identified as a promising approach to overcoming the challenges facing the realization of continuous remote sensing networks. We approached the underlying challenge to realizing remote monitoring networks by aiming to optimize the sensitivity of the sensor modules themselves in order to reduce the dependence on expensive components.

Urine samples were identified as a convenient sample that can be obtained non-invasively on a regular basis with significant diagnostic potential. A critical review of urine analysis methods was conducted and optofluidic sensors were identified as promising candidates for PoC diagnostic applications. Optofluidic devices for urine analysis may also be expanded to the analysis of blood and saliva, water quality monitoring, process control applications, and gas sensing (14). It was also realized that these sensors can be used in conjunction with other optical and electrochemical sensors as well as monitors for activities of daily living. The ability to integrate these devices suggests even greater potential for continuous monitoring systems by providing additional context to measurements. Ammonia was identified as a common analyte of interest found in groundwater and urine samples. It was determined that the development of an optofluidic ammonia sensor would demonstrate the significance of sensor optimization for enabling continuous remote monitoring networks for a range of applications.

In the work of Ms. Du (15) a fluorescence-based optofluidic sensor for DO was reproduced and optimized experimentally using the TIR of excitation light. The limit of detection of the experimentally tested DO sensor is similar to the accuracy of the commercial DO sensor used to calibrate the device at 0.2 ppm DO. Three types of TIR were observed and categorized based on the layers within the multilayered sensor that the incident light is confined within. The importance of incident angle and the refractive indices of the materials in the sensor structure are identified as significant design parameters. Other design parameters such as detector placement were also tested, but the incident angle and film thickness proved to be the most significant. The simplified numerical model considers the number of reflection sites that are observed along the length of the device, where the proportion of available energy absorbed is the same for each subsequent spot. In an ideal case where partial reflection losses are neglected and the thickness of the water layer and PDMS cap were negligibly thick, then larger incident angles could be expected to

demonstrate greater absorbance of incident light. If it is estimated that 28% of available energy is absorbed at each site of reflection based on the 14% of measured energy absorbed for a single pass, then approximately 82% of the available incident light can be absorbed over the number of reflections observed at a 34° angle of incidence. If the losses due to partial reflections are not neglected and the coupling efficiency is considered to be proportional to the cosine of the incident angle, then the quantity of light absorbed is reduced. After correcting the predicted energy absorbed by the cosine of the 34° angle of incidence to account for partial reflected losses, this value becomes 68%. The reduction of energy absorbed is expected because although more reflections may be observed along the length of the device, less light is effectively coupled to the substrate and is not available to generate fluorescence. The results suggested that it is important to consider losses due to partial reflections when selecting an incident angle, and thinner sensitive films demonstrate improved sensitivity.

It is expected that the best coupling efficiency should be observed when using a collimated source because all of the light is capable of entering the sensitive volume at the ideal incident angle. However, the diameter of the beam should be smaller than the thickness of the glass substrate to be coupled effectively. If the beam diameter is larger than the substrate, then the light source can be focused into the glass substrate. When focusing a laser source, we start with a collimated beam that can be reduced significantly using an objective lens. When focusing a divergent source such as an LED it needs to be coupled with a lens relay. A 1:1 lens relay will reduce the spot only to the diameter of the emitter which is often much larger than the thickness of the substrate, and projects an image of the emitter. Coupling efficiency is much reduced due to the additional optical surfaces and the apertures required to eliminate the image of the emitter to obtain a uniform illumination. When employing a focused light source for excitation a range of angles injected and the coupling efficiency of each ray depends on its angle relative to the surface of the substrate. The overall coupling efficiency will depend on the NA of the incident light, and the intensity distribution profile of the light source. In both of these cases there will be light injected with lateral angle. The DO sensor testing demonstrated that the sensitivity of fluorescence-based water sensors can be optimized by leveraging TIR, and optimized optical DO sensors have potential for continuous DO sensing.

The DO sensing experiment results were used as a foundation for a 3D ray tracing based optical model demonstrating the path of light inside the device, sites of fluorescence generation, and predicted device sensitivity. The model was validated by comparison with the experimental results as an example of using focused light to generate fluorescence in the multilayered device. Significant design parameters were better understood as the model was adjusted to find agreement with the experiment results. The importance of light source diameter, intensity distribution, and Numerical Aperture (NA) of the coupling optics was identified. The light source parameters were especially important in the focused coupling scenario due to the lateral dispersion of incident light that is not typically observed when using collimated inputs. The model was used to predict how different common coupling scenarios compare under similar experimental conditions. Simulations demonstrated that the optimal angle and coupling scenario used may vary depending on the purpose of the sensing device. The model also identified when to use different coupling strategies depending on whether spatial information is required, how many layers are in the device, and the Refractive Index (RI) of each layer. The results obtained from the experiment and simulation results were used to redesign the setup for fluorescence-based sensing of ammonia.

Finally, work was done to translate the environmental DO sensor platform to PoC urine analysis sensing by using the TIR design to produce an optofluidic ammonia sensor. Other groups have indicated that once an ammonia sensor is developed, variations can be used to indirectly detect other ammonia containing compounds such as Creatinine, Creatine, and Urea in urine samples (4,5). A low-cost portable fluorescence chip reader based on a Raspberry Pi with a camera module is in the final troubleshooting stages. Initial challenges regarding capturing consistent scientific images were overcome (16), and drifting background was corrected by adjusting measurement timing and power management. It was discovered that the signal intensity was low because the fluorescent spot moved out of the center of the field of view after sample injections due to the coupling scenario used, preventing accurate measurements of fluorescence intensity. The model suggests implementing the prism-assisted coupling mechanism should overcome the current design limitations. Although the sensitivity of the current ammonia sensing device has not been demonstrated, several design challenges have been overcome and a portable fluorescence chip reading platform has been developed. A

roadmap has been prepared to complete the testing of the current ammonia sensor, and to adapt the sensor for the detection of Creatinine, Urea, and Creatine.

Significant contributions have been made to the fields of Optical sensing and biomedical engineering as a direct result of the research efforts presented in this dissertation. The critical review of urine analysis will encourage readers to consider integration of sensing methodologies in the development of fluid monitoring systems. Readers are encouraged to consider unconventional measurements such as activities of daily living to provide additional context to measurement results. The experiment setup and results presented by optimizing optical DO sensors are expected to assist future researchers in selecting materials and initial measurement conditions for future sensor designs. The importance of layer thicknesses and incident angle of light are identified as significant design parameters impacting the path length of incident light within the sensitive volume. As a result of the 3D ray tracing simulations, researchers will be able to select an optimal coupling and detection scheme for their specific sensor structure and application. The work towards remote ammonia measurement is not complete but we are now much closer to producing a device capable of remote measurements. A fluorescent chip reading platform capable of measuring optofluidic chips using low-cost consumer electronics is under development. Completion of the portable ammonia sensing platform will reduce the cost of optofluidic sensors towards the realization of portable urinalysis and water monitoring networks.

6.2.2.   Future Developments
The research presented in this dissertation can be advanced by further improving the sensitivity of optofluidic ammonia sensors and reducing the cost and power requirements of remote sensing systems. With sensitivity enhancement and cost reduction the widespread deployment of remote monitoring devices into an integrated sensing network may be realized.

Regarding the 3D optical model, it is expected that the design considerations highlighted in this work will be applied to improving the performance of future optofluidic devices. Sections of the model can be updated to more accurately predict device sensitivity for specific sensor designs with respect to light source parameters, sensor module structure, and detector parameters. In more advanced simulations, the model can be used to determine the location, size, and shape of reflection spots within

multilayered sensors. Further improvements of existing optofluidic devices using the model may enable the use of inexpensive detectors and light sources as a benefit of resulting sensitivity enhancement.

With regard to the remote monitoring device for ammonia detection, with future work improvements can be made in the measurement of the fluorescent spot in order to demonstrate sensitivity to ammonia. With implementation of a prism, the excitation efficiency using bottom side coupling can be improved while reducing the sensitivity to changes in refractive index of the sample. The alignment of the light source to the sensor module is simplified using the prism-assisted coupling scheme considering the relatively large entrance window it provides compared to the edge of the glass substrate. The stability of the laser source during activation and dimming should be improved by limiting the current supplied to the laser. Alternatively, an LED can be used instead of the laser and collimated for further cost reduction if the LED is filtered to remove wavelengths of light that can be measured by the detector. It is possible that thinner sensitive films and protective silicone membranes could provide improvements in device sensitivity and response time if they can be reproduced reliably. The concentration of MSA used in sensitive film sensitization and incubation time may be optimized to adjust the sensitivity of the film to ammonia. Optimizing the gains of the camera and the alignment of the detector to the fluorescent spot may improve the sensitivity of the detector to changes in the scene brightness while reducing noise in the image. An alternative configuration employing a power meter probe or photodiode can be used instead of the camera module for situations where spatial information is not required for cost reduction. Ideally the sensor would have a high sensitivity to wavelengths of light emitted by the fluorescent dye, and the detector element would have a large active area and acceptance angle to improve the collection of signal at the detector. A series of ammonia standards should be measured using the modified device to establish sensitivity to ammonia.

Once an ammonia standard curve has been established, the indirect sensing of additional analytes as ammonia can be demonstrated. Standards of alternative analytes can be processed using an enzymatic reaction to produce ammonia before sensing. The concept can be demonstrated by injecting samples after a reaction is conducted, or by incorporating the appropriate enzyme(s) into a hydrogel layer to be added in future devices.

When the ideal incident angle is used the light coupled to the device is expected to reflect internally from the interface of the sensitive layer and silicone membrane. In this case the light is confined in the sensitive volume and glass substrate, and it is not coupled to the hydrogel layer. The hydrogel layer will not influence the distance between sites of reflection or attenuate the incident light when the ideal incident angle is used. The water channel design used can also be adjusted to provide additional channels that can be accessed sequentially as sensitivity is reduced due to biofouling and photobleaching, extending the time between device maintenance.

The integration of compatible low-cost sensing modules such as recently developed PEDD devices (17) into a single remote monitoring platform provide additional information from each platform. Integration of remote fluid monitoring systems with ADL monitoring and can provide additional context to longitudinal data used in decision making (11, 18). Improvements in security, privacy, and cost reduction are expected to lead to better acceptance of the remote monitoring network, and systems will become more accessible to users. Initially, remote monitoring systems will likely be deployed in areas with access to power where they may benefit larger numbers of people such as in retirement homes, care centers, and hospitals. With further reduction of dependency on power, deployment into remote communities is expected and the emergence of remote monitoring networks for environment quality may be realized.

It is speculated that similar optofluidic devices may even be used to monitor the health of astronauts while in space. NASA has expressed interest in studying changes in the health of astronauts in space and in monitoring the health of crew members on the International Space Station (19). Analysis of biological fluids including urine would be useful to monitor the health and immune status of astronauts, but the collection, storage, and real-time analysis of samples remain challenging (19,20).

6.3. CONCLUSIONS

In conclusion, this thesis contributes to the understanding of sensitivity enhancement and optofluidic sensor design through the optimization of an optofluidic DO sensor using TIR, and the development of an experimentally validated 3D optical model. The model was applied to begin producing an optofluidic sensing platform for the fluorescence-based detection of ammonia for urine analysis and water quality monitoring applications. A

critical review of urine analysis methods was presented as **Chapter 2**. Sensitivity enhancement experiment results and the simplified numerical model explaining the enhancement mechanism were presented in **Chapter 3**. The experimentally validated 3D ray tracing model established from the DO sensor design and a simplified model was presented in **Chapter 4**. The current progress towards the optofluidic ammonia sensor development was presented in **Chapter 5**. Ongoing work to further reduce cost and power requirements of sensing systems will improve the feasibility of optofluidic sensors in remote monitoring networks. Future studies to optimize the fabrication of multilayered optofluidic sensors will enable cost reduction and integration of sensitive films to detect several analytes from a single platform. Future work to improve antifouling coatings, and to observe the impact of antifouling coatings on device sensitivity is expected to improve the useful lifetime of remote sensing platforms.

References

[1]   Lin C-C, Tseng C-C, Chuang T-K, Lee D-S, Lee G-B. Urine analysis in microfluidic devices. Analyst. 2011;136(13):2669–88.

[2]   Mahoney E, Kun J, Smieja M, Fang Q. Review — Point-of-Care Urinalysis with Emerging Sensing and Imaging Technologies. J Electrochem Soc. 2020;167(037518).

[3]   Liu J, Geng Z, Fan Z, Liu J, Chen H. Point-of-care testing based on smartphone: The current state-of-the-art (2017–2018). Biosens Bioelectron [Internet]. 2019;132(November 2018):17–37. Available from: https://doi.org/10.1016/j.bios.2019.01.068

[4]   Waich K, Mayr T, Klimant I. Talanta Fluorescence sensors for trace monitoring of dissolved ammonia. Talanta. 2008;77:66–72.

[5]   Deng S, Doherty W, McAuliffe MAP, Salaj-Kosla U, Lewis L, Huyet G. A low-cost, portable optical sensing system with wireless communication compatible of real-time and remote detection of dissolved ammonia. Vol. 6, Photonic Sensors. 2016.

[6]   Mahoney E, Hsu H-H (Leo), Du F, Xiong B, Selvaganapathy PR, Fang Q. Optofluidic Dissolved Oxygen Sensing with Sensitivity Enhancement Through Multiple Reflections. In: Biotechnology and Bioengineering Conference. Waterloo: University of Waterloo; 2019.

[7]   Xiong B, Mahoney E, Lo JF, Fang Q. A Frequency-domain optofluidic dissolved oxygen sensor with total internal reflection design for in situ monitoring. IEEE J Sel Top Quantum Electron [Internet]. 2021;27(4):1–7. Available from: https://ieeexplore.ieee.org/document/9103235/

[8]   Axelrod D. Total Internal Reflection Fluorescence Microscopy in Cell Biology. Traffic. 2001 Nov;2(11):764–74.

[9]   Le NCH, Dao DV, Yokokawa R, Wells J, Sugiyama S. Design, simulation and fabrication of a total internal reflection (TIR)-based chip for highly sensitive fluorescent imaging. J Micromechanics Microengineering [Internet]. 2007;17(6):1139–46. Available from: http://stacks.iop.org/0960-1317/17/i=6/a=006?key=crossref.da3a64c9a0ab265b3d39ccafc02bfafd

[10]   Ezbakhe F. Addressing Water pollution as a Means to Achieving the Sustainable iMedPub Journals Addressing Water Pollution as a Means to Achieving the Sustainable Development Goals. J Water Pollut Control [Internet]. 2018;1(1:6). Available from: https://www.researchgate.net/publication/330400361

[11]   Nathan V, Paul S, Prioleau T, Niu L, Mortazavi BJ, Cambone SA, et al. A Survey on Smart Homes for Aging in Place: Toward Solutions to the Specific Needs of the Elderly. IEEE Signal Process Mag [Internet]. 2018 Sep;35(5):111–9. Available from: https://ieeexplore.ieee.org/document/8454407/

[12]   Demchenko AP. Introduction to Fluorescence Sensing. Second Edi. Springer International Publishing; 2015.

[13]   Zheng YL, Ding XR, Poon CCY, Lo BPL, Zhang H, Zhou XL, et al. Unobtrusive sensing and wearable devices for health informatics. IEEE Trans Biomed Eng. 2014;61(5):1538–54.

[14]   Aubrecht J, Kalvoda L. Development of Ammonia Gas Sensor Using Optimized Organometallic Reagent. J Sensors. 2016;2016.

[15]   Du F. Development of an Optofluidic Platform Based on Total Internal Reflection- Application of Dissolved Oxygen Sensing for Water Monitoring. 2015;(August):1–86.

[16]   Pagnutti M, Ryan RE, Cazenavette G, Gold M, Harlan R, Leggit E, et al. Laying the foundation to use Raspberry Pi 3 V2 camera module imagery for scientific and engineering purposes module imagery for scientific and engineering purposes. J Electron Imaging. 2017;26(1):013014.

[17]   Perez De Vargas-Sansalvador IM, Fay C, Fernandez-Ramos MD, Diamond D, Benito-Lopez F, Capitan-Vallvey LF. LED-LED portable oxygen gas sensor. Anal Bioanal Chem. 2012;404(10):2851–8.

[18]   Majumder S, Aghayi E, Noferesti M, Memarzadeh-Tehran H, Mondal T, Pang Z, et al. Smart Homes for Elderly Healthcare—Recent Advances and Research Challenges. Sensors [Internet]. 2017 Oct 31;17(11):2496. Available from: http://www.mdpi.com/1424-8220/17/11/2496

[19]   Robinson JA, Thumm TL, Thomas DA. NASA utilization of the International Space Station and the Vision for Space Exploration. Acta Astronaut. 2007;61(1–6):176–84.

[20]   Aponte VM, Finch DS, Klaus DM. Considerations for non-invasive in-flight monitoring of astronaut immune status with potential use of MEMS and NEMS devices. Life Sci. 2006;79(14):1317–33.

Appendix A.

Ammonia Sensing Platform Code Diagrams

Eric James Mahoney

School of Biomedical Engineering, McMaster University, 1280 Main St. West, Hamilton, ON L8S 4K1, Canada

Diagrams of Custom Python Code Developed for Fluorescence Measurement

© The Author (2020)

Launch Program

- Import Libraries
- Initialize Variables
- Initialize Settings
- Set GPIO Pins
- Call Deactivate Laser
- Generate Arrays
- Generate the GUI

Deactivate Laser

- Laser Off

Update Time Stamp → **Update Time Stamp**

Duty Cycle Entry ↔ **Update Duty Cycle**

- Update the Duty Cycle to a user defined value
- Call Report Logs
- Call Force Calibration

Frequency Entry ↔ **Update Frequency**

- Update the PWM Frequency to a user defined value
- Call Report Logs
- Call Force Calibration

Framerate Entry ↔ **Update Framerate**

- Update the Framerate to a user defined value
- Call Report Logs
- Call Force Calibration

User Defined Settings

Accumulations Entry ↔ **Update Accumulations**

- Update the Accumulations to a user defined value
- Call Report Logs
- Call Force Calibration

Force Calibration

- Disable Measurement buttons
- Enable Calibration buttons

ISO Entry ↔ **Update ISO**

- Update the ISO to a user defined value
- Ensure ISO is a multiple of 100 and within range
- Call Report Logs
- Call Force Calibration

Report Logs

- Write an update to the terminal

Exposures Entry ↔ **Update Exposures**

- Update the Exposures to a user defined value
- Call Report Logs

Intervals Entry ↔ **Update Intervals**

- Update the Exposure Interval to a user defined value
- Call Report Logs

Exit Commands

- Call Deactivate Laser
- Release GPIO pins
- Close the GUI

Deactivate Laser

- Laser Off

New Glass Calibration

- Fix exposure settings
- Enable AWB Gain Adjustment
- Prompt user to insert control
- Call Activate Laser
- Wait 2 seconds
- Start Preview
- Wait 1 second
- Disable AWB Gain Adjustment
- Update Logs and Labels
- Continue on click
- For each exposure from 1 to number of accumulations
    - Save PNG image
    - Save YUV image
    - Add to Numpy arrays
    - Loop after laser delay time
- Call Deactivate Laser
- Call Report Logs
- Call Initialize File
- Update button states

Open Bright Calibration
- Not functional

Open Dark Calibration
- Not functional

Open I_0 Calibration
- Not functional

User Defined Settings

New I_0 Calibration

- Fix exposure
- Disable AWB Gain Adjustment
- Update logs
- Prompt user to Insert I_0 control
- Start exposure timer
- Call Activate Laser
- For each exposure from 1 to number of accumulations
    - Save PNG image
    - Save YUV image
    - Add to Numpy arrays
- Call Deactivate Laser
- Stop exposure timer
- Update exposure timer
- Update Button states
- Call Append Exposure

Initialize File
- Write experiment settings to file
- Write result to file

Checkpoint
- Create message box for user feedback

Report Logs
- Write update to terminal

Capture Object
- Capture image as YUV array

Activate Laser
- Call Calculate Frequency and Duty Cycle
- Laser on

Calculate Duty Cycle
- Return Duty cycle as floating point value

Deactivate Laser
- Laser Off

New Dark Calibration

- Fix exposure
- Disable AWB Gain Adjustment
- Update logs
- Call deactivate laser
- Prompt user to ensure lights in enclosure are off
- For each exposure from 1 to number of accumulations
    - Save PNG image
    - Save YUV image
    - Add to Numpy arrays
    - Loop after laser delay time
- Call Append File
- Update Button states

Append Exposure
- Write result to file

Align Laser

- Update Logs file
- Fix exposure settings
- Disable AWB Gain Adjustment
- Start Exposure Time Counter
- Laser ON
- Camera ON and display preview
- Display a message box for the user to end the laser alignment. When clicked:
    - Laser Off
    - Call Report Logs

Report Logs
- Write update to terminal

Test Laser

- Laser ON
- Wait 2 seconds
- Laser OFF
- Call Report Logs

User Defined Settings

Report and Save
- Write logs to terminal
- Write logs to file

Measurement Series
- Determine user defined exposures
- Call Begin Measurement
  - Update first exposure flag
- For each exposure from 1 to number of exposures
  - Wait for the user defined interval
  - Call Begin Measurement
  - Report Logs
- Call Update Time stamp
- Reset flags
- Call Report Logs

Begin Measurement
- Fix exposure settings
- Disable AWB Gain Adjustment
- Update logs
- Prompt user to inject sample
- Wait 2 seconds
- Start exposure timer
- Call Activate Laser
- For each exposure from 1 to number of accumulations
  - Save PNG image
  - Save YUV image
  - Add to Numpy arrays
- Call Deactivate Laser
- Update exposure timer
- Perform Image Math
- Update logs, labels and time stamp
- Call Report and Save

Checkpoint
- Create a message box for user feedback

Report Logs
- Write update to terminal

Capture Object
- Capture image as YUV array

Calculate Duty Cycle
- Return Duty cycle as floating point value

Activate Laser
- Call Calculate Frequency and Duty Cycle
- Laser on

Deactivate Laser
- Laser Off

Appendix B.

Conference Paper - Experiential Learning Of Data Acquisition And Sensor Networks With A Cloud Computing Platform

Eric James Mahoney[1,=], Colleen Chau[1,=], and Qiyin Fang[1,2,z]

[1]School of Biomedical Engineering, McMaster University, 1280 Main St. West, Hamilton, ON L8S 4K1, Canada

[2]Department of Engineering Physics, McMaster University, 1280 Main St. West, Hamilton, ON L8S 4K1, Canada

[=]Contributed equally.

[z]Corresponding Author qiyin.fang@mcmaster.ca

Introduction to conference paper

This work was delivered at the SPIE ETOP 2019 conference in Quebec City by Professor Fang and Ms. Colleen Chau. Professor Fang challenged me to develop a portable sensor station to collect data to be used for teaching and learning applications. As an equally contributing first author I built two identical sensor stations based off of an Arduino UNO to continuously read from a series of sensors. Then I connected both sensor stations to a Raspberry Pi in order to transmit the sensor readings to a server where it could be remotely accessed by students. I prepared the original figures and data sets used in assignment examples from sensor station measurements. Ms. Collen Chau compiled the sensor station results and worked with Dr. Fang to prepare the article manuscript and associated poster.

Contents of conference paper

Abstract

Experimental data acquisition and statistical data analysis are core components in photonics undergraduate curriculum. Although it focuses on experimental data, the content is usually delivered by a lecture-based format. This is partially because the contents are delivered at the beginning of the program when experimental data acquisition techniques have not yet been introduced. In a second-year data acquisition and applied statistics course, we have designed an experiential learning module that covers the fundamental content of data acquisition and statistical analysis. This module uses a single physical experimental setup that is continuously measuring environmental parameters (temperature, humidity, light, imaging, etc.) using a set of multiple modality sensors in an Internet-of-things (IoT) big data platform (Pi Vision, OSI Soft). Different types of sensors measuring the same parameters are also used for cross-validation purposes. The data is streamed to a cloud computing platform, allowing each student to acquire their own subset of data, and then perform processing and analysis. The capability of remote access a physical sensing experiment provide the students hands-on learning opportunities on a managed complex data acquisition system. The platform provides a set of powerful visualization tools to allow a multi-dimension view of complex data streams (e.g. time-lapse of statistical distribution). Such IoT data acquisition platform allows key concepts to be demonstrated, applied, and tested including error propagation, distribution and test of distribution,

correlation and cross-validation, data rejection, and signal processing. This experiential learning module has been demonstrated to be more effective in achieving related learning objectives through quantitative graduate attribute measurements as well as qualitative feedback.

B.1. INTRODUCTION

Most undergraduate engineering curriculum requires applied statistics. A key aspect of applied statistics is closely associated with experimental data acquisition, processing, and analysis. Typically, statistics for engineers is taught through a traditional lecture-based format and provides students with the background and tools necessary for application in engineering concepts. However, students often find it difficult to apply the tools to practical engineering problems because statistics is taught as a theory heavy math course that has limited relationships to their engineering speciality [1].

In the McMaster Engineering Physics program, the first statistics course that the students take is Eng Phys 2W03, "Applied Statistics for Engineering" with a focus on experimental data acquisition and analysis. This course introduces second year engineering physics students to estimation of true value, probability density functions, analysis of variance, experiment design, and application of statistical analysis. The 3-credit unit course consists of three-hour lectures and a tutorial every week over the span of one semester. In the past years, theoretical concepts were delivered through lectures and Matlab and Microsoft Excel was taught in tutorials for data processing and plotting (including curve fitting). The assignments were analytical problems from the textbook (John R. Taylor: "An Introduction to Error Analysis: The study of uncertainties in physical measurements," 2nd Edition, 1997, University Science Books).

Often in early level engineering classes, students have not yet learned data acquisition instrumentation. As a result, the data acquisition and analysis are taught on paper using hypothetical experiments and simulated data sets. The lack of opportunity to connect statistics with other engineering courses causes students to view the course as an entirely separate topic rather than an essential part of engineering practice [1].

Experiential learning is a process through which the learner constructs knowledge, skill, and value from direct experiences. At the undergraduate level for engineers, experiential learning is delivered through course projects, internships, and capstone projects. However, these types of

vehicles for delivery are usually introduced in the senior years when students have the fundamental theoretical knowledge to use during the experience. Engineering students should be introduced to real problems and application of theoretical knowledge as early as possible since they build the critical skills that are vital to the engineering profession [2]. Experiential learning can also provide the means of learning through action as students who chose to study engineering enjoy "doing things" which should translate to better learning outcomes [3].

To address these challenges, we developed an experiential learning module that uses a smart environmental sensing system providing students hands-on experiences to apply the statistics concepts and theories to process and analyze real engineering data. The smart sensor system is capable of continuously measuring multiple environmental factors (temperature, humidity, light, images) with different sets of sensors. The data acquisition is achieved by an Arduino based platform and experimental control and data communication is managed by a Raspberry PI. The data is continuously uploaded to a cloud data platform, PI Vision, created by our industry partner, OSIsoft, where the students can view and download the data for analysis.

B.2. Data Acquisition System (DAQ)

The smart sensor station system that has been developed can be described as a sensing module that periodically measures the local environment, a relay module that sends the data to a remote server, and a webpage-based user interface used to view and export data as shown in Figure B.1.
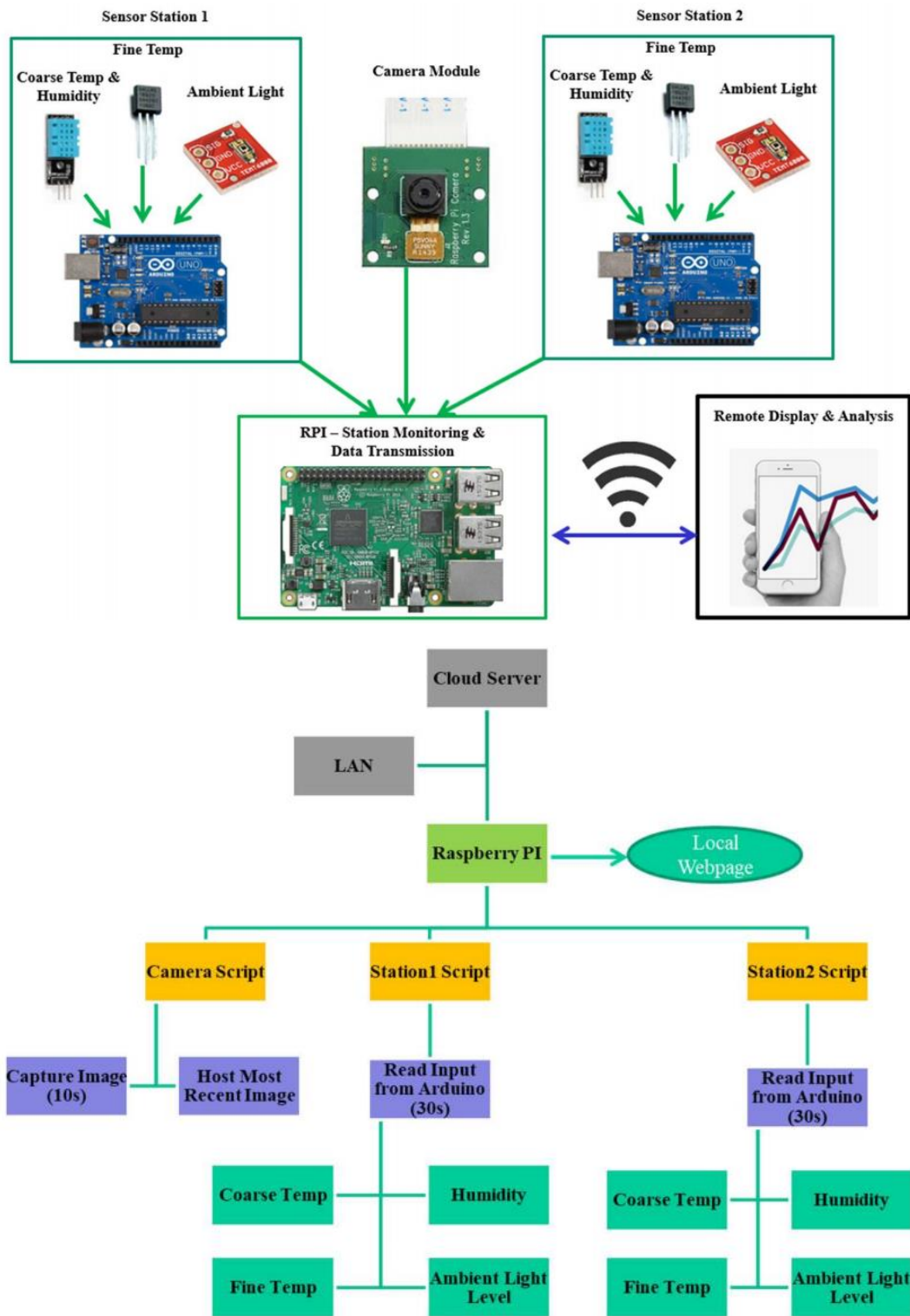
Figure B.1 Sensor station system schematics and process flow

B.2.1. Sensing Module

The sensing module of the DAQ system consists of an Arduino UNO and several sensors for climate monitoring. The sensor set includes an ambient light sensor, two temperature sensors with different precisions, and a humidity sensor. The Arduino UNO is used to measure each group of sensors through its inputs once every 30 seconds. The ambient light sensor is measured as an analog input between 0 and 3.3V where the voltage measured is proportional to the intensity of light in the room. The temperature and humidity sensors are connected as digital inputs and the digital signal is processed to determine the temperature and relative humidity. Two sets of sensors were built into two separate sensor stations. The DAQ system is controlled by a Raspberry Pi (v3 Model B+) equipped with a CMOS camera module to capture pictures of the environment at the moment of each measurement.

The Raspberry Pi serves to distribute power from the supply to the sensor modules, formats the data retrieved from the sensor modules, and relays the results to the cloud based OSIsoft PI Vision server over the internet. The Raspberry Pi runs a python script that allows it to read the sensor results from each Arduino using serial communication; then stream the data to the server as a formatted message that identifies the station, the time the data was captured, the data type, and the measurement result. The data can then be viewed from the PI Vision display in real time and exported for analysis from a computer or wireless device.

B.2.2. Cloud Data Storage and User Interface

The OSIsoft PI Vision is a web enabled user interface that is accessed remotely over the internet as shown in Figure B.2. This enables multiple concurrent users to access results from a browser. After logging in, the display can be configured to show all of the data collected or it can show data for fixed time frames in the form of graph indicators. The data can then be exported from the display for further processing and analysis. Alternatively, gauges and dials can be added to the display to show the most recent results reported by each sensor module. These indicators can be arranged over a schematic such as a floor plan or a front panel display to provide additional context to the data being collected. The display can be easily reconfigured or updated to include additional indicators as additional DAQ modules are added to the system.
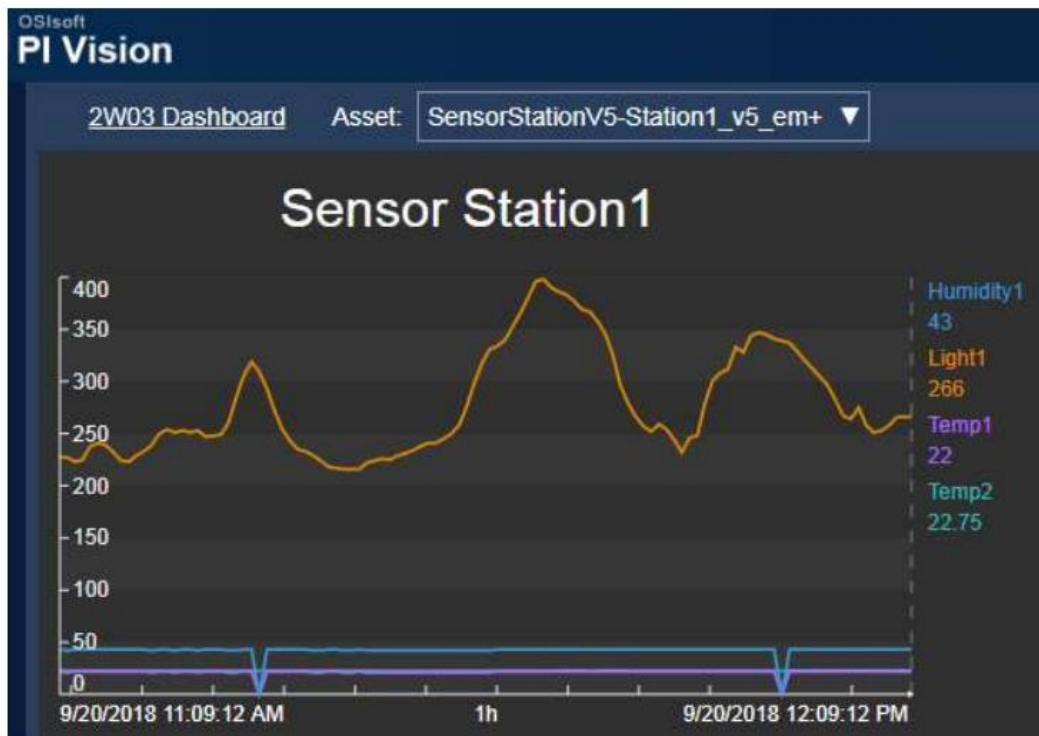
Figure B.2 OSIsoft PI Vision display

B.3. Learning Objectives and Outcomes

The DAQ system was placed facing a window in a room in the Burke
Science Building (BSB) at McMaster University, where all Eng Phys 2W03
students performed their introductory Electromagnetism lab. Hence all
students in this course can physically see, but not adjust, the system
(Figure B.3). Building the unit for the students allows separation of the
challenges in electronics hardware so that they can focus on the data
acquisition aspects, which is the emphasis of the course. In addition, the PI
Vision cloud data platform gives all students access to the data using one
data acquisition module, significantly reducing costs associated with labs,
such as experimental hardware, maintenance, and space. PI Vision also
gives students the flexibility to visualize and analyze the data on their own
time, from any device with internet access. The design allows the
development of additional lectures that cover basic smart sensor technology
and, most importantly, how to deal with real experimental data including
noise, systematic errors, random errors, and multisensor validation (from
different temperature and humidity sensors), correlation, system response,
etc. Abstract concepts (e.g. distributions of random error, correlations

between different sensors (e.g. light vs temperature), erroneous data rejection, digital signal processing, etc.) introduced in the lecture can now be associated with real data sets. At the same time, students still learn to use Matlab and Excel as they are required to process, plot, and analyze data.
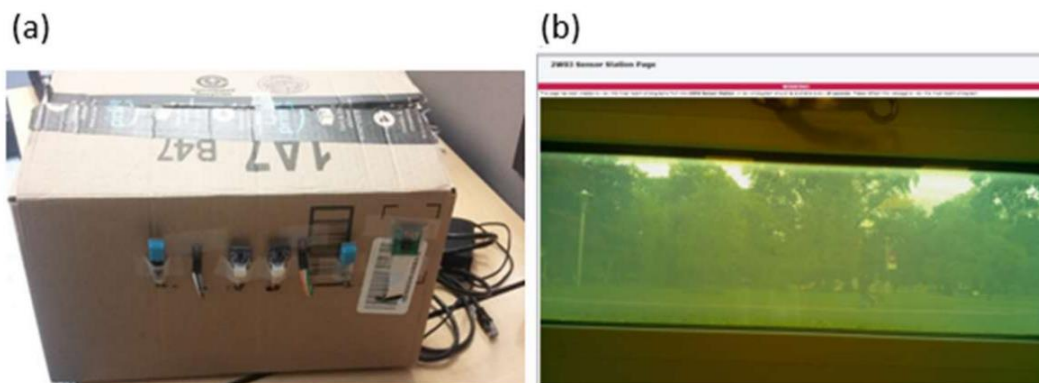
Figure B.3 DAQ sensor system (a) and camera view of the window (b)

The following concepts were taught with the DAQ module:

- Plotting data with error bars
- Understanding differences between different types of sensors of the same sensing parameter
- Plotting sensor data distributions
- Using Chi-squared test of distributions
- Developing hypothesis to explain data trends and hypothesis testing
- Determining outlier rejection
- Making conclusions about whether variables are correlated and how correlated variables can be used to predict each other
- Calculating and determining if variances are caused by random or systematic errors

B.3.1. Assignments and Tutorials

The DAQ system was mostly introduced and discussed in tutorials and assignments so that students would obtain theoretical background knowledge in the lectures. In the first tutorial, students were introduced to the DAQ station. The system was brought to the tutorial session and students were able to physically see the components as the component specifications were being reviewed. The students would be able to view the system anytime in the lab where it is constantly acquiring data, if they wish to see the setup again. The data acquisition process and equipment were

also explained to them. They were then shown how to extract data from the PI Vision dashboard. In subsequent tutorials, the assignments were brought up and the students would self-grade their assignments which will be discussed in the next section of the paper.

The assignments associated with the DAQ system were developed as case studies and followed the flow of the course. The DAQ assignments allowing the students to acquire selected sets (e.g. time frame) of data and work with the data set. Since the DAQ module is acquiring data 24/7, assignments can be designed so that different data sets can be used for different students, preventing plagiarism and promoting higher critical thinking. The learning outcomes for each case study are listed Table B.1 below.

Table B.1 Case Study Learning Outcomes

Case Study 1	Case Study 2	Case Study 3
• Set up remote access, data download • Preprocess the data in Excel or Matlab • Plot selected data with error bars • Understand the differences between different types of sensors of the same sensing parameter	• Plot sensor data distributions • Chi-squared test of distributions • Develop hypothesis to explain data trends and hypothesis testing • Outlier rejection	• Correlation between different sensing modalities • Variances

B.3.2. Case Studies
B.3.2.1.   *Case Study 1*
In the first case study, students learn how to export data from PI Vision and either pre-process it in Excel or import it directly into Matlab. They are then asked to calculate the running average and running standard deviation for a 1-hour window over a 12-hour period. Depending on their student numbers, students were split into two groups, so that each group used a different 12-hour data set. Each of the 4 sensors were plotted as a running average and must include standard deviations with error bars. The students were then asked to give an explanation for the shape of the error bars observed in each series and learn the statistical significance associated with each type of sensor.

The plot of the data is shown in Figure B.4. For regions where the slope looks to be relatively flat, the data is not changing over a long period of time. Therefore, the standard deviation must be small. Where the slope

increases, there is a greater difference between values over time, so the standard deviation must increase.
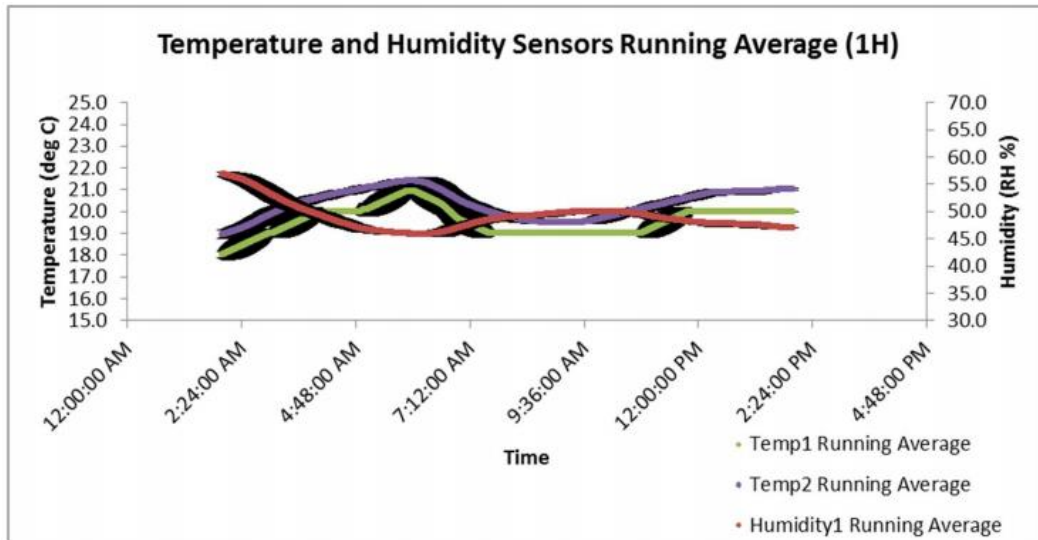
Figure B.4   Temperature and humidity sensor running average plot with standard deviations

For the coarse temperature sensor, there is an egg-shaped error where the temperature changes with greatest error observed when the average is between two discrete temperature values. Error appears to be close to zero when the values are equal to discrete temperature readings. The coarse temperature sensor can only predict temperature in 1-degree increments. To plot an average of 1/2 degree, half of the values must be above and half must be below the average, this is where the error is greatest. When a reading is equal (or almost equal) to a discrete temperature, the temperature reading has been ~constant for 1 hour, so the error is small.

B.3.2.2.   Case Study 2

For the second case study, students were asked to plot histograms of two humidity sensors in the same figure and assume the data follows a normal distribution. They then had to prove or disprove the assumption using a reduced Chi-squared test. If there was any outlier data that they had rejected, they must explain why.

The plots associated with case study 2 is presented in Figure B.5. Figures B.5a and B.5b shows the short and long term humidity sensor plots. After outlier rejection, Figures B.5c and B.5d show the normal distribution and Chi-square tests. The expected counts are determined by looking at the

range of data, average, and standard deviation. Based on the large Chi-squared value, the distribution is determined not normally distributed. Data outliers were defined as data that was greater than 3 standard deviations from the average or if readings of 0% RH are accompanied by 0 on the other sensors.
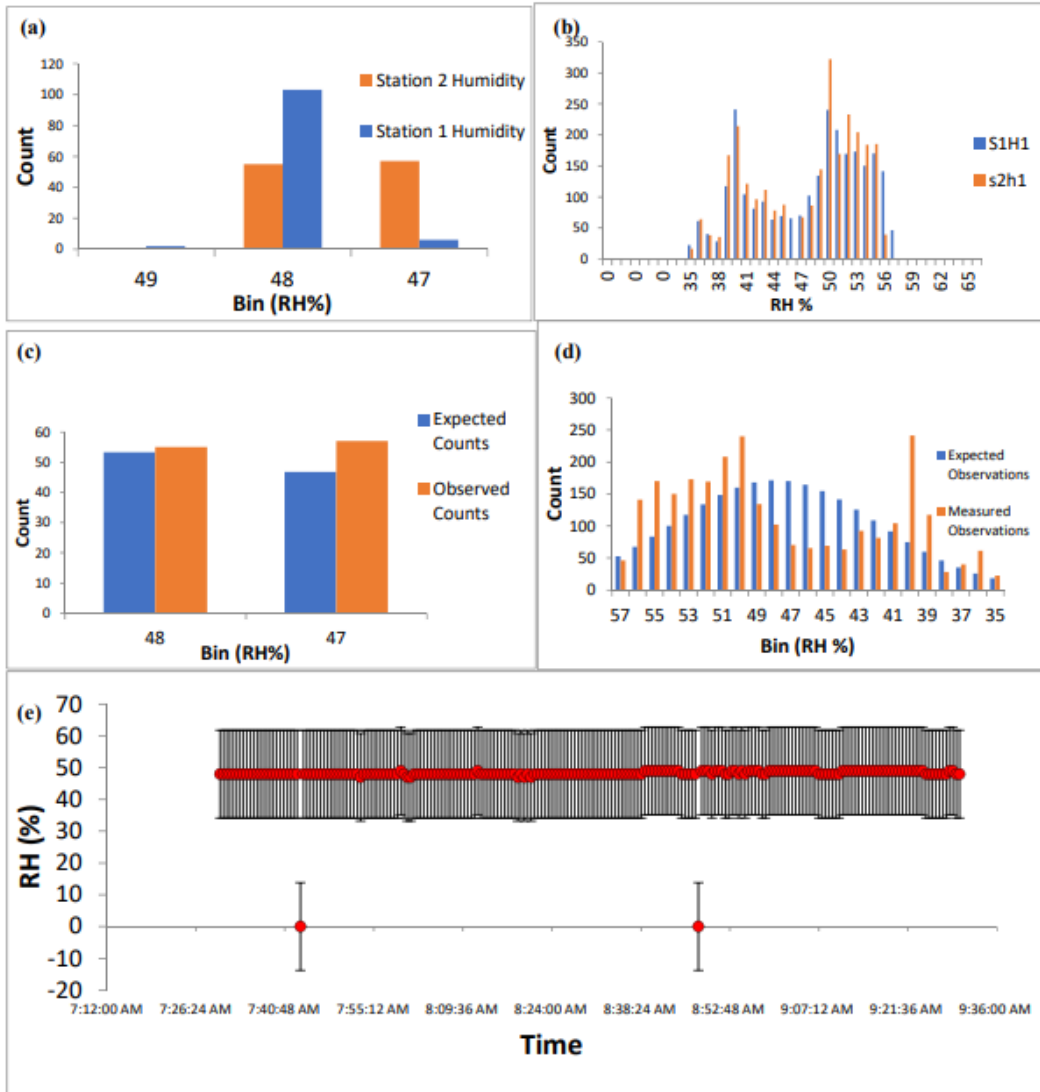
Figure B.5 Short term relative humidity (RH) measurements for two sensor stations (a), and long-term relative humidity measurements for two sensor stations (b). Short term observed vs. expected counts for sensor station 1 after outlier rejection (c) and long term observed vs. expected counts for sensor station 1 after outlier rejection (d). Station 1 relative humidity outlier rejection (e).

B.3.2.3.   *Case Study 3*

Case study 3 tasks the students with producing correlation plots for a 24-hr period to determine if the measured values are correlated with one another. They also compare the fine and course temperature sensors in the same manner. They are then asked to plot the data as a 15-minute moving average with standard deviations for each of the sensors. A trendline is added to determine the R^2 value and trendline equation. The final exercise is to determine the variance for temperature and light levels and whether the observed variance is random or systematic.
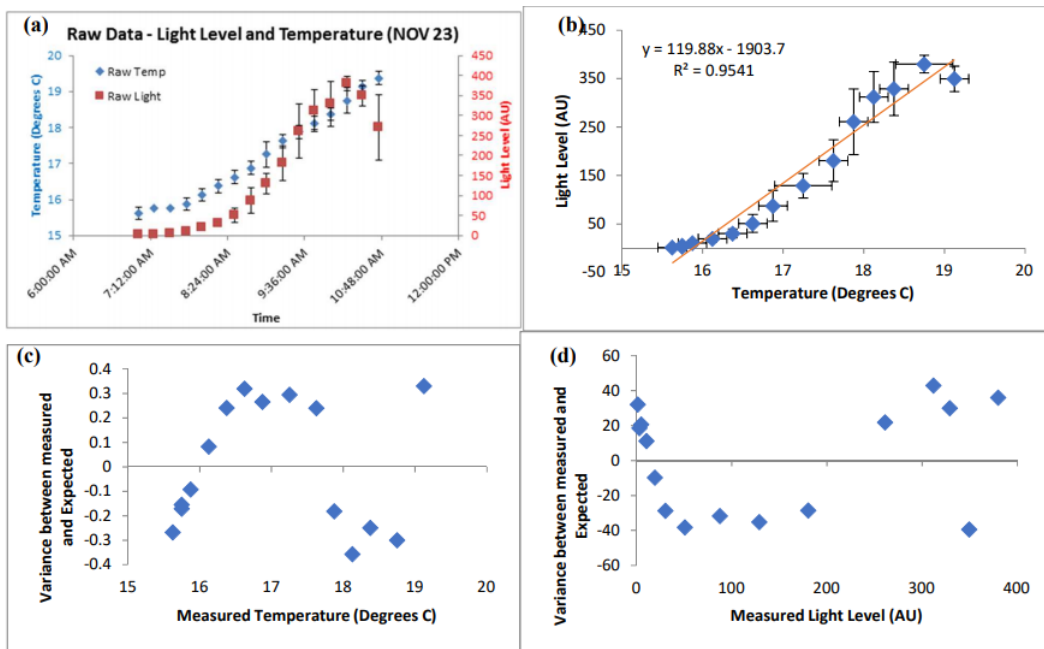
Figure B.6 Temperature and light level over a 4-hour period (a); correlation of temperature and light level (b); variance between measured and expected temperature (c); and variance between measured and expected light level (d).

Figure B.6b shows that when the data is binned into 15 minute averages and after outlier removal, the temperature and light level trends seem to be correlated with each other as indicated by the R^2 value. This case study shows the importance of allowing the students to see the experimental setup and the conditions that the system was in. One would expect that temperature and humidity would correlate well with each other and temperature would also correlate with the light level. However, we see little correlation between temperature and humidity because the DAQ system was placed inside a building that is regulated by HVAC circulation. There is a loose correlation between the temperature and light levels. The DAQ

system is placed at the window where it is exposed to the difference of light levels throughout the day. Despite the HVAC system in the building, the temperature near the glass window will change throughout the day as the sun warms the material, hence the slight correlation.

Having dual temperature sensors and different precision temperature sensors allows for verification and comparison between the same types of sensors. Both the coarse and fine temperature sensors are highly correlated, showing that the variances for temperature sensors indicate systematic error. The camera allows the students to observe the lighting in the window to compare with light level sensor readings throughout the day.

B.3.3. Self – Grading of Assignments

In traditional assignments where the students solve analytic problems, one issue is that they would do the homework but usually will not look at them afterwards. Since identifying their own mistakes is an important learning method, the students brought their completed assignment to tutorial to mark along with the TA, based on a given rubric. The intent is for the students to review their own assignments and reinforce the learning.

B.3.4. Evaluation Structure

The previous year's evaluation structure is compared to this year's evaluation structure in Table B.2. The intent of the DAQ module is to replace the theoretical questions with hands-on data acquisition and provide real data sets to work with. The material developed for the module does not add extra work to the course as the assigned questions from the textbook are reduced to accommodate for the DAQ module. The overall load of the course is not significantly changed.

Table B.2 Evaluation Structure Comparison

	Previous Year's Evaluation structure without DAQ	**Revised Evaluation Structure with DAQ**
Assignments	40%	10%
Mid-term exam 1	20%	20%
Mid-term exam 2	-	20%
DAQ module – hands-on data processing	-	10%
Final exam	40%	40%

B.3.5. Metrics

The metrics used to evaluate the learning outcomes with the new DAQ module was by comparing the midterm and exam scores from previous years and through the Canadian Engineering Accreditation Board (CEAB) graduate attribute measurement in knowledge base competence.

Although the questions in the midterms and exams vary from year to year, the difficulty level and concepts tested are comparable. In the first midterm, the class average was 78±12%, which is significantly better than the average grade of 66±15% during 2014-2015 using similar questions. We also saw significant increase in final exam grade: 75±14 %, over 55±15% in 2014-2015. However, the final exam questions are different between the two years so the results are not directly comparable.

The Canadian Engineering Accreditation Board (CEAB) accredits undergraduate engineering programs. One of their accreditation evaluation criteria is graduate attributes which means that the institution must demonstrate that the graduates of a program possesses competency in certain areas. The indicator for knowledge base competence in natural sciences and engineering fundamentals was chosen to evaluate the performance outcomes of the effectiveness of the DAQ. The 2018 assessment is compared to the last assessment done in 2014. The data presented in Figure B.7 indicates that there was no statistical significance between the two years.
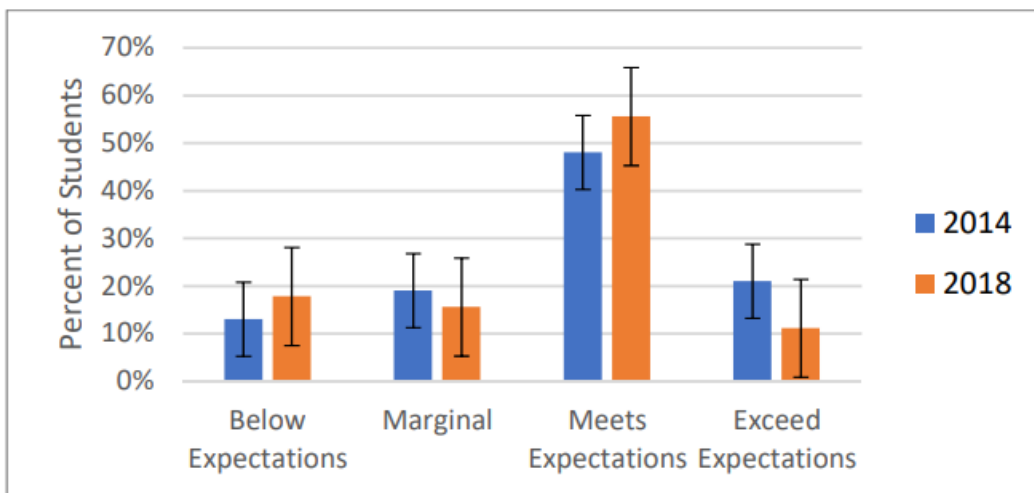
Figure B.7 Eng Phys 2W03 graduate attributes assessments

These measurements do not show a systematic and statistically significant measurement on student's learning outcomes. Without a control group, it reduces the ability to make casual conclusions. In order for this to be a robust pedagogy research experiment, we would need to run a control group that does not include the DAQ module alongside a group that uses the DAQ module. We need to take into account the student's experience about the addition of the new module as this module is meant to be an experiential learning experience. We would also need a way to measure the carry over of knowledge to other courses and projects. However, based on the midterm and exam data that we have, we can hypothesize that the DAQ module may improve engineering students' fundamental tool box in math and statistics through a hands-on experience that allows them to see and understand the experimental conditions based on exam scores. We hope that the they will be able to link the material learned in this course to their future courses and labs.

B.4. Conclusion

As technological advances are made and are accessible to students and educational institutions, our methods of teaching are also able to evolve to more efficiently teach our future engineers. With this DAQ system, students perform and learn data acquisition, processing, and statistical analysis through IoT big data platform. The experiential learning module that we have created encourages a hands-on approach to statistics which is what engineers need to see their theory put into practice. As a result, students achieved higher test results and can link the content learned in this course to other courses, laboratories, and hopefully in their professional careers.

B.5. Acknowledgement

B.6. References

[1]   S. Bisgaard, "Teaching statistics to engineers," The American Statistician, vol. 45, no. 4, pp. 274-283, 1991.

[2]   A. Hajshirmohammadi, "Incorporating Experiential Learning in Engineering Courses," IEEE Communications Magazine, vol. 55, no. 11, pp. 166-169, 2017.

[3]   R. J. Wilson, ""WHAT DOES THIS HAVE TO DO WITH US?" TEACHING STATISTICS TO ENGINEERS," in ICOTS-6, the Sixth International Conference on Teaching Statistics, Cape Town, 2002.

B.7. Arduino UNO Code

The code flashed to the Arduino UNO determines the maximum rate of sensor readings. When it is not connected to a Raspberry Pi the device will report the sensor readings to an LCD screen so it can still be used locally but the results are not saved. When connected to a Raspberry Pi or other computer it will send the results in a CSV format where it can be directly plotted on the receiving end, or the results can be saved and sent to a server for visualization.

```
// Prepared by: Eric Mahoney
// Date: 20190125
// Source: original concept from maker.pro rpi tutorial
// Purpose: Establish connection between Arduino and Pi
//    Read input from sensors and pass data to Pi as text

#include <Wire.h>     //Wire Library
#include <OneWire.h>  //OneWire Library is used for communicating with the
DS18B20 chain
#include <DallasTemperature.h>
#include <Adafruit_Sensor.h>
#include <DHT.h>  //libraries for the humidity sensors
#include <DHT_U.h>
#include <LiquidCrystal.h>

/*Variables*/
unsigned long mstime;   //time in ms since launch
#define DS18S20_Pin 3   //DS18S20 Signal pin
#define DHTPin_1 2      //DHT-11 signal pin
#define LightPin A1     //Analog Light sensor signal pin

int temp1;
float temp2;
int humidity1;
```

```
int light1;

//Temperature chip i/o
OneWire ds(DS18S20_Pin);  //pin defined above

//Telling Dallas Temp to use the Onewire Library
DallasTemperature sensors(&ds);
DHT dht(DHTPin_1,DHT11);
LiquidCrystal lcd(8, 13, 9, 4, 5, 6, 7);

void setup() {
  // put your setup code here, to run once:
  delay(500);
  Wire.begin();
  delay(500);
  Serial.begin(9600); //Start the serial connection
  delay(500);
  lcd.begin(16, 2);
  delay(500);
  lcdinitialize(); //wait for initialization
  delay(1000);

  pinMode(LightPin, INPUT);

  //serialinitialize();
  sensors.begin();
  dht.begin();
  delay(250);
}

void loop() {
  // put your main code here, to run repeatedly:

  //read from the sensors
  humidity1 = dht.readHumidity();
  temp1 = dht.readTemperature();
  light1 = analogRead(LightPin);

  //get temperatures and assign to variables
  sensors.requestTemperatures(); //command to get temps
  temp2 = sensors.getTempCByIndex(0);

  delay(1000);
  Serial.print(temp1);
  Serial.print(",");
  Serial.print(temp2);
  Serial.print(",");
  Serial.print(humidity1);
  Serial.print(",");
  Serial.println(light1);
```

```
  lcdwrite();
  delay(500); //always wait .5 seconds
  delay(30000); //limit the loop speed here.
}

void lcdwrite(){
  //reset the LCD and print the newest measurements
  lcdinitialize();
  delay(500);

  lcd.setCursor(3,0);
  lcd.print(temp1);
  lcd.setCursor(5,0);
  lcd.print(char(223));
  lcd.setCursor(6,0);
  lcd.print("c");
  lcd.setCursor(12,0);
  lcd.print(light1);
  lcd.setCursor(3,1);
  lcd.print(temp2);
  lcd.setCursor(12,1);
  lcd.print(humidity1);
  lcd.setCursor(14,1);
  lcd.print("%");
}

void lcdinitialize(){
//  Serial.print("Initializing LCD");
  lcd.clear();
  lcd.setCursor(0,0);
  lcd.print("T1:");
  lcd.setCursor(9,0);
  lcd.print("L1:");
  lcd.setCursor(0,1);
  lcd.print("T2:");
  lcd.setCursor(9,1);
  lcd.print("H1:");
//  Serial.print("Completed!");
}

/*
void serialinitialize(){
  Serial.println("Connection established");
  Serial.println("Temp1 | Temp2 | Temp3 | Humidity1 | Humidity2 | Light");
}
*/
```

B.8.   Python Code

The Python code on the Raspberry Pi allows the device to connect to the remote server through a configured internet connection. If a connection is lost the program will automatically try to reconnect to the server once the connection is restored. The Pi can be set to read from the Arduino more slowly than the Arduino makes measurements, setting the minimum reporting frequency. The code may have to be updated as the login credentials for the remote server are changed. A separate python script is run to listen to each connected Arduino sensor station to uniquely identify each data stream. In future versions the Arduino can report an ID to the Pi or computer, or report directly to the remote server. An example python code for one of the two sensor stations is presented here. The major differences between variants of this code are to uniquely identify streams, and to accommodate the different sensors on each individual sensor station. Each sensor station was updated and deployed in different spaces after the initial build including for basement temperature and water heater monitoring, and bathroom monitoring with a medication compliance monitoring device.

```
# Prepared by: Eric Mahoney
# # # With python script from OSIsoft for communication
# Date: 2018 09 04
# Purpose: Establish connection between RPi station and OSIsoft server
# Description:
# # # Arduino is continuously monitoring a constant number of sensors for input
# # # The arduino is connected to the RPi by serial on /dev/ttyACM0
# # # Arduino is sending results on one line as a string through serial.
# # # The data is received as a string and human readable data are printed
# # # The results are read as a csv string, filtered to extract the values
# # # A time stamp is captured by the Pi when the values are read from arduino
# # # The individual values with time stamp are sent to the OSIsoft servers
#
#
######### Each sensor station will need to have its own unique ID, the sensors read
on each station can be common.


# Import packages - for Arduino
import serial
import RPi.GPIO as GPIO
import time
# Additional Imports for OSIsoft
import datetime
import json
```

```
import random
import requests
import sys
import time
import warnings
# NOTE: May require uninstall --purge of old pip, reinstall pip and pip3 to solve
requests errors
from requests.packages.urllib3.exceptions import InsecureRequestWarning
from picamera import PiCamera

##camera = PiCamera()

# DO NOT CHANGE THE VALUES BELOW UNLESS TOLD TO DO SO
# CONNECTION TO ACADEMIC HUB MAY STOP IF INCORRECT VALUES ARE
PROVIDED
APIM_KEY = '                                    '
DEFAULT_OMF_URL = '                                              '
PRODUCER_TOKEN = "                   "




####################################
### Code by Eric starts here ###
####################################

# ESTABLISH SERIAL CONNECTION TO ARDUINO UNO STATION #
ser=serial.Serial("/dev/ttyACM1",9600) #ACM1 for Arduino2, can be updated
ser.baudrate=9600    #A dummy connection is implemented

with ser: #reset the DTR - reset arduino
    ser.setDTR(False)
    time.sleep(1)
    ser.flushInput()
    ser.setDTR(True)


ser=serial.Serial('/dev/ttyACM1',9600)#reestablish the serial connection for Arduino1
ser.baudrate=9600

'''
## Header rows not used anymore, only sending data ##
read the header rows for print only
time.sleep(0.25)
read_ser=ser.readline()
print(read_ser)
time.sleep(0.25)
read_ser=ser.readline()
print(read_ser)
#headerrows are now initialized
'''
```

```
##################################
### END CODE BY ERIC ##########
##################################
```

```
# OMF Messages generated and sent below are compliant with the following
specification:
#   The OSIsoft Message Format, v1.0: http://omf-docs.osisoft.com/en/v1.0/
#

# To avoid certificates and deprecation warning
warnings.filterwarnings("ignore", category=DeprecationWarning)
requests.packages.urllib3.disable_warnings(InsecureRequestWarning)


def create_data_values_stream_message(target_stream_id):
    timestamp = datetime.datetime.utcnow().isoformat() + 'Z'

    ##################################
    ### Code by Eric starts here ###
    ##################################
    # READ INPUT STREAM FROM ARDUINO #

    time.sleep(1)
    read_ser=ser.readline()#read the input from the arduino
    ## variable used by OSIsoft ----- timestamp = time.time()#take a time stamp (epoch)
at measurement

    inputstr = (str(read_ser))#read the input from arduino as string

    #using formatting to extract the values from the string into an array
    newstr = ''.join((ch if ch in '0123456789.-e' else ' ') for ch in str(inputstr))
    inputVariables = [float(i) for i in newstr.split()]#build array of sensor values
    ###inputVariables = [1.1, 2.2, 3.3, 4.4]

    #Values extracted from Arduino1
    temp1 = inputVariables[0]
    temp2 = inputVariables[1]
    humidity1 = inputVariables[2]
    light1 = inputVariables[3]

    #Capture an image when the input is received
    ##camera.capture('/home/pi/Desktop/image.jpg')

    print ("time: " + str(timestamp) + " T1: " + str(temp1) + " T2: " + str(temp2) + " H1: "  +
str(humidity1) + " Light1: " + str(light1))

    ##################################
```

```
        ### END CODE BY ERIC ##########
        ###############################


    data_values_json = [
        {
            "containerid": target_stream_id,
            "values": [
                {
                    "Time": timestamp,
                    "Temp1": temp1,
                    "Temp2": temp2,
                    "Humidity1": humidity1,
                    "Light1": light1
                }
            ]
        }
    ]
    return data_values_json



    # ************************************************************************
    def sendOMFMessageToEndPoint(relay_url, message_type, omf_data, echo=True):
        try:
            msg_header = {'producertoken': producer_token,
                        'messagetype': message_type,
                        'action': 'create',
                        'messageformat': 'JSON',
                        'omfversion': '1.0',
                        'connection': 'keep-alive',
                        'Ocp-Apim-Subscription-Key': APIM_KEY}
            data = json.dumps(omf_data)
            if echo:
                print('> ------ Message sent begin -------')
                print('>> Headers:', msg_header)
                print('>> Message: ', data)
                print('> ------ Message sent end   -------')
            response = requests.post(relay_url, headers=msg_header, data=data, verify=False,
timeout=30)
            if echo:
                print('< ------ Response received begin -------')
                print('>> Status code:', response.status_code)
                print('>> Headers:', response.headers)
                print('>> Message: ', response.text)
                print('< ------ Response received end -------')
            print('Response from relay from the initial "{0}" message: {1} {2}
(len={3})'.format(message_type,
                                                    response.status_code,
                                                    response.text, len(data)))

            return response.status_code
```

```
        except Exception as e:
            print(str(datetime.datetime.now()) + " An error occurred during web request: " +
str(e))
            return 500


    # *********************************************************************


    types = [
        {
            "id": "type_SensorStation_v5",
            "type": "object",
            "classification": "static",
            "properties": {
                "Name": {
                    "type": "string",
                    "isindex": True
                },
                "Location": {
                    "type": "string"
                }
            }
        },
        {
            "id": "type_measurement_v5",
            "type": "object",
            "classification": "dynamic",
            "properties": {
                "Time": {
                    "format": "date-time",
                    "type": "string",
                    "isindex": True
                },
                "Temp1": {
                    "type": "number"
                },
                "Temp2": {
                    "type": "number"
                },
                "Humidity1": {
                    "type": "number"
                },
                "Light1": {
                    "type": "number"
                }
            }
        }
    ]
```

```python
def container_value(name):
    containers = [{
        "id": "measurement_%s" % name,
        "typeid": "type_measurement_v5"
    }]
    return containers


def static_value(name):
    static_data = [{
        "typeid": "type_SensorStation_v5",
        "values": [{
            "Name": "SensorStationV5-%s" % name,
            "Location": "Hamilton, ON"
        }]
    }]
    return static_data


def link_value(name):
    link_data = [{
        "typeid": "__Link",
        "values": [{
            "source": {
                "typeid": "type_SensorStation_v5",
                "index": "_ROOT"
            },
            "target": {
                "typeid": "type_SensorStation_v5",
                "index": "SensorStationV5-%s" % name
            }
        }, {
            "source": {
                "typeid": "type_SensorStation_v5",
                "index": "SensorStationV5-%s" % name
            },
            "target": {
                "containerid": "measurement_%s" % name
            }
        }]
    }]
    return link_data

if __name__ == "__main__":
    #print("Enter custom URL for Relay, or <ENTER> for Academic Hub:\n  >> ", end='')
    #relay_url = input()
    #if len(relay_url) == 0:
    relay_url = DEFAULT_OMF_URL
    producer_token = PRODUCER_TOKEN
    print("@@@ current producertoken= %s" % producer_token)
```

```
      #print("> Enter a word to name test tank element in AF: ", end='')
      #name_input = input()
      af_name = "Station2_v5_em"
      if len(af_name) == 0:
         print("\n >>> Input word cannot be empty. Stopping.")
      else:
      ########### LOOP STRUCTURES HAVE BEEN ADDED TO ALLOW THE DEVICE
TO RESTABLISH CONNECTION ############
         while True:
            if sendOMFMessageToEndPoint(relay_url, "Type", types) > 202:
               #sys.exit(1)
               time.sleep(1)
            else:
               break

         while True:
            if sendOMFMessageToEndPoint(relay_url, "Container",
container_value(af_name)) > 202:
               #sys.exit(1)
               time.sleep(1)
            else:
               break
         while True:
            if sendOMFMessageToEndPoint(relay_url, "Data", static_value(af_name)) > 202:
               #sys.exit(1)
               time.sleep(1)
            else:
               break
         while True:
            if sendOMFMessageToEndPoint(relay_url, "Data", link_value(af_name)) > 202:
               #sys.exit(1)
               time.sleep(1)
            else:
               break
         # ********************************************************************
         while True:
            values = create_data_values_stream_message("measurement_%s" % af_name)
            while True:
               if sendOMFMessageToEndPoint(relay_url, "Data", values) > 202:
                  #sys.exit(1)
                  time.sleep(1)
               else:
                  break
            time.sleep(1)
```